Synthesis of novel single-source precursors for CVD of mixed-metal tungsten oxide

Choujaa, Hamid

Award date:
2008

Awarding institution:
University of Bath

Synthesis of novel single-source precursors for CVD of mixed-metal tungsten oxide

Hamid Choujaa

A thesis submitted for the degree of Doctor of Philosophy

University of Bath

Department of Chemistry

March 2008

TABLE OF CONTENTS

Choujaa,

ABSTRACT

There is a considerable interest in the use of tungsten oxide in the research and development of new materials and devices, such as gas sensors and as photocatalysts. In order to improve the photocatalytic properties of WO_3, its combination with metals which allows the preparation of WM_xO_y materials are believed to be promising photocatalysts under visible light. The present work deals with the synthesis of homo- and hetero-metallic tungsten alkoxide and amide compounds using the single source precursor approach for potential chemical vapour deposition precursors of mixed-metal oxide films.

Chapter 1 provides the general background about the structure of tungsten oxide in relation with its properties and the different methods of WO_3 film deposition. It also reviews the precursors previously used for the chemical vapour deposition of WO_3 and mixed-metal tungsten oxides.

Chapter 2 deals with functionalized tungsten alkoxides/amino-alkoxides, their hydrolysis and pyrolysis. The reaction of $[WO(OPr^i)_4]_2$ with L = $HOCH_2CH_2NMe_2$ (dmae); $HOCH(CH_2CH_2NMe_2)_2$ (bdmap); $HOC(CH_2CH_2NMe_2)_3$; (tdmap) generated $WO(OPr^i)_3(L)$ which have been characterized. The use of multi-dentate chelating alkoxides enhanced the solubility and the stability of these oxo-alkoxides. Micro-hydrolysis of these alkoxides produced a range of oxo-tungsten clusters [$W_4O_4(\mu_2\text{-}O)_6(tdmap)_4$, $W_4O_4(\mu_2\text{-}O)_4(OPr^i)(bdmap)_4$, $W_6O_6(\mu_2\text{-}O)_9(bdmap)_6$] which have been structurally characterised. The pyrolysis of $W_4O_4(\mu_2\text{-}O)_6(tdmap)_4$ in the air at 600°C provided WO_3 nanoparticles.

Chapter 3 deals with the synthesis and pyrolysis of novel heterobimetallic tungsten alkoxide/amino-alkoxide and alkoxide/acetylacetonate. The interaction of $WO(OPr^i)_3(bdmap)$ with $Ti(OPr^i)_4$, $Al(OPr^i)_3$ and $Zn(acac)_2$ in presence of moisture lead to a range of hetero-metallic compounds which have been characterised. An innovating synthetic pathway was investigated which produced $[M(acac)WO(OMe)_5]_2$ (M = Co, Ni, Mg, Zn) in quantitative yield by using M(acac)(OMe) and $WO(OMe)_4$. The pyrolysis of $[M(acac)WO(OMe)_5]_2$ (M = Co, Mg) at 700°C in a closed container produced carbon nanotubes filled with an *in situ* grown WO_3 and nanoparticles of $MgWO_4$.

Chapter 4 deals with the synthesis and characterization of heterobimetallic tungsten amides complexes from $W(^tBuN)_2(^tBuNH)_2$. The solid state and gas phase structure of the used intermediate $W(NHBu^t)_2(NBu^t)_2$, which is an important CVD precursor for WN_x, have been determined. Highly soluble heterobimetallic compounds has been prepared and fully

characterized by the interaction of $W(NHBu^t)_2(NBu^t)_2$ with $ZnMe_2$ giving by multi-step reaction the unexpected compound $MeZn(NH_2{}^tBu)(\mu\text{-}N^tBu)_2(N^tBu)WMe$ **(17)**.

Also, the reaction of $Li_2W(NBu^t)_4$ with $SbCl_3$ produces a remarkable compound $Sb_2W(NBu^t)(\mu_2\text{-}NBu^t)(\mu_3\text{-}Bu^tN)_2Cl_3(\mu_2\text{-}Cl)$ **(19)** which has been fully characterised. However, the presence of moisture produces also a range of hydrolysis products which have been identified by and characterized structurally.

ACKNOWLEDGEMENTS

First of all, I would like to thank my supervisor, Pr. Kieran Molloy for all his guidance and support during this work, and especially during this writing of this thesis.
I am also grateful to Dr. Andrew L. Johnson for all his help and his guidance during this research project. I must also thank Dr. Mary Mahon and Dr. Gabriele Kociok-Köhn for all the crystallographic data including crystal structures and powder X-ray crystallography, Alan carver for the elemental analysis, Dr. John Lowe for his help for some NMR characterisations, Dr. Mark Russell for his help concerning IT.

I would also like to thank all my friends, my officemates, labmates, my flatmates, my mates, Graeme, Nathan, Andy, Ali, Adama, Anaga, Vedad, Marcia Van Gool.

Finally, I would like to a special thank to my family for their support.

ABBREVIATIONS AND ACRONYMS

Acac	Acetylacetanate
AA-CVD	Aerosol-Assisted Chemical vapour deposition
AP-CVD	Atmospheric Pressure CVD
ALD	Atomic layer deposition
bdmap	1,1-bis(dimethylamino)propan-2-olate
CVD	Chemical Vapour Deposition
Cy	Cyclohexyl
C.N	Coordination number
COSY	COrrelation SpectroscopY
1D	One dimensional
2D	Two dimensional
DEPT	Distortionless Enhancement by Polarization Transfer
diars	ortho-phenylenebis(dimethylarsine)
dmae	Dimethylaminoethanolate
dppe	1,2-bis(diphenylphosphino)ethane
DSC	Differential Scanning Calorimetry
E_g	Band-gap energy
EC	Electrochromic
EDX	Energy dispersive X-ray
EI	Energy Ionisation
ESI	Electro Spray Ionization
Et	Ethyl
FT-IR	Fourier Transform Infra-Red
GC-MS	Gas chromatography-Mass spectrometry
h	hexagonal
$h_{exp.}$	Experimental hydrolysis ratio
$h_{t.}$	Theoritical hydrolysis ratio
hfac	1,1,1,5,5,5-hexafluoroacetylacetonate
HMQC	Heteronuclear Multiple Quantum Coherence
LI-CVD	Liquid injection CVD
LP-CVD	Low Pressure CVD

m	monoclinic
M	Metal
Me	Methyl
MFC	Mass Flow Controller
MOX	Metal Oxide
NHE	Normal Hydrogen Electrode
NMR	Nuclear Magnetic Resonance
o	orthorhombic
O.S	Oxidation State
Pr^i or ^iPr	Isopropyl
PVD	Physical Vapour Deposition
PXRD	Powder X-ray Diffraction
R.T	Room temperature
SEM	Scanning electron microscopy
SSP	Single Source Precursor
^tBu, Bu^t	Tertiary butyl
tdmap	1,3-bis(dimethylamino)-2-(dimethylaminomethyl)propan-2-olate
TEM	Transmission electron microscopy
tfac	trifluoroacetylacetonate
TGA	Thermo Gravimetric Analysis
THF	Tetrahydrofuran
Tof	Time of flight
vs	Versus
VT	Variable Temperature

Chapter 1

Introduction

1.1 Generality about tungsten(VI) oxide

1.1.1 The different lattice structures of tungsten oxide

Tungsten trioxide **(WO_3)** shows a cubic perovskite-like structure based on the corner sharing of WO_6 regular octahedral (Figure 1.1). This structure is based on the ideal perovskite-like structure (ReO_3) from which it takes its common name (ReO_3-structure). This type of structure, which forms the basis of perovskites, is one of the most important ternary systems. In the case of $W^{VI}O_3$, the center of the unit cell is unoccupied due to the valence state of W(VI) which is 6+ with the 5d shell being empty. The crystal network of WO_3 can also be viewed as the result of an alternating disposition of O and WO_2 planes. The perovskite structure can become more compact by the incorporation of a cation in the centre of the unit cell. For $Sr^{II}Ti^{IV}O_3$, the vacant twelve-coordinate position at the centre is occupied by Sr(II) due to the valence state of Ti(IV) which is 4+ .[1, 2]

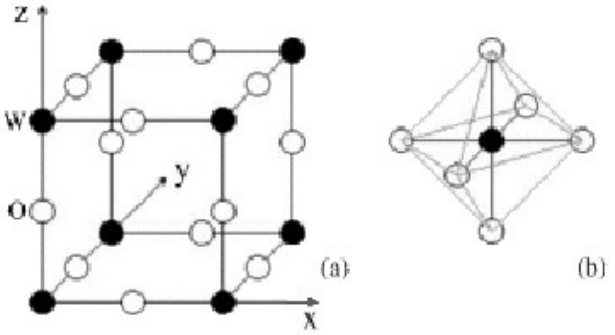

Figure 1.1 The Rhenium-type structure of WO_3.[1] (a) The ideal cubic structure of WO_3. (b) The WO_6 octahedra

The symmetry of tungsten oxide is slightly distorted due to the tilting of WO_6 octahedra and displacement of tungsten from the centre of its octahedron. The details of these distortions give rise to several temperature dependant phase transitions. In fact, tungsten oxide adopts at least five distinct crystallographic structures from 900 to -180°C, changing on cooling from tetragonal (α-WO_3) → orthorhombic (β-WO_3) → monoclinic (γ-WO_3) → triclinic (δ-WO_3) to monoclinic (ε-WO_3).[3] The triclinic and monoclinic modifications are stable at room temperature.[4] Stoichiometric WO_3 is pale yellow in colour. The cell parameters of γ-WO_3 are: a = 7.297, b = 7.539, c = 7.688 Å, β = 90.91°.[3, 5]

The second stoichiometric form of tungsten oxide is tungsten dioxide **(WO_2)**. The WO_2 structure exists as a monoclinic phase at ambient pressures over the temperature range 273 < T < 1803 K.

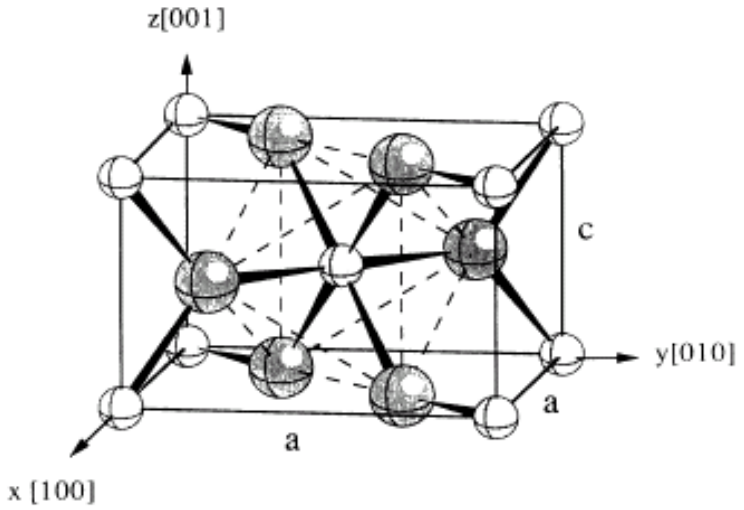

Figure 1.2 Structure of rutile WO_2

Tungsten dioxide has a distorted rutile structure (Figure 1.2). The tungsten dioxide structure is again built up from WO_6 octahedra.[6] The cell parameters of WO_2 are: a = 5.563, b = 4.896, c = 5.663 Å, β = 120.47°. In addition, the tungsten oxide structure has several kinds of defects. As in most **M**etal **OX**ides (**MOX**), the most elementary defect is the lattice oxygen vacancy, where an oxygen atom is absent from a normal lattice site. WO_3 easily forms sub-stoichiometric compounds, such as WO_x, also known as Magnéli phases. From an electronic point of view, tungsten oxide acquires semiconducting properties due to the oxygen vacancies which increase the electronic density on the adjacent metallic (W) cations.[1, 7]

The sub-stoichiometric tungsten oxide WO_x (x<3) is coloured blue. This is generally attributed to an excess of electron charge localised at the octahedral base unit $W^{5+}O_6$.[8] Moreover, tungsten trioxide, due to this vacant centre, is able to incorporate fully or fractionally alkali metals, ammonium ions, hydrogen at the centre of the perovskite to form tungsten bronzes, such as Na_xWO_3. For sufficiently high concentrations of interstitial ions, these bronzes become metals, and in some cases even superconductors.[9]

1.1.2 Electronic and surface structure of WO_3

Unlike metals which have a continuum of electronic states, semiconductors possess a void energy region where no energy levels are available to promote recombination of an electron **(e^-)** and hole **(h^+)** produced, for example, by photo-activation. This region, which extends from the top of the filled **V**alence **B**and **(VB)** to the bottom of the vacant **C**onduction **B**and **(CB)**, is called the band gap **(E_g)**.

For semiconductors, as the temperature increases, the electrons from the VB acquire enough energy, allowing more of them to breach the energy gap into the CB. This leaves behind vacancies. The vacancies produced can be thought of as a carrier of positive charge, called a hole (h^+), as displayed in Figure 1.3. Thereby, they are intrinsic semiconductors.[10]

It is possible to increase the intrinsic conductivity by adding impurity atoms to the crystal in a process known as doping. The dopants that create holes **(h^+)**, positive charge carriers, are known as acceptors. This type of extrinsic semiconductor is known as **p-type**. Dopants that add electrons **(e^-)** to the crystal are known as donors and the semiconductor material is said to be **n-type**. In fact, the characteristic properties of semiconductors come from the thermal agitation, the doping effect and the defects in the crystal. These give rise to new materials and new properties.[10]

Tungsten trioxide (WO_3) is an indirect, wide band gap, n-type semiconductor with E_g = 2.6 eV, like most of the MOX such as TiO_2, SnO_2, ZnO and Cr_2O_3 due to the presence of bulk defects.[8, 11, 12]

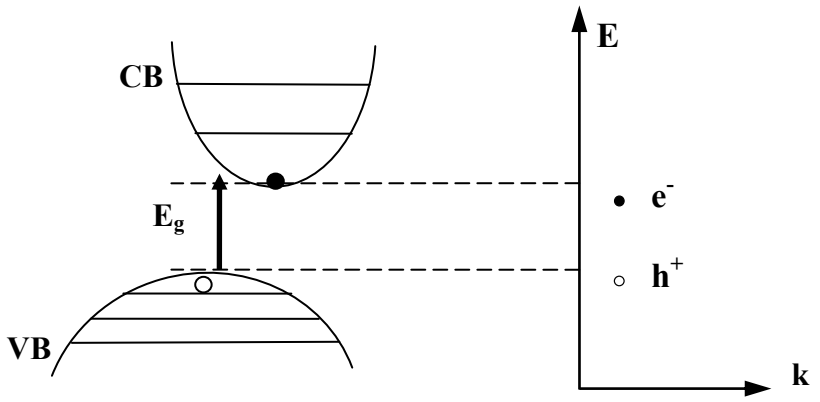

Figure 1.3 Schematic band structure and diagram of the generation electron (e^-) – hole (h^+) pairs (E = energy, E_g = forbidden energy gap, k = wave vector)

Another point worth noting is about the superficial properties of tungsten oxide which have an important role for its applications. The way to explain the structure from the bulk to the surface has been proposed by Kuzmin et al.[8] It was suggested that the reduced tungsten ions (W^{5+}) are formed when a crack along the (100) crystallographic plane is considered for example. Two different situations can be present on the surface of tungsten oxide, as displayed in the Figure 1.4. In the first one, half of the tungsten atoms remain in the valence state 6+ and are connected to the terminal oxygen ions giving one of their electrons to the nearest tungsten ion which transforms into the W^{5+} stable state. In the second situation, all tungsten atoms at the surface change their valence state to 5+, and the surface is represented by a $W^{5+}O_2$ terminal layer. In both cases, the surface W^{5+} sites react with oxidising atmosphere of air, leading presumably to a formation of the W^{6+} –OH bonds in a humid atmosphere.

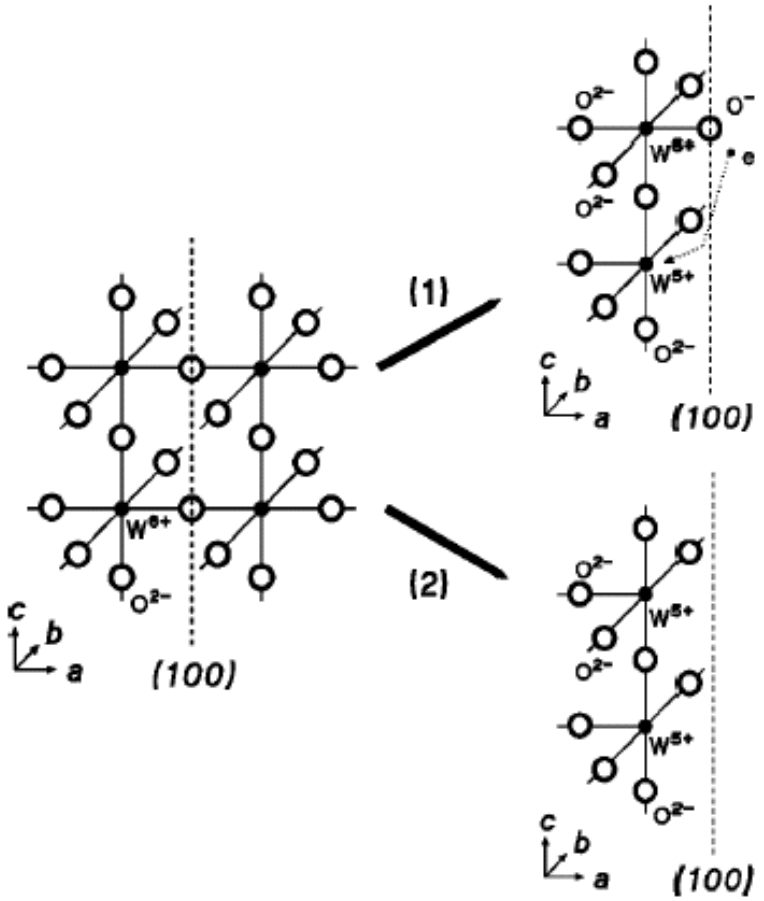

Figure 1.4 Model of the WO_3 grain surface.[8] **Left panel:** idealised WO_3 structure with the (100) fracture planes shown. **Right panel:** two possible states of the grain surface: in both cases the formation of the reduced tungsten ions W^{5+} is required by the neutrality condition.

1.1.3 Properties and Applications

1.1.3.1 Electrochromism, photochromism and thermochromism

Electrochromism **(EC)** is the reversible change in optical properties that occurs when a material is electrochemically oxidised (loss of electron(s)) or reduced (gain of electron(s)). Traditionally, materials have been considered as being electrochromic when they display distinct visible colour changes, commonly between a transparent (bleached) state and a coloured state. There are a large number of materials that exhibit electrochromism.[12-14] EC was first reported in thin films of WO_3 in 1969;[15] this material remains the most promising candidate for large-scale uses of electrochromic devices.[16] Many EC device constructions are possible. The basic design described in Figure 1.5 shows a number of layers.[17] The electrochromic layer, ion conductor, ion storage are sandwiched between two transparent conductive oxide coated on a glass substrate (Figure 1.5). The transparent conducting layers are usually **F**luorine or **I**ndium doped **T**in **O**xide, so respectively called **FTO** and **ITO**. Tungsten trioxide films represent the best option for the EC layer. There is still a matter of debate about the choice of the ion storage film.[18] It depends on whether the layer contains or not EC properties and its cost effectiveness. A potential candidate can be nickel oxide-based films which gives currently the best performance.[17, 19] However, little progress in this technology has been achieved to make it emerging.[20] The principle of EC is the following: upon application of a voltage, simultaneous intercalation of ions from the ionic conductor and electrons from the transparent conductor into the electrochromic film occurs, this inducing the colour change (Figure 1.5). During bleaching, this process is reversed.[13] Indeed, upon electrochemical reduction, W^{5+} sites are generated to give the electrochromic effect. The charge injection in WO_3 can be represented by the equation (1.1):

$$\underset{\text{Colourless}\\ \text{Bleached}}{WO_3} + x M^+ + x e^- \leftrightarrow \underset{\text{Blue}\\ \text{Coloured}}{M_xWO_3} \qquad M^+ = Li^+, H^+, Na^+, K^+ \qquad (1.1)$$

At low values of *x*, the films have an intense blue colour due to intervalence electron transfer between adjacent W^{5+} and W^{6+} sites stimulated by absorption of a visible photon.[17] At higher values of *x*, insertion irreversibly forms a metallic 'bronze' which is red or golden in colour.

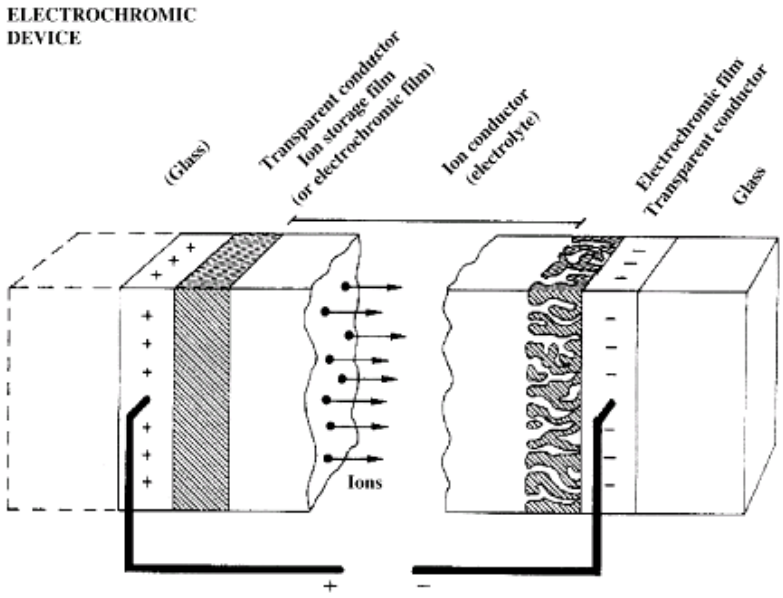

Figure 1.5 Basic design of an electrochromic device, indicating transport of positive ion under the action of an electric field

In addition, tungsten oxide displays photochromism (PC) which is reversible light induced-coloration. Contrary to EC, the change of colour in a photochromic device does not require an external applied voltage. Moreover, the electrochromic devices also exhibit constraints due to the choice and the number of conductive layers, as a result that the device becomes larger and thus a higher voltage is required. Nevertheless, the Photochromism of WO_3 has received less attention compared to electrochromism,[21, 22] because the actual practical problem with MOX is that most WO_3 coatings requires UV-light excitation,[23] and they are unstable in an oxygen environment.[24] It is known that the photochromic performance of WO_3 is related to the optically excited electron-hole pairs. When photons with energy above the optical band gap E_g excite WO_3 [Eq. (1.2)], the photogenerated hole can decompose the adsorbed water into H^+ [Eq. (1.3)]. This proton and the photogenerated electrons finally lead to the formation of blue-colored tungsten bronze [Eq. (1.4)].

$$WO_3 \xrightarrow{hv > Eg} WO_3 + h^+(vb) + e^-(cb) \quad (1.2)$$

$$h^+ + H_2O \rightarrow H^+ + OH \quad (1.3)$$

$$WO_3 + xH^+ + xe^- \leftrightarrow H_x W^{6+}_{1-x} W^{5+}_{x} O_3 \quad (1.4)$$

A new method of injection of hydrogen H^+ into WO_3 and other MOX was proposed by Gavrilyuk,[22] and called **P**hoto-**I**njection of **H**ydrogen (PIH). By using organic molecules such as alcohols, aldehydes, organic acids instead of atmospheric

humidity, the photochromic properties of amorphous and crystalline WO_3 films upon a UV light excitation have been studied. This method improves significantly the photochromic effect of WO_3.[11, 22, 25, 26]

The photochromic performance can also be improved greatly by modification of the surface with Au nanoparticles. The barrier formed at the WO_3/Au interface can facilitate the separation of photo-generated carriers and hence suppress the detrimental recombination process. The production of tungsten bronze is promoted via a higher adsorption of water by the nanoparticles resulting in improved UV-light photochromism.[27]

Efforts have also been made to shift the light absorption band from the near UV range to the visible range. So, the photochromic properties of WO_3 upon a UV-visible light, called **V**isible-**L**ight **P**hotochromism **(VLP)** can be observed in doped and undoped WO_3 films,[25, 28] by using a CdS-WO_3 interface,[29] and by activating them electrochemically.[28, 30]

Moreover, there is also another property of WO_3 which finds practical use, in combination with VO_2 as "Smart windows".[20, 31] Hence, thermochromism is the reversible change in optical properties with temperature, via a semiconductor-to-metal phase transition at a critical temperature τ_c (from infrared (IR) transmissive below τ_c to IR reflecting above τ_c).[31] It appears that tungsten has been shown to be one of the most effective dopant in adjusting the critical temperature τ_c of VO_2 to the ambient temperature.[32] So, $W_xV_{1-x}O_2$ have been prepared on different substrates (silicon, glass, quartz, and sapphire) by sol-gel,[33] CVD,[34, 35] sputtering techniques,[36] in order to lower τ_c from 68°C ($x = 0$) to about 36°C ($x = 0.015$ of W).[37]

1.1.3.2 Photocatalysis

In recent years, applications for environmental clean-up have been one of the most active areas in heterogeneous photocatalysis. Titania films have been shown to have remarkable ability to totally destroy the organic and inorganic compounds in polluted air and wastewaters.[38] The use of wide band gap semiconductors, such as TiO_2, as a photocatalyst has been investigated for the last thirty years.[38, 39] Also, Pilkington Glass commercialised the world's first self-cleaning photoactive coating from the deposition by CVD of an anatase phase titania thin film on glass: Pilkington Activ™.[40] This thin transparent layer functions in two ways, by having

both photocatalytic and hydrophilic properties. The photocatalysis permits cleaning of the windows by breaking down organic dirt on the glass to produce mainly CO_2 and H_2O. The hydrophilicity causes water to form an almost uniform film at the surface of the windows. The contact angle is reduced to the very low values in sunlight. So, the coating become "super-hydrophilic" and the dirt is washed away.[40] Despite the fact that "smart windows" are now available, some problems still remain which have not yet been solved. First, the band gap of TiO_2 (E_g = 3.2 eV; λ < 383 nm) that photogenerates the e^-/h^+ pairs limits the efficiency of the catalyst in utilizing solar irradiation as energy source. Therefore, TiO_2 does not absorb enough light in the visible region of the solar radiation, rather in the near UV. WO_3 could be another candidate as a photocatalyst because it shows a broad band absorption in the visible compared TiO_2. The band gap of WO_3 is 2.6 eV and corresponds to an excitation wavelength below 460 nm. As a consequence, the solar energy reaching the earth surface (λ > 400 nm) can increase the promotion of the e^-/h^+ pairs. Secondly, its conductance band electrons are sufficiently reducing (E° = -0.5 V vs NHE) to be able to reduce oxygen to water (E° = 1.23 V vs NHE) and its valence band holes (E° = 3.23 V vs NHE) are more oxidising than those of TiO_2 (E° = 3.0 V vs NHE). Already, some reports have been made describing attempts to photosensitize TiO_2 photocatalyst to the solar irriadiation. The catalyst could be doped by deposition of metal particles (Pt, V, Fe, Pb, Ag, Cr, Cu), by coupling with others compounds (CdS, SnO_2) and by the chemisorption and physisorption of dyes.[39, 40]

By modifying the surface of the semiconductor, the limitations of a particular semiconductor for a particular use can be influenced. So, the doped wide-band semiconductor increases the visible light absorption to promote the different charges (see above Figure 1.3). Afterwards, the fate of the separated e^- and h^+, as displayed in Figure 1.6, follow several pathways:

a) At the surface, the semiconductor can donate e^- to reduce an electron acceptor, usually oxygen.

b) A hole can migrate to the surface and combine with an e^- oxidizing the donor species which can be a polluant.

Both pathways (a&b) occur concomitantly according to the redox reactions. The probability and rate of the charge transfer depends upon the respective positions of the band edges for the conduction and valence bands and the redox potential levels of the adsorbate species.

c&d) In competition with the transferred charge, the separated charges can recombined on the surface and in the volume of the semiconductor particle with release of heat.

As a result, the efficiency of the photocatalytic process will increase dramatically by inhibiting the recombination with a metal dopant.

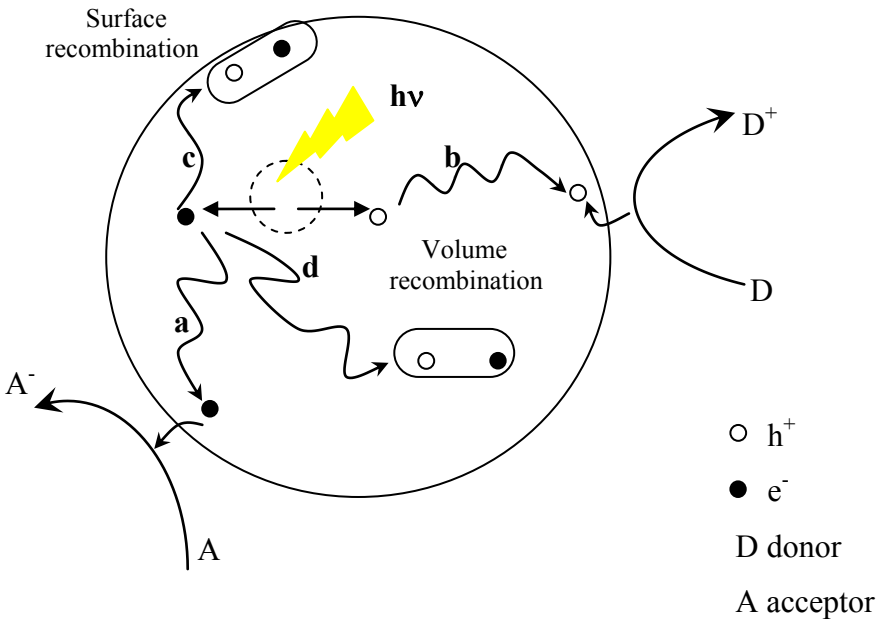

Figure 1.6 Schematic photoexcitation in a solid followed by de-excitation events

To restate, the dopants are found to introduce isolated energy levels within the band gap of the semiconductor. Also, the incident light is absorbed at two levels: the band gap and the sub-band-gap. Besides, such levels trap the h^+ and e^- formed during irradiation in order to prevent the e^-/h^+ recombination.

Furthermore, another way to obtain a higher photo-activity is to reduce the size of the particle of the order of 10 – 100 Å. Subsequently, others properties can appear in the nanoparticles compared to the bulk, it is the quantum size effect.[39, 40] Also, by increasing the ratio of surface to volume, the phenomenon of recombination decreases because the charges can reach more easily the surface. Moreover, metallic nanoparticles, such as gold or platinium can be incorporated onto the surface of a coating in order to improve photocatalysis by acting as charge separators, preventing recombination of photo-generated carriers.[40]

It has been shown, as well, that the super-hydrophilicity and so the photocatalytic activity increases with the insertion of other metals with high oxidation

state ($Nb^{5+,}$ Mo^{5+}) due to the higher proportion of hydroxyl groups adsorbed onto the surface.[40] Coupled semiconductor photocatalysts, such as WO_x-TiO_2[41] enhance the efficiency of the photocatalytic process by increasing the charge separation and extending the energy range of photoexcitation from near UV light to visible light. Currently, transition metal-doped WO_3 has been synthesised by sintering at high temperature and used for the decomposition of $S_2O_8^{2-}$ into SO_4^{2-},[42] HSO_5^- into SO_5^-.[43]

Copper(II)-doped WO_3 is found to be the best among the first row of the transition metal in order to increase the photocatalytic efficiency. Iron(III), and the noble metals Au, Pd, Pt, Rh can also increase the yield, while in contrast chromium(III) increases the e^-/h^+ recombination.[39] However, metals, such as Mn(II) and Fe(III) look to be more effective to photosensitize WO_3 to solar radiation.[38] A recent paper has shown that metals such as Mg, Al, In, Fe, Zr-doped into WO_3 produce a band gap range from 1.90 eV to 2.58 eV.[44, 45] Also, non-metallic elements, such as nitrogen can be used as a dopant into substitutional sites of WO_3[46] and TiO_2.[47-49] The resulted materials show the possibility to narrow the band-gap and hence to increase the photocatalytic activity and hydrophilicity of the film surface.

1.1.3.3 Gas sensors

During recent years, tungsten oxide has become the second most studied MOX for gas sensing applications after tin(IV) oxide, due probably to its high reactivity to many gaseous species. In this respect, WO_3 has already been successfully commercialized. Semiconductor oxides are used for two different types of gas sensing application. One is where the partial pressure of oxygen is determined. The second application involves situations where the oxygen partial pressure remains constant and the concentration of a minor constituent is to be determinated. For the case of tungsten oxide, films were shown to detect NO_x, NH_3, H_2, H_2S, O_3 and SO_2 gases.[50] For semiconductor materials, the sensor effects are dominated by direct adsorption and surface reactions with pre-adsorbed molecules. Depending on whether the sensor material is of n- or p-type and whether the gaseous species are reducing or oxidising agents, the sensor characteristic will be different. Taking for example a n-type sensor and a reducing sample gas (CO or H_2), the gas will then react with oxygen-ions at the semiconductor surface to form neutral molecules. This leads to an electron transfer to

the sensor material, and then gives rise to a decreasing of the resistance; for an oxidizing gas such as NO_x, the resistivity increases.[50]

Also, the deposited WO_3 film on an electronic device allows the electrical response to be measured, which has an excellent sensitivity toward NO_x species. The sensitivity and selectivity of the sensor to NH_3-NO_x can be enhanced by adding a metallic impurity, including noble metals.[51, 52] Nanoparticle films based on WO_3 or TiO_2 have proved to give high performance towards analytes.[53-55]

The properties of tungsten oxide which display several potential switching technologies can be combined to obtain a self-cleaning and optical switching device, making this technology even more attractive.

It is known that the properties of a WO_3 film dramatically depend on its fine microstructure which depends on also the method of preparation. There are a large number of methods to make the WO_3 films, such as sputtering or chemical vapor deposition (CVD), vacuum evaporation or the sol-gel route. As this thesis deals exclusively with CVD, only this technique will be discussed in detail. Having presented the microstructure of WO_3, its properties based on the electronic density of charges, we will now discuss of the design of molecular precursor related to the processes of film deposition and the background chemistry of tungsten.

1.2 Fundamentals of Chemical Vapour Deposition (CVD)

1.2.1 Basic principles of CVD

CVD is an important technique that has found wide utilization in modern industry for the production of microelectronic devices, optical, tribologic and decorative coatings, in order to produce a broad range of novel materials, such as thin metal films, metallic oxide and metallic nitride films. CVD (Figure 1.7) is a process where one or more precursors are transported **(1)** in the vapour phase, often in a carrier gas, to the reactor chamber where they adsorb **(2)** and react **(3)** to liberate the supporting ligands which are subsequently desorbed **(6)** and transported out of the reactor **(7)**. The metal atoms then diffuse **(4)** to form a stable nucleus, where subsequent growth occurs **(5)**. Under certain circumstances gas reactions can also happen.

All these processes occur on a heated substrate which decomposes the precursor. The CVD process of creating a film has to be reproducible and controllable. As a result, the intrinsic properties, such as the purity, composition, thickness, adhesion, microstructure and surface morphology have to be reproducible for the same reactor conditions.

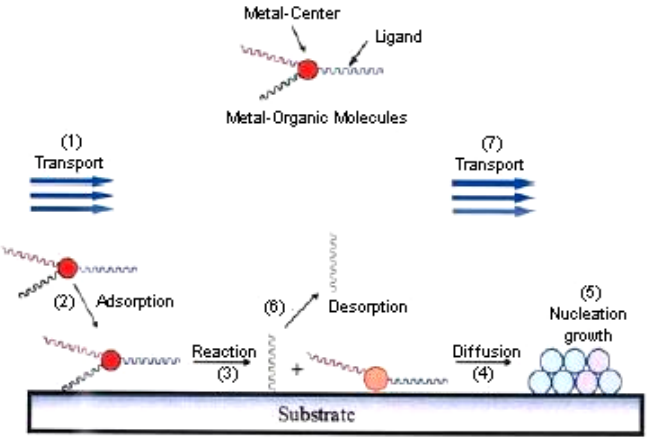

Figure 1.7 Illustration showing the elementary processes involved in the CVD of a metal-organic molecule

1.2.2 CVD growth modes

The atoms incorporated on the surface can be adsorbed to form small clusters of adatoms which can merge to give several growth configurations of film. The growth of the cluster is localized preferentially around the defects on the surface, such as vacancy and steps. The mechanisms, governed by the thermodynamics of adsorption and the kinetics of crystal growth, are displayed in Figure 1.8:

a) ***Island or Volmer-Weber growth***: This occurs when there is a higher affinity between the atoms of the deposition rather than the substrate. The adatoms nucleate on the substrate and grow into islands. These islands eventually coalesce to form a continuous film of columns.

b) ***Layer or Franck-van der Merwe growth***: Opposite to the island growth mode, the affinity of atoms and the atoms of the substrate during the deposition are closely similar. As a result, the film grows by subsequent growth of one monolayer after another.

c) ***Layer plus island or Stranski-Krastanov growth***: The deposited atoms are less weakly bound to each other than to the substrate surface. A monolayer (type Franck-Van den Meer) is firstly formed, afterwards the following layer grows under the form of columns (type Volmer-Weber).

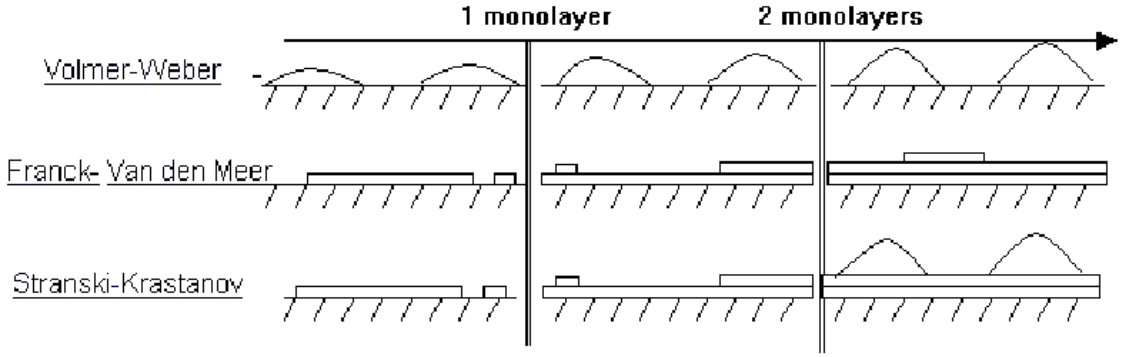

Figure 1.8 CVD growth modes as a function of film thickness

1.2.3 Reactor design

1.2.3.1 Hot- and Cold-wall reactors

The CVD of metal oxides has been carried out in several types of reactors which are essentially either hot-wall, cold-wall and in some cases, a plasma reactor. The type of reactor and its operating conditions can have a profound effect on the deposition process. The differences between these two types of reactor will be explained below.

In a **"hot wall"** reactor, the reactor is surrounded by a heating source.[56] They have been used preferentially at the laboratory scale rather than industry. The advantages of hot wall systems are the following. First, they are very simple to operate. Also, it is possible to accommodate several substrates in different orientations relative to the gas flow, and under a range of temperatures and pressures.
However, they do have significant disadvantages; the major problem is that deposition can occur not only on the substrate but also on the reactor walls. Subsequently, these deposits will eventually contaminate the substrate surface. Then, the precursor consumption is high due to the large area coated. This can lead to problems reproducing deposition conditions because the fraction of the reactor surface area can change with time during an experiment and from one experiment to another. Therefore, hot-wall reactors are used principally in laboratories to study the viability of new precursors for the CVD. All these disadvantages limit quantitative studies. Nevertheless, industry utilizes them sometimes for CVD of various materials when the vapour pressure of the precursor is high.[57]

In a **"cold-wall"** reactor, only the substrate is generally heated, by radio frequency or induction.[56] They are generally more widely used in industry. Cold-wall reactors usually accommodate only a single substrate in various orientations with the control of pressure and temperature. Since the risk of depositing a film on the reactor wall is reduced, the quantity of precursor required is generally smaller and the deposition rate increases significantly compared to the previous type of reactor. Moreover, cold-wall reactors are more suitable for selective CVD and to measure kinetic parameters.[58] This allows better control of the deposition behaviour, thus a high reproducibility can be attained. However, some problems about the gas flow can create turbulence and unstable flow that does not lead to a uniform film due to the high temperature gradient within the reactor. Reactor and process designers have developed ways to combat successfully these effects in most reactor geometries.

1.2.3.2 Parameters influencing the film growth

A homogeneous and uniform film is formed when a laminar flow reaches the surface of the substrate. In this case, a region called "boundary layer" is formed close to the surface. In theory, this model of the boundary layer assumes that the temperature is uniform, and the velocity, the concentration of the reactive gaseous species tend to zero.[56, 59] As a result, the gaseous reactants should diffuse through this zone to be decomposed and deposited. Afterwards, the film growth can encounter certain kinetic limitations because the growth rate depends upon rate of diffusion through layer to substrate. The deposition process involves a series of three steps: introduction of the precursor vapour, transport of precursor to the surface of the substrate and surface reaction of the precursor, as described in section 1.2.1. Also, the growth kinetics can be divided into three main regions, as displayed in Figure 1.9:

I) The ***kinetically limited region***, which occurs in the field of low temperature because the rate reaction increases with temperature

II) The ***diffusion region***, which leads to a plateau. In this region, the growth rate does not depend on the temperature. This is the most ideal growth region to obtain uniform films with reproducibility and homogeneity in composition.

III) The ***pre-reaction region***, which is reached in the field of high temperature. Therefore, the precursors react with each other in the gaseous phase. This leads to the depletion of the reactive species in the gas to grow the film. Also, the sublimation of the deposited film enters into competition with the film growth.

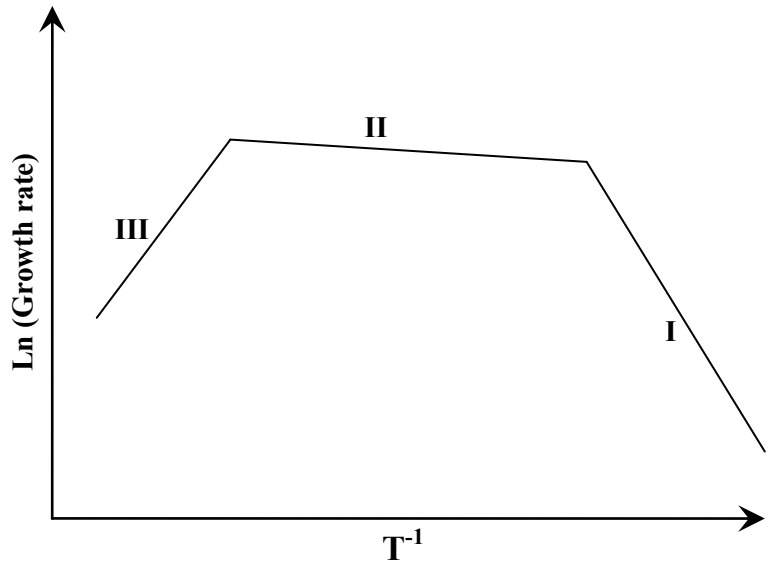

Figure 1.9 Diagram of deposition rate behaviour as a function of temperature (**I** = kinetically limited region, **II** = diffusion region, **III** = pre-reaction region)

1.2.4 Precursor Design

The precursors for CVD can be broadly classified into three types:[60]

- The *inorganic* precursors, which do not contain carbon
- The *metal-organic* precursors which contain organic ligand, but do not possess metal-carbon bonds
- The *organometallic* precursors, which possess organic ligands and metal-carbon bonds

1.2.4.1 Requirements

Among all these kind of precursors, the necessary requirements for CVD precursor design to deposit a metal oxide thin film have to meet the following properties:[60, 61]

- The precursor should have good volatility, to be able easily to be transported to the reactor. Liquids are preferred to solids owing to the difficulty to have constant flux of source vapours.
- The precursor must be chemically and thermally stable between the evaporation and the thermal decomposition avoiding premature decomposition and irreproducible film growth.
- The decomposition of the precursor should be clean; thereby no residual impurities can be incorporated in the film.

- The precursor should be relatively easy to synthesise with high yield at low cost and be both air and moisture stable. It should also be non-toxic, non-pyrophyric, non-flammable and non-explosive.

It is highly unlikely that all these requirements will be met in a single precursor. Most of the time, precursor selection and design is almost always a compromise among all these criteria.[57, 62] However, the quality of the deposited material is more decisive, especially for microelectronic applications. Conventionally, volatility, clean decomposition, solubility and purity are crucial. All of these properties are achieved by designing and functionalizing the CVD precursor.

1.2.4.2 Molecular Design

Volatility, the key pre-requisite for CVD applications, can be increased by choosing the appropriate ligand, for example with metal β-diketonates. For Cr(III) complexes, the evaporation rate increases in the order $Cr(acac)_3 < Cr(tfac)_3 < Cr(hfac)_3$. The substitution of CH_3 with fluorinated ligands causes intermolecular repulsion due to the "resulting negative charge envelope" and thus exhibit higher vapour pressures.[63] Also, volatility can be increased in the order $M(OBu^t)_n > M(OPr^i)_n > M(OEt)_n$, indicating the significant effect of ligand size on the extent of polymerization.[64] One possible problem with this strategy is that it might incorporate intrinsic impurities into the film, such as carbon.[65] Furthermore, high vapour pressure depends on low molecular weight and a low degree of oligomerization favoured by the highest oxidation state of metal. For example, WF_6 where the coordination sphere of W^{VI} is satisfied by six fluoride ligands resulting in the formation of a highly volatile complex.[57] The halides $SnCl_4$ and $TiCl_4$ are other examples where the metal coordination number and oxidation state are satisfied with the result that oligomerisation is unnecessary and these species exist as volatile liquids at room temperature and atmospheric pressure.[66] In contrast, $SnCl_2$ is an infinite polymer in the solid state because the number of ligands is lower than the preferred coordination number and makes $SnCl_2$ unstable with respect to oligomerisation. However, $SnCl_2$ can be thermally de-oligomerized to form monomeric species in the gas phase.

Moreover, the oxidation state of the metal in the deposited film is usually controlled by the oxidation state of the SSP, suggesting the conservation of the oxidation state from the precursor to the materials.[67, 68] This is also consistent with the

deposition of $TaN_{1.33}$ at the +IV O.S from the Ta(IV) amido complex $Ta(NEt_2)_2(NCy_2)_2$ and NH_3.[69]

The nature of the ligand and type of metal-ligand bonds determine and control the decomposition pathway. Indeed, a precursor should ideally decompose on the growth surface without incorporating unwanted atoms from the precursor. This is best accomplished by having the unwanted atoms of the precursor eliminated as a stable molecule. A simple example of this is the elimination on decomposition of carbon monoxide from a metal carbonyl such as in the decomposition of iron pentacarbonyl:

$$Fe(CO)_5 \xrightarrow{\Delta} Fe + 5\,CO \qquad (1.5)$$

A more complicated but more useful example is the loss of ethylene from a molecule containing an ethyl group attached to an atom with a vacant and accessible orbital. Under this condition, a process known as β-hydride elimination can occur, as shown in Figure 1.10. Also, other types of decomposition pathway can occur, such as α- or γ-elimination. However, the carbon incorporation rate depends on the kind of metal and the ligands involved, for example cyclopentadienyl complexes of the noble metals Pd, Pt, Cu, and Ag have lower carbon incorporation than films derived from cyclopentadienyl complexes of metals earlier in the Periodic Table. Impurity incorporation can be avoided in certain cases by the addition of a reducing agent (*e.g* H_2) or an oxidizing agent (*e.g* O_2) during the CVD.[57]

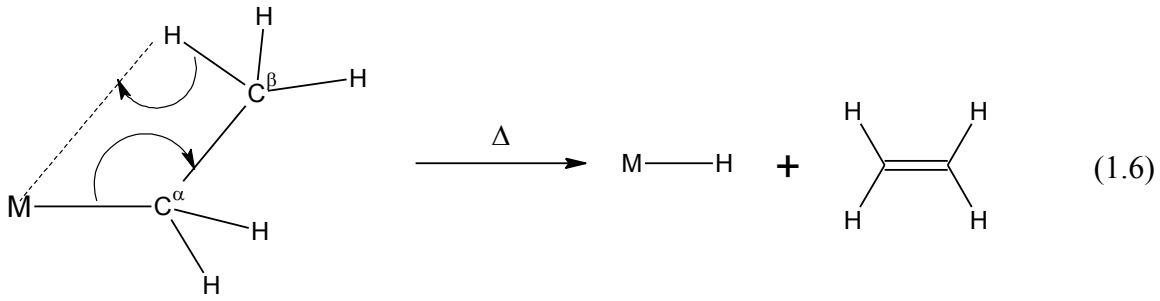

(1.6)

Figure 1.10 β-hydride elimination of ethylene from an organometallic compound

Another method for achieving facile decomposition is to use as CVD precursor a molecule with an adduct bond which has a weak dissociation energy. These prevent the oligomerization of coordinatively unsaturated molecules, and to stabilize electron-deficient species by the donation of electron density via an intermolecular dative bond.

Examples demonstrating both of these properties are the $AlH_3(NMe_3)$, $AlMe_3(NMe_3)$, adducts, to deposit aluminium films of very high purity.[70]

These types of precursor complexes also lower the reactivity towards air and moisture and thus are often non-pyrophoric solids compared to the pyrophoric base-free R_3M compounds (M = Al, Ga and R = H, Me).[65] Also, a similar way to improve the stability of the usual CVD precursors, such as metal alkoxides $[M(OR)_x]_n$ towards air and moisture, is to use the "donor-functionalization" concept. This approach to increase the coordinative saturation of the metal centre M consists of introducing polyfunctionalized donor. Hence, the modification of the simple alkoxides by functionalization of the metallic center with amino-alkoxo ligands containing $-NR_2$ group increases the coordination number of the charged metal center via an intramolecular bond.[71, 72] This permits to avoid the decomposition and the disproportion at high temperature of the precursors during its transport to the reactor chamber.[73] This approach will be discussed in more details in Chapter 2 and 3.

1.2.4.3 Single-Source approach for multi-component compounds

The most common approach for CVD of multi-component materials is to use two or more separate precursors that react individually at the substrate surface. This assumes that no reaction occurs in the gas phase between the compatible precursors. An example of this is the preparation of epitaxial GaAs films from trimethylgallium and arsine:[70]

$$Ga(CH_3)_3 + AsH_3 \xrightarrow{\Delta} GaAs + CH_4 \qquad (1.7)$$

A problem associated with a multiple-source precursor approach is the reproducible control of film stoichiometry and the decomposition pathway leading to a clean deposition without incorporating impurities. This arises because the precursors or intermediates formed during film deposition have different volatilities and reactivities.

A second approach, preventing the reaction before the growth chamber, is to use one molecule, a **S**ingle-**S**ource **P**recursor (**SSP**) containing all the desired elements of the final film, for example one or more metals, nitrogen, phosphorus and oxygen.[74, 75] However, the element oxygen can be introduced *in-situ* during the film growth using a gas carrier, such as O_2, coupled or not with H_2O, or ex-situ by post-annealing the film

in an oxygen environment. Most of the time, the post-annealing process is a necessary step to obtain the right stoichiometry with precursors containing oxygen.

The control of film stoichiometry is not always governed by the stoichiometry of the precursor, that is to say a molecule comprising M and N elements with the desired atomic ratio M/N = *m*/*n* will not necessarily deposit the material having formula M_mN_n. It is also difficult from a single-source molecule to deposit stoichiometric materials, doped-films, or materials containing two or more metals. It depends more on a delicate balance between the energies of the bonds that must be broken and those that should be maintained. Moreover, the control of the stoichiometry, as well as the purity, is largely dependent on the choice of ligands. Subsequently, the single-source precursor approach solves many of the problems of multiple-source precursors and allows for a simplification of the delivery system. However, SSP often have higher molecular weights and thus potentially lower volatility.[76] As an example, to make the spinel $MgAl_2O_4$, the SSP $Mg[(\mu\text{-}OPr^i)_2AlMe_2]_2$ has been used and is now subject of a patent.[77] This heterometallic precursor shows a high volatility with a β-hydrogen elimination reaction pathway[57]. It is converted cleanly to an equimolar mixture of methane and propylene as gaseous by-products, leaving a minimal amount of residual carbon in the deposited oxide film.[78] Also, it shows the control of film stoichiometry due to the stoichiometry of SSP. Subsequently, a CVD process has been attempted in the preparation of the same spinel using vaporisable $MgAl_2(OPr^i)_8$ which seems problematic due to its dissociation into less volatile compounds, such as $\{Mg[Al(OPr^i)_4]_2\}_2$ and $Mg_3Al_3(OPr^i)_{13}$.[56, 60, 78] Moreover, as a result of the formation of such high molecular weight compounds, carbon contamination occurs during the deposition due to the high number of carbon atoms in the single-source precursors.[79, 80] This example underlines the difficulty of optimizing precursors for conventional CVD.

The most attention has been focussed on the SSP for III-V compounds which attract a large interest due to their microelectronic applications.[65, 81] For example, $[Et_2GaAs^tBu_2]_2$ allows control of the film stoichiometry due to a strong "pre-formed" bond between the two elements to be incorporated and a clean decomposition giving by-products as displayed in the following equation (1.8).

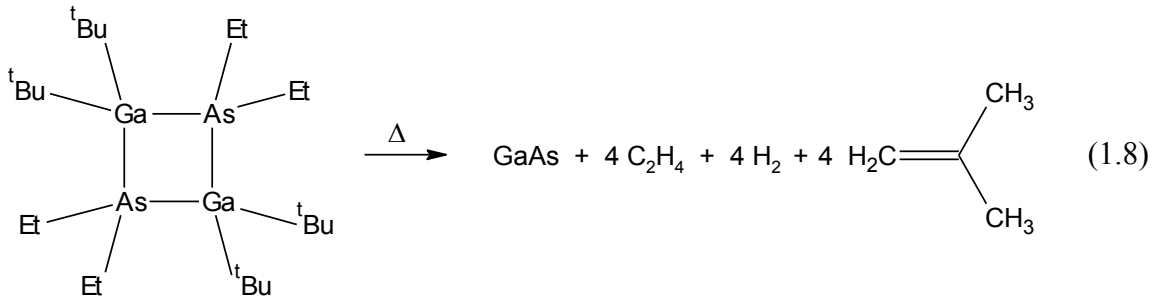

(1.8)

In addition to the reactor and precursor design, the *precursor delivery system* plays also a crucial role because it is the first critical source of film defects during the growth. There are different kinds of deliveries system: Liquid injection system (LIS), Gas delivery system (GDS), solid delivery system (SDS) and aerosol-assisted delivery system (AADS),[81, 82] [Appendix 1]. So, the new deliveries system, such as AADS and LIS allow the deposition from soluble single-source precursors which are generally non-volatile[57] and may possess many advantages over conventional CVD precursors, such as being more stable toward air and moisture than metal alkyls and also having low toxicities.[65]

1.2.5 Film deposition techniques

Many techniques permit the deposition of thinner or thicker coatings (in the order of one atomic monolayer to one centimeter). They can be classified as two approaches: the wet technique necessitating the use of a liquid (electrodeposition, sol-gel: spin-coating,[83] dip-coating); the dry technique (**P**hysical **V**apour **D**eposition: **PVD)**[84] using solid source and CVD,[57] using vapour source.

1.2.5.1 Others variants of CVD

The majority of chemical reactions in traditional CVD are thermodynamically endothermic. The methods of energy input can be supplied by a variety of means: heat, laser and plasma. In fact, these others types of energy assist the CVD process and permit a dramatic decrease in the temperature of the deposition, about several hundred degrees compared to conventional CVD.[85, 86] These different sources give rise to various techniques (Table 1.1). Usually, two ways other than CVD are used to deposit WO_3 on glass, namely PVD and sol-gel.

First of all, the **PVD processes** which are divided into two main techniques:

- **Evaporation** is a process which evaporates the target material by heating under high vacuum (10^{-7} – 10^{-8} torr).[84, 87] Heating can be achieved by resistive, inductive, electron beam and arc techniques. Then, the vaporized species condense on the substrate surface or items to be deposited.

- **Sputtering** is a process to deposit a film on the substrate surface via a physical mechanism. The high energy ions are accelerated from a plasma in a partial vacuum (10^{-2} torr) towards the target having a negative potential. Subsequently, the surface atoms of the target material are vaporized towards the substrate surface where they condense to form a film.

CVD methods	Principles and Implications for CVD growth
AP-CVD	It is the formation of non-volatile solid film on substrate by thermal reaction of vapour phase chemicals at atmospheric pressure. High growth rates or wide temperature window available, efficient heat transfer from substrate to boundary layer, suitable for both continuous and batch processes, some parasitic gas phase reactions may occur leading to dust formation.
LP-CVD	It is the formation of non-volatile solid film on substrate by thermal reaction of vapour phase chemicals under reduced pressure. Low growth rates, temperature window reduced in size, reduced flexibility compared AP-CVD, reduces undesirable gas-phase reactions leading to dust, improves uniformity.
LI-CVD	The precursors, liquid or solid dissolved in a convenient solvent are injected in a vaporization chamber towards injectors[88] High growth rates can be reached using this technique
AA-CVD	The precursor, dissolved in an organic solvent is transported to the substrate in the form of an aerosol due to a carrier gas. The aerosol is generated by an ultrasonic technique, which implies a piezoelectric transducer vibrating on contact with the solution containing the precursor [appendix 1].[89] Similar to AP-CVD and difficulty to control the continuous mass transport from the precursor to the substrate.
C-CVD	The precursors, dissolved in an organic or aqueous[90] solvent are delivered via a nebulised mist (or spray) directly into the gas mixture supporting the flame.[59, 86, 91] AP operation, high growth rates, ability to tune chemistry by selecting appropriate mixtures of gases, easy control of flame temperatures, very low temperature, inexpensive and easy process, no reactor.
LE-CVD	A laser-assisted thermal CVD, which is perpendicularly directed onto a heated substrate, pyrolyses sensitised mixtures of gaseous precursors transported by a carrier gas.[92] Low temperature of deposition (<500°C), high incorporation of C and O.
PE-CVD	The plasma enhanced CVD method generates a glow discharge in a chamber by a high frequency voltage applied to both electrodes.[93] Low temperature of deposition (<400°C), usually operated under vacuum using D.C, microwave or radio frequency. Sometimes, the plasma leads to damage the deposited film.

Table 1.1 The various forms of CVD: AP = Atmospheric Pressure, LP = Low Pressure, LI = Liquid Injection, AA = Aerosol Assisted, C = Combustion, LE = laser Enhanced and PE = Plasma Enhanced

The PVD techniques permit the deposition of tungsten oxide films with high quality. Moreover, the E_g values of WO_3 films prepared by the evaporation technique are varied between 3.25 and 2.70 eV with the substrate temperatures from 50 to 500°C. This variation is certainly due to the oxygen ion vacancies. The same observation was made with the sputtering technique wherein the sputtering pressures and O_2 concentrations change. As a result, the high temperatures of deposition influence the decreasing of the band gap.[94]

Then, the **sol-gel process** is a chemical way for the synthesis of materials under different forms: powder, thin films. This versatile process, which is in fact based on inorganic polymerisation reactions, is then achieved in two stages:

1) An initiation stage, in general, a hydroxylation of a metallic alkoxide via hydrolysis

$$M(OR)_n + H_2O \Leftrightarrow M(OH)(OR)_{n-1} + ROH \quad (1.9)$$

The precursor can be a heterometallic compound: $MM'(OR)_{n-x}(OR'')_x$

2) A propagation or condensation stage

$$M(OH) + M(OH) \Rightarrow M\text{-}O\text{-}M + H_2O \quad (1.10)$$

$$M(OH) + M(OR) \Rightarrow M\text{-}O\text{-}M + ROH \quad (1.11)$$

These processes lead to a solid network via oxygen bridges. The films can be deposited on glass substrates by spin-coating, dip-coating or spray pyrolysis and afterwards dried by annealing between 300 and 900°C.[83]

This technique has been used extensively to deposit most doped and undoped tungsten oxide films.[21] Sol-gel production of films has several advantages over other deposition techniques:

- Low temperature sintering capability (usually 200-600°C)
- Simple, economic and effective method
- Easy control of the film thickness, its purity and uniformity
- Ability to shape materials into complex geometries in a gel state

1.2.5.2 Comparison

It is interesting to compare the different coating methods that are routinely used for the production of coated glass products (Table 1.2). Despite the advantages of sol-gel technique, it never arrives at its full industrial potential due to some limitations: weak bonding to the substrate, low wear-resistance.

In particular, the limit of the maximum coating thickness is 0.5 μm when the crack-free property is an indispensable requirement.[95]

Methods	Growth rate	Uniformity	Density	Adhesion	Batch	Continuous
AP-CVD	High	Good	Variable	Good	yes	yes
PVD	Low to medium	Excellent	High	Good	yes	yes
Sol-gel	Variable	Variable	Variable	Variable	yes	yes

Table 1.2 Comparison between AP-CVD, PVD and sol-gel techniques for the production of coatings on glass.[59]

The PVD techniques show a high quality of coating compared to the non-PVD techniques but they are extremely expensive. AP-CVD can achieve unique combinations of growth rates, film durability and properties with low cost required by the glass industry. The possible incorporation of a CVD coating unit on a float glass production plant is currently in application in the float glass industry.[59] The key issue for AP-CVD is the need to obtain a precursor with enough volatility. Nevertheless, it is possible to increase the range of depositable materials with AA-CVD which do not require a volatile precursor.

1.3 Chemical background

This section describes essential chemistry of the element, tungsten, and the bonding modes commonly observed for a range of ligands that are found in the metal-organic precursors described in this thesis. The ligands described in this part will be discussed according to the covalent (neutral) model.[96]

1.3.1 Tungsten chemistry

Tungsten occurs in the form of the two main minerals: *tungstates scheelite* $CaWO_4$ and *wolframite* $(Fe,Mn)WO_4$ which was first discovered in 1781; the element $^{183}_{74}W$ was finally isolated two years later. A major use of tungsten metal has been the production of numerous heat-resistant alloys and electric light bulb filaments, due to its melting point (3695 K) which is the highest of all known metals.[97]

The element tungsten belongs to the 3rd row *d*-block metals and to the group 6 with an electronic configuration $4f^{14}6s^{2}5d^{4}$. The availability of *d*-orbitals permits the formation of both σ and π bonds with different type of ligands, which gives a wide

range of compounds with different oxidation states (from -IV to VI) and thus different geometries.[96, 98] The oxidation states, the coordination number, and the stereochemistry of selected tungsten complexes are summarised in Table 1.4.

Oxidation state (O.S)	Tungsten Compounds	Coordination number (C.N)	Stereochemistry
-IV (d^{10})	$[W(CO)_4]^{4-}$	4	Tetrahedral
-II (d^8)	$[W(CO)_5]^{2-}$	5	Trigonal bipramidal
0 (d^6)	$W(CO)_6$	6	Octahedral
I (d^5)	$[W(\eta\text{-}C_6H_6)_2]^+$	6	Octahedral
II (d^4)	$W_2Cl_4(dppe)_2$	5	Pentagonal pyramidal
	$Me_2W(PMe_3)_4$	6	Octahedral
III (d^3)	$[WF_6]^{3-}$	6	Octahedral
IV (d^2)	[34]2-	6	Octahedral
	$[W(CN)_8]^{4-}$	8	Dodecahedral
V (d^1)	WF_6^-	6	Octahedral
VI (d^0)	$[WO_4]^{2-}$	4	Tetrahedral
	WCl_6	6	Octahedral
	$WOCl_4$(diars)	7	Pentagonal pyramidal

Table 1.3 O.S, stereochemistry and C.N of selected tungsten compounds

Tungsten has similar chemistry to molybdenum, but they share little in common with the lightest member of this triad: chromium. This is reflected particularly in their oxidation state (O.S), atom size, coordination number (C.N) and chemical and physical stability. These differences, which are usually seen across the *d*-block, are due to the lanthanide contraction. The heavy elements, molybdenum and tungsten, show generally a higher O.S and C.N than chromium. One major difference between the two heavier elements of the chromium triad is their solubility.[99] Tungsten(VI) oxide is soluble in neutral and alkaline solutions but insoluble in acid solution. Meanwhile, molybdenum(VI) oxide dissolves in acid solutions to the formation of chloro-complexes.[100] Chromium at the oxidation state +VI is really a strong oxidizing but

stable for the +III state, while molybdenum and tungsten are relatively stable at +VI oxidation state. The coordination and organometallic chemistry of chromium, molybdenum and tungsten has been reviewed annually covering the literature since the beginning of the 70s until now.[101-116] There are a plethora of recent reviews on tungsten, showing an extensive and rich chemistry which is in constant progress.[117-119]

1.3.2 Electronic and structural aspects of metal Ligand M-L bonding

1.3.2.1 Bonding modes of Ligands

M-O and M-N bonds have proved to be very strong and thus suitable for the deposition of metal oxide and nitride. Both amido-/imido- and alkoxo- ligands acting respectively as a N-donor and O-donor show a tendency to form bridged structures due to their lone pairs, but this is more favoured in the case of O-donor ligand due to the higher ionic character of the M-O bond.

Bonding modes	Metal alkoxides	Metal imides
Terminal	M—OR	M—NR
Doubly bridging	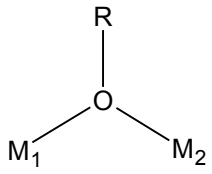	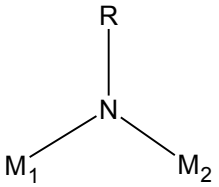
Triply bridging	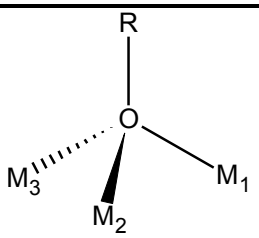	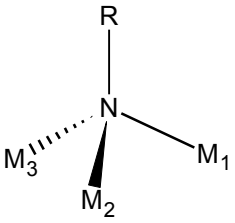

Table 1.4 Coordination modes of metal alkoxides M(OR) and metal imides M(NR)

As a result, most of these M-O systems, such as metal alkoxides, have oligomeric and polymeric structures. The bulky substituents R will usually inhibit the formation of an alkoxide bridge and so polymeric structures. As illustrated in Table 1.4, the metal imides display similar types of coordination modes compared to the alkoxides, but have less tendency to bridge metals. The μ_2-bridging mode is the one more commonly encountered.

1.3.2.2 Alkoxo ligand (-OR)

In terms of the covalent model and as illustrated in Figure 1.11, the ligand (-OR) can donate up to 5 electrons to the metal M. This depends on the electron deficiency of the metal centre. Hence, the alkoxo ligand (-OR) can be classified as a:

1) one electron ligand, forming of a M-L_σ bond, *i.e* 1σ ligand.

This occurs mainly for the late transition metal complexes which have 18 electrons and filled *d*-orbitals. For this type of metals, π-donation will result in a destabilization of these orbitals because of the repulsion between lone pair and d_π-electrons giving rise to a weak M-O bond with a M-O-R angle of about 120°.

2) three electron ligand, forming of a M-L_σ and a M-L_π bond, *i.e* 1σ+1π ligand.

This type of interaction is found in the most cases, in which π-bonding occurs from one lone pair of the sp hybridized oxygen atom to the metal. Most of the angles (M-O-R) are about 140°.

3) five electron ligand, forming of M-L_σ and 2 M-L_π bonds, *i.e* 1σ+2π ligand

The oxygen atom re-hybridizes to place two lone pairs in the empty metal d-orbitals, forming an sp hybridized oxygen atom.[120, 121] This gives rise to a stronger and shorter bond with angles (M-O-R) reaching 180°. This happens mostly in bulky alkoxide and in the case of an early transition d^0 metal, with less than 18 electrons and high oxidation state, which has empty d_π-orbitals available for overlapping.

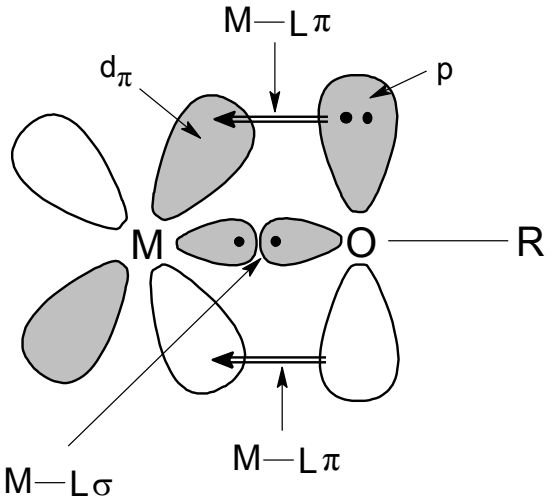

Figure 1.11 Molecular orbital diagram of the Metal (M) and alkoxide (-OR) interaction

The alkoxo- ligand is isoelectronic with the amido- ligand (NR_2), and the two groups can often be interchanged in transition metal complexes.

1.3.2.3 Amido ligand (-NR_2)

A terminal metal dialkylamido complex shows two bonding possibilities:

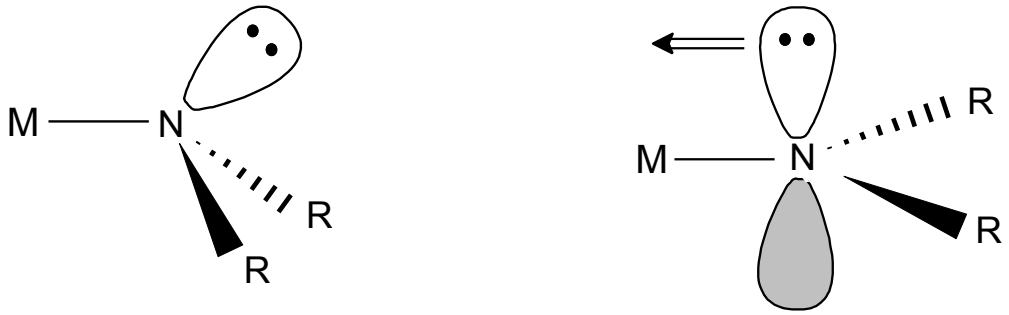

(A) **(B)**

Figure 1.12 Schematic bonding molecular orbital diagram of the Metal (M) and amido (-NR_2) interaction[122]

The amido ligand can behave as either a one electron ligand **(A)**, or a three electron ligand **(B)** (Figure 1.12). The structure **(A)** illustrates a metal-nitrogen (M-L) σ-bond with a pyramidal sp^3 hybridised nitrogen atom. The structure **(B)** shows a situation in which π-donation occurs from p-orbital orthogonal to planar N(sp^2), mainly found in the early transition d^0 metal complexes having high O.S. The M-N bond distance is generally shorter than the predicted single bond due to the presence of p_π-d_π bonding occurring between the nitrogen and metal atom.[123]

The synthesis of homoleptic dialkylamido- complexes seems difficult for the later transition metals compared to the early transition metals. The π-donation requires suitable vacant metal *d*-orbitals, which are only available for the complexes of the early transition metal. The use of silylamide -N($SiMe_3$)$_2$ as an amido- ligand has allowed the synthesis of M(N($SiMe_3$)$_2$)$_n$ for all the first row transition metals and several of the lanthanides due to the partial delocalisation of the nitrogen π-electrons onto the silicon atoms which permit to the ligand to behave as a weak π-donor.[123]

1.3.2.4 Imido ligand (-NR)

A terminal metal alkylimido- complex shows three bonding possibilities:

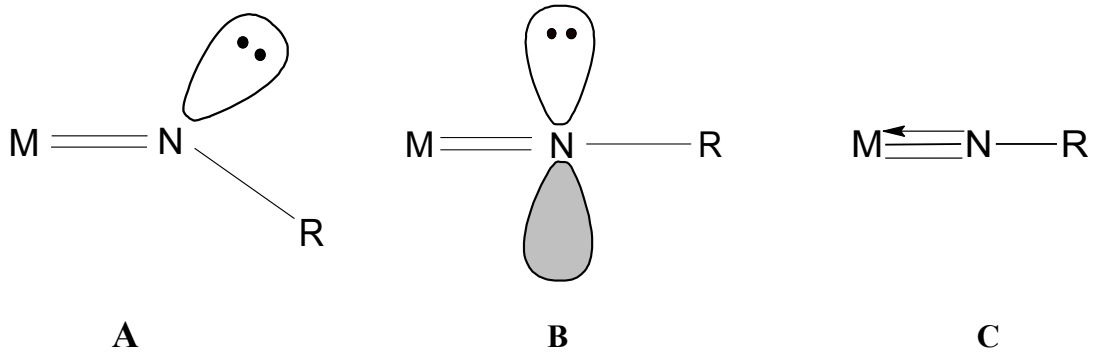

A **B** **C**

Figure 1.13 Schematic bonding diagrams of the Metal (M) and imido- ligand (=NR) interaction[122]

The imido ligand (NR^{2-}), which is isoelectronic with the oxo ligand (O^{2-}), can have either terminal or bridging bonding modes. The imido ligand can bind a transition metal via one σ and either one or two π-bonding ligands.

The structure **A** (Figure 1.13) depicts an sp^2 hybridised nitrogen atom, resulting in a double bond M=N (1σ+1π) and a bent M-N-R with one lone pair on the N(sp^2) orbital. In terms of the covalent model, the bent alkylimido- ligand behaves as a 2 electron donor to the metal.

Structure **B** (Figure 1.13) shows a hybridised N(sp) with a near linear M-N-R bond angles, giving rise to the M=N double bond ($1\sigma+1\pi$). This situation occurred when the $p\pi \rightarrow d\pi$ donation will result in a destabilization of these orbitals due to the repulsion between the lone pair electrons in N(sp) and filled d_π orbitals electrons. This results in a weaker M-N bond.

However, in most cases, such as W^{6+} (d^0 metal), π-donation is a favourable interaction and leads to stronger linear M≡N bond order of 3, illustrated in the structure **C** (Fig. 1.13). In this case, the imido ligand acts as a 4 electron donor to the metals, *i.e* $1\sigma+2\pi$ ligand.

1.4 CVD chemistry of WO_3 and mixed Metal/Tungsten oxide: WM_xO_y

Tungsten metal is largely used in industry due to its hardness and high stability against chemical attack even at high temperatures. These attractive applications can be enhanced by adding small element of O, N, S and C. This leads, respectively, to new materials such as WO_3, WN, WS_2 and WC with also new properties, respectively electrochromic devices, diffusion barriers, solid lubricating materials and protective coatings. However, the different precursors used for depositing these films are few and especially the SSP approach (see section 1.2.4.3). In fact, the precursors generally derive from those used for the deposition of tungsten metal and a gaseous additive: O_2, NH_3, H_2S, CH_4, H_2.[124, 125] This chapter gives an overview of the different systems of precursors studied in order to deposit WO_3 and mixed-tungsten oxides.

1.4.1 Inorganic precursors: Tungsten (VI) Halides

Tungsten hexafluoride (WF_6) is a colorless gas at room temperature while tungsten hexachloride (WCl_6) is a black-red moisture sensitive solid. WF_6 is the dominant tungsten CVD precursor which has been extensively studied and used routinely in the microelectronics industry due to its high vapour pressure.[125]

It also permits deposition of fluorine-doped tungsten oxide films. Indeed, WF_6 reacts with oxygen contained in isopropanol and fluorine coming from 1,1-difluoroethane at 400°C.[124] WF_6 and WCl_6 have been used to deposit WO_3 with an oxygen source, such as O_2 or H_2O.[7] The major disadvantage with this WF_6/O_2 system is the generation with water of a highly corrosive by-product (HF), which causes spots and pinholes on the substrate surface. However, it is possible to deposit WO_3 with the system WF_6/H_2O if certain precautions are taken.[7] Moreover, tungsten oxychloride $WOCl_4$ can be used as precursor as well with acetylacetate and ethanol to obtain a photoactive WO_3 films.[126]

1.4.2 Metal organic precursor

1.4.2.1 Tungsten(VI) alkoxides and polyoxotungstate complexes

Both tungsten(V) and tungsten(VI) ethoxide have been used to deposite sub-stoichiometric tungsten oxide thin films in the O/W ratio of 2.7-3.2. The films were deposited in a single step at atmospheric pressure with a carrier gas. Because of the high sensitivity of $W(OEt)_n$ (n = 5, 6) towards air and moisture, the reactants were

separated to ensure the alkoxide did not react with the oxygen source prior to entering the reactor. The temperatures used were between 100-350°C to deposit amorphous sub-stoichiometric tungsten oxide.[127]

A range of volatile tungsten(VI) oxo-alkoxides, $WO(OR)_4$ (R = ^{t}Bu, ^{i}Pr, Et, $OCH_2{}^t$Bu) and tungsten (VI) oxo-alkoxide/β-diketonates, $WO(OR)_3L$ (R = ^{t}Bu, ^{i}Pr and L = acac, hfac, tfac) have been synthetised and used for the deposition of tungsten oxide thin films via LP-CVD.[89, 128] The added bidentate β-diketonate ligands were used to enhance the volatility of the precursors. All the films deposited, in a temperature range between 120 and 390°C depending on the precursor used, were initially amorphous. Once annealed during several hours at 400°C, the film of WO_3 becomes polycrystalline. Films annealed at 1000°C displayed XRD patterns which indicated the presence of both WO_3 and WO_2.[128] Usually, annealing of a film in an oxidising atmosphere generates the right stoichiometry and the desired properties compared to the as-deposited film.[129]

Bi_2WO_6 films have been prepared at 500°C by AP-CVD using $Bi(CH_3)_3$ and $W(OEt)_5$ as the Bi and W sources. Oxygen gas was used as an oxidant carrier gas. The growth was carried out on polycrystalline substrate, such as (100)$LaAlO_3$, (100)$SrTiO_3$.[128] The tungsten(VI) oxo-tetra-alkoxide, $WO(OCH_2CF_3)_4$, and the donor functionnalized tungsten(VI) alkoxide $WO(O^iPr)_3$(dmae) [dmae = $-OCH_2CH_2N(CH_3)_2$] were used also to deposit WO_3 in a single step in N_2/O_2.[89]

Using $W(OPh)_6$ as precursor, a tungsten oxide film has been deposited by AA-CVD on glass substrate. The AA-CVD depositions were carried out at substrate temperatures of 400°C. All films were deep blue, robust and adherent to the glass. After annealing in air at 400°C for 20 minutes, they become pale yellow, indicating the stoichiometry WO_3.[89, 129] Moreover, $W(OPh)_6$ and $Ti(OPr^i)_4$ in acetone were used to deposit a titanium doped tungsten oxide film by AA-CVD.[130]

The synthesis of the polyoxotungstate complexes, derivatives of tungsten oxoalkoxide, have been used as a CVD precursors.[131] Hence, AA-CVD of polyoxotungstate precursors $[^nBu_4N]_2[W_6O_{19}]$ at 410°C and $[^nBu_4N]_4H_3[PW_{11}O_{39}]$ at 480°C in acetone produces on glass substrates films of γ-WO_{3-x} and γ-WO_3 after post-annealing.[132] Moreover, AA-CVD reactions of $[^nBu_4N]_4[W_{10}O_{32}]$ and $[^nBu_4N]_2[W_6O_{19}]$ and $[^nBu_4N]_3[WO_4]$ using acetonitrile, and of $[NH_4]_6[W_{12}O_{39}]$, $[NH_4]_{10}H_2[W_2O_7]_6$, using water as a solvent and transport medium were used as a single

source precursor for the deposition of WO_{3-x} and WO_3 on glass substrate in the range 500–600°C.[133] Consequently, the unconventional polyoxometallate precursors which are large, charged and simple to prepare can be employed in AA-CVD for the preparation of WO_3.[134, 135]

1.4.2.2 Tungsten(VI) amides

$W(NBu^t)_2(NHBu^t)_2$ has been proved to be an unimolecular precursor to grow WN_x (x = 0.8-1.8). The deposition of thin films on silicon and glass substrates was performed in a low-pressure cold-wall reactor at temperatures 500-650°C while the precursor was vaporized into the reactor at 60-100°C. Argon or hydrogen was used as carrier gas to assist the LP-CVD process; the pressure was at 0.5 torr.[136] The annealing studies over different substrates demonstrated the ease of oxygen incorporation via moisture attack. Nevertheless, WN_x formed proving that the W-N bond is quite strong.[137] The deposition of WN_x from $W(NBu^t)_2(NHBu^t)_2$ has been studied and various mechanisms in competition has been proposed, such as ligand losses producing tert-butylamine, γ-hydrogen elimination responsible of isobutylene, or β-methyl activation giving rise to methyl bond to the surface and acetonitrile.[136, 138]

Alternatively, some analogues such as $W(NBu^t)_2(NMe_2)_2$, $W(NBu^t)_2(NEtMe)_2$,[139] $(^tBuN)_2W(NEt_2)_2$,[102] have been synthesised and used as precursor to deposit conformally WN_x with no carbon incorporation due to the β-hydride elimination. $(^tBuN)_2W(NMe_2)_2$ which gives excellent deposition, has become a commercial precursor.

As already noted, tungsten oxide can be deposited *in situ* using these oxygen-free precursors. For example, WO_xN_y (x>y) has been grown using $W(NBu^t)_2(NMe_2)_2$ and water vapour.[139] $W(NBu^t)_2(NHBu^t)_2$ and a co-reactant like H_2O carried by an inert gas (Ar) or/and an oxidizing gas (O_2) can deposit WO_x. These examples have shown the possibility of growing a metal oxide from a free-oxygen precursor.

Recently, the deposition of $W_2^{III}O_3$ films by ALD was studied using $W_2(NMe_2)_3$ and water as precursors, showing that the oxidation state of the metal-containing precursor has been conserved in the coating.[68]

1.4.3 Organometallic precursors

1.4.3.1 Tungsten carbonyl and derivatives

Tungsten oxide thin films can be prepared by the CVD of tungsten hexacarbonyl. Initially, a tungsten oxide film has been deposited in a single step process using $W(CO)_6$ with an Ar/O_2 atmosphere. The O_2 flow has been tuned to obtain the highest rate of deposition. Initially, a tungsten metal film is deposited and then subsequently annealed in an oxygen atmosphere to give the desired WO_3 film. The first step was carried out in an argon atmosphere at 400°C and then annealed for 4 hours at 600°C.[140] Also, tungsten trioxide was deposited at 500°C from $W(CO)_6$ at atmospheric pressure using other co-reactant gases to obtain the pale yellow film with O_2/H_2O and an intensive blue film with N_2/H_2.[141]

Recently, a precursor, which is air and moisture stable, $C_5H_{11}NCW(CO)_5$, has been synthesised and used to grow WO_3 films by AP-CVD in N_2/O_2 atmosphere at 300°C.[142]

Amorphous WO_3 oxide films doped with phosphorus have been deposited on a glass substrate by LP-CVD using volatile single-source precursors. The precursors synthesised were *trans*-$W(CO)_4[P(OEt)_3]_2$, $W_2(CO)_8(\mu\text{-}PR_2)_2$ with R = Me, Et and *trans*- and *cis*-$W(CO)_4(PEt_3)_2$. The ratio P/W in the final films were respectively 1/1, 1/4 and 1/10. Also, the quantity of dopant incorporated could be tuned by choosing the appropriate precursor. All of the deposition experiments were carried out at 400°C using O_2 or N_2/O_2 as carrier gas and the films deposited were all amorphous and were characterised by XPS. The use of a single-source precursor containing the dopant and the growth of an amorphous film at high temperature is unprecedented.[143]

Usually, the multi-source approach is used to grow mixed-metal oxides due to its simplicity compared to the single-source approach. Indeed, a thin film of mixed Mo-W oxides was prepared by AP-CVD at 200°C using $Mo(CO)_6$:$W(CO)_6$ in a 1:4 in Ar/O_2. To improve film structure and electrochromic properties, annealing was performed in the temperature range 200-500°C. However, an amorphous mixed-metal Co:W of 1:1 film on Si(100) was prepared by AP-CVD with the use of $[(\eta\text{-}C_5H_5)(CO)_3WCo(CO)_4]$ as a single-source precursor. Annealing of the film under oxygen at 900°C produced a $CoWO_4$ polycrystalline film. The Co/W ratio depends on the deposition temperature and was not necessarily unity. At higher temperature, the deposition lead to a higher Co content.[81, 144]

1.4.3.2 Tungsten allyl

Thin films of tungsten oxide were grown by AP-CVD using tetra(allyl)tungsten $W(\eta^3\text{-}C_3H_5)_4$ under a flow Ar/O_2. X-ray diffraction (XRD) analyses showed amorphous films at substrate temperatures T<350°C and polycrystalline films at T>350°C. The film as-deposited contained significant amounts of carbon (17 at.%). However, using $W(\eta^3\text{-}C_3H_5)_4$, Meda et al. reports a concentration of 8 at.% of carbon detected by RBS during a growth where a high flow of oxygen was used. After annealing, the carbon contamination dropped below the detection limit.[145, 146]

Also, the precursor tris(methylvinylketone)tungsten or $[W(CH_3COCHCH_2)_3]$ has been investigated to deposit WO_3 at low pressure at 450°C under oxygen.[146]

Using the multi-source approach, there have been very few reports on the preparation of mixed metallic oxide films including the element tungsten.[80, 87]

1.5 Motivations, objectives and strategies

Understanding all the properties of WO_3 and the decomposition chemistry of known CVD precursors are key points in the development and design of single-source molecular precursors. Most of the papers concerning mixed-metal tungsten oxide $M_xW_yO_z$ are made from sintering powder and soft chemistry (sol-gel technique). Only a few precursors suitable for CVD have been synthesised to make thin films. It will be for the CVD route a real challenge to prepare advanced target materials from single-source precursors.

The goal of this thesis work, through the SSP precursor approach, is to prepare films containing more than one element, such as mixed metal-tungsten oxide, that is to say at least three elements. In order to transport the two metal elements in the gas phase for the deposition, it is proposed to use a single-source precursor, that is, in the present case, multi-element complexes, such as heterobimetallic complexes. Moreover, they need to respond to the criteria of CVD, either being soluble in an organic solvent, such as toluene or volatile at low pressure or even at atmospheric pressure.

Also, the choice of the metal M, for example *d*-transition metal (Fe, Cu, Mg, Zn, Co, Ni), alkali metals (Na, Li), pnictogen (As, Sb, Bi), noble metal (Pd, Pt, Rh) will be considered in relation with their properties.

All these important parameters are connected to the precursor chemistry, that is to say mainly to the choice of ligand. For instance, amino-alcohols and alcohols used as

multidentate ligands, allow in a first step the preparation of homometallic tungsten alkoxides. Then, they can also potentially bridge two or more metals in order to generate original hetero-bimetallic amino-alkoxide precursors.

Others types of precursors, based on monodentate amido-/imido- ligands will be developed to synthesise heterobimetallic amides suitable for the deposition by CVD of WM_xN_y, and $WM_xN_yO_z$/WM_xO_y films in the absence or presence, respectively, of an oxidative environment.

Due to the desire to synthesise precursors for the deposition of tungsten(VI) oxide based films, the aim of this thesis will focus on the synthesis of a range of hetero-bimetallic tungsten compounds at the +VI oxidation state which contain the element oxygen and nitrogen. Indeed, the N- and O-donor functions will be included in the design of the ligand which could chelate and bridge different elements.[80]

1.6 References

[1] F. Bussolotti, L. Lozzi, M. Passacantando, S. La Rosa, S. Santucci and L. Ottaviano, *Surf. Sci.* **2003**, *538*, 113.
[2] P. A. Cox, *Transition Metal Oxides*, Clarendon Press, Oxford, **1992**.
[3] P. M. Woodward, A.W. Sleight and T. Vogt, *J. Sol. State Chem.* **1997**, *131*, 9.
[4] A. Souza-Filho, V. Freire, J. Sasaki, J. Mendes-Filho, J. Juliao and U. Gomes, *J. Raman Spect.* **2000**, *31*, 451.
[5] D. W. Bullett, *J. Phys. C: Solid State Phys.* **1983**, *16*, 2197.
[6] D. J. Palmer and P. G. Dickens, *Acta Cryst.* **1979**, *B35*, 2199.
[7] P. Tagtstrom and U. Jansson, *Thin Solid Films* **1999**, *352*, 107.
[8] A. Kuzmin, J. Purans, E. Cazzanelli, C.Vinegoni and G. Mariotto, *J. Appl. Phys.* **1998**, *84*, 5515.
[9] M. Sato , B. H. Grier, G. Shirane and T. Akahane, *Phys. Rev. B* **1982**, *25*, 6876.
[10] A.C. Jones, in *CVD of Compounds Semiconductors*, Wiley-VCH, **1996**.
[11] E. Kikuchi, K. Iida and A. Fujishima, *J. Electroanal. Chem.* **1993**, *351*, 105.
[12] C.Granqvist, *Sol. energy mater. sol. cells* **2000**, *60*, 201.
[13] N. A. Rowley, R.J. Mortimer, *Science Progress* **2002**, *85*, 243.
[14] C. Granqvist, *Electrochim. Acta* **1999**, *44*, 3005.
[15] S.K. Deb, *Appl. Opt. Suppl.* **1969**, *3*, 192.
[16] C.O Avellaneda, P. R. Bueno and L. O. S. Bulhoes, *J. Non-Cryst. Solids* **2001**, *290*, 115.
[17] G. A. Niklasson, C. Granqvist, *J. Mater. Chem.* **2007**, *17*, 127.
[18] U.O Krasovec, B. Orel, *Sol. energy mater. sol. cells* **2002**, *73*, 21.
[19] C.Granqvist, *J. of the European Ceramic Soc.* **2005**, *25*, 2907.
[20] C. G. Granqvist, A. Azens, P. Heszler, L. B. Kish, L. Osterlund, *Sol. Energy Mater. Sol. cells* **2007**, *91*, 355.
[21] C.O. Avellaneda, L. Bulhoes, *Solid State Ionics* **2003**, *165*, 117.
[22] A.I Gavrilyuk, *Electrochim. Acta* **1999**, *44*, 3027.
[23] J. N. Yao, Y. A. Yang, J.N. Yao, *J. Phys. Chem. B* **1998**, *102*, 1856.
[24] M. R. Goulding, C. B. Thomas, J. Hurditch, *Solid State Communications* **1983**, *46*, 451.
[25] P. Maruthamuthu and M. Ashokkumar, *Solar Energy Materials* **1988**, *17*, 433.
[26] R. A. Boudreau and H. M. Haendler, *Synthesis and Reactivity in Inorganic and Metal-Organic Chemistry* **1982**, *12*, 611.
[27] T. He, Y. Ma, Y-A Cao, W-S Yang, J-N Yao, *Phys. Chem. Chem. Phys.* **2002**, *4*, 1637.
[28] J. N. Yao, K. Hashimoto and A. Fujishima, *Nature* **1992**, *355*, 624.
[29] C. Bechinger, E. Wirth, P. Leiderer, *Appl. Phys. Lett.* **1996**, *68*, 2834.
[30] Y. A. Yang, Y. W Cao and J.N. Yao, *J. Phys. Chem. Solids* **1998**, *59*, 1667.
[31] C. Sella, M. Maaza, O. Nemraoui, J. Lafait, N. Renard and Y. Sampeu, *Surf. Coat. Tech.* **1998**, *98*, 1477.
[32] P. Jin, S. Nakao and S. Tanemura, *Thin Solid Films* **1998**, *324*, 151.
[33] K. R. Speck, H.S.W. Hu, M.E. Sherwin and R.S. Potember, *Thin Solid Films* **1988**, *165*, 317.
[34] T. D. Manning and I. P. Parkin, *J. Mater. Chem.* **2004**, *14*, 2554.
[35] T. D. Manning, Ivan P. Parkin, M. E. Pemble, D. Sheel and D. Vernardou, *Chem. Mater.* **2004**, *16*, 744.
[36] M. A. Sobhan, R. T. Kivaisi, B. Stjerna and C.G. Granqvist, *Sol. Energy Mater. Sol. Cells* **1996**, *44*, 451.
[37] I. Takahashi, M. Hibino and T. Kudo, *Jpn. J. Appl. Phys.* **1996**, *35*, L438.

[38] S. Sitkiewitz and A. Heller, *New J. chem.* **1996**, *20*, 233.
[39] A. L. Linsebigler, G. Lu and J. T. Yates, *Chem. Rev.* **1995**, *95*, 735.
[40] I. P. Parkin and R. G. Palgrave, *J. Mater. Chem.* **2005**, *15*, 1689.
[41] X.Z. Li, F.B. Li, *Journal of Photochemistry and Photobiology A: Chemistry* **2001**, *141*, 209.
[42] M. Ashokkumar and P. Maruthamuthu, *New J. chem.* **1990**, *14*, 43.
[43] M. Ashokkumar and P. Maruthamuthu, *J. Photochem. and photobiol. A : Chem.* **1989**, *49*, 249.
[44] T. Junwang, in *Materials Science Forum*, **2003**, p. 423.
[45] A. Hameed, M.A. Gondal and Z.H. Yamani, *Catalysis Communications* **2004**, *5*, 715.
[46] D. Paluselli, B. Marsen, E. Miller and R. Rocheleau, *Electrochem. Solid-State Letters* **2005**, *8*, G301.
[47] R. Asahi, T. Morikawa, T. Ohwaki, K. Aoki and Y. Taga, *Science* **2001**, *293*, 269.
[48] Shinri Sato, R. Asahi, T. Morikawa, T. Ohwaki, K. Aoki and Y. Taga, *Science* **2002**, *295*, 626.
[49] M-S. Wong, W-C. Chu, D-S. Sun, H-S. Huang, J-H. Chen, P-J. Tsai, N-T. Lin, M-S. Yu, S.-F. Hsu, S-L. Wang and H-H. Chang, *Appl. Environ. Microbiol.* **2006**, *72*, 6111.
[50] D.E. Williams, *Solid state gas sensors*, P.T. Moseley and B.C. Tofield, **1987**.
[51] X. Wang, N. Miura and N. Yamazoe, *Sens. Actuators B* **2000**, *66*, 74.
[52] H. Kawasaki, T. Ueda, Y. Suda and T. Oshima, *Sens. Actuators B* **2004**, *100*, 266.
[53] L.F. Reyes, S. Saukko, *J. of the European Ceramic Soc.* **2004**, *24*, 1415.
[54] A. Hoel, L. F. Reyes, S. Saukko, P. Heszler, V. lantto and C. G. Granqvist, *Sens. Actuatuors B* **2005**, *105*, 283.
[55] X. Chen, S. S. Mao, *Chem. Rev.* **2007**, *107*, 2891.
[56] W. S. Rees, in *CVD of Nonmetals, Vol. 18*, Wiley-VCH, **1996**, p. 205.
[57] M.J. Hampden-Smith, *Chem. Vap. Deposition* **1995**, *1*, 8.
[58] M. J. Hampden-Smith, *Chem. Vap. Deposition* **1995**, *1*, 39.
[59] D. W. Sheel, M. E. Pemble, in *CVD Coatings on Glass, ICCG4*, **November 2002**.
[60] P. O' Brien, N. L. Pickett, D. J. Otway, *Chem. Vap. Deposition* **2002**, *8*, 237.
[61] A.C. Jones, *J. Mater. Chem.* **2002**, *12*, 2576.
[62] W. S. Rees, in *CVD of nonmetals*, Wiley-VCH, **1996**, p. 30.
[63] W. A. Herrmann, N.W. Huber and O. Runte, *Angew. Chem. Int. Ed. Engl.* **1995**, *34*, 2187.
[64] A.C Jones, *Chem. Vap. Deposition,* **1998**, *4*, 169.
[65] P. O' Brien, in *Comprehensive Coordination Chemistry II, Vol. 9*, Elsevier, **2004**, p. 1005.
[66] T. Kodas, in *The chemistry of Metal CVD*, Wiley-VCH, **1994**, p. .
[67] R. G. Gordon, R. Fix and D. M. Hoffman, *Chem. Mater.* **1993**, *5*, 614.
[68] C. L. Dezelah, O. M. El-Kadri, I. Sziligyi, J. M. Campbell, K. Arstila, L. Niinistö and C. H. Winter, *J. Am. Chem. Soc.* **2006**, *128*, 9638.
[69] J.-S M. Lehn, P. Van der Heide, Y. Wang, S. Suh and D. M. Hoffmann, *J. Mater. Chem.* **2004**, *14*, 3239.
[70] D. B. Beach, *IBM J. Res. Develop.* **1990**, *34*, 796.
[71] Anthony C. Jones, *J. Mater. Chem.* **2002** *12*, 2576.

[72] A. C. Jones, P. A. Williams, J. F. Bickley, A. Steiner, H. O. Davies, T. J. Leedham, A. Awaluddin, M. E. Pemble, G. C. Critchlow, *J. Mater. Chem.* **2001**, *11*, 1428.
[73] M. J. Crosbie, P. J. Wright, H. O. Davies, A. C. Jones, T. J. Leedham, P. O'Brien, G. W. Critchlow, *Chem. Vap. Deposition* **1999**, *5*, 9.
[74] W. E. Buhro, *Advanced Materials for Optics and Electronics* **1996**, *6*, 175.
[75] Lisa McElwee-White, *Dalton Trans.* **2006**, 5327.
[76] A. N. Gleizes, *Chem. Vap. Deposition* **2000**, *6*, 4.
[77] K. Yun-Soo, K. Won-Yong, in *Eur. Pat. Appl., Vol. EP0897925*, **1999**.
[78] S. Mathur, M. Veith, T. Ruegamer, E. Hemmer and H. Shen, *Chem. Mater.* **2004**, *16*, 1304.
[79] K. Yun-Soo, in *Eur. Pat. Appl., Vol. 5,998,664*, **1999**.
[80] L. G. Hubert Pfalzgraf, *J. Mater. Chem.* **2004**, *14*, 3113.
[81] A. C. Jones, in *CVD of compounds semiconductors*, Wiley-VCH, **1996**.
[82] W. S. Rees, in *CVD of nonmetals*, Wiley-VCH, **1996**, p. 12.
[83] R.W. Jones, in *Fundamental principles of sol-gel technology*, Institute of Metals, **1989**.
[84] K. N. Strafford, in *Surface engineering practice*, Ellis Horwood, **1990**, p. 36.
[85] W. S. Rees, in *CVD of nonmetals*, Wiley-VCH, **1996**, p. 21.
[86] W. S. Rees, in *CVD of nonmetals*, Wiley-VCH, **1996**, p. 5.
[87] T. Kodas, in *The chemistry of Metal CVD*, Wiley-VCH, **1994**, p. 28.
[88] I. P. Parkin, W. B. Cross, in *222nd ACS National Meeting*, Chicago, IL, United States, **2001**.
[89] P. A. Williams, Ph.D thesis (Bath), **2000**.
[90] Martin J. Davis, *Chem. Vap. Deposition* **2004**, *10*, 29.
[91] T.A. Polleya, *Thin Solid Films* **1999**, *357*, 132.
[92] M. Rothschild, A. R. Forte, *Appl. Phys. Lett.* **1991**, *59*, 1790.
[93] W. B. Henley, G. J. Sacks, *J. Electrochem. Soc.* **1997**, *144*, 1045.
[94] R. Sivakumara, *Materials Chemistry and Physics* **2004**, *87*, 439.
[95] T. Olding, M. Sayer and D. Barrow, *Thin Solid Films* **2001**, *398-399*, 581.
[96] M.L.H. Green, *J. of Organometallic Chemistry* **1995**, *500*, 127.
[97] N. Greenwood, A. Earnshaw, in *Chemistry of the elements*, **1984**.
[98] T. Okamura, N. Ueyama, in *Comprehensive Coordination Chemistry II, Vol. 4* (Ed.: Elsevier), **2003**, p. 529.
[99] C. Housecroft, A. G. Sharpe, *Inorganic Chemistry*, Prentice Hall, **2001**.
[100] K. Mackay, W. Henderson, *Introduction to Modern Inorganic chemistry*, 6th ed., **2002**.
[101] E. H. Wong, *Journal of Organometallic Chemistry* **1994**, *477*, 45.
[102] Jin-Bao Wu, *J. Vacuum Science & Technology A* **2003**, *21*, 1620.
[103] G. R. Dobson, *Organomet. Chem. Rev., Sect. B* **1969**, *5*, 568.
[104] G. R. Dobson, *Organomet. Chem. Rev., Sect. B* **1970**, *6*, 1035.
[105] D. J. Darensbourg, *J. Organomet. Chem.* **1972**, *45*, 257.
[106] Donald J. Darensbourg, *J. Organomet. Chem.* **1973**, *62*, 299.
[107] Donald J. Darensbourg, *Journal of Organometallic Chemistry* **1976**, *115* 221.
[108] Gerard R. Dobson, *Journal of Organometallic Chemistry* **1977**, *143*, 385.
[109] J. D. Atwood, *J. Organomet. Chem.* **1979** *180*, 205.
[110] J. D. Atwood, *J. Organomet. Chem.* **1980**, *196*, 79.
[111] J. D. Atwood, *J. Organomet. Chem.* **1981**, *223*, 49.
[112] J. D. Atwood, *J. Organomet. Chem.* **1982**, *237*, 95.
[113] J. D. Atwood, *J. Organomet. Chem.* **1983**, *257*, 105.
[114] D. J. Darensbourg, *J. Organomet. Chem.* **1974**, *83*, 309.

[115] G. R. Dobson, *Organomet. Chem. Rev., section B* **1972**, *10*, 1.
[116] H. Sloan, *Annu. Rep. Prog. Chem., Sect. A* **1995**, *91*, 177.
[117] Alvin A. Holder, *Annu. Rep. Prog. Chem., Sect. A* **2005**, *101*, 161.
[118] Alvin A. Holder, *Annu. Rep. Prog. Chem., Sect. A* **2006**, *102*, 194.
[119] John Malito, *Annu. Rep. Prog. Chem., Sect. A* **2001**, *97*, 157.
[120] T. S. Kleckley, J. L. Bennett, P. T. Wolczanski, E. B. Lobkowski, *J. Am. Chem. Soc.* **1997**, *119*, 247.
[121] A. S. Veige, T.S. Kleckley, R. L. M. Chamberlin, D. R. Neithamer, C. E. Lee, P.T Wolczanski, E. B. Lobkovsky, W. V. Glassey, *J. Organomet. Chem.* **1999**, *591*, 194.
[122] A. L. Johnson, Ph.D thesis (Durham), **1999**.
[123] M. F. Lappert, P. P. Power, A. R. Sanger and R. C. Srivastava, in *Metal and Metalloid amides*, Ellis Horwood, **1980**, p. 487.
[124] W. S. Rees, in *CVD of nonmetals*, Wiley-VCH, **1996**, p. 367.
[125] T. Kodas, in *The chemistry of Metal CVD*, Wiley-VCH, **1994**.
[126] S. O'Neill, I. P. Parkin, *ChemInform* **2004**, *35*, 37.
[127] U. Riaz, *Thin Solid Films* **1993**, *235*, 15.
[128] D. V. Baxter, M. H. Chisholm, S. Doherty and N. E. Gruhn, *Chem. Comm.* **1996**, 1129.
[129] W. B. Cross, I. P. Parkin, S. A. O'Neill, P. A. Williams, M. F. Mahon and K. C. Molloy, *Chem. Mater.* **2003**, *15*, 2786.
[130] Robert G. Palgrave, Ivan P. Parkin, *J. Mater. Chem.* **2004**, *14*, 2864.
[131] R. J. Errington, M. D. Kerlogue, D. G. Richards, *J. Chem. Soc., Chem. Commun.* **1993**, 650.
[132] W. B. Cross, I. P Parkin, *Chem. Commun.* **2003**, 1696.
[133] S. Ashraf, C. S. Blackman, R. G. Palgrave and I. P. Parkin, *J. Mater. Chem.* **2007**, *17*, 1063.
[134] A. P. Ginsberg, in *Inorganic Synthesis, Vol. 27*, Wiley, **1990**, p. 72.
[135] W. Clegg, M. R. J. Elsegood, R. J. Errington and J. Havelock, *J. Chem. Soc., Dalton Trans.* **1996**, 681.
[136] H-T. Chiu, *Mat. Res. Soc. Symp. Proc.* **1992**, *250*, 317.
[137] Y. W. Yang, J. B. Wu, Y. F. Lin and H. T. Chiu, in *CVD reaction of metal Nitride Precursors*, NSRRC, **2002/2003**, p. 68.
[138] E. L. Crane, H-T Chiu and R. G. Nuzzo, *J. Phys. Chem. B* **2001**, *105*, 3549.
[139] J. S. Becker, S. Suh and Roy G. Gordon, *Chem. Mater.* **2003**, *15*, 2969.
[140] D.Gogova, G. Stoyanov, K. A. Gesheva, *Renewable energy* **1996**, *8*, 546.
[141] D. Barreca, S. Bozza, G. Carta, G. Rossetto, E. Tondello, P. Zanella, *Surface Science* **2003**, *532-535*, 439.
[142] R. G. Gordon, S. Barry, J. T. Barton, Randy and N. R. Broomhall-Dillard, *Thin Solid Films* **2001**, *392*, 231.
[143] E. Brescacin, M. Basato and E. Tondello, *Chem. Mater.* **1999**, *11*, 314.
[144] S. Shin-Guang, W. U. Juan-Seng, *Chem. Commun.* **1996**, 2239.
[145] L. Meda, R. C. Breitkopf, T. E. Haas, R. U. Kirss, *Thin Solid Films* **2002**, *402*, 126.
[146] L. Meda, R. U. Kirss, R. Breitkopf, T. Haas, in *214th ACS National Meeting*, Las Vegas, **1997**.

Chapter 2
Homo-metallic Tungsten amino-Alkoxide complexes

2.1 Introduction

Metal homo-alkoxides $[M(OR)_x]_n$ and metal oxo-alkoxides $[MO(OR)_{x-2}]_n$, with M = metal or metalloid of valency *x* and R = simple or substituted alkyl, n = degree of molecular association, have been widely studied due to their attractive applications either as catalysts for a range of organic reactions or as precursors for sol-gel processes and MO-CVD of metal oxides, heterometal oxide films, ceramic materials and glass.[1] Metal oxo-alkoxides species which are the intermediates between homo-alkoxides $[M(OR)_x]_n$ and oxides MO_x received recently more and more attention because of the increasing interest of sol-gel and MO-CVD techniques, principally as new routes to new materials. Thus, metal oxo-alkoxides represent the ideal precursor in order to obtain metal oxide MO_x because of structural similarities to the target materials and their higher stability.

Metal alkoxides, both metal homo-alkoxides and oxo-alkoxides, can be synthesised by a variety of methods.[2-5] A series of tungsten alkoxides $W(OR)_6$ (R = Me, Et, ^{n}Pr, ^{i}Pr, allyl) and tungsten oxo-alkoxides $[WO(OR)_4]_2$ (R = Me, Et, ^{i}Pr, ^{t}Bu, *cyclo*-C_6H_{11}) have been synthesised respectively by reactions of tungsten dialkylamides with alcohol [Eq. (2.1)],[6] by the ammonia method [Eq. (2.2)],[6] and metathesis of tungsten (oxo)chloride and an alkali metal alkoxide in an anhydrous solvent, such as toluene or THF [Eq. (2.3)].[7]

$$W(NR_2)_6 + 6\ R'OH \rightarrow W(OR)_6 + 6\ R_2NH\uparrow \qquad (2.1)$$

$$W(O)Cl_4 + ROH + NH_3 \rightarrow W(O)(OR)_4 + NH_4Cl\downarrow \qquad (2.2)$$

$$W(O)Cl_4 + MOR \rightarrow W(O)(OR)_4 + MCl\downarrow \qquad (M = Li, Na, K) \qquad (2.3)$$

The series of tungsten oxo-alkoxides with tungsten in the +VI oxidation state will be the candidate precursor for the preparation of $W^{VI}O_3$ due to the conservation of the O.S from the precursor to the target material.[8] They also represent the last stage before making the metal oxide. Generally, the metal alkoxides tend to aggregate to form polymeric structures because of the high polarity of the metal-oxygen bond $M^{\delta+}$—$O^{\delta-}$—C. Thus, the formation of oligomeric species through dative bonds is a dominant feature of the metal alkoxides.

As an example, the tungsten(VI) oxo-tetra-alkoxides $WO(OR)_4$ (R = Me, Et, ^{i}Pr and *cyclo*-C_6H_{11}) exists as dimers in the condensed state through alkoxo bridges of the following type:[7]

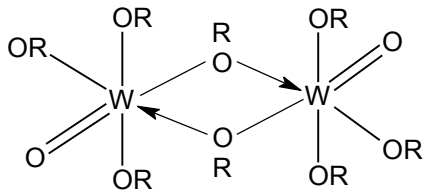

Figure 2.1 Alkoxo bridged dimeric structure

As a result, most of them show a fairly low degree of volatility and solubility in common organic solvents. Their degree of polymerisation is principally dependent on the steric demand of the alkyl substituent. Also, the extent of aggregation decreases with increasing steric demand. This is illustrated by compounds containing bulky groups, such as $WO(OBu^t)_4$ which reduces the degree of polymerisation to a monomeric solid. As a consequence, $WO(OBu^t)_4$ adopts in the solid state a distorted square pyramidal structure (Figure 2.2):[9]

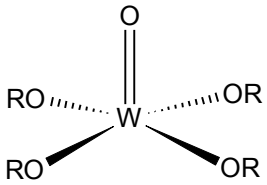

Figure 2.2 Square pyramidal monomeric structure

Minimizing molecular oligomerisation, and thus cohesive lattice energies, by saturating the metal coordination sphere with sterically encumbered (mono- and/or multi-dentate) or halogenated (preferably fluorinated) and/or donor-functionalised alkoxo ligands, is an attractive strategy for the design and synthesis of soluble and volatile compounds.[10, 11]
To achieve volatility and solubility, the strength of the polar interactions has to be minimized. This can be achieved either by:

- Increasing the distance between the polar metal oxygen bonds by means of large organic ligands ("steric shielding concept").
- Reducing the polarizing strength of the metal ion by charge transfer from donor ligands the so-called ("donor functionalization concept").
- Reducing the basicity of the alkoxy oxygen by using high electronegative perfluorinated alkyl substituents (*e.g* -OCF_3).

Tungsten(VI) oxo-tetra-alkoxide $[WO(OR)_4]_2$ and tungsten(VI) oxo-alkoxide/β-diketonate complexes $WO(OR)_3(L)$ (R = ^{i}Pr; L = acac, hfac) have been synthesised as precursors for LP-CVD studies in order to deposit WO_3 films on different types of substrate. Their volatility could be enhanced by minimizing all types of intermolecular attractive interactions between precursor molecules in the condensed state. Hence, the reaction of β-diketonate (L = acac, hfac) with $[WO(OR)_4]_2$ gives rise to the corresponding monomeric alkoxide $WO(OR)_3(L)$ from the use of a bidentate ligand to replace one of the monodentate ligands.[12]

The bidentate β-diketonate ligand (L), equivalent to an O-donor functionalised alkoxide, brings about the break-up of the alkoxide bridges between the tungsten atoms to give monomeric molecules with a six membered chelate ring, as depicted in the following Figure:

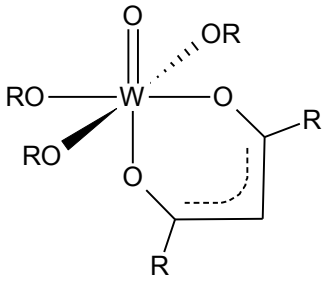

L = acac ; R = CH_3

L = hfac ; R = CF_3

Figure 2.3 Proposed structure of $WO(OR)_3L$ complexes

This gives rise to products which are liquids rather than solids, so no structural characterisation has been possible. In fact, this does not enhance significantly the volatility but does increase dramatically the solubility and the thermal stability.[13] Instead of using a β-diketonate ligand, an N-donor functionalised ligand, such as an amino-alcohol of the type $HOCHR^1CHR^2NR^3R^4$ (R^1-R^4 = H, Me, alkyl, CF_3 or aryl) have been used extensively in the synthesis of metal mixed alkoxide/amino-alkoxides by reacting the metal alkoxide with the amino-alcohol:

$$M(OR)_n + x\ HOCHR^1CHR^2NR^3R^4 \rightarrow M(OR)_{n-x}(OCHR^1CHR^2NR^3\ R^4)_x + x\ ROH \qquad (2.4)$$

Also, $WO(OR)_3$(dmae) and related species have been synthesised by the reaction of $[WO(OR)_4]_2$ with N,N'-dimethyl aminoethanol (Hdmae). The increase in volatility was limited whereas the solubility increases dramatically compared to the parent alkoxide.[13] As a result, tungsten oxide films have been deposited by AA-CVD on a glass substrate.

The SSP approach, via donor polydentate ligand, has opened up new possibilities for the design of CVD precursors which does not focus only on the aspect of volatility, decomposition pathway and thermal stability, but also on their stability toward air and moisture and

their solubility, which is the main key pre-requisite for LI-CVD and AA-CVD.[14] For example, homoleptic titanium alkoxides can also be modified by the presence of dmae groups. As a result, the new precursors $[Ti(OPr^i)_3(dmae)]$ **(I)** and $[Ti(OPr^i)_2(dmae)_2]$ **(II)** have been prepared and characterised. These compounds are significantly less moisture sensitive than the parent alkoxide, which is likely to be of significance in LI-CVD, where trace water in the solvent may lead to decomposition of the precursor on extended storage. Both **(I)** and **(II)** have been used to deposit good quality TiO_2 films by LI-CVD.[15] VT NMR studies indicate that $[Ti(OPr^i)_3(dmae)]$ **(I)** is a monomer whereas $[Ti(OPr^i)_2(dmae)_2]$ **(II)** exists as a monomer at high temperature and a dimer in solution at low temperature. Thus, those compounds of the type $[Ti(OR)_{4-x}(dmae)_x]$ are good alternatives to $Ti(OR)_4$ in term of moisture sensitivity.

Similar work starting from the zirconium alkoxide $[Zr(OPr^i)_4(^iPrOH)]_2$ give rise to the monomeric $Zr(OPr^i)_2(dmae)_2$ liquid which is analogous to the titanium derivative.[16] These precursors are convenient for the CVD of ZrO_2 while the parent alkoxides "$[Zr(OR)_4]$" are poor.[17] The donor-functionalization approach using Hdmae has been used successfully to produce an MO-CVD precursor for Ta_2O_5 by breaking-up the dimer $[Ta(OEt)_5]_2$, giving rise to $[Ta(OEt)_4(dmae)]$.[18] This allows the highly electropositive metal center to achieve its favoured six coordination geometry within a monomeric unit and hence increase significantly its volatility. $Ta(OEt)_4(dmae)$ is also a liquid which therefore has not been characterised by X-ray crystallography. However, the ^1H NMR analysis confirms the monomeric nature of the compound, which is believed to be octahedral, as depicted in the following figure:

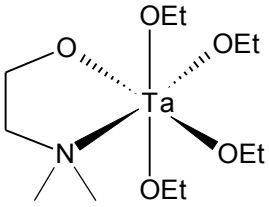

Figure 2.4 Probable structure of $Ta(OEt)_4dmae$

An interesting feature of primary and secondary amino-alkoxides of the type $[M(OCHRCH_2NMe_2)_x]_n$ (R = H, Me), is their low molecularity and higher volatility compared to those of 2-methoxy-ethoxide analogues. For example, $Cu[OCH_2CH_2NMe_2]_2$ **(III)** and $Cu[OCHMeCH_2NMe_2]_2$ **(IV)** have been prepared and are both monomeric and volatile, whereas copper(II) alkoxy-alkoxides $Cu(OR)_2$ [R = $-CH_2CH_2Me$, $-CH_2CH_2OCH_2CH_2OMe$, $(CH_2)_6Me$] are oligomeric or even polymeric.[19] X-ray crystal structures reveal a mononuclear square-planar geometry for **(III)** and **(IV)**. CVD of **(III)** gives a mixture of copper Cu_2O and

CuO whereas thermal deposition of **(IV)** gives metallic copper metal. Other derivatives, such as $Cu[OC(CF_3)_2CH_2NHBu^t]_2$ and $Cu[OC(CF_3)_2CH_2NMe_2]_2$ combine the donor functionalised effect and the addition of fluorinated ligand to enhance even more the volatility.[10]

This chapter will describe firstly the synthesis of tungsten mixed oxo-isopropoxide/amino-alkoxides via the starting material $[WO(OPr^i)_4]_2$.[7] It will also describe the physical and chemical properties of these precursors including, chemical reactivity towards moisture and thermal decomposition. The thermal decomposition has been carried out in air and under an inert atmosphere. Thus, the CVD and RAPET techniques are actually the methods employed to synthesise new types of material which include films and tungsten oxide nanomaterial. The term RAPET, Reaction under Autogenic Pressure at Elevated Temperature, involves decomposing thermally a molecular precursor at elevated temperature in a closed vessel under an inert atmosphere. The reaction takes place at an autogenic pressure from the precursor. A few studies directed by Gedanken et al. have proved that the RAPET of homo-metallic and hetero-metallic metal alkoxides leads through a one-step process, to a wide range of structures: core-shell, nanorods.[20-22] This novel method, using only metallic alkoxide precursor, in the absence of catalyst, can also lead to core-shell structures. All these structures and morphologies give rise mainly to carbon-coated metal oxide under nanoscale forms. Besides, it has previously been shown that carbon-coated $W_{18}O_{49}$ under visible light proved to be a good photocatalyst due to the presence of oxygen vacancies.[23] According to this methodology and the single-source precursor approach, we might expect to make carbon-coated tungsten oxide and also WO_3 films prepared by CVD which are known to be photocatalysts under visible light.

2.2 Results and discussion

2.2.1 Synthesis of mononuclear tungsten amino-alkoxides

The donor-functionalised tungsten(VI) oxo-amino-alkoxides were synthesised by the reaction of one equivalent of the appropriate chelating amino-alcohol (Hdmae, Hbdmap and Htdmap) with the dimer $[WO(OPr^i)_4]_2$ in toluene (Table 2.1).[7] As soon as the amino-alcohol is added to the suspension of $[WO(OPr^i)_4]_2$ in toluene at R.T, the oxo-alkoxide immediately solubilised, meaning that a reaction has occurred. The mixture was refluxed for several hours to ensure the reaction was complete before removing the solvent.

$$[WO(OPr^i)_4]_2 + 2\ HOCR_1R_2CH_2N(CH_3)_2 \xrightarrow[-\ ^iPrOH]{\Delta,\ Toluene} 2\ [WO(O^iPr)_3(OCR_1R_2CH_2N(CH_3)_2)] \qquad (2.5)$$

Table 2.1 Different types of amino-alkoxide complexes with their resulting molecular weight (M.W), temperature of vaporisation (b.p)

Type of ligands	Complexes	M.W	b.p (°C, 0.02 mmHg)
$R_1 = R_2 = H$; dmae	$WO(OPr^i)_3$dmae **(1)**	465.23	100
$R_1 = H$; $R_2 = CH_2N(CH_3)_2$; bdmap	$WO(OPr^i)_3$bdmap **(2)**	522.32	120
$R_1 = R_2 = CH_2N(CH_3)_2$; tdmap	$WO(OPr^i)_3$tdmap **(3)**	579.41	142

The resulting waxy oils were purified by vacuum distillation to yield monomeric liquids $WO(OPr^i)_3$(dmae) **(1),** $WO(OPr^i)_3$(bdmap) **(2),** $WO(OPr^i)_3$(tdmap) **(3)** which are air and moisture sensitive pale yellow oils. The volatility of these complexes provides convenient methods for their purification. As noticed during their purification, the temperature of vaporisation at constant pressure (P = 0.02 mmHg) increases in the order **(1)** < **(2)** < **(3)** with the increase of the steric factor, the nitrogen content and hence molecular weight (Table 2.1). Attempts were made to substitute two of the isopropoxide ligands for two dmae ligands via the same methodology. However, the ^{1}H NMR analysis of the recovered compounds indicated the presence of only one dmae ligand.

2.2.1.1 NMR Spectroscopy

1D NMR [^{1}H, ^{13}C(DEPT), ^{183}W NMR] and 2D NMR (COSY, HMQC) analysis were performed on **(1)**, **(2)** and **(3)** to determine the following shifts, δ ^{1}H, δ ^{13}C and δ ^{183}W. Also, the

^{183}W NMR of $W_4O_4(\mu\text{-}O)_6(tdmap)_4$ **(4)** will be included in comparison with all the previous monomeric compounds. $[WO(OPr^i)_4]_2$, as a starting material, has previously been fully characterised by variable temperature ^1H NMR, FT-IR and elemental analysis.[7] Therefore, only confirmation by ^1H NMR that the compound had been synthesised was required for this work.

2.2.1.1.1 ^1H NMR and ^{13}C NMR spectroscopy

The ^1H NMR spectrum recorded for $WO(OPr^i)_3$dmae **(1)** showed the expected peaks for the dmae ligand at 2.41 ppm for -N(C***H*****3**)$_2$, at 2.60 ppm for -OCH$_2$C***H*****2**N(CH$_3$)$_2$, and at 4.54 ppm for -OC***H*****2**CH$_2$N(CH$_3$)$_2$. As expected and indicated by early reports,[12, 13] the integrals indicated that one dmae ligand had replaced one -OPr^i group. The dialkylamino -N(C***H*****3**)$_2$ signals are equivalent, meanwhile the two -C***H*****2**- and C***H*****2**N signals from the dmae ligand are diastereotopic and hence inequivalent, showing two well resolved multiplet. This results from germinal and vicinal ^2J- and ^3J-coupling ($^2J_{H,H}$ = 5.5 Hz, $^3J_{H,H}$ = 1.2 Hz). The ^1H NMR analysis demonstrates in solution the presence of two types of isopropoxides –OC***H*****a-b** groups which are overlapped with each other at 4.80 ppm and three types of -OCH(C***H*****3**)$_2$ at 1.23 ppm (Figure 2.5). Hence, the respective signals of -OC***H*****b** are equivalent to each other but inequivalent to those obtained for -OC***H*****a**. In addition to the well defined spectrum at R.T, the resulted compounds can be formulated as a pseudo-octahedral complex which is monomeric (Figure 2.5). This tendency confirms that the N-donor functionalisation concept permits to break-up the dimeric starting material $[WO(OPr^i)_4]_2$ into monomers $WO(OPr^i)_3(L)$ [cf. Eq.(2.5)].

The ^1H NMR spectrum of $WO(OPr^i)_3$bdmap **(2)** is more complex than that for **(1)** due to the increasing number of ^2J- and ^3J-coupling introduced by the bdmap ligand. The NMR analysis shows similarities with **(1)** in term of signals ratio for the different hydrogen nuclei of the isopropoxide ligand. Nevertheless, the symmetry is lower than that of (**1**) which introduces the inequivalence of the two methyl groups of the coordinated amine η^2-N(C***H*****3**)$_2$ which become diastereotopic. Subsequently, the amine group -N(C***H*****3**)$_2$ chelating to the tungsten metal are not equivalent, displaying peaks at 2.36 and 2.43 ppm. Also, the spectrum of **(2)** shows also other signals of the amino-alkoxide: a multiplet at 4.51 ppm for the CH proton, a triplet at 2.59 ppm ($^2J_{H,H}$ = 11.62 Hz) and a pair of doublet 2.47 ppm ($^2J_{H,H}$ = 11.62 Hz, $^3J_{H,H}$ = 3.26 Hz) corresponding to the two diastereotopic -CH$_2$- groups which overlaps the signal of η^2-N(C***H*****3**)$_2$.

With another more bulky ligand (tdmap), the ^1H NMR spectrum of **(3)** showed similar signals to **(1)**, in particular a multiplet at about 1.2 ppm and the two types of septet for the CH

group of the isopropoxide ligand at 4.8 ppm. It also displays a complicated spectrum due to overlapping of certain peaks by three doublets ($^2J_{H,H}$ = 13.6 Hz, 13.6 Hz and 16 Hz) consistent with the three inequivalent -C***H₂***N$(CH_3)_2$ groups of the tdmap ligand. However, the structure revealed an equivalent chemical and magnetic environment for the two terminal methyl amino groups at δ = 2.28 ppm. The other amino group which is coordinated to the metal has two equivalent methyl substituents at δ = 2.48 ppm. These types of complexes adopt preferentially the *mer* configuration (Figure 2.5), assumed according to the NMR data. As already reported, VT ^{1}H NMR of tungsten(VI) oxo-isopropoxide/β-diketonate[12] and tungsten(VI) oxo-isopropoxide/amino-ethoxide complexes[13] confirm their monomeric structure in a *mer* configuration of -OPr^i groups, as illustrated in the Figure 2.5. The ^{1}H NMR and ^{13}C NMR analysis of respectively **(1)**, **(2)** and **(3),** which are in concordance with the *mer* configuration and show also the symmetry increasing in the order **(2)** < **(3)** < **(1)**.

Another aspect of tungsten oxo-alkoxides is that their structures in solution are often not static resulting from dynamic interchange of alkoxo groups. The modification of the alkoxide by amino-alkoxide eliminates the fluxionality of $[WO(OPr^i)_4]_2$ and facilitates the analysis of new derivatives. The NMR spectrum of **(1)**, **(2)**, **(3)** are not indicating fluxionality of compounds in solution due to the formation of a monomer which does not possess labile bridging alkoxide, contrary to the starting material $[WO(OPr^i)_4]_2$. The exact configuration of the new amino-alkoxide compounds cannot be determined with certainty by NMR. Only the molecular structure determined by X-ray crystallography can provide this information. However, the monomeric liquid precursors don't crystallize.

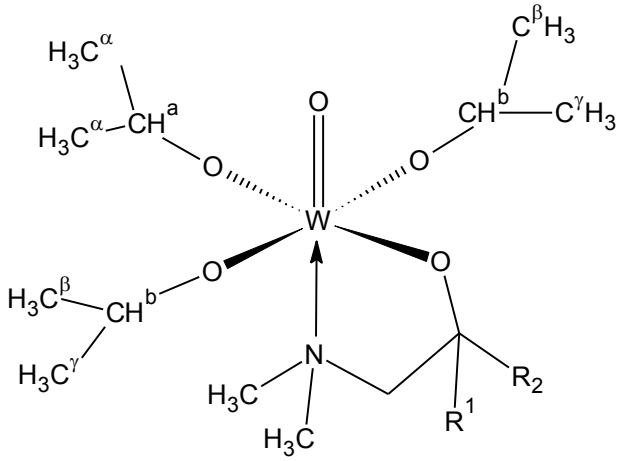

(1) $R^1 = R^2 = H$; dmae

(2) $R^1 = H$; $R^2 = CH_2N(CH_3)_2$; bdmap

(3) $R^1 = R^2 = CH_2N(CH_3)_2$; tdmap

Figure 2.5 *Mer* configuration of **(1)**, **(2)** and **(3)**

2.2.1.1.2 ^{183}W NMR spectroscopy

Tungsten (^{183}W) has a very low sensitivity NMR active nucleus with a spin of ½ and yields sharp signals over a very wide chemical shift range of 6720 ppm (from - 4670 to 2050).[24-26] Two of the highly shielded compounds are $W(CO)_6$ and WF_6 which have a chemical shift of - 3500 and - 1117 ppm, respectively. Substitution of the fluorine by ligands containing oxygen donors causes deshielding of the tungsten nucleus, for example the chemical shift of $WF_5(OMe)$ is -1065 ppm. The chemical shifts for tungstates are in the range of + 268 ppm to - 300 ppm.[26, 27] The ^{183}W NMR gives information about the direct environment of the metal concerned. Good solubility and high concentration are required for the ^{183}W NMR spectra to be recorded in a reasonable time. ^{183}W NMR studies have been carried out on a series of tungsten oxo-tetra-alkoxide compounds of the type $WO(OR)_4$ (R = Me, Et, *cyclo*-C_6H_{11}, ^{t}Bu, $C_6H_3{}^i Pr_2$-2,6). Also, all these compounds, apart from the $C_6H_3{}^i$Pr-2,6 and ^{t}Bu derivatives, are dimers with alkoxo- bridges.[7]

Table 2.2 ^{183}W NMR data[7] for the oxoalkoxides $[WO(OR)_4]_n$

Compounds	Extent of aggregation (n)	[a]Chemical shift (ppm)	Temperature (K)
Me	2	- 62.9	295
Me	2	- 272.4	370
Et	2	- 126.3	293
***cyclo*-C_6H_{11}**	2	- 140.3	298
^{t}Bu	1	- 386.9	300
$C_6H_3{}^i Pr_2$-2,6	1	- 493.6	295

[a]Chemical shifts in ppm referenced to 2 mol.dm^{-3} aqueous Na_2WO_4

These results show that as either the steric bulk of the substituent (^{t}Bu, $C_6H_3{}^i Pr_2$-2,6) or the temperature (Me) are increased, the chemical shift value moves up field (Table 2.2). This trend is also noticed when the degree of polymerisation decrease.[7, 24, 26] As a general rule, we can notice that decreasing positive charge, that is to say increasing of electronic population on the metal cation results in a downfield chemical shift. Hence, the shielding increases with increasing coordination number (C.N) of the metal center.[26] The ^{183}W NMR spectra were recorded for all four compounds **(1)-(4)** synthesised and the results are displayed in Table 2.3.

Table 2.3 ^{183}W NMR data for the oxo-amino-alkoxides **(1)-(4)**

Compounds	**[a]Chemical shift δ(ppm)**	**Temperature (K)**
$WO(OPr^i)_3(dmae)$ **(1)**	- 88.5	293
$WO(OPr^i)_3(dmae)$ **(1)**	- 99.9	373
$WO(OPr^i)_3(bdmap)$ **(2)**	- 99.9	373
$WO(OPr^i)_3(tdmap)$ **(3)**	- 114.1	373
$W_4O_4(\mu\text{-}O)_6(tdmap)_4$ **(4)**	- 42.6	373

[a]Chemical shifts in ppm referenced to 2 mol.dm^{-3} aqueous Na_2WO_4

The synthesised compounds were all reasonably soluble in d_8-toluene. Nevertheless, the spectrum were all recorded at 373 K in order to improve the intensity of the signals.[7] All four compounds showed a single peak in the spectra, indicating that each tungsten in the molecule possess an identical environment. The values are consistent with ^{183}W NMR chemical shift values recorded for six-coordinate oxo-tetra-alkoxide complexes (C.N = 6). The ^{183}W NMR chemical shift value of - 88.5 ppm for $WO(OPr^i)_3(dmae)$ in d_8-toluene at 293 K has been already reported in a previous work,[13] and is in concordance with the results reported in Table 2.3.[7] One aspect to notice in term of increasing temperature and bulky substituent is that the increase of the chemical shift values are relatively attenuated for the functionalised tungsten amino-alkoxide compared to the simple monomeric alkoxide complexes (cf. Table 2.2 and 2.3). For example, the difference of values for $[WO(OMe)]_2$ at 295 K and 370K does not reflect the same variation for $WO(OPr^i)_3(dmae)$ at 273 K and 373 K. The dative bond N:→W is responsible of the unexpected diminution of the chemical shift for $WO(OR)_3L$ at high temperature regardless of the recorded values for the oxo-tetra-alkoxide.

Hence, **(1)** remains six-coordinate (C.N = 6) at R.T unlike $[WO(OR)_4]_2$ (R = Me, ^{i}Pr) which dissociate at high temperature to become five-coordinate (C.N = 5). Subsequently, the dative bond N:→W belonging to the multi-dentate amino-alkoxide seems to be in solution relatively strong as the temperature increases.

2.2.2 Synthesis of polynuclear tungsten amino-alkoxides

During the synthesis (cf. section 2.2.1) and the handling of the monomeric liquid **(1)-(3)**, it was noticed that their sensitivity towards moisture decreased in the order **(1)** > **(2)** > **(3)**. Indeed, $WO(OPr^i)_3$(dmae) **(1)** reacts quickly with air and moisture, resulting in a cloudy solution due to the precipitation of an insoluble oxide. It is very difficult to keep a clear solution over time. However, $WO(O^iPr)_3$(bdmap) **(2)** and $WO(OPr^i)_3$(tdmap) **(3)** can be stored more easily. In contrast to **(2)**, which seems to behave like **(1)** in presence of moisture, **(3)** seems to evolve with time by becoming slightly viscuous and by the appearance of crystals along the glass of the schlenk tube in which **(3)** was stored. These crystals are the hydrolysis product, a poly-nuclear tungsten amino-alkoxide $[W_4O_4(\mu_2\text{-}O)_6(tdmap)_4]$. Based on this observations and the serendipidous isolation of $W_4O_4(\mu_2\text{-}O)_6(dmae)_4$ reported earlier,[13] this type of reaction was subsequently repeated in order to control the partial hydrolysis of $WO(OPr^i)_3$(bdmap) **(2)** and $WO(OPr^i)_3$(tdmap) **(3)**.

Hence, the starting material $WO(OPr^i)_3$(tdmap) **(3)** was prepared as mentioned above but without further purification by distillation. As water is poorly soluble in toluene, the hydrolysis in this case was performed with a toluene-isopropanol solution. So, the crude product **(3)** was hydrolysed in a 4:1 mixture of anhydrous toluene and isopropanol at 0°C in a controlled way by adding dropwise a water-isopropanol solution (2 mL) through a syringe over a period of 1 h under vigorous stirring. Indeed, the hydrolysis product $W_4O_4(\mu_2\text{-}O)_6(tdmap)_4$ **(4)** was isolated from a solution having an experimental hydrolysis ratio of 1 $\{h_{exp.} = [H_2O]/[WO(OPr^i)_3tdmap] \approx 1\}$ which allows the control of the hydrolysis. The choice of hydrolysis ratio h_{exp} was kept under the theoretical value $h_{t.} = 1.5$, according to the equation 2.6, in order to control successfully the micro-hydrolysis.

$$4\ WO(OPr^i)_3tdmap + 6\ H_2O \longrightarrow W_4O_4(\mu\text{-}O)_6(tdmap)_4 + 12\ {}^iPrOH \qquad \textbf{(2.6)}$$

(3) **(4)**

After allowing the reaction medium to warm up, it was stirred for 20 h at R.T, and then refluxed for 24 h. The solution was filtered and then concentrated to afford an oily residue which was re-dissolved in the smallest amount of warm hexane. After cooling to R.T and then to - 20°C for a few days, colourless crystals which formed were separated by decantating, washed three times with 3 mL of hexane (0°C) and dried *in vacuo*.

Unsuccessful attempts were made to synthesise in a reproducible way the hydrolysis products of $WO(OPr^i)_3$(dmae) **(1)** and $WO(OPr^i)_3$(bdmap) **(2)** using the same procedure with

a motor driven syringe. However, two different hydrolysed products of **(2)** were isolated adventitiously in very small amounts which didn't permit a full chemical characterisation. The hydrolysis-condensation reaction of tungsten amino-alkoxide **(2)** gives rise to $W_4O_4(\mu_2\text{-}O)_4(OPr^i)_4(bdmap)_4$ **(5)** and $W_6O_6(\mu_2\text{-}O)_9(tdmap)_6$ **(6)**. Compounds **(5)** and **(6)** have been obtained by controlling the exposure of **(2)** to atmospheric water which induced formation of individual crystals.

$W_4O_4(\mu_2\text{-}O)_4(OPr^i)_4(bdmap)_4$ **(5)** has been synthesised by adding a layer of an anhydrous mixture of 2-propanol and hexane in a ratio 1:1 to the single-neck round bottom flask containing the yellow monomeric liquid **(2)**. The water was introduced by opening the flask to the atmosphere from time to time, allowing the introduction and solubilisation of atmospheric moisture in the dipolar solvent and hence allows the formation of individual crystals after a few weeks. The micro-hydrolysis reaction of **(2)** to form **(5)** follows equation 2.7.

$$\underset{\textbf{(2)}}{4\ WO(OPr^i)_3bdmap} + 4\ H_2O \longrightarrow \underset{\textbf{(5)}}{W_4O_4(\mu_2\text{-}O)_4(OPr^i)_4(bdmap)_4} + 8\ {}^iPrOH \qquad (2.7)$$

$W_6O_6(\mu\text{-}O)_9(tdmap)_6$ **(6)** was recovered by the natural introduction of atmospheric moisture in a standard NMR tube sealed by a simple cap. After evaporation of all the $CDCl_3$ solvent, the formation of crystals growing in a spiral along the glass tube was observed. The hydrolysis-condensation reaction can be summarized in equation 2.8.

$$\underset{\textbf{(2)}}{6\ WO(OPr^i)_3bdmap} + 9\ H_2O \longrightarrow \underset{\textbf{(6)}}{W_6O_6(\mu_2\text{-}O)_9(tdmap)_6} + 18\ {}^iPrOH \qquad (2.8)$$

In the Equation **(2.6)**, **(2.7)** and **(2.8)**, we consider that one molecule of water reacts in a ratio 1:1 with the amino-alkoxide to produce a polynuclear compound. The elimination of 2 molecules of ^iPrOH is necessary for the formation of one oxo bridge in **(4), (5)** and **(6)**.

2.2.2.1 Crystal structures

Crystal structure determination was not possible for **(1)**, **(2)** and **(3)** as these compounds were oils. $WO(OPr^i)_3(tdmap)$ **(3)**, under the presence of moisture, gives rise to crystals of **(4)** which was suitable for single crystal X-ray diffraction. The structure determined from the crystals recovered from the controlled hydrolysis of **(3)** is displayed in Figure 2.6 with relevant bond lengths and angles depicted in Table 2.4.

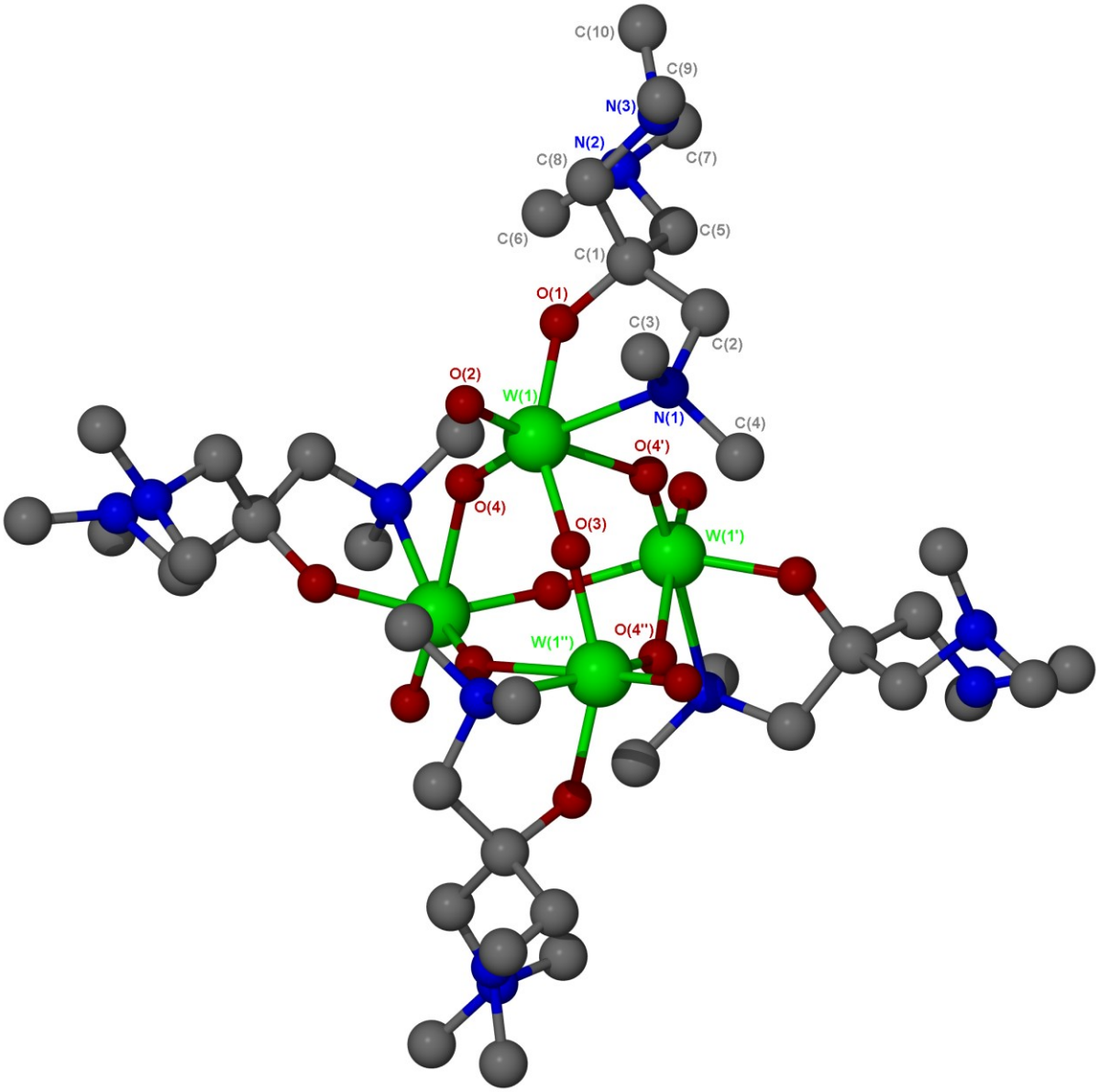

Figure 2.6 Molecular structure of $W_4O_4(\mu_2\text{-}O)_6(tdmap)_4$ **(4)**

Compound $W_4O_4(\mu_2\text{-}O)_6(tdmap)_4$ **(4)** crystallizes in the tetragonal space group $I4_1/a$ with unit cell parameters, a = b = 24.9270(2), c = 9.68400(10) Å, Z = 4. The asymmetric unit consists of one $WO(\mu\text{-}O)_3(tdmap)$ with the remainder of the tetramer generated by symmetry (Figure 2.6). The central W_4O_6 core possesses a distorted adamantane-like structure (Figure 2.7). **(4)** has a tetranuclear tungsten cage with tungsten atoms forming a tetrahedron with the six oxygen atoms bridging each of the four metal centres.

The tungsten atoms of $W_4O_4(\mu_2\text{-}O)_6(tdmap)_4$ **(4)** are six-coordinate (C.N = 6) with each tungsten atom having a terminal oxo- ligand in addition to the potentially tetradentate tdmap ligand, though this retains two pendant uncoordinated dialkylamido- groups $-NMe_2$. One of the three dialkylamido- groups Me_2N- belonging to the tdmap ligand forms a five-

membered chelate ring on each tungsten atom which thus adopts a distorted octahedral geometry.

Table 2.4 Selected Bond lengths (Å) and bond angles (°) of $W_4O_4(\mu\text{-}O)_6(tdmap)_4$ **(4)**

Bond lengths			
W(1)-O(1)	1.911(2)	W(1)-O(2)	1.719(2)
W(1)-O(3)	1.9090(9)	W(1)-O(4)	1.770(2)
W(1)-O(4')	2.2443(19)	W(1)-N(1)	2.345(2)
Bond angles			
O(2)-W(1)-O(4')	104.41(10)	O(2)-W(1)-O(3)	96.29(10)
O(4)-W(1)-O(3)	97.90(9)	O(2)-W(1)-O(1)	97.76(9)
O(4)-W(1)-O(1)	99.05(9)	O(3)-W(1)-O(1)	154.51(6)
O(2)-W(1)-O(4')	170.53(9)	O(4)-W(1)-O(4')	85.05(8)
O(3)-W(1)-O(4')	82.11(7)	O(1)-W(1)-O(4')	80.54(8)
O(2)-W(1)-N(1)	94.96(10)	O(4)-W(1)-N(1)	160.45(9)
O(3)-W(1)-N(1)	82.34(7)	O(1)-W(1)-N(1)	75.36(9)
O(4')-W(1)-N(1)	75.59(8)		

Symmetry equivalent atoms generated by symmetry transformation (‘; 1/4-y, 1/4+x, 5/4-z); (“ ; 1/2-y, -x, z)

The description of the structure will be focused around W(1) due to the equivalence of the bond length and angles of each metal centre. Hence, the *trans* bond angles [O(3)-W(1)-O(1)], [O(4)-W(1)-N(1)] and [O(2)-W(1)-O(4')] are respectively 154.51(6)°, 160.45(9)° and 170.53(9)°. Also, the variation in W-O bond length in **(4)** is between 1.719(2) Å for the shortest bond [W(1)-O(2)] which is the terminal oxo bond W=O and 2.2443(19) Å which is the longest bond [W(1)-O(4')]. The W=O terminal bond length of 1.719(2) Å is similar to those seen in the tungsten(VI) oxo-tetra-alkoxide.[7] The bond W(1)-O(4) [1.770(2) Å] is quite short compared to those typically recorded for oxo-bridges. This value is very close to the terminal oxo- bond length of W=O and shows a reduced double bond character (W=O:→W). However, W(1)-O(1) associated to the multi-dentate ligand (bdamp) and W(1)-O(3) present, respectively, distances of 1.911(2) and 1.9090(9) Å, which are typical lengths for W-O single bonds. The adamantane core is identical to the structure $W_4O_4(\mu_2\text{-}O)_6(dmae)_4$ obtained in a previous report with analogous bond lengths and angles.[13] The bond length W(1)-N(1) [2.345(2) Å] is considerably longer than a W-N bond length seen in $W(NMe)_6$ (2.032 Å),[28] but consistent with a tertiary amine dative bonds in tungsten(VI) chemistry.[29]

Moreover, the longest bonds W(1)-O(4') [2.2443(19) Å] and W(1)-N(1) [2.345(2) Å] are respectively *trans* to the shortest bond W(1)-O(2) [1.719(2) Å] and W(1)-O(4) [1.770(2) Å]. One

thing to notice is that the bond length W(1)-O(4') [2.2443(19) Å] is longer than the usual bond lengths observed in such oxo bridges.[27] Hence, there is a strong *trans* influence.

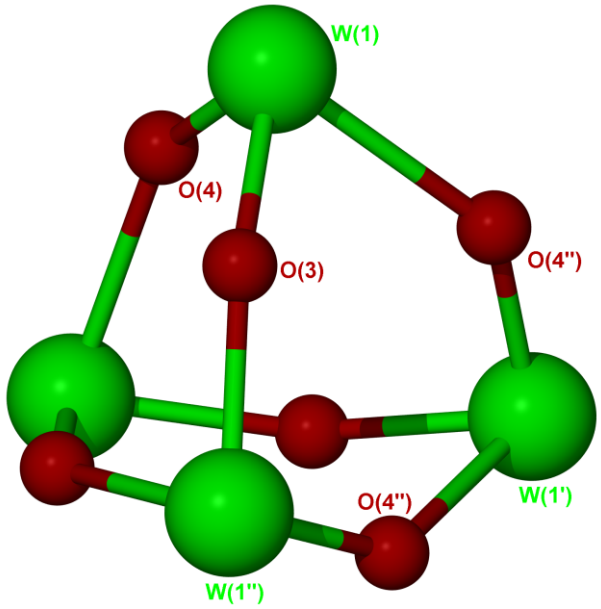

W(1)-O(4') = W(1')-O(4") = 2.2443(19) Å
W(1')-O(4') = W(1")-O(4") = 1.770(2) Å
W(1)-O(3) = W(1")-O(3) = 1.9090(9) Å

Figure 2.7 Molecular structure of the W_4O_6 adamantane-like core of $W_4O_4(\mu_2\text{-}O)_6(tdmap)_4$ **(4)**

A structure of hydrated $W_4O_4(\mu\text{-}O)_6(tdmap)_4.4H_2O$ **(4')** was also obtained and analyzed by X-ray crystallography and shows the presence of water in the unit cell, one molecule of water per tungsten atom. The complex crystallizes in the same symmetry and space group as **(4)** but with different unit-cell parameters, a = b = 24.9270(2), c = 9.7720(10) Å, Z = 4. Only the c-axis of the unit cell increases by about 0.09 Å due the incorporation of water. The presence of water in the cell structure of **(4)** does not modify notably the dimension of the adamantane core possessing comparable bond length and angles. This hydrated structure revealed surprisingly a robust and stable structure towards the moisture capable of incorporating water without its immediate decomposition. However, it seems that the solubility has changed and is therefore reduced in hydrocarbon solvent. The crystal structure (Figure 2.8) displays the three dimensional molecular unit of **(4')** showing the square cavities containing in total 4 molecules of water [O(5)]. The four edges of each cavity are composed of dialkylamido-group belonging to the complex **(4')**.

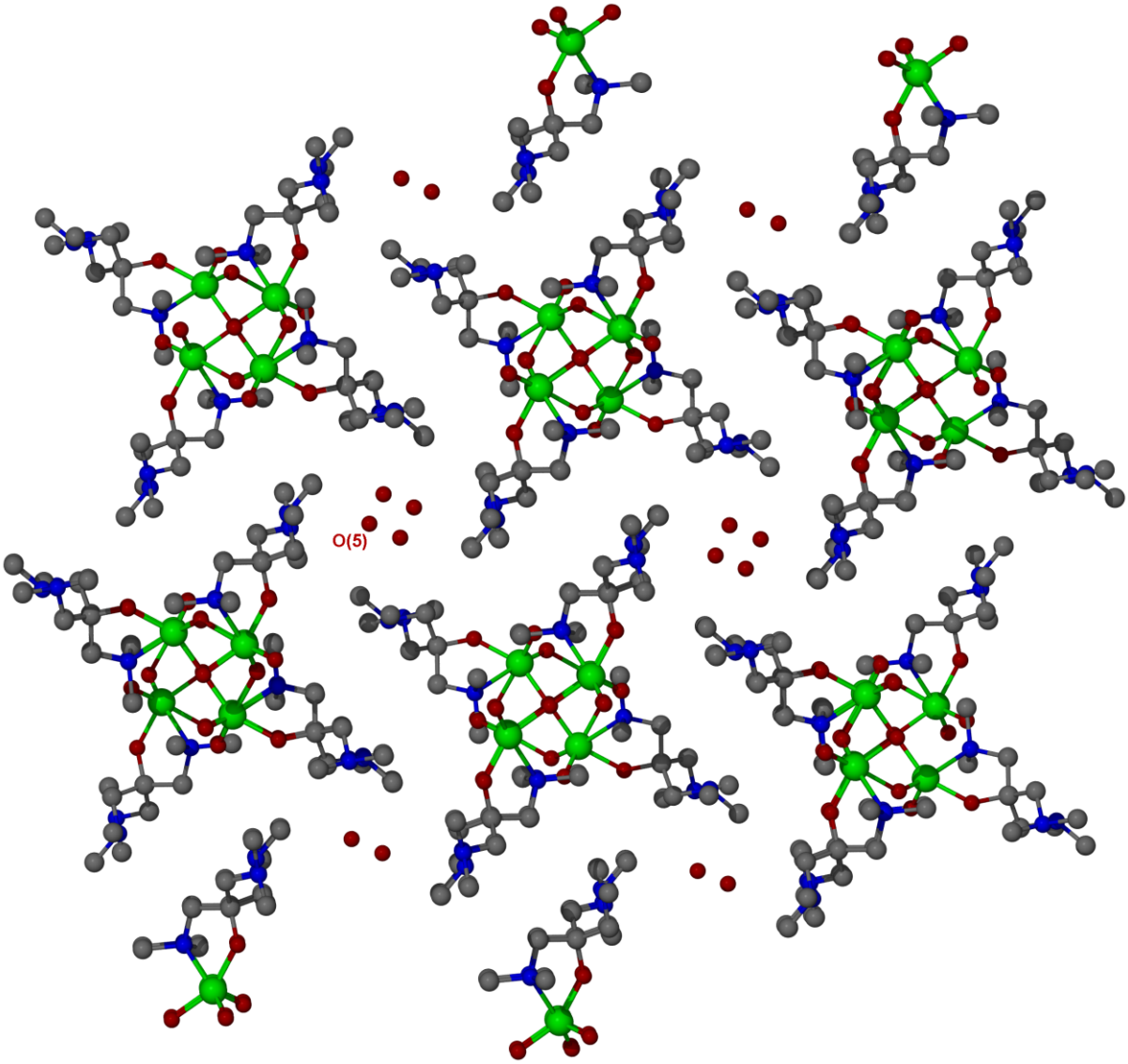

Figure 2.8 Three dimensional molecular unit of $W_4O_4(\mu_2\text{-}O)_6(tdmap)_4.4H_2O$ **(4')** showing the water O(5) in the cavities. Hydrogen atoms are omitted for clarity.

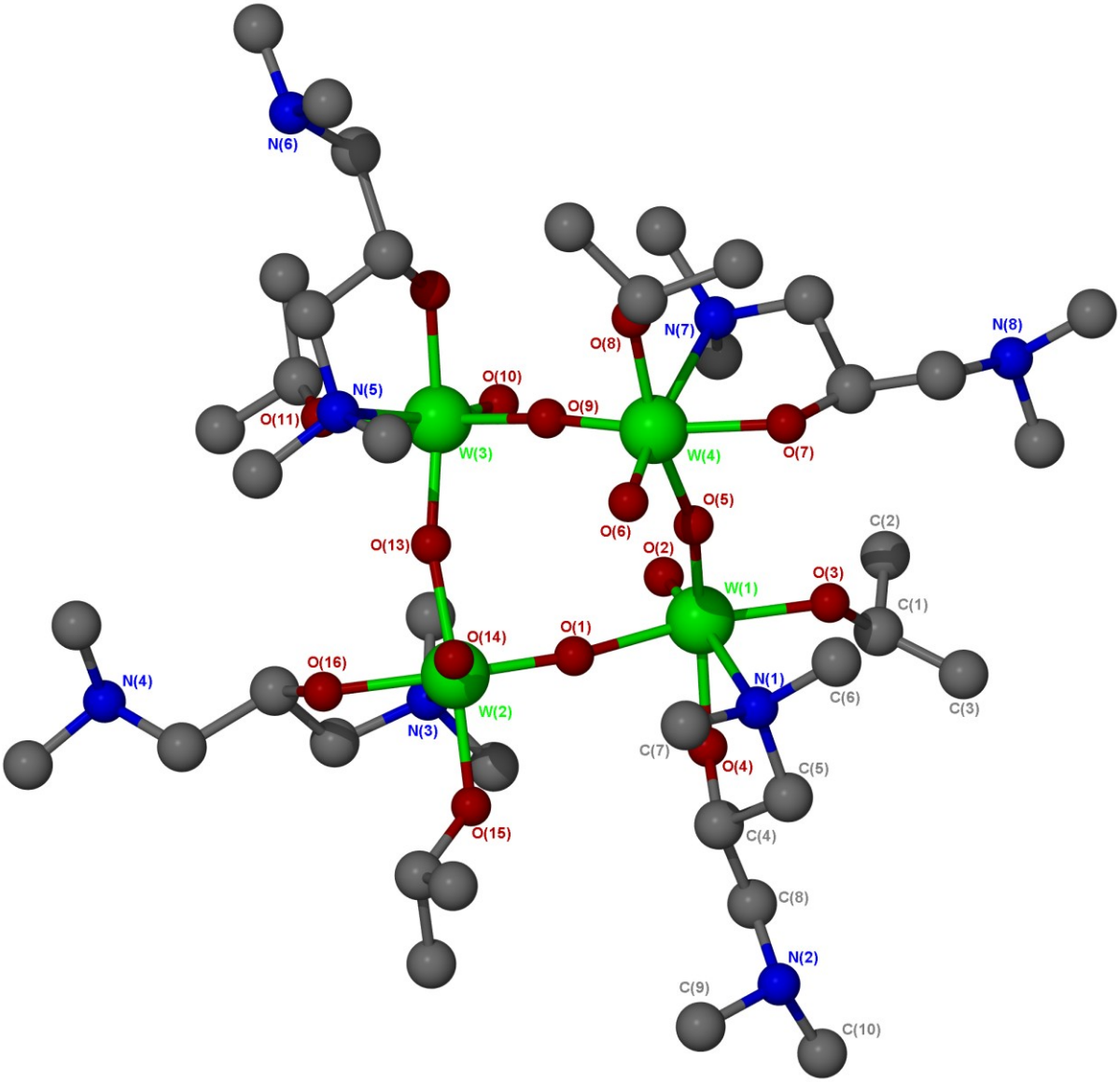

Figure 2.9 Molecular structure of $W_4O_4(\mu_2\text{-}O)_4(OPr^i)_4(bdmap)_4$ **(5)**

Table 2.5 Selected bond lengths (Å) and angles (º) of **(5)**

Bond lengths			
W(1)-O(1)	2.015(8)	W(1)-O(2)	1.721(7)
W(1)-O(3)	1.914(8)	W(1)-O(4)	1.937(7)
W(1)-O(5)	1.815(7)	W(1)-N(1)	2.460(9)
W(2)-O(1)	1.809(8)	W(2)-O(13)	1.990(9)
W(2)-O(14)	1.711(8)	W(2)-O(15)	1.921(8)
W(2)-O(16)	1.937(9)	W(2)-N(3)	2.485(10)
W(3)-O(9)	2.010(8)	W(3)-O(10)	1.698(8)
W(3)-O(11)	1.905(8)	W(3)-O(12)	1.929(8)
W(3)-O(13)	1.835(9)	W(3)-N(5)	2.428(10)
W(4)-O(5)	2.029(7)	W(4)-O(6)	1.707(7)
W(4)-O(7)	1.946(8)	W(4)-O(8)	1.907(7)
W(4)-O(9)	1.828(8)	W(4)-N(7)	2.466(9)
Bond angles			
O(2)-W(1)-O(5)	106.5(4)	O(2)-W(1)-O(3)	96.9(3)
O(5)-W(1)-O(3)	93.0(3)	O(2)-W(1)-O(4)	95.4(3)
O(5)-W(1)-O(4)	157.0(3)	O(3)-W(1)-O(4)	91.4(3)
O(2)-W(1)-O(1)	96.3(3)	O(5)-W(1)-O(1)	86.0(3)
O(3)-W(1)-O(1)	166.6(3)	O(4)-W(1)-O(1)	84.5(3)
O(2)-W(1)-N(1)	169.7(3)	O(5)-W(1)-N(1)	83.8(3)
O(3)-W(1)-N(1)	82.0(3)	O(4)-W(1)-N(1)	74.4(3)
O(1)-W(1)-N(1)	84.6(3)	O(14)-W(2)-O(1)	105.0(4)
O(14)-W(2)-O(15)	98.6(4)	O(1)-W(2)-O(15)	91.6(3)
O(14)-W(2)-O(16)	95.4(4)	O(1)-W(2)-O(16)	159.1(4)
O(15)-W(2)-O(16)	89.4(4)	O(14)-W(2)-O(13)	98.2(4)
O(1)-W(2)-O(13)	87.4(3)	O(15)-W(2)-O(13)	162.8(3)
O(16)-W(2)-O(13)	85.6(4)	O(14)-W(2)-N(3)	170.1(4)
O(1)-W(2)-N(3)	84.9(3)	O(15)-W(2)-N(3)	81.7(4)
O(16)-W(2)-N(3)	74.7(4)	O(13)-W(2)-N(3)	81.2(3)
O(10)-W(3)-O(13)	106.5(4)	O(10)-W(3)-O(11)	94.5(4)
O(13)-W(3)-O(11)	92.0(4)	O(10)-W(3)-O(12)	96.0(4)
O(13)-W(3)-O(12)	156.7(3)	O(11)-W(3)-O(12)	92.5(4)
O(10)-W(3)-O(9)	96.4(4)	O(13)-W(3)-O(9)	87.4(3)
O(11)-W(3)-O(9)	168.9(3)	O(12)-W(3)-O(9)	83.7(3)
O(10)-W(3)-N(5)	168.9(4)	O(13)-W(3)-N(5)	83.8(3)
O(11)-W(3)-N(5)	80.6(4)	O(12)-W(3)-N(5)	74.4(4)
O(9)-W(3)-N(5)	88.3(3)	O(6)-W(4)-O(9)	105.5(4)
O(6)-W(4)-O(8)	95.6(4)	O(9)-W(4)-O(8)	92.8(4)
O(6)-W(4)-O(7)	95.9(4)	O(9)-W(4)-O(7)	157.4(3)
O(8)-W(4)-O(7)	92.3(3)	O(6)-W(4)-O(5)	98.6(3)
O(9)-W(4)-O(5)	87.0(3)	O(8)-W(4)-O(5)	165.4(3)
O(7)-W(4)-O(5)	82.5(3)	O(6)-W(4)-N(7)	169.6(4)
O(9)-W(4)-N(7)	84.5(3)	O(8)-W(4)-N(7)	81.0(3)
O(7)-W(4)-N(7)	74.6(3)	O(5)-W(4)-N(7)	84.4(3)

The compound $W_4O_4(\mu_2\text{-}O)_4(OPr^i)_4(bdmap)_4$ **(5)** (Figure 2.9) contains two almost identical molecules in the asymmetric unit, only one of which will be described. The complex crystallizes in the monoclinic space group $P2_1/n$ with unit-cell parameters, a = 27.4610(3), b = 14.6920(2), c = 30.7850(3) Å, β = 106.243(4)°, Z = 4. The molecular structure displays a folded square M_4O_4 core (Figure 2.10).

Contrary to the structure of $W_4O_4(\mu_2\text{-}O)_6(tdmap)_4$ **(4)**, a monodentate isopropoxide group remains after hydrolysis of $WO(OPr^i)_3(bdmap)$ **(2)** on each tungsten atom. Similarly to **(4)**, the tridentate bdmap on each tungsten atom shows a coordinated dialkylamido- Me_2N- group which forms a five-membered chelated ring leaving the remaining dialkylamido- Me_2N- group uncoordinated.

The tungsten atoms are also six coordinate and adopt a distorted octahedral structure. The description of the structure will centre mainly around W(1) due to the similarities of the bond length and angles of each metal centre (Table 2.6). Indeed, the *trans* bond angles [O(5)-W(1)-O(4)], [O(2)-W(1)-N(1)] and [O(3)-W(1)-O(1)] are respectively 157.0(3)°, 169.7(3)° and 166.6(3)°. Another bond related to the bridging oxo ligand W(1)-O(5) of length 1.815(7) Å seems to have a reduced double bond character. Nevertheless, the oxo bridge W(1)-O(1) [2.015(8) Å], slightly shorter than the oxo bridge [2.2443(19) Å] observed in **(4)**, appear to be a single bond like the amino-alkoxide ligand with a bond length W(1)-O(4) of 1.937(7) Å. The isopropoxide -OPr^i ligand shows a W(1)-O(3) distance of 1.914(8) Å and a bond angle C(1)-O(3)-W(1) associated to the alkoxide of 124.6(8)° is consistent with a single bond character.[7]

The bond W(1)-O(3) and W(1)-O(5) are respectively in positions *trans* to the long bond W(1)-O(1) and W(1)-O(4). The *trans* influence, compared to **(4)**, is particularly strong for W(1)-O(2) *trans* to W(1)-N(1). Indeed, the terminal oxo ligand with a short W(1)=O(2) bond of 1.721(7) Å is in *trans* position to the long W(1)-N(1) bond [2.460(9) Å]. The terminal oxo ligands of W(1)-O(2) and W(3)-O(10) are in *cis* position to each other whereas they are in position *trans* to the other terminal oxo ligands W(2)-O(14) and W(4)-O(6).

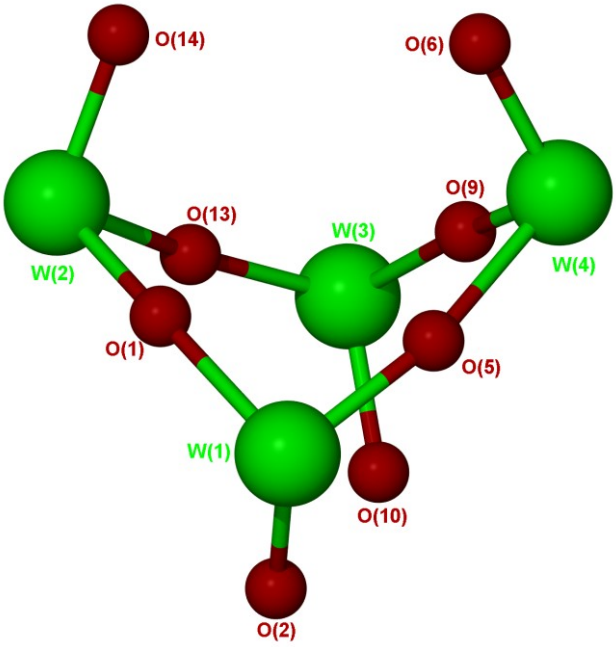

Figure 2.10 Other view of the molecular structure of $W_4O_4(\mu_2\text{-}O)_4(OPr^i)_4(bdmap)_4$ **(5)** Only the bridging oxo and terminal oxo ligand are represented.

The compound $W_6(O)_6(\mu_2\text{-}O)_6(bdmap)$ **(6)** (Figure 2.11) contains two almost identical molecules in the asymmetric unit, only one of which will be described. The complex crystallizes in the triclinic space group P $\bar{1}$ with unit-cell parameters, a = 17.8400(3), b = 18.8680(4), c = 22.7710(5) Å, α = 81.0700(10)°, β = 72.2060(10)°, γ = 87.8660(10)°, Z = 4. The molecular structure shows a distorted trigonal prism W_6O_9 (Figure 2.12). Similarly to $W_4O_4(\mu\text{-}O)_6(tdmap)_4$ **(4)**, each tungsten (C.N = 6) is coordinating to oxo bridges and the chelating bdmap ligand through the N-donor dative bonds.

The terminal oxo ligand W=O and the dialkylamido Me_2N- group, belonging to the amino-alkoxide bdamp ligand, are all pointing to the outside of the trigonal prism, as depicted in Figure 2.11. The description of the structure will center around W(1) due to the similarities of the bond length and angles of each metal centre. Each octahedral tungsten is distorted with *trans* bond angles of 152.7(3)°, 163.7(3)° and 168.0(3)°. Also, the variation in bond length of **(6)** is between 1.725(7) Å for the shortest bond W(1)=O(3) which is the terminal oxo ligand and 2.398(9) Å for W(1)-N(1) which is the longest. Also, W(1)-O(9) with a bond length of 1.786(7) Å appears to have a double bond character. Meanwhile, W(1)-O(1) [2.179(6) Å] and W(1)-O(2) [1.892(6) Å] are typical single bond distances. The N:→W bond is *trans* to the oxo bridge W(1)-O(9) with a W(1)-N(1) bond length of 2.398(9) Å. Hence, the longest bond W(1)-N(1) and W(1)-O(1) are respectively in positions *trans* to the shortest W(1)-O(9) and

W(1)-O(3). The phenomenon of *trans* influence is also observed like in the previous structures **(4)** and **(5)**. The values of W(1)-O(1) [2.179(6) Å] and W(1)-O(9) [1.786(7) Å] are very similar to the oxo bridges observed for **(4)**, but different compared to **(5)**.

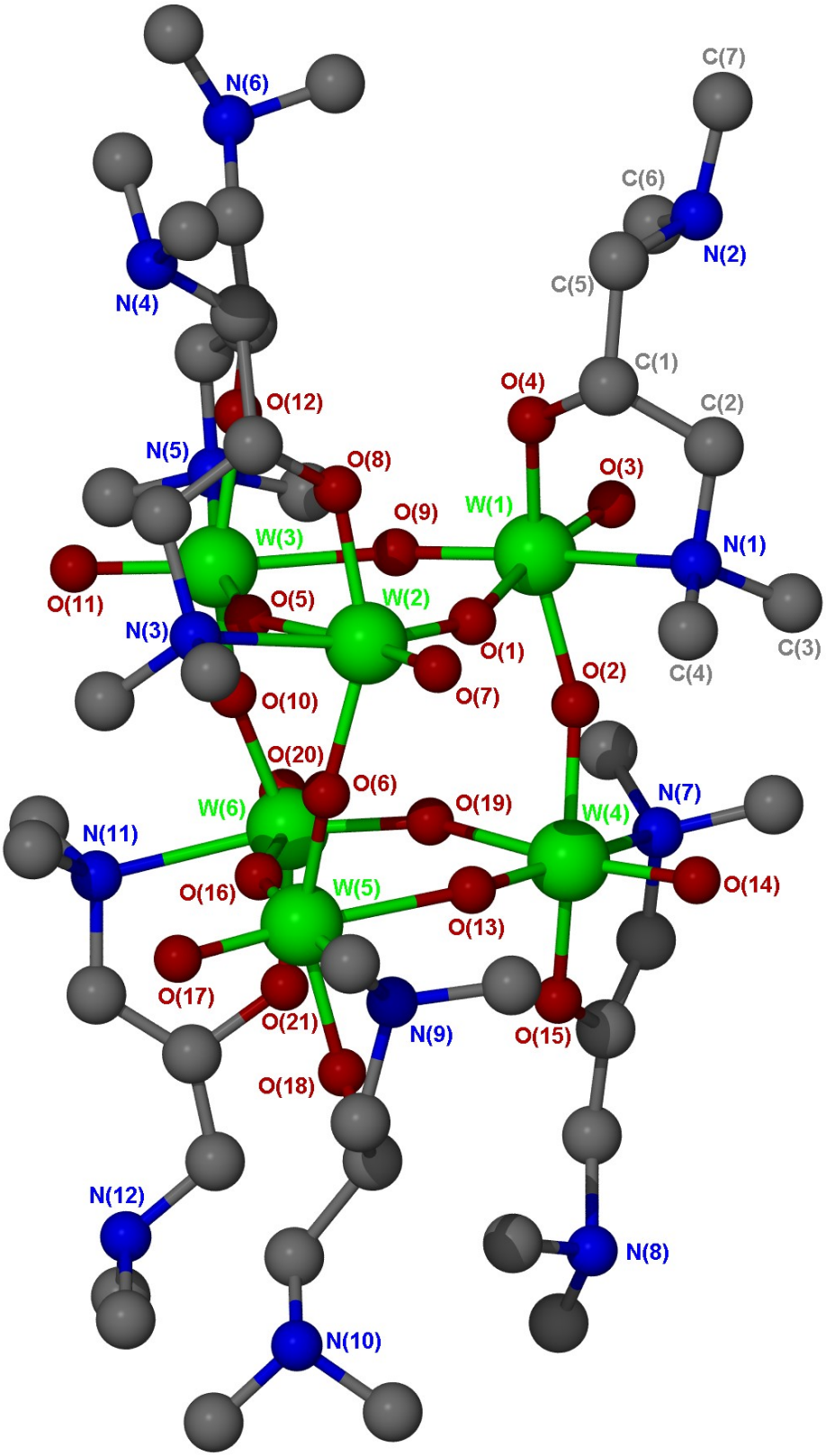

Figure 2.11 Molecular structure of $W_6O_6(\mu_2\text{-}O)_9(bdmap)_6$ **(6)**

Table 2.6 Selected bond lengths (Å) and angles (º) of $W_6O_6(\mu_2\text{-}O)_9(bdmap)_6$ **(6)**

Bond lengths			
W(1)-O(1)	2.179(6)	W(1)-O(2)	1.892(6)
W(1)-O(3)	1.725(7)	W(1)-O(4)	1.904(7)
W(1)-O(9)	1.786(7)	W(1)-N(1)	2.398(9)
W(2)-O(1)	1.753(6)	W(2)-O(5)	2.196(7)
W(2)-O(6)	1.917(7)	W(2)-O(7)	1.724(7)
W(2)-O(8)	1.908(7)	W(2)-N(3)	2.339(10)
W(3)-O(5)	1.760(6)	W(3)-O(9)	2.208(7)
W(3)-O(10)	1.902(7)	W(3)-O(11)	1.717(7)
W(3)-O(12)	1.920(8)	W(3)-N(5)	2.367(9)
W(4)-O(2)	1.884(7)	W(4)-O(13)	1.762(7)
W(4)-O(14)	1.732(7)	W(4)-O(15)	1.907(8)
W(4)-O(19)	2.175(7)	W(4)-N(7)	2.431(10)
Bond angles			
O(3)-W(1)-O(9)	103.9(3)	O(3)-W(1)-O(2)	95.6(3)
O(9)-W(1)-O(2)	102.1(3)	O(3)-W(1)-O(4)	96.9(3)
O(9)-W(1)-O(4)	98.3(3)	O(2)-W(1)-O(4)	152.7(3)
O(3)-W(1)-O(1)	168.0(3)	O(2)-W(1)-O(1)	81.3(3)
O(4)-W(1)-O(1)	81.6(3)	O(3)-W(1)-N(1)	92.0(3)
O(9)-W(1)-N(1)	163.7(3)	O(2)-W(1)-N(1)	79.9(3)
O(4)-W(1)-N(1)	75.5(3)	O(1)-W(1)-N(1)	76.1(3)
O(7)-W(2)-O(1)	103.3(3)	O(7)-W(2)-O(8)	97.4(4)
O(1)-W(2)-O(8)	95.3(3)	O(7)-W(2)-O(6)	96.0(4)
O(1)-W(2)-O(6)	102.0(3)	O(8)-W(2)-O(6)	155.0(3)
O(7)-W(2)-O(5)	169.4(3)	O(1)-W(2)-O(5)	87.2(3)
O(8)-W(2)-O(5)	82.6(3)	O(6)-W(2)-O(5)	80.5(3)
O(7)-W(2)-N(3)	92.3(3)	O(1)-W(2)-N(3)	162.4(3)
O(8)-W(2)-N(3)	74.5(4)	O(6)-W(2)-N(3)	83.9(3)
O(5)-W(2)-N(3)	77.4(3)	O(11)-W(3)-O(5)	101.4(3)
O(11)-W(3)-O(10)	95.6(4)	O(5)-W(3)-O(10)	102.5(3)
O(11)-W(3)-O(12)	98.5(4)	O(5)-W(3)-O(12)	96.0(3)
O(10)-W(3)-O(12)	154.0(3)	O(11)-W(3)-O(9)	169.7(3)
O(5)-W(3)-O(9)	88.9(3)	O(10)-W(3)-O(9)	81.8(3)
O(12)-W(3)-O(9)	80.5(3)	O(11)-W(3)-N(5)	90.2(4)
O(5)-W(3)-N(5)	166.4(4)	O(10)-W(3)-N(5)	83.2(3)
O(12)-W(3)-N(5)	75.1(4)	O(9)-W(3)-N(5)	79.6(3)
O(14)-W(4)-O(13)	104.5(4)	O(14)-W(4)-O(2)	95.6(3)
O(13)-W(4)-O(2)	103.1(3)	O(14)-W(4)-O(15)	98.2(4)
O(13)-W(4)-O(15)	96.6(4)	O(2)-W(4)-O(15)	152.2(3)
O(14)-W(4)-O(19)	167.3(3)	O(13)-W(4)-O(19)	88.1(3)
O(2)-W(4)-O(19)	79.5(3)	O(15)-W(4)-O(19)	81.8(3)
O(14)-W(4)-N(7)	90.4(4)	O(13)-W(4)-N(7)	163.8(4)
O(2)-W(4)-N(7)	81.1(3)	O(15)-W(4)-N(7)	74.8(4)
O(19)-W(4)-N(7)	77.2(3)		

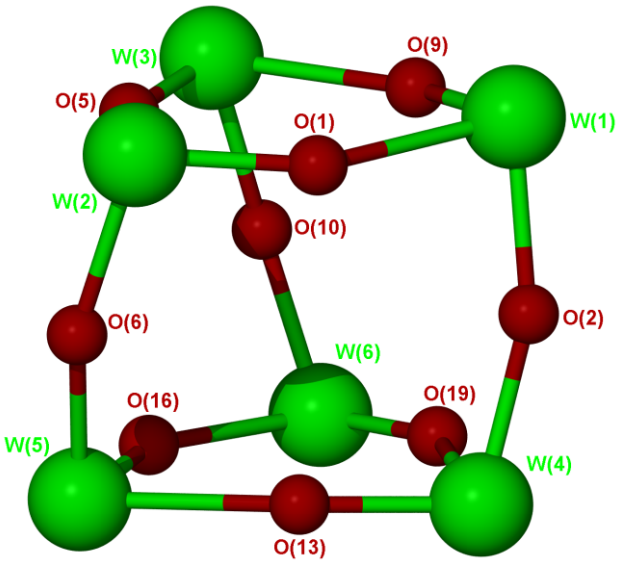

Figure 2.12 Molecular structure of $W_6O_6(\mu_2\text{-}O)_6(bdmap)_6$ **(6)**

In all the structures **(4)-(6)** described above, each one of them are composed of a number of tungsten atoms which are coordinated to different ligands, in particular amino-alkoxide (bdmap or tdamp) which forms a five-membered chelate ring, μ_2-oxo ligands bridging two metal centres, terminal isopropoxides and oxo ligands. Also, **(4)-(6)** display for each metal centre a WO_5N coordination sphere.

Compounds (**4**)-(**6**) present the phenomenon of *trans* influence. Moreover, **(4)** and **(6)** look very similar in term of bond lengths and angles, except for the W-O(μ-oxo) bridges bonds of **(5)**. Probably, the linkage N→W=O→W=O which is observed in **(4)** and **(6)** is responsible of these difference of bond length differences between **(4)**, **(6)** and **(5)** (Table 2.4, 2.5 and 2.6). The N:→W bond in structures **(4)** and **(6)** are *trans* to the oxo bridges ligands meanwhile **(5)** possesses a position *trans* to the terminal oxo ligand.

The ^{1}H NMR analysis on the monomeric compounds $WO(OPr^i)_3(L)$ (L = dmae, bdmap and tdmap) has suggested a *mer* configuration which shows that the N:→W dative bond is *trans* to the terminal oxo ligand W=O. According to the crystal structures (**4**)-(**6**), only **(5)** confirms this type of configuration (Figure 2.6, 2.9 and 2.11).

The formation of the tetramer $W_4O_4(\mu_2\text{-}O)_4(OPr^i)_4(bdmap)_4$ **(5)** could be explained by starting with the hydrolysis of the monomeric compound $WO(OPr^i)_3(L)$ (L = bdmap and tdmap) which gives rise to a dimeric compound $W_2O_2(\mu_2\text{-}O)(O^iPr)_4(L)_2$ via hydrolysis-condensation reactions. In all the following equations [(2.9), (2.10) and (2.11)], we assume

that terminal isopropoxide ligands, and hydroxides resulting from the hydrolysis of -OPr^i, are involved in the creation of the oxo bridges. This is a schematic and simplistic representation of this hydrolysis-condensation mechanism which is, in all probability, complex.

$$WO(OPr^i)_3(L) + H_2O \rightarrow WO(OH)(OPr^i)_2(L) + HO^iPr \quad (2.9)$$

$$WO(OH)(OPr^i)_2(L) + WO(O^iPr)_3(L) \rightarrow W_2O_2(\mu_2\text{-}O)(OPr^i)_4(L)_2 + HO^iPr \quad (2.10)$$

(7)

$$2\ W_2O_2(\mu_2\text{-}O)(OPr^i)_4(L)_2 + 2\ H_2O \rightarrow W_4(O)_4(\mu_2\text{-}O)_4(OPr^i)_4(bdmap)_4 + HO^iPr \quad (2.11)$$

(5)

Hence, each isopropoxide ligand leads, in the presence of moisture, to oxo bridges by elimination of isopropanol. The folded pseudo-square distorted core **(5)**, as illustrated in Figure 2.10, can join its opposite edges by hydrolysis of terminal OPr^i groups leading to the adamantane-like structure **(4)** (Figure 2.13). The structure **(6)**, which represents a further hydrolysis-condensation step [Eq.(2.8)] can be seen as the poly-condensation of a folded structure **(5)** with a linear dimer **(7)** (Figure 2.14). The schematic representations described below (cf. Figure 2.13 and 2.14) don't show all the chemical functions in order to simplify the models of nucleation of (**4)** and **(6)** from **(5)**; only the isopropoxide ligands are represented for clarity.

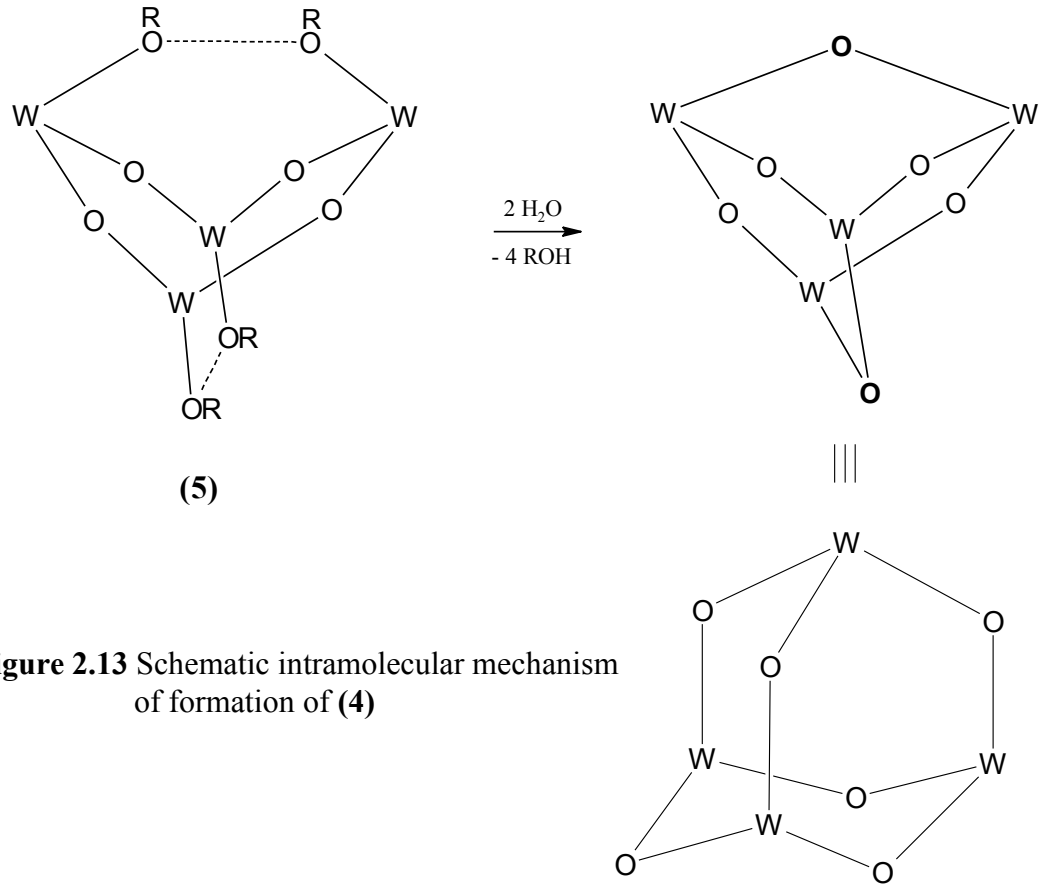

(5) **(4)**

Figure 2.13 Schematic intramolecular mechanism of formation of **(4)**

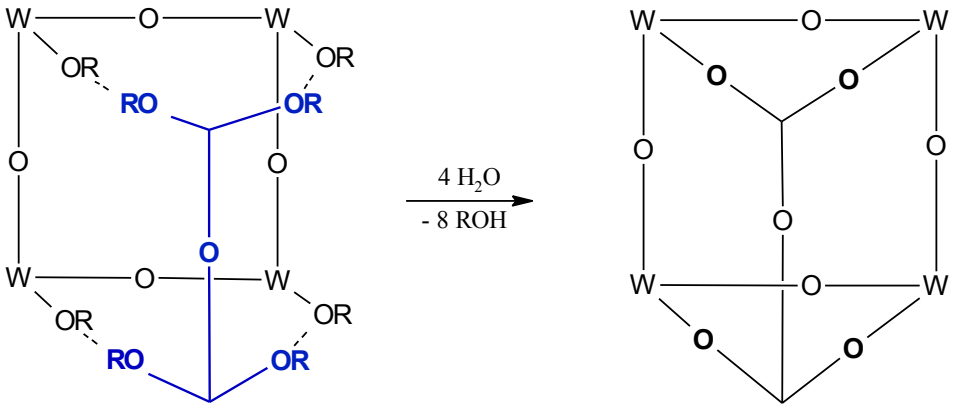

(5) + (7) **(6)**

Figure 2.14 Schematic intermolecular mechanism of formation of **(6)**

2.2.2.2 NMR spectroscopy

The hydrolysis of $WO(OPr^i)_3$(tdmap) **(3)** gives rise to $W_4O_4(\mu\text{-}O)_6$(tdmap)$_4$ **(4)** which displays a spectrum with two inequivalent methyl groups bonded to the terminal tertiary uncoordinated amino group -N(C***H₃***)$_2$ at 2.37 and 2.48 ppm (ratio 1:1). The remaining amino group chelating to the tungsten appears at δ = 2.88 and 2.96 ppm, suggesting that the methyl protons -N(C***H₃***)$_2$ are inequivalent (ratio 1:1). Each hydrogen of the three -C***H₂***- groups of one tdmap ligand which are diastereotopic displays six doublets at 2.71, 2.78, 2.94, 2.98, 3.02 and 3.22 ppm with equivalent coupling constants $^2J_{H,H}$ = 13.3 Hz for each signal.

The ^{13}C NMR analysis displays the signals at 48.3 and 48.4 ppm matching with the two uncoordinated methyl dialkylamido ligand -N(***C***H$_3$)$_2$ of the amino-alkoxide tdmap. The methyl groups bonded to each nitrogen atom are equivalent but inequivalent between each nitrogen atom. The coordinated methyl dialkylamido ligand -N(***C***H$_3$)$_2$ shows two inequivalent signals at 53.2 and 55.0 ppm corresponding to each carbon bonded to the chelated nitrogen atom. The -***C***H$_2$N(Me)$_2$ substituants are inequivalent. The quaternary carbon of the ligand has a signal at 89.7 ppm. This compound does not display any -O^{i}Pr group, as confirmed by the ^{1}H and ^{13}C NMR analysis and the molecular structure (Figure 2.6).

The chemical shift of ^{183}W NMR for $W_4O_4(\mu\text{-}O)_6$(tdmap)$_4$ **(4)** which is - 42.6 ppm at 373K is displayed in comparison with the oxo-tetra-alkoxide and the monomeric compounds **(1)-(3)**, respectively in Table 2.2 and 2.3.

Due to the small amount obtained for **(5)-(6)** and their insolubility, their ^{183}W NMR analyses have not been performed.

2.2.3 Thermal decomposition studies and applications

Prior to the CVD study and thermal decomposition of the precursors, the Thermal Gravimetric Analysis (TGA) for each compound under inert atmosphere (N_2) at atmospheric pressure were performed in order to study the thermal behaviour and then to predict the product resulting from pyrolysis.

2.2.3.1 TGA measurements

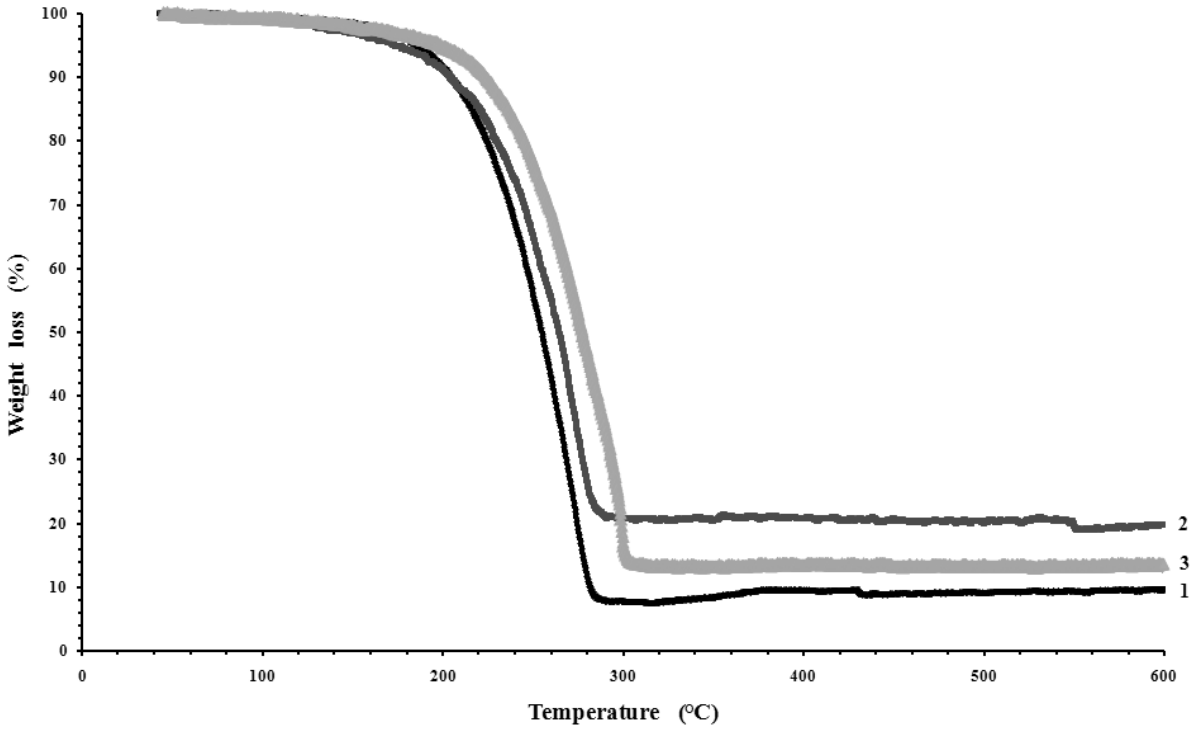

Figure 2.15 TG curves for thermal decomposition in dry nitrogen atmosphere of **(1)**, **(2)** and **(3)** at atmospheric pressure with an heating rate of 20 °C/min

The TG curves for each compound displays an abrupt weight loss in one decomposition step from 200°C to 300 °C with no compositional change on further heating (Figure 2.15). The TG curve onset values for volatilisation of the monomeric liquids **(1)**, **(2)** and **(3)** are respectively 220°C, 230°C, 260°C. The residues of **(1)**, **(2)** and **(3)** after measurement give 8, 12 and 20% respectively, which are lower than the theoretical value for the formation of WO_3 *e.g* **(1)** 49.8%, **(2)** 44.4% and **(3)** 40.0%. The TG studies of the thermal behaviour of **(1)**, **(2)** and

(3) in dry nitrogen gas at atmospheric pressure indicate almost complete volatility for all three compounds. This reveals that the remaining products appeared on heating due to a probable *in situ* ligand decomposition of the monomeric liquids. Also, the inadvertent introduction of air and moisture could increase the partial decomposition phenomenon, leading to a significant residue. Overall, it is clear that the complexes **(1)**, **(2)** and **(3)** are quite volatile.

The TG curves for compound **(4)** display several stages of decomposition. The first decomposition occurring at 240°C with a weight loss of 21% is quite abrupt while the second one with a weight loss of 20% is smooth from 300°C to 500°C with no change on further heating. The total weight loss is about 40%, hence, the remaining weight of the thermal decomposition of **(4)** under nitrogen atmosphere is 59%, which is in prediction with the weight obtained for WO_3 (theoretical value = 54.4%) .

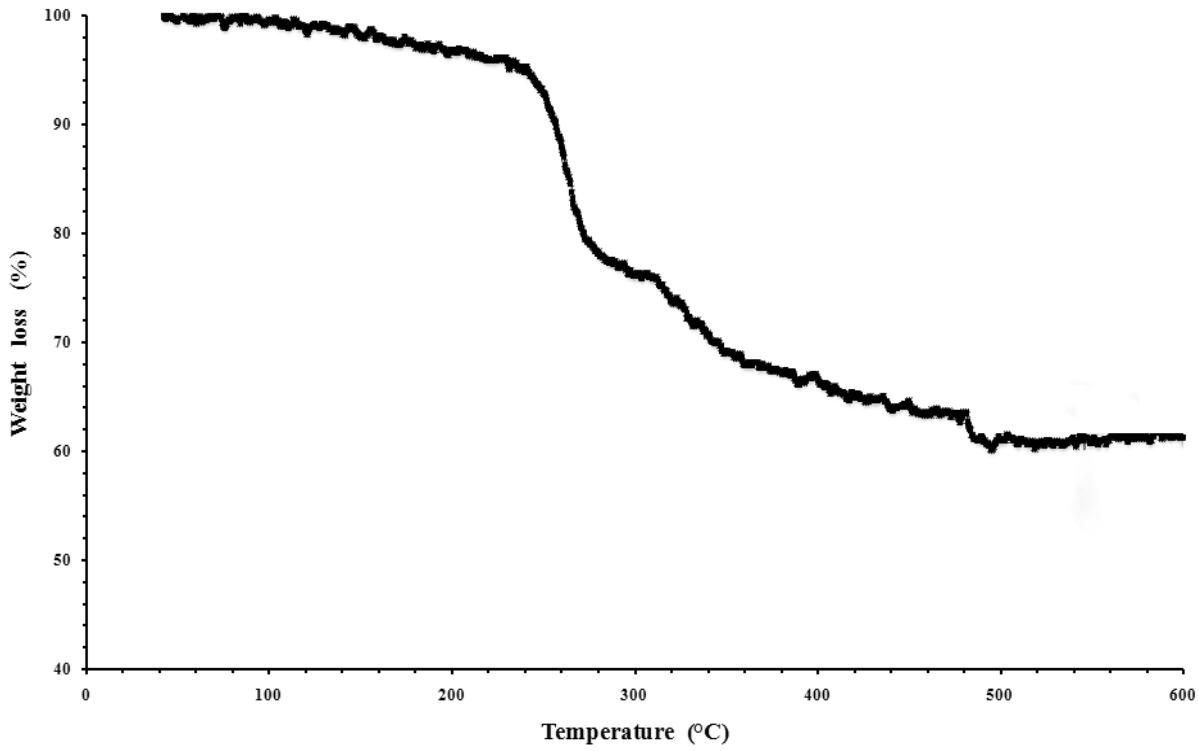

Figure 2.16 TG curve for thermal decomposition of **(4)** in dry nitrogen gas at atmospheric pressure with a heating rate 20 °C/min

2.2.3.2 Thermal decomposition applications

After having studied the thermal behaviour of different compounds in inert atmosphere by the TGA measurements, the single-source precursors have been decomposed under specific conditions. On one hand, the compounds **(1)**, **(2)** and **(3)** have been decomposed in a closed Swagelok reactor under inert atmosphere at 700°C, as the experiments of type A (Table 2.7). These reactions were carried out using the reaction under autogenic pressure at elevated temperature (RAPET) method by dissociating the precursor. On the other hand, **(4)** has been pyrolysed in a graphite melting pot open to the air at 500°C, as experiment of type B (Table 2.7). The decompositions under RAPET conditions are known to produce in one step process and without catalyst, tungsten oxide nanomaterials, which should exhibit photocatalytic properties.

Table 2.7 Precursors, conditions and yields of different experiments (N*=Non-measured)

Experiments	A1	A2	A3	A4	B1
Type of precursors	**(1)**		**(2)**	**(3)**	**(4)**
T(°C)	700 °C	700 °C	700 °C	700°C	500 °C
Time Δt (h)	1h	4h	1h	2h	1h
Yield (%)	55%		57%	59%	N*

The experiments A1, A2, A3, A4, B1 illustrated in the above table follow the temperature profile described below with a heating and cooling rate respectively at $\Delta T_1/\Delta t$ = +10°C/min., $\Delta T_2/\Delta t$ = -1°C/min., plateau temperature T and time lapse Δt (Figure 2.17).

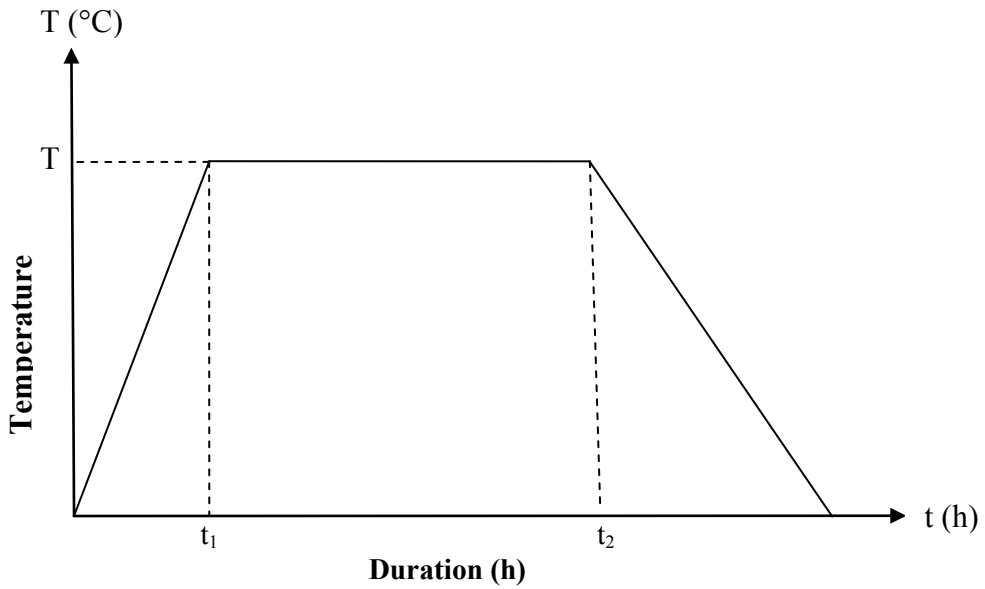

Figure 2.17 Temperature profile of the experiments A1-A4, B1

Because the decomposition of **(1)**, **(2)** and **(3)** was carried out in a closed Swagelok cell, it is expected to have residues such as carbon, nitrogen, hydrogen in addition to the probable WO_x. The content of carbon, hydrogen and nitrogen in the product material A1-A4 and B1 was examined by an elemental analysis measurement (Table 2.8). For comparison, the elemental analysis of the different precursors **(1)-(4)** is reported. Also, the weights of the resultant products were measured after thermolysis in order to give the yield of the thermodecomposition process.

2.2.3.3 Characterisation

All these prepared samples have been characterised by the following analysis: PXRD, SEM/EDX and TEM/EDX in order to determine their structure and morphology.

2.2.3.3.1 Structural determination

Powder X-ray diffraction studies were performed to determine if the samples were crystalline or amorphous. This technique also gives information about the nature and the phases present in the material. The X-ray diffraction patterns were acquired over the 2θ range from 0° to 90° with a Bruker Powder X-ray diffractometer using Cu Kα radiation (λ = 1.5418Å). The powder XRD patterns of the thermally decomposed $WO(OPr^i)_3L$ with L = dmae, bdmap, tdmap in a closed Swagelok cell under inert atmosphere (A1-A4) and in the air (B1) are presented in the Figures 2.18 to 2.22. The intensity of all the spectra below is in arbitrary units. The thermal decomposition of **(1)**, **(2)**, **(3)** and **(4)** either in a graphite vessel open to the air or in a Swagelok closed cell under inert atmosphere show peaks due to the crystallinity of its components.

The XRD pattern of the as-prepared A1 sample is presented below in Figure 2.18. Peak match software suggested a mixture of WO_3 and WO_2. The major diffraction peaks observed at 2θ = 25.789, 36.871, 53.041° are assigned as (011), (020), (-220) reflection lines of the primitive monoclinic phase of WO_2 which seems to be the principle phase in this material. These values are in good agreement with the diffraction peaks intensities of crystalline WO_2 (PDF 32-1393). Peaks at 2θ = 23.489, 29.692, 37.108, 48.098, 53.295° suggest also the presence of the primitive orthorhombic phase of WO_2 (PDF 82-0728). Other relevant peaks of the XRD pattern could match as well with the primitive hexagonal phase of WO_3 (PDF 85-2460). The diffraction peaks are observed at 2θ = 13.661, 23.297, 27.740, 33.944, 55.342, 56.666° and are assigned as (100), (002), (200), (112), (222), (204) refection lines of the hexagonal

phase of WO_3. The relative intensities of the two first peaks 13.661° and 23.297° are different from the standard ICDD-PDF table, revealing a preferred orientation growth along (002) plane in the material.

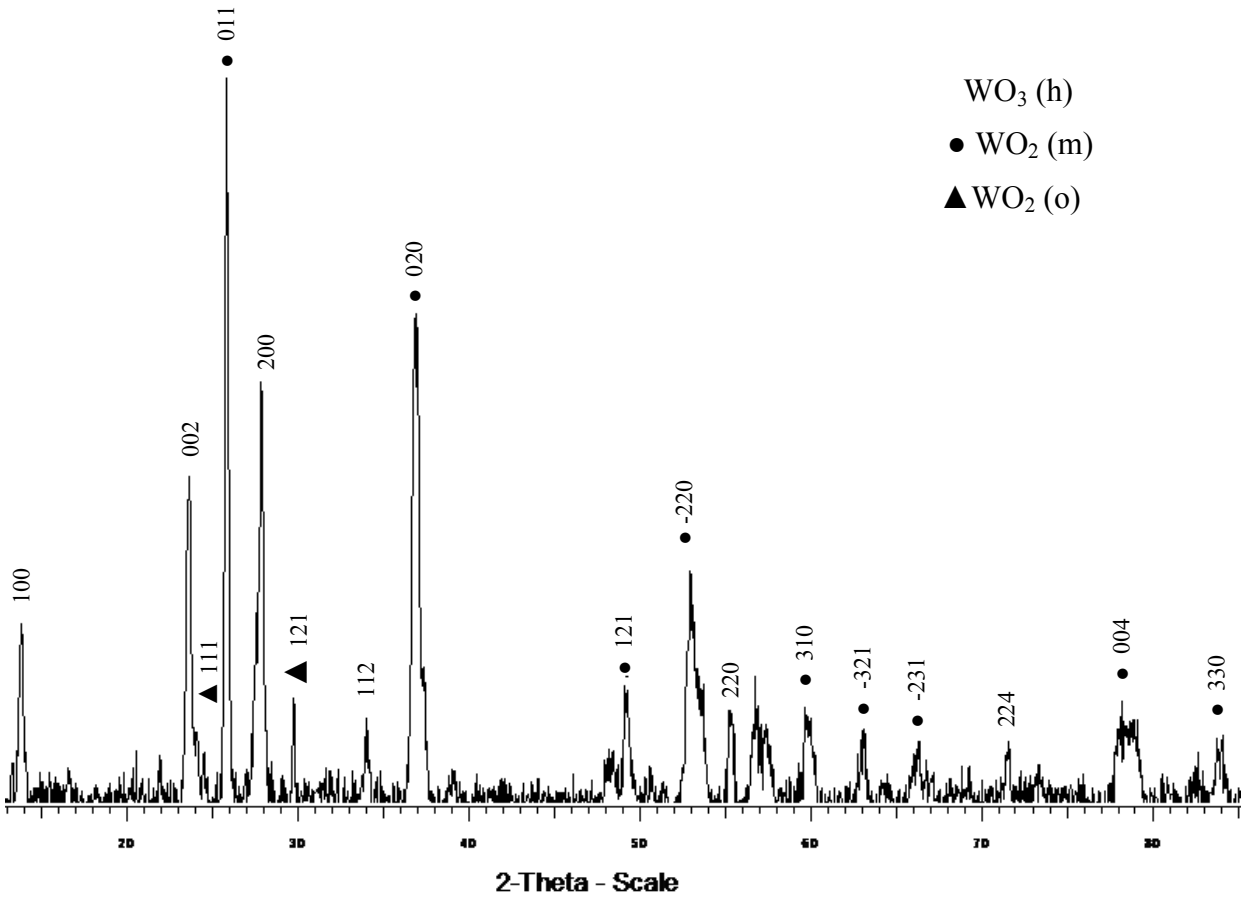

Figure 2.18 PXRD pattern of the thermal decomposition product of $WO(OPr^i)_3(dmae)$ **(1)** under RAPET conditions (A1)

The below spectrum (Figure 2.19) is for the A2 sample, which has been prepared under the same conditions as the A1 sample but on a larger scale and for a longer period of decomposition (cf. Table 2.7). The diffraction pattern of A2 sample shows similar peaks to the pattern of A1 sample. However, it is interesting to notice that the biggest peak in the XRD pattern of A1 at $2\theta = 25.789$, matching with the monoclinic phase of WO_2, does not appear any more in the XRD pattern of A2 sample. It is replaced by the primitive orthorhombic phase of WO_2 (PDF 82-0728). The RAPET decomposition under inert atmosphere of $WO(OPr^i)_3(dmae)$ **(1)** for a long period gives rise to the preferential formation of orthorhombic WO_2. Thus, the principle phase present in the A2 sample is now the primitive hexagonal phase of WO_3 (PDF 85-2460) and the primitive orthorhombic phase of WO_2.

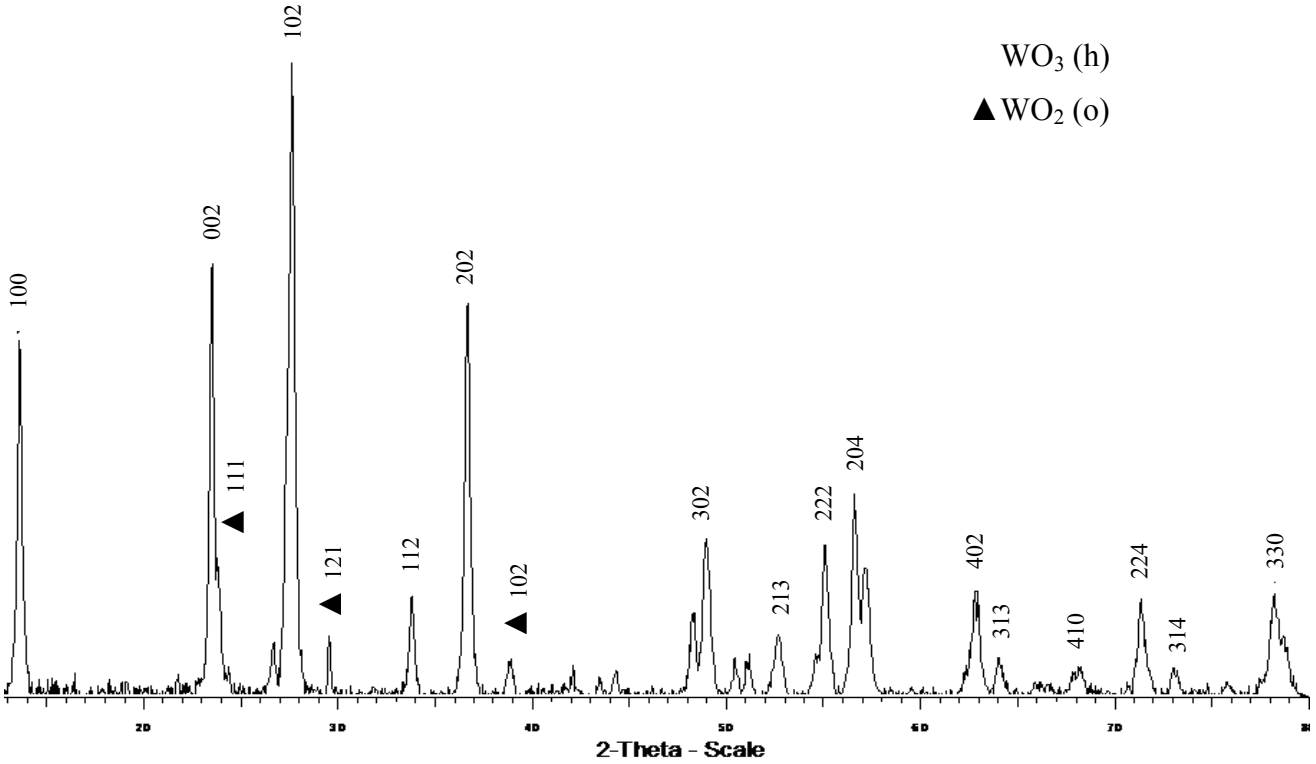

Figure 2.19 The PXRD pattern of the thermal decomposition product of $WO(OPr^i)_3$dmae **(1)** under RAPET conditions (A2)

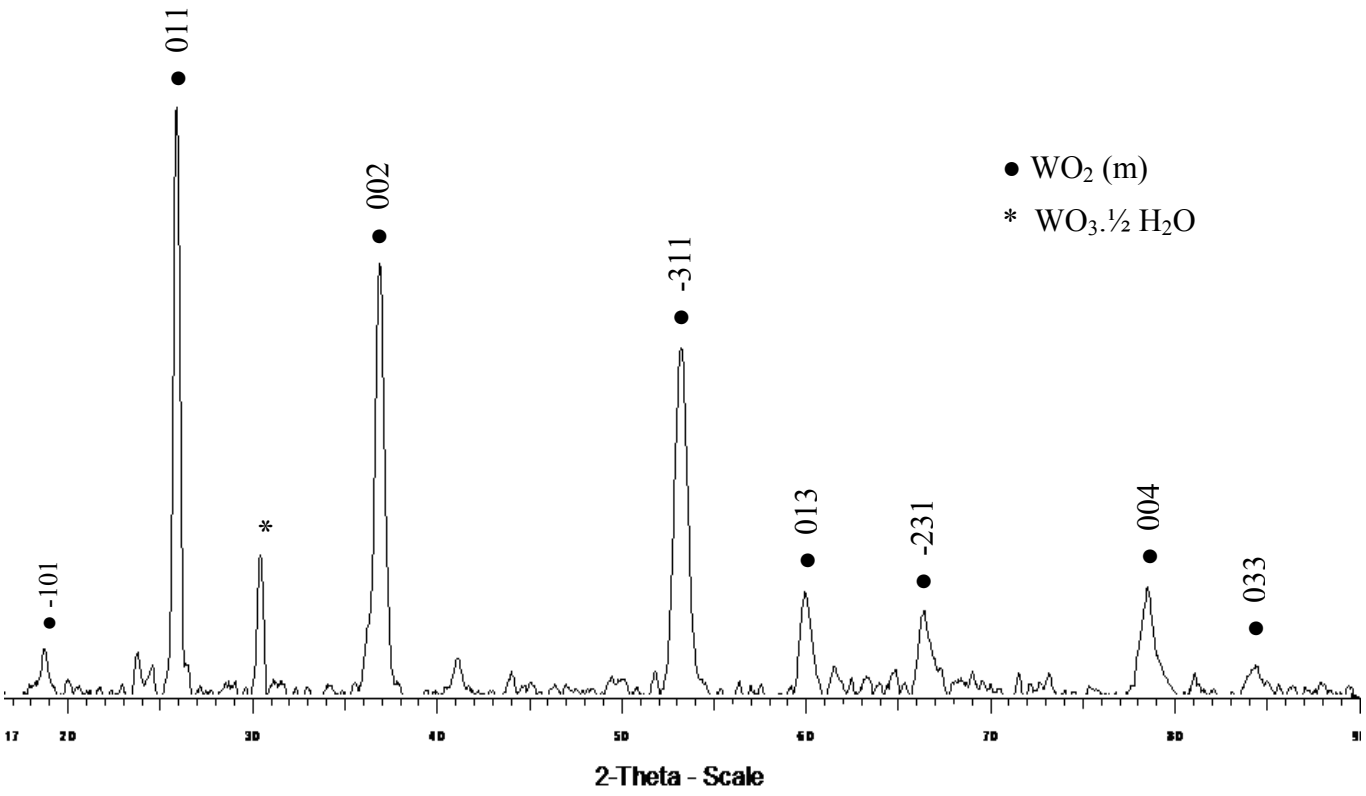

Figure 2.20 PXRD pattern of the the thermal decomposition product of $WO(O^iPr)_3$(bdmap) **(2)** under RAPET conditions (A3)

The XRD pattern of the as-prepared A3 sample is presented in Figure 2.20. The major diffraction peaks observed at 2θ = 18.612, 25.830, 36.865, 53.210 are assigned as (-101), (011), (002), (-220) reflection lines of the primitive monoclinic phase of WO_2. These values are in good agreement with the diffraction peaks and peak intensities of crystalline WO_2 (PDF 32-1393) which is the main component of A3 sample. Also, the peak at 30.363° could match with the $WO_3.½\ H_2O$ (PDF 36-1143) which is believed to be an impurity of the sample.

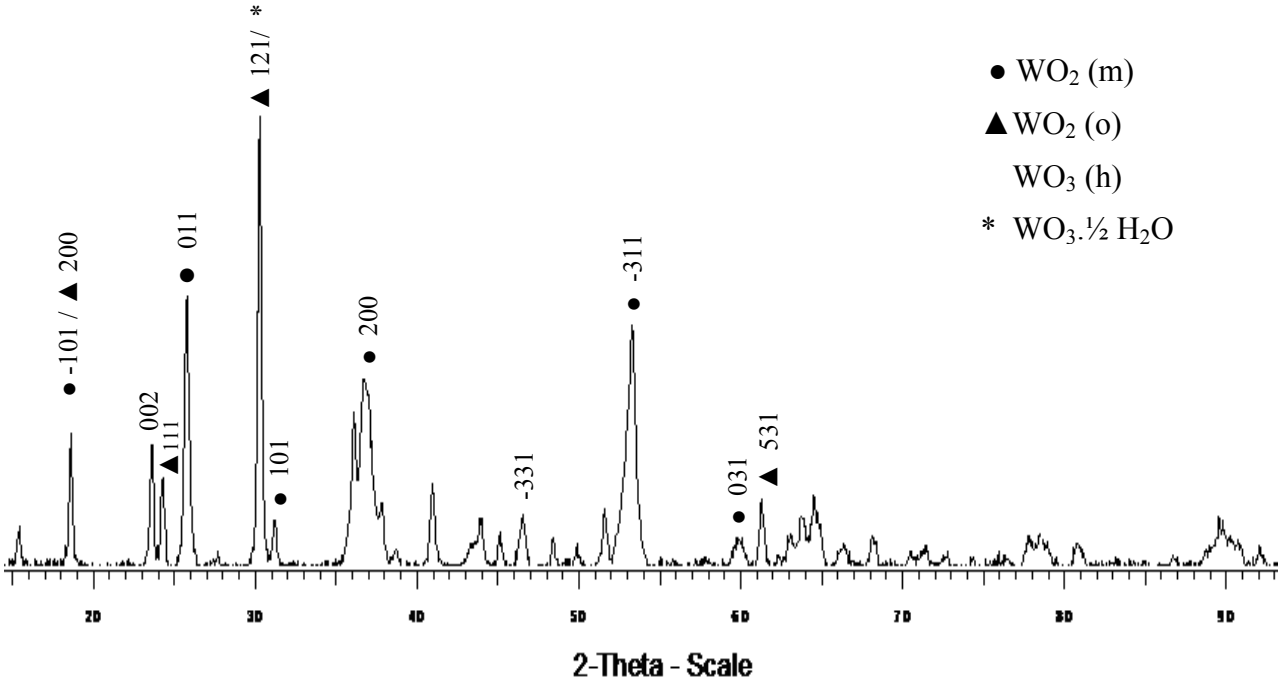

Figure 2.21 PXRD pattern of the thermal decomposition product of $WO(OPr^i)_3$(tdmap) **(1)** under RAPET conditions (A4)

The XRD pattern of the as-prepared A4 sample (Figure 2.21) is complex and suggests a mixture of WO_2 and WO_3. The diffraction peaks observed at 2θ =18.370, 25.558, 36.740, 53.222 are assigned as (-101), (011), (200), (-220) reflection lines of the primitive monoclinic phase of WO_2. These values are in good agreement with the diffraction peaks and peak intensities of crystalline WO_2 (PDF 32-1393). Other relevant peaks of the XRD pattern at 2θ = 23.525, 30.133, 35.869 could also match to the primitive orthorhombic phase of WO_2 (PDF 82-0728). Moreover, the minor peaks at 2θ = 23.53, 24.39 fit with the primitive hexagonal phase of WO_3 (PDF 85-2460). Hence, one phase of WO_3 and two phases of WO_2 coexist in different proportions in the A4 sample. The primitive orthorhombic WO_2 seems to be the major phase compared to the primitive monoclinic phase, as suggested by the main peak at 2θ = 30.133°. However, this peak can also suggest that the prepared material is hygroscopic, result-

ing in the formation of tungsten oxide hydrate $WO_3.½H_2O$ (PDF 36-1143). Contrary to the previous XRD pattern (Figure 2.20), the phase $WO_3.½ H_2O$ appears to be in a larger proportion (Figure 2.21).

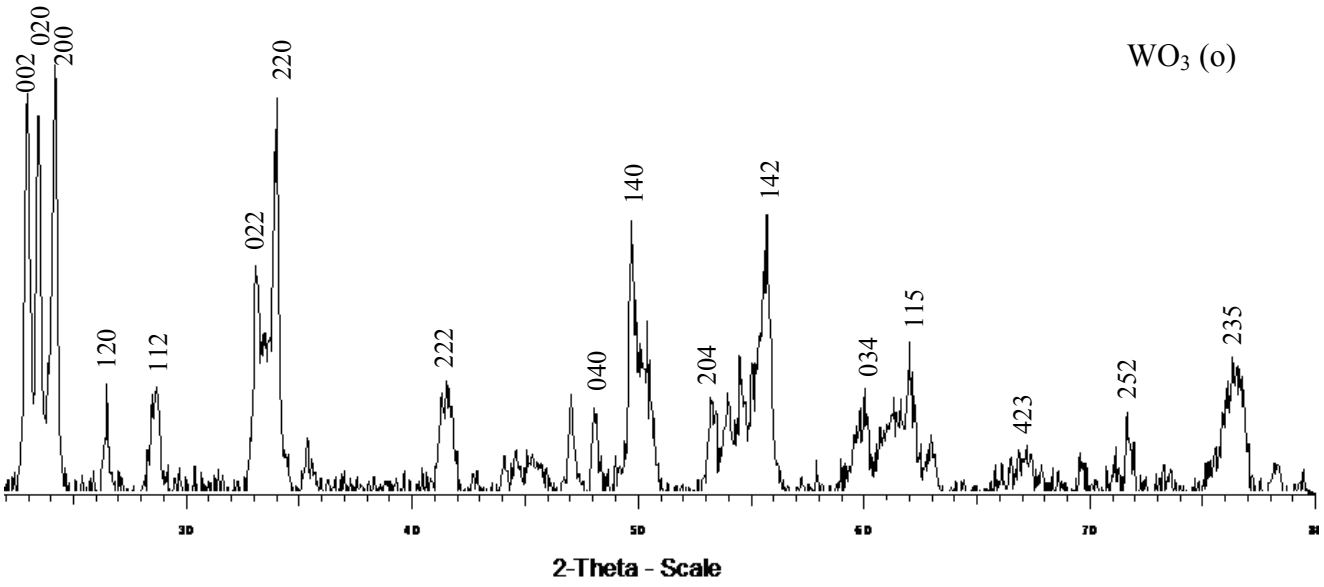

Figure 2.22 Powder XRD of the thermal decomposition product of $W_4O_4(\mu\text{-}O)_6(tdmap)_4$ **(4)** under RAPET conditions (B1)

The XRD pattern of the as-prepared B1 sample is presented in Figure 2.22. Peak match software suggested the presence of the primitive orthorhombic phase of WO_3 in the B1 sample. The diffraction peaks observed at 2θ = 22.824, 23.518, 24.089, 33.920, 49.950 are assigned as (002), (020), (200), (220), (140) reflection lines of the primitive orthorhombic phase of WO_3. These values are in good agreement with the diffraction peaks, peak intensities of crystalline orthorhombic WO_3 (PDF 89-4480). The pale yellow color of the B1 product is also consistent with the presence of stoichiometic WO_3. Assuming that the width of the diffraction is only due to the size of the particle and not a result of microstrains and lattice defects, the decomposition of **(4)** in the air would imply the formation of WO_3 having smaller size particle than the pyrolysis in a closed cell under inert atmosphere.

The XRD patterns for A1-A4 sample are complex due to the coexistence of mixtures, except for B1 which presents only one phase (orthorhombic WO_3). The mixtures display the monoclinic, orthorhombic phases of WO_2 and hexagonal phase of WO_3. WO_2 can result of either the decomposition of the precursors or the reduction of tungsten oxide WO_3 by carbon present in the decomposed complexes of **(1)-(3)**. WO_3 is present in the samples A1-A4. The

formation of WO_3 seems to result either from direct dissociation of **(1)-(3)** or an oxidation of WO_2 in WO_3 by oxygen coming from air and moisture contamination. Also, tungsten oxide hydrate $WO_3.½H_2O$ is present in the sample A3 and A4 which may be hygroscopic. To summarise, all the experimental data suggested by the PXRD are combined in Table 2.8.

Table 2.8 Elemental analysis and components of the samples

Samples	A1	A2	A3	A4	B1
Type of precursors	**(1)**		**(2)**	**(3)**	**(4)**
C,H,N (%) of A1-A4, B1	20.3, 0.94, 2.4	21.1, 1.03, 2.56	21.0, 0.46, 1.62	24.9, 0.60, 2.49	0.92; 0.15; 0.06
C,H,N (%) of **(1)-(4)**	36.8,7.38, 6.25	36.8,7.38, 6.25	36.8,7.38, 6.25	39.9, 7.7, 8.82	29.1, 5.86, 8.87
Compounds (PXRD)	WO_3(h), WO_2 (m, o)	WO_3(h), WO_2 (o)	WO_2 (m) WO_3. ½ H_2O	WO_3(h), WO_2 (m, o) WO_3. ½ H_2O	WO_3(o)

It is important to notice that the percentage of carbon, hydrogen and nitrogen in all the different type A and B experiments decrease considerably compared to those of the different precursors **(1)-(4)** (Table 2.8). For type A experiments, this means that the weight loss of carbon, hydrogen and nitrogen is due to the formation of hydrocarbon and amido compounds that exist in the cell as a result of the high pressure. This is observed when the closed Swagelok reactor is opened at R.T, a release of a pressure occurs. About the type B experiment, the decrease in the amount of the chemical elements comes from the oxidation in the air of the light element (C, H, N). None of the XRD patterns depicted above, from the Figures 2.18 to 2.22, displays any peak due to the remaining carbon. Indeed, the elemental analysis reveals a high carbon content in each sample prepared by the RAPET process (Table 2.8). This supposed that the carbon formed in this process is amorphous or disordered.

Due to the complexity to determine the exact nature of the sample A1-A4, in the next section, we consider for clarity that WO_x (x = 2 or 3) is present overall in these samples.

2.2.3.3.2 Structural Morphology

The Scanning Electron Microscopy (SEM) and Transmission Electron Microscopy (TEM) were performed to provide visual indications concerning the morphologies of the different samples prepared by thermal decomposition under autogenic pressure and in the air. Also, the Energy Dispersive X-ray spectroscopy (EDX) has been used to give information about the chemical elements present in the samples.

The A1 sample has a morphology composed of elongated and spherical particles (Figure 2.23). The elongated particles, illustrated by a white arrow, are very thin, probably on average less than 100 nm and a length of a few micrometers. It is difficult to distinguish the needle-like structure by SEM due to its low resolution. However, they are present and visible at the surface of the spheres. A few spherical bodies, indicated by a black arrow, having a diameter around 2 µm are identified by EDX as carbon spherules. This is in agreement with a report showing also that the spherical bodies, obtained by RAPET reactions, are made of carbon.[30]

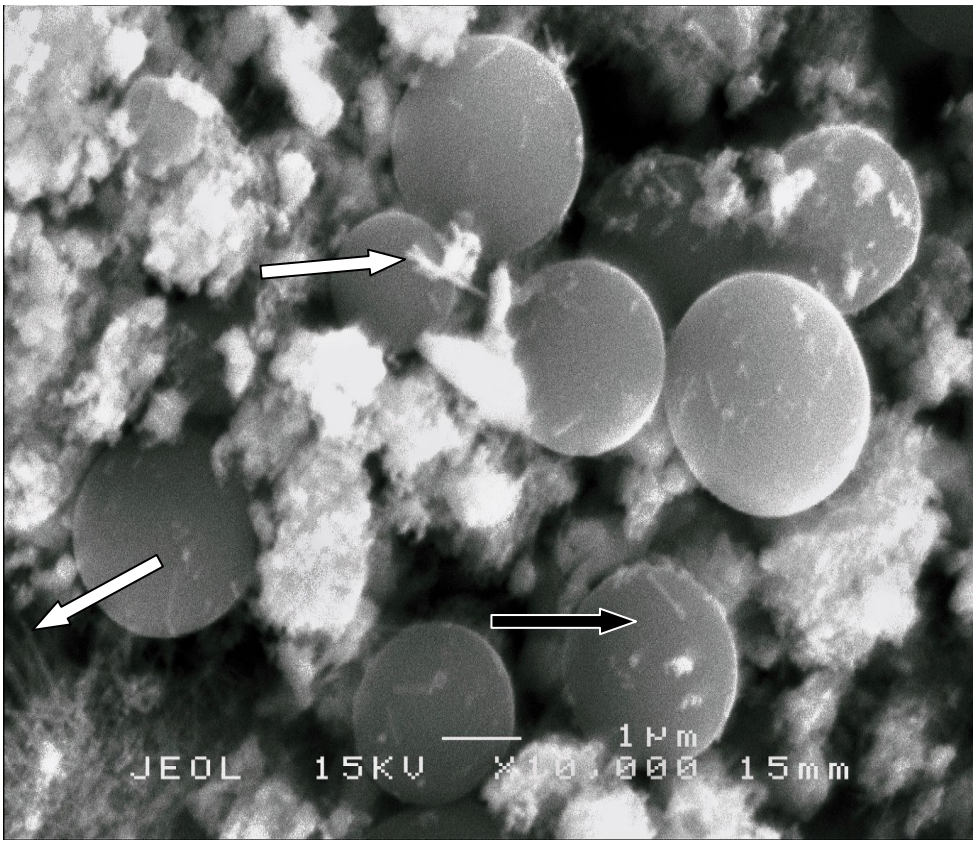

Figure 2.23 Scanning electron micrograph of A1 sample

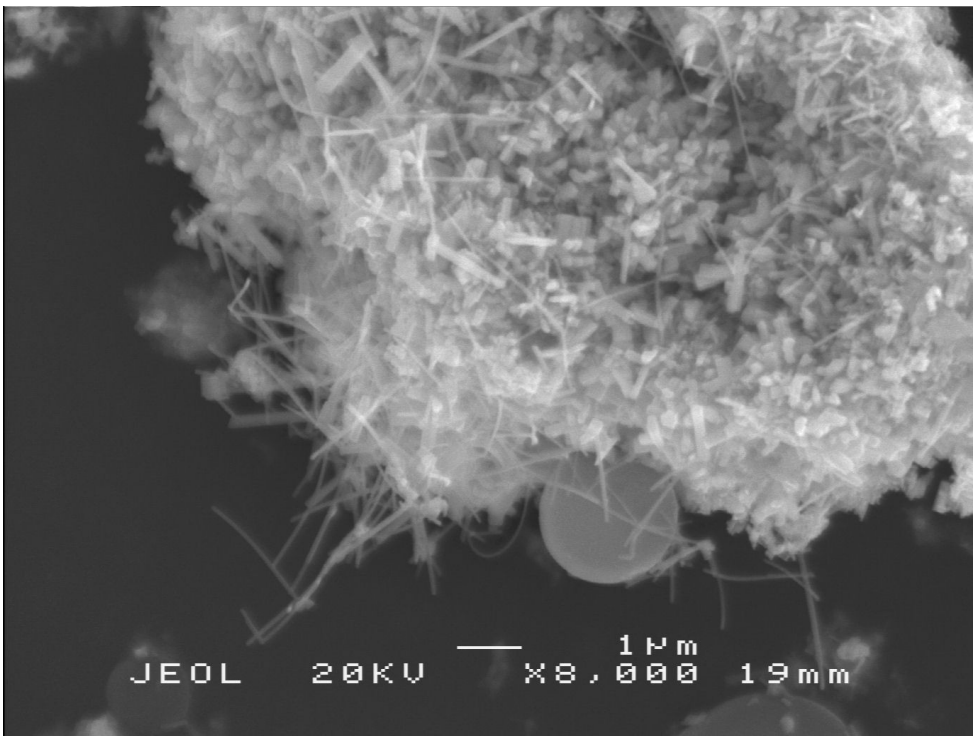

Figure 2.24 Scanning electronic micrograph of A2 sample

The A2 sample (Figure 2.24), from the same precursor as A1 sample, has the same morphology, composed of spherical and elongated particles in the same range of size (Figure 2.23). However, A2 sample, resulting from the decomposition of **(1)** under RAPET reaction for a longer time and in a bigger scale, displays easily a greater density of elongated particles compared to the spherical particles (Figure 2.24).

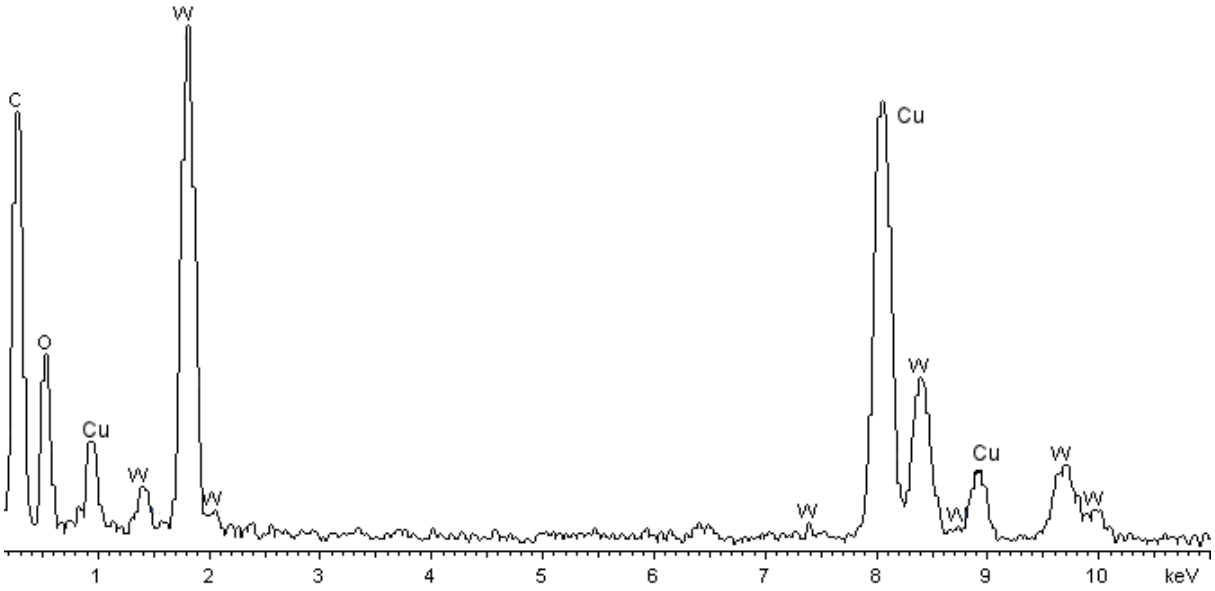

Figure 2.25 EDX spectrum of the A2 sample

EDX measurement reveals the existence of the elements W, O, C and Cu (Figure 2.25). The presence of Cu peaks in the EDX spectra belongs to the copper grid that is used for the TEM sample preparation. Figure 2.26 shows a conventional bright-field TEM image which displays a bright and a dark material, respectively matching with a light and a heavy chemical element. Indeed, components of Figure 2.26 containing high atomic mass Z elements are darker. From the elemental analysis, the EDX measurements and the PXRD (Table 2.8), the bright element might be carbon (C) and the dark element is composed of tungsten oxide (WO_x). This is also confirmed by the Figure 2.27 which shows a dark compound (WO_x core) embedded in a carbon shell. Hence, the carbon in bright colour surrounding tungsten oxide WO_x which is the core, contributes to the formation of core-shell structures. Other reports about the RAPET reaction of molecular precursors which dissociate to form core-shell nanostructures confirm this tendency. As illustrated by TEM, the needle-like structures with diameters from about 40 nm to 100 nm and lengths of a few micrometers, have different shapes. Indeed, the tubes can be either filled or not with an *in situ* tungsten oxide WO_x. The carbon can in some cases form a structure without an *in situ* grown WO_x constituting the so-called nanotubes of carbon (Figure 2.26).

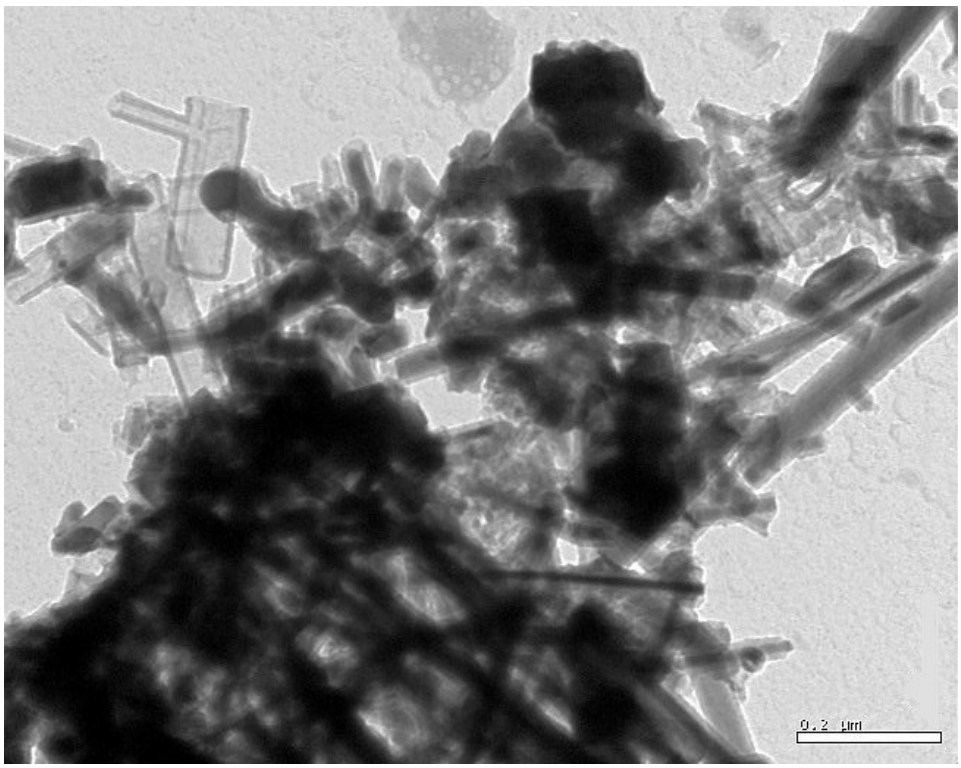

Figure 2.26 Transmission electron micrograph of A2 sample

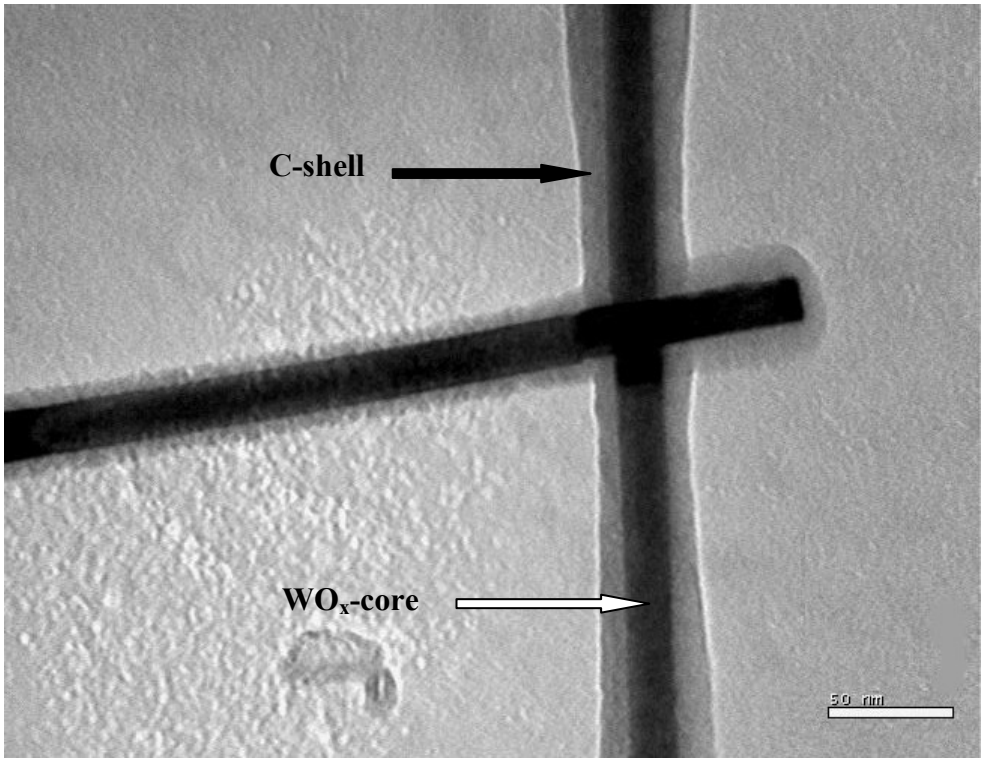

Figure 2.27 Transmission electron micrograph of C(core)-WO_x(shell) structure of A2 sample

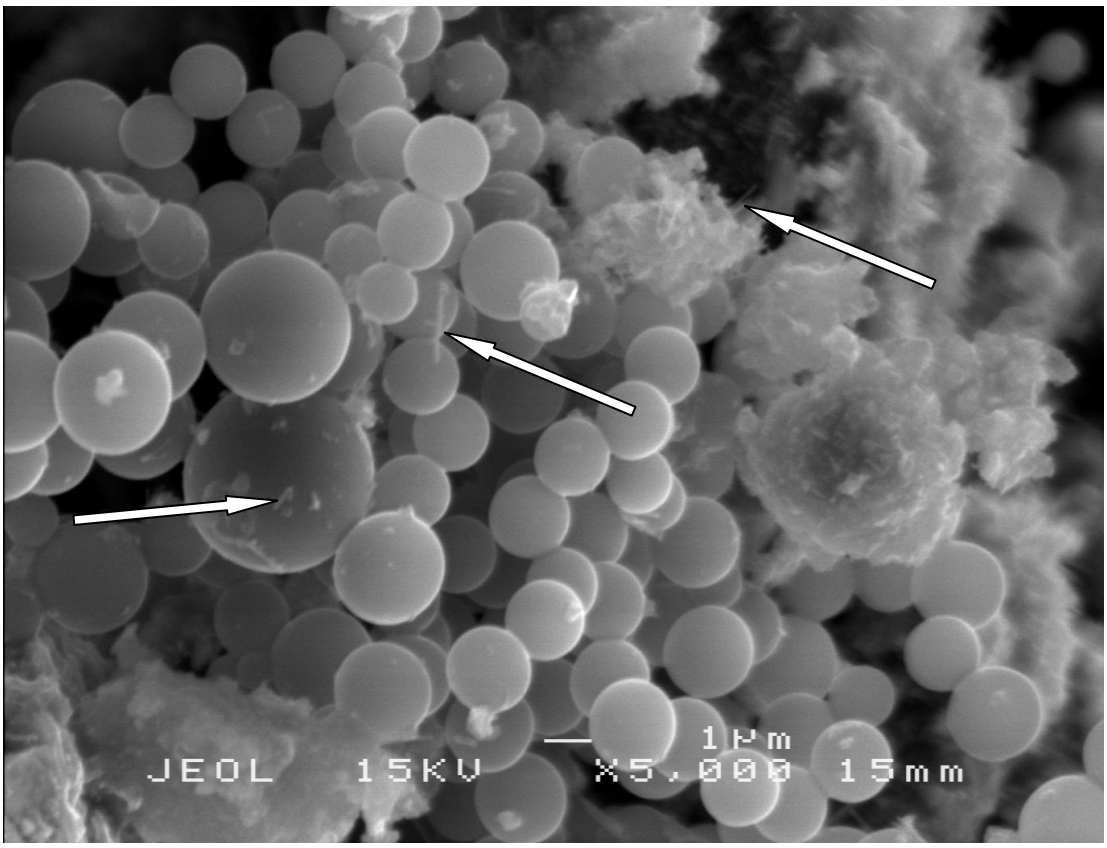

Figure 2.28 Scanning electron microscope of A3 sample

As already reported previously for the experiment A1 and A2, A3 sample (Figure 2.28) shows a large number of carbon spherical particles of an average size 2-3 µm and a few very thin elongated particles, indicated by white arrows which are difficult to distinguish from the background.

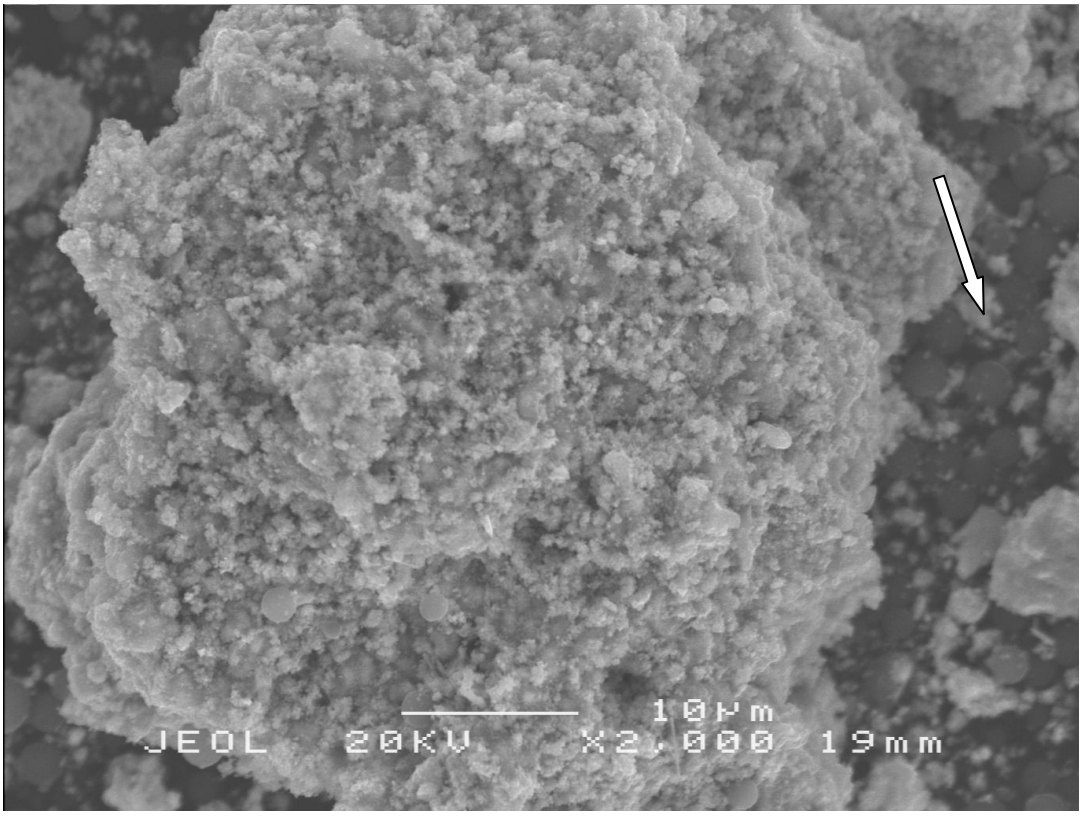

Figure 2.29 Scanning electron microcraph of A4 sample

Figure 2.29 describes in the middle of the SEM image agglomerates formed of small particles at the nanoscale. Also, on the right side of this lump is found dark carbon spheres of an average size of 1-3 µm, indicated by a white arrow. The use of the TEM (Figure 2.30) gave details of the A4 sample which displays, like the previous thermal decomposition of the compounds **(1)** and **(2)**, core-shell nanostructures and nanotubes of carbon. However, the shape and the size of these particles, more or less dense, are quite irregular (Figure 2.29 and 2.30) compared to those detailed previously.

Figure 2.31 reveals the elements C, W, and O present in the A4 sample, as also described in all the previous samples A1, A2 and A3 and confirmed by the formation of core-shell nanostructure.

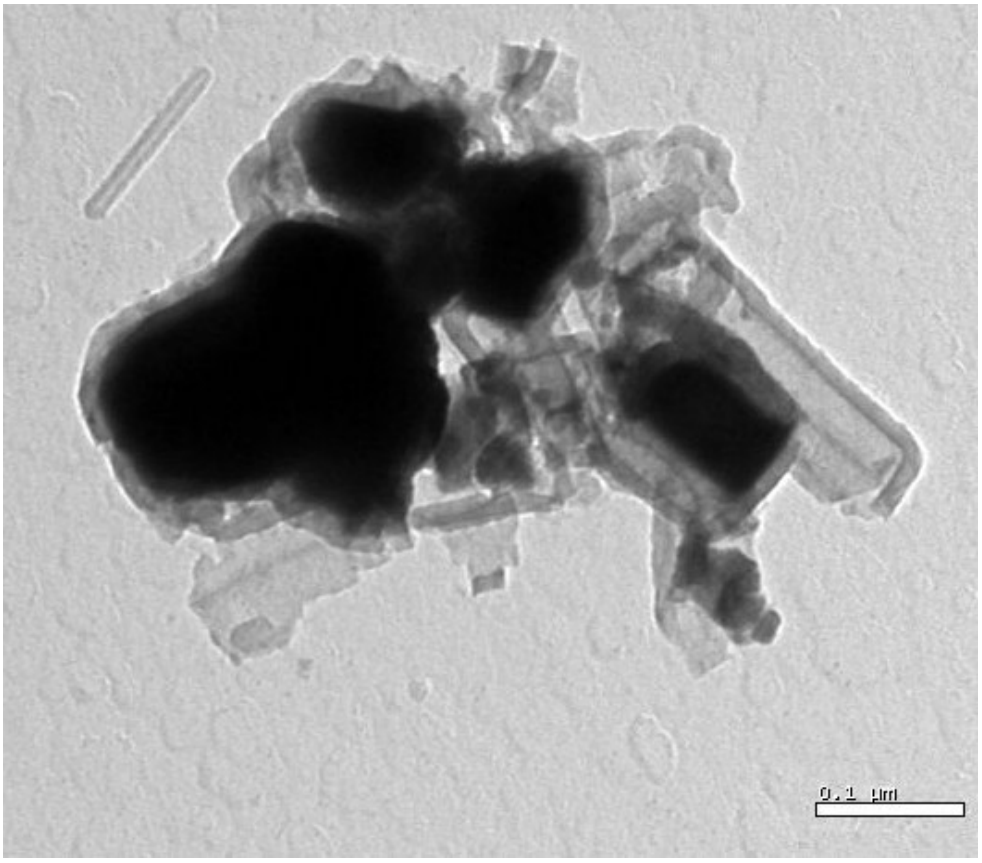

Figure 2.31 Transmission electron micrograph of A4 sample

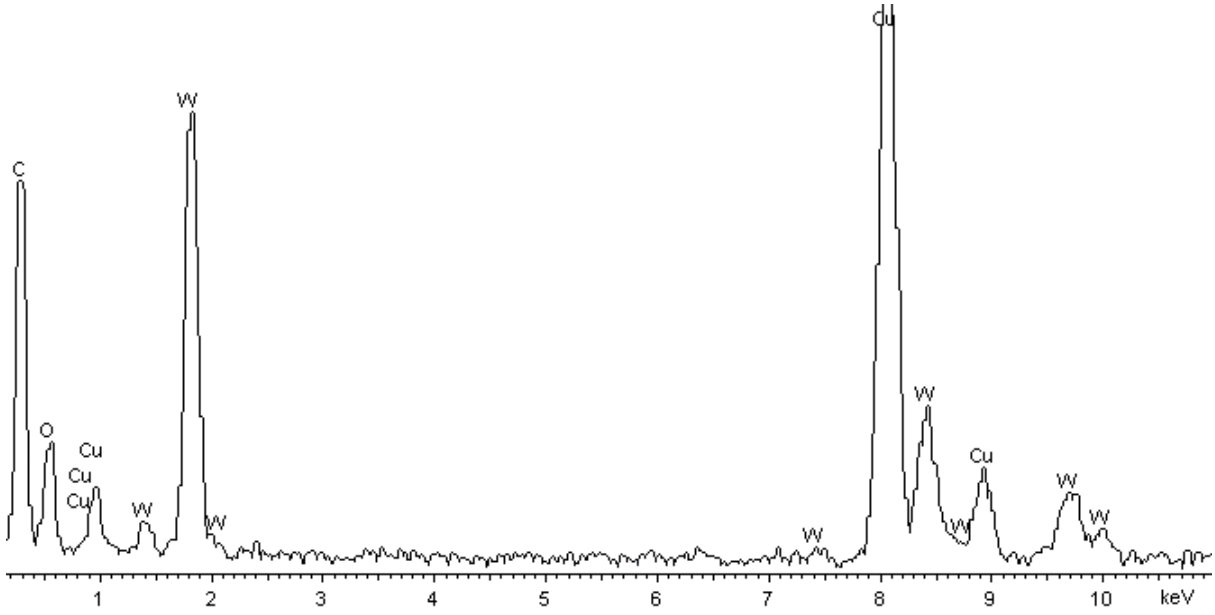

Figure 2.30 EDX spectrum of A4 sample

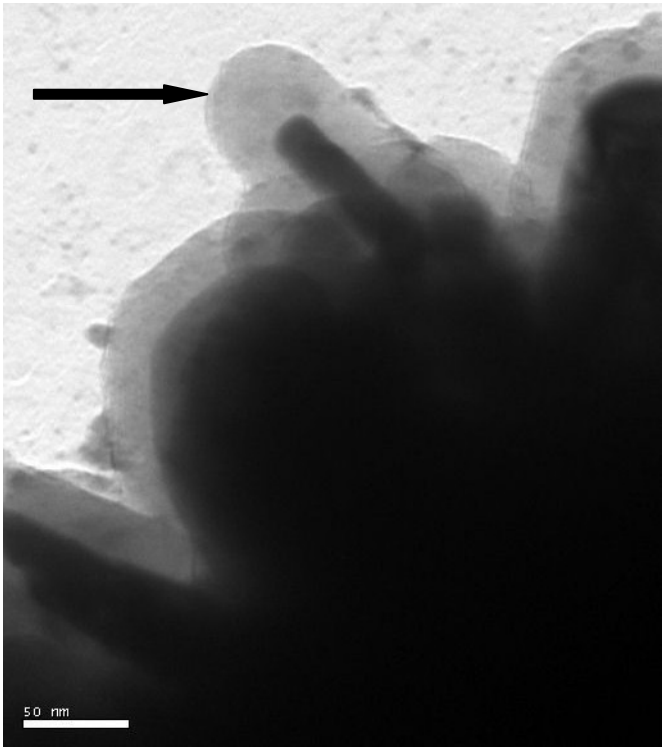

Figure 2.33 Transmission electron micrograph of A4 sample

The TEM picture (Figure 2.32) shows in the A4 sample the WO_x-core/C-shell nanostructures which display various WO_x core diameters but with regular shell thickness except at the tip of a small diameter core, indicated by a black arrow.

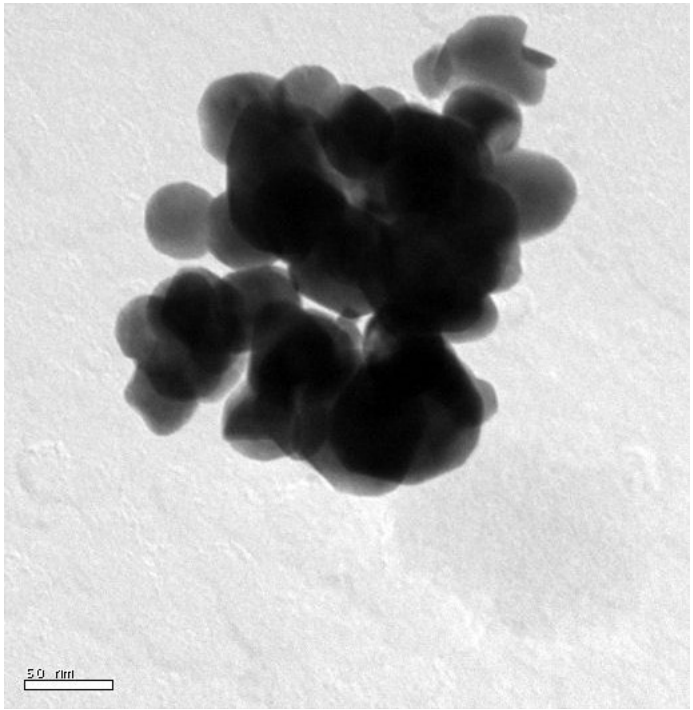

Figure 2.32 Transmission electron micrograph of B1 sample

The thermal decomposition of **(4)** at 500°C in the air gives rise to a nanostuctured pale yellow product, indicating the presence of stoichiometric tungsten oxide WO_3. The analysis of B1 sample displays some irregular spherical particles of an average of 40 nm (Figure 2.33). Figure 2.34 revealed the elements C, W, and O present in the B1 sample.

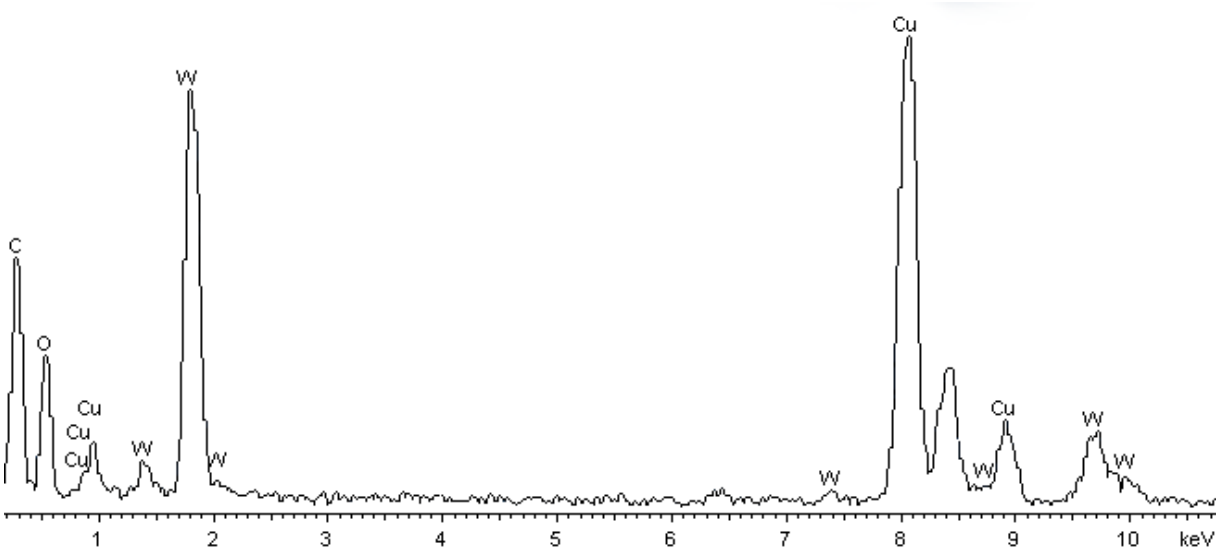

Figure 2.34 EDX analysis of B1 sample

Early reports about the RAPET decomposition of $WO(OPr^i)_4$ and $WO(OMe)_4$ at 700°C under inert atmosphere give rise respectively to $W_{24}O_{68}$/C and $W_{18}O_{49}$/C core/shell nanostructures. Hence, the cores and shells are respectively made of tungsten oxide WO_x and carbon. In one case only, WO_2 has been formed under specific conditions during the thermal decomposition in a closed swagelok cell of $WO(OMe)_4$ in combination with ethanol.[30] However, other types of metal, such as molybdenum, have allowed the preparation of MoO_2 from the RAPET decomposition of $MoO(OMe)_4$ at 700°C due to the ease of reducing MoO_3 to MoO_2 via carbon. First of all, the formation of core-shell can be explained by the solidification of the metal oxide in the first place and then kinetic formation of the carbon shell surrounded the oxide.[31] The element carbon and/or hydrogen allow the reduction of stoichiometric and sub-stoichiometric WO_{3-x} which gives rise to the monoclinic and orthorhombic phase of WO_2 in the products obtained during the RAPET experiments. Hence, the closed Swagelok cell comprises a thermodynamic system of four chemical elements which interact closely in a complex way between each other favouring the oxidation of the sub-stoichiometric WO_{3-x} to WO_3, the reduction of WO_{3-x} and WO_3, and the formation of gases responsible of the increasing pressure inside the Swagelok vessel.

2.3 Conclusion

Highly soluble homometallic tungsten oxo-amino-alkoxides complexes $W(O)(OPr^i)_3(L)$ [L = dmae **(1)**, bdmap **(2)** and tdmap **(3)**] have been successfully synthesised and characterised. The use of donor functionalised ligands, such as amino-alcohols, in the modification of the dimeric tungsten oxo-isopropoxides $[WO(OPr^i)_4]_2$ has allowed the isolation of monomeric compounds **(1)-(3)**.

The thermal stability of **(1)-(3)** has been evaluated by TGA, indicating some volatility. A simple method for fabricating core(WO_x)-shell(C) nanostructures has been investigated by dissociating under RAPET conditions the precursors **(1)-(3)** in a closed Swagelok vessel at 700°C. The decomposition of **(4)** in the air at 500°C produces nanoparticles of WO_3, as predicted by the TGA analysis. The materials prepared by RAPET reaction are mainly mixtures from different phases of WO_2 (monoclinic and orthorhombic) and WO_3 (hexagonal). Post-annealing experiments of the resulting sample A1-A4 at different temperatures is probably required to purify these materials avoiding carefully the change of their core-shell morphology. At the same time, impurities, such as carbon could be reduced, resulting in the decrease of the carbon spheres number observed by electron microscopy.

The use of bulky ligands, such as tdmap enhanced the solubility and stability of **(3)** towards air and moisture. So, the combination of steric demand and donor functionalisation which increases dramatically the stability of the compounds towards moisture has been observed. This has allowed controlled hydrolysis of the precursor. Hence, **(3)** has been hydrolysed to lead to a tetranuclear homometallic tungsten complex $W_4(O)_4(\mu\text{-}O)_6(tdmap)_4$ **(4)**. Also, other complexes $W_4(O)_4(\mu_2\text{-}O)_4(OPr^i)_4(bdmap)_4$ **(5)** and $W_6(O)_6(\mu_2\text{-}O)_9(bdmap)_6$ **(6)** have been adventitiously isolated. Compounds **(4)-(6)** give rise to interesting structures having different type of core. A possible mechanism of the different product **(4)-(6)** from the hydrolysis-condensation of the monomeric compounds **(2)** and **(3)** has been proposed. The nature of ligand plays clearly a significant role in the stabilisation of the produced core.

2.4 Experimental section

All manipulations were carried out under a dry nitrogen or argon atmosphere using standard Schlenk techniques and standard glove-box. All solvents were purified by an Innovative Technology inc. solvent purification system (SPS). Anhydrous 2-propanol, Hdmae, was purchased from Aldrich and dried over 3Å molecular sieves. $[W(O)(OPr^i)_4]_2$,[7] Hbdmap[32] and Htdmap[33] were synthesised according literature procedures. The amino-alcohol Hdmae, Hbdmap and Htdmap were distilled over sodium metal and then freeze-pump-thawed three times.

Synthesis of $W(O)(OPr^i)_3$(dmae) (1)

$[W(O)(OPr^i)_4]_2$ (2.00 g, 9.17 mmol) was dissolved in toluene (ca. 60 mL) and one equivalent of Hdmae (0.92 mL) was added, with stirring. The solution was then refluxed for 2 hours and allowed to cool. Removal of all volatiles *in vacuo* gave a cloudy orange-yellow oil which was then purified by distillation to give **(1)** as a clear pale yellow liquid. Yield (54 %).

^{1}H NMR ($CDCl_3$, 300 Mhz, 298 K, δ ppm): 1.23 (m, 18H, -OCH(C***H*****$_3$**)$_2$), 2.41 (s, 6H, -N(C***H*****$_3$**)$_2$), 2.60 (m, 2H, ^3J = 5.5 Hz, $^2J_{H,H}$ = 1.2 Hz, -C***H*****$_2$**N), 4.54 (m, 2H, ^3J = 5.5, $^2J_{H,H}$ = 1.2 Hz, -C***H*****$_2$**-), 4.80 (m, 3H, -OC***H***Me_2)

^{13}C NMR ($CDCl_3$, 300 Mhz, 298 K, δ ppm): 24.2 (-OCH(***C***H_3)$_2$), 24.8 (-OCH(***C***H_3)$_2$), 24.8 (-OCH(***C***H_3)$_2$), 48.0 (-N(C***H*****$_3$**)$_2$), 62.7 (-CH_2**C**H_2)NMe_2), 68.2 (-**C**H_2CH_2)NMe_2), 77.0 (-O**C**H$(CH_3)_2$), 77.6 (-O**C**H$(CH_3)_2$)

^{183}W NMR (d_8-toluene, 373 K, δ ppm) = - 99.9

E.S.I (tof) M. S. [M-C_3H_8O] + H^+ = 406.1222 m/z (3.12 ppm error)
Expected $C_{13}H_{31}NO_5W + H^+$

Synthesis of $W(O)(OPr^i)_3$(bdmap) (2)

$[W(O)(O^iPr)_4]_2$ (3.00 g, 6.87 mmol) was dissolved in toluene (ca. 60 mL and one equivalent of Hbdmap (1 mL) was added with stirring. The solution was then refluxed for 2 hours and allowed to cool. Removal of all volatiles *in vacuo* gave a cloudy orange-yellow oil which was then purified by distillation under vaccum (120°C) to give **(2)** as a clear pale yellow liquid. Yield (58 %)

Analysis found (Calc. for) %: C 36.8 (36.8) H 7.38 (7.33) N 6.25 (5.36)

^{1}H NMR ($CDCl_3$, 300 Mhz, 298 K, δ ppm): 1.2 (m, 18H, -OCH(C***H*****$_3$**$)_2$), 2.19 (s, 6H, -N(C***H*****$_3$**$)_2$), 2.36 (s, 3H, -N(C***H*****$_3$**), 2.43 (s, 3H, -N(C***H*****$_3$**$)_3$, 2.47 (dd, 2H, -C***H*****$_2$**N, $^{2}J_{H,H}$=11.62 Hz, $^{3}J_{H,H}$ =3.26 Hz), 2.59 (t, 2H, -OCHC***H*****$_2$**NMe_2, $^{2}J_{H,H}$ = 11.62 Hz), 4.51 (m, 1H, -OC***H***$CH_2(N(CH_3)_2)$, 4.75 (m, 2H, OC***H***Me_2), 4.86 (m, 1H, -OC***H***Me_2)

^{13}C NMR ($CDCl_3$, 300 Mhz, 298 K, δ ppm): 24.6 (-OCH(***C***$H_3)_2$, 25.1 (-OCH(***C***$H_3)_2$, 24.8 (-OCH(***C***$H_3)_2$, 25.4 (-OCH(***C***$H_3)_2$, 25.7 (-OCH(***C***$H_3)_2$, 26.1 (-OCH(***C***$H_3)_2$, 47.0 (-N(***C***$H_3)_2$), 47.5 (-N(***C***$H_3)_2$), 50.3 (-N(***C***$H_3)_2$), 65.0 (-***C***$H_2N(CH_3)_2$), 66.7 (-O***C***$H(CH_2N(CH_3)_2)$, 77.8 (-O***C***$H(CH_3)_2$)

^{183}W NMR (C_7D_8, 500 Mhz, 373K, δ ppm): - 99.9

E.S.I (tof) M. S. $[M-C_3H_8O] + H^+$ = 463.1781 m/z (1.43 ppm error)
Expected $C_{16}H_{38}N_2O_5W + H^+$

Synthesis of W(O)(OPr^{i})$_3$(tdmap) (3)

$[W(O)(OCH(CH_3)_2]_2$ (3.00 g, 6.87 mmol) was dissolved in toluene (ca. 60 mL and one equivalent of Htdmap (1.80 g, 3.19 mmol) was added with stirring. The solution was then refluxed for 3 hours and allowed to cool. Removal of all volatiles *in vacuo* gave a cloudy orange-yellow oil which was then purified by distillation to give **(3)** as a clear pale yellow liquid. Yield (48%).

Analysis found (Calc. for) %: C 39.9 (39.4) H 7.70 (7.83) N 8.82 (7.25)

^{1}H NMR ($CDCl_3$, 300 Mhz, 298 K, δ ppm): 1.25 (m, 18H, -OCH(C***H*****$_3$**$)_2$), 2.28 (s, 12 H, -N(C***H*****$_3$**$)_2$), 2.36 (d, 1H, $^{3}J_{H,H}$ =16 Hz, -C***H*****$_2$**NMe_2), 2.48 (s, 6H, -N(C*H*$_3$$)_2$), 2.45 (d, 2H, $^{3}J_{H,H}$ =13.6 Hz, -C***H*****$_2$**$N(CH_3)_2$), 2.56 (d, 2H, $^{3}J_{H,H}$ =16 Hz, -C***H*****$_2$**$N(CH_3)_2$), 2.57 (d, 2H, $^{3}J_{H,H}$=13.6 Hz, -C***H*****$_2$**NMe_2), 4.74 (m, 2H, OC***H***Me_2), 4.84 (m, 1H, OC***H***Me_2)

^{13}C NMR ($CDCl_3$, 300 Mhz, 298 K, δ ppm): 24.57 (-OCH(***C****H*$_3$$)_2$), 24.62(-OCH(***C***$H_3)_2$, 25.1 (-OCH(***C***$H_3)_2$), 47.76 (-N(***C***$H_3)_2$), 51.27 (-N(***C***$H_3)_2$), 63.68 (-OC(***C***$H_2NMe_2$), 66.82 (-OC(***C***$H_2NMe_2$), 76.41 (-O***C***$HMe_2$), 76.5 (-O***C***$HMe_2$), 87.89 (-O***C***$(CH_2NMe_2)_3$

^{183}W NMR (C_7D_8, 500 Mhz, 373K, δ ppm): - 114.1

E.S.I (tof) M. S. [M-C_3H_8O] + H^+ = 406.1222 m/z (3.12 ppm error)
Expected $C_{13}H_{31}NO_5W + H^+$

Synthesis of $W_4O_4(\mu\text{-}O)_6(tdmap)_4$ (4)

First of all, $W(O)(OPr^i)_3(tdmap)$ was prepared by mixing $[W(O)(OPr^i)_4]_2$ (3.30 g, 7.56 mmol) and Htdmap (1.90 g, 9.34 mmol) in hot toluene, as mentioned above but without distillation. This oily crude product, obtained by removing the volatiles, was then hydrolysed in a (4:1 mL) mixture of anhydrous toluene and isopropanol at 0°C by adding dropwise a water-isopropanol solution (0.1:2 mL) through syringes over a period of 1-2 h under vigorous stirring. The reaction medium was stirred for 20 h at room temperature, and then refluxed for 24 h. The solution was filtered though Celite® and then concentrated to leave about 3 mL. The resulting oil was dissolved in warm hexane until beginning of recrystallisation. Yield = 37%, mp = 108°C

Analysis found (Calc. for) %: C 29.1 (28.2) H 5.86 (5.67) N 8.87 (9.86)

^{1}H NMR (C_6D_6, 400 Mhz, 298 K, δ ppm) 500Mhz: 2.37 (s, 6H, N(C***H***$_3$)$_2$), 2.48 (s, 6H, N(C***H***$_3$)$_2$), 2.71 (d, 1H, -C***H***$_2$NMe$_2$, $^2J_{H,H}$ = 13.3 Hz), 2.78 (d, 1H, -C***H***$_2$NMe$_2$, $^2J_{H,H}$ = 13.3 Hz), 2.88 (s, 3H, NC***H***$_3$)$_2$) 2.94 (d, 3H, -C***H***$_2$NMe$_2$), 2.96 (s, 3H, NC***H***$_3$)$_2$), 2.98 (d, 1H, -C***H***$_2$NMe$_2$, $^2J_{H,H}$ = 14.3 Hz,), 3.02 (d, 1H, -C***H***$_2$NMe$_2$, $^2J_{H,H}$ = 12.7 Hz), 3.22 (d, 1H, -C***H***$_2$NMe$_2$, $^2J_{H,H}$ = 12.7 Hz)

^{13}C NMR (C_6D_6, 400 Mhz, 298 K, δ ppm): 48.34 (-N(***C***H$_3$)$_2$, 48.43 (-N(***C***H$_3$)$_2$), 53.17 (-N(***C***H$_3$)$_2$), 55.01 (-N(***C***H$_3$)$_2$), 64.45 (-***C***H$_2$NMe$_2$), 66.8 (-***C***H$_2$NMe$_2$), 71.53 (-***C***H$_2$NMe$_2$), 89.71 (-***C***CH$_2$NMe$_2$)

^{183}W NMR (C_7D_8, 500 Mhz, 373K, δ ppm) : - 42.6

E.S.I (tof) M. S. [M + H^+]= 1705.5211 m/z (3.99 ppm error)
Expected $C_{13}H_{31}NO_5W + H^+$

Thermodecomposition under "Reaction under autogenic pressure at elevated temperatures"(RAPET)

The thermal decomposition under RAPET conditions of $WO(OPr^i)$(dmae) **(1)**, $WO(OPr^i)$(bdmap) **(2)** , $WO(OPr^i)$(tdmap) **(3)** were carried out in a 5 mL closed vessel cell. The cell was assembled from stainless steel Swagelok parts. A ½ inch union part was capped on both sides by standard plugs. For these syntheses, 0.5 g and 1.2 g of **(1)**, 0.41g of **(2)** and 0.36 g of **(3)** are introduced into the vessel at R.T in the nitrogen atmosphere of the glove-box. The filled cell was closed tightly with the other plug and then placed inside an iron pipe in the middle of the furnace. The temperature was raised at a rate of 10°C per minute. The closed vessel reactor (Swagelok) was heated at 700°C for 2 h, then gradually cooled (1°C/min.) to room temperature, opened with the release of a little pressure, and a dark black powder is collected. The total yields of the above RAPET reactions are respectively 55%, 57% and 59%. All yields are relative to the weight of the starting materials.

Thermodecomposition in the air

The decomposition in the air was carried out by introducing in a graphite pot 0.15 g of **(4)**. The graphite reactor was placed in the middle of the furnace. The temperature is raised at a rate of 10°C per minute. The graphite vessel is heated at 500°C for 1 h and then gradually cooled (1°C/min.) to room temperature, a grey-blue powder is collected. The product obtained after pyrolysis was not measured.

.

2.5 References

[1] J. A. Crayston, in *Comprehensive Coordination Chemistry II, Vol. 1*, **2004**, p. 711.
[2] D. C. Bradley, I. P. Rothwell, R. C. Mehrotra, A. Singh, in *Alkoxo and Aryloxo Derivatives of Metals*, **2001**.
[3] D. C. Bradley, R. C. Mehrotra, in *Metal Alkoxides*, **1978**.
[4] R. C. Mehrotra, A. Singh, *Chem. Soc. Rev.* **1996**, *25*, 1.
[5] U. Schubert, in *Comprehensive Coordination Chemistry II, Vol. 7*, **2004**, p. 629.
[6] D. C Bradley, M. H. Chishlom, M. W. Extine and M. E. Stager, *Inorg. Chem.* **1977**, *16*, 1794.
[7] W. Clegg, R. J. Errington, P. Kraxner and C. Redshaw, *J. Chem. Soc., Dalton Trans.* **1992**, 1431.
[8] C. L. Dezelah, O. El-kadri, I. Szilįgyi, J. M. Campbell, K. Arstila, L. Niinistö and C. H. Winter, *J. Am. Chem. Soc.* **2006**, *128*, 9639.
[9] S. I. Kucheiko, N. Y. Turova, *Koordinatsionnaya Khimiya* **1985**, *11*, 1521.
[10] Y. Chi, P-F. Hsu, C.-S. Liu, W-L. Ching, T.-Y. Chou, A. J. Carty, S.-M. Peng, G.-H. Lee and S.-H. Chuang, *J. Mater. Chem.* **2002**, *12*, 3541.
[11] R. Anwander, F. C. Munck, T. Priermeier, W. Scherer, O. Runte and W.A. Herrmann, *Inorg. Chem.* **1997**, *36*, 3545.
[12] D.V. Baxter, M. H. Chisholm, S. Doherty, *J. Chem. Soc., Chem. Commun.* **1996**, 1129.
[13] P. A. Williams, Ph.D thesis, Bath **2000**.
[14] L. McElwee-White, *Dalton Trans.* **2006**, 5327.
[15] A. C. Jones, T.J. Leedham, P.J. Wright, M.J. Crosbie, K.A. Fleeting, D.J. Otway, P. O'Brien, M.E. Pemble, *J. Mater. Chem.* **1998**, *8*, 1773.
[16] A. C. Jones, *J. Mater. Chem.* **2002**, *12*, 2576.
[17] K. A. Fleeting, P. O'Brien., A. C. Jones, D. J. Otway, A. J. P. White, D. J. Williams, *J. Chem. Soc., Dalton Trans.* **1999**, 2853.
[18] A. C. Jones, *Chem. Vap. Deposition* **1998**, *4*, 169.
[19] S. C. Goel, K.S. Kramer, P.C. Gibbons and W.E. Buhro, *Inorg. Chem.* **1989**, *28*, 3619.
[20] S. V. Pol, V. G. Pol, A. Gedanken, *Chem. Eur. J.* **2004**, *10*, 4467.
[21] S. V. Pol, V. G. Pol, V. G. Kessler and A. Gedanken, *New J. Chem.* **2006**, *30*, 370.
[22] S. Liu, S. Boeshore, A. Fernandez, M. J. Sayagués, J. E. Fischer, and Aharon Gedanken, *J. Phys. Chem. B* **2001**, *105*, 7606.
[23] F. Kojin, M. Mori, T. Morishita, M. Inagaki, *Chem. Lett.* **2006**, *35*, 388.
[24] G. A. Carriedo, F. J. García Alonso, J. L. García, R. J. Carbajo and F. López Ortiz, *Eur. J. Inorg. Chem.* **1999**, 1015.
[25] M. Minelli, J. H. Enemark, R. T. C. Brownlee, M.J. O'Connor and A.G. Wedd, *Coord. Chem. Rev.* **1985**, 169.
[26] L. P. Kazansky, T. Yamase, *J. Phys. Chem. A* **2004**, *108*, 6437.
[27] W. Clegg, M. R. J. Elsegood, R. J. Errington and Joanne Havelock, *J. Chem. Soc., Dalton Trans.* **1996**, 681.
[28] D. C. Bradley, M. H. Chisholm, C. E. Heath and M. B. Hursthouse, *J. Chem. Soc., Chem. Commun.* **1969**, 1261.
[29] P. A. Van der Schaaf, J. Boersma, W. J. J. Smeets, A.L. Spek, G. Van Koten, *Inorg. Chem.* **1993**, *32*, 5108.
[30] S. V. Pol, V. G. Pol, V. G. Kessler, G. A. Seisenbaeva, L. A. Solovyov, A. Gedanken, *Inorg. Chem.* **2005**, *44*, 9938.
[31] S. V. Pol, V. G. Pol, V. G. Kessler, G. A. Seisenbaeva, M. Sung, S. Asai, A. Gedanken, *J. Phys. Chem. B* **2004**, *108*, 6322.

[32] K. N. Campbell, R. A. Laforge, in *Studies in the quinoline in the quinoline series, Vol. Chap IX*, **1948**, p. 346.
[33] G. Mueller, T. Schaetzle, *Z. Naturforsch. B* **2004**, *59*, 1400.

Chapter 3
Hetero-metallic Tungsten alkoxide complexes

3.1 Introduction

The precursor chemistry for the fabrication of mixed-metal oxides is an emerging field which attracts more and more interest. The study and development of organometallic precursors for example, has been intimately connected within thin film processing over the last few decades, in particular CVD and sol-gel techniques.

The conventional, or multi-source, approach utilizes predominantly the usual precursors, such as metal alkoxides $M(OR)_n$, halides and β-diketonates $M(RCOCHCOR')_n$ and to some extent, alkyl, hydride or cyclopentadienyl derivatives. The related traditional delivery techniques use solids and/or liquids with low vapour pressures in secured bubblers. These require well-controlled, high-temperature delivery lines in order to avoid condensation of the precursors. The complexity of the delivery systems increases with the number of lines required for a multi-component material. Moreover, different precursors bringing the elements to the target materials possess generally different physical properties and decomposition characteristics, making them incompatible for conventional CVD. One of the solutions is the use of "single-source precursors" (SSP) in which different metals are associated within the same molecule. These related process techniques allow the production of advanced inorganic materials from the molecular chemistry which combines the necessary elements for the creation of novel materials and hence new properties. This recent approach of so-called single-source precursors contributes to the development of hetero-metallic complexes for a variety of multi-component materials, for example piezoelectric ceramics, doped metal oxides and superconductors.

The SSP approach implies the optimisation by molecular chemistry of the physical properties, such as volatility. As already explained in the previous chapters, volatility depends on all the types of intermolecular interactions (dative bonds, van der Waals, π-stacking or hydrogen bonds) which affect the molecular weight. In order to enhance overall the volatility and solubility, and hence to minimize the degree of oligomerisation, different approaches have been proposed. This is achieved by ligands of increasing steric demand and/or using fluorinated ligands and/or by blocking the empty coordination sites by intra- or inter-molecular ligand which plays the role of Lewis base. In particular, it is really challenging to meet the CVD criteria for heavy metals such as Ba^{2+}, which show significant problem with respect to its low charge and high coordination number. However, some Ba-Cu heterobimetallic systems, such as $Ba[Cu(OCMe(CF_3)_2)_3]_2$ and $BaCu(C_2H_6O_2)_3(C_2H_4O_2)_2$ have been reported to be quite volatile and hence potential CVD precursors.[1-3] The SSP approach

has been successfully used as well for the deposition of $LiNbO_3$ by LI-CVD from the hetero-metallic alkoxide $LiNb(OEt)_6$.

The physical and chemical properties of these complexes (volatility, solubility and reactivity) can be modified and thus tailored by adding other types of ligand, such as β-diketonates and amino-alcohols. The alkoxide ligand (-OR) can adopt different bridging mode (μ_2- or μ_3-) allowing the formation of a bridge between different or equivalent metals. Alkoxo bridges can either increase the nuclearity of a compound by forming oligomer (*e.g.* homo-metallic alkoxides) and/or link different metals together by bridging (*e.g.* hetero-metallic alkoxides) .

Volatile and soluble homoleptic heterobimetallic complexes $M[Al(OPr^i)_4]_n$ (M = Cr, Fe; n = 3; M = Co, Cu, Mn, Ni; n = 2) based on the ligand $[Al(OPr^i)_4]^-$ have been prepared via salt elimination (metathesis).[4-6] Other homoleptic bimetallic compounds of type $M'M(OR)_{x+y}$, such as $[BaTi_2(OPr^i)_{10}]_2$, $Ba[Ti_2(OPr^i)_9]_2$ and $[Ti_2(OPr^i)_9]Ba[Ti(OPr^i)_5]$ (Figure 3.1) can be synthesised by Lewis acid-base reactions with different stoichiometry, in order to make ferroelectric ceramic barium titanates. The heterobimetallic complexes become more and more robust as the number of alkoxo-bridges increases to provide a cage, as depicted in the Figure 3.1. This also illustrates the different type of μ_2- and μ_3- bridging of the isopropoxide ligand. This preparation of heterometallic heteroleptic acetylacetonate alkoxide complexes of type $M_aM_b(acac)_x(OR)_y$ has been already reported.[7] $MAl_2(acac)_4(OPr^i)_4$ (M = Co, Ni, Mg) has been first synthesised by Mehrotra et al. using the modification of homoleptic alkoxides.[8] Since then, other compounds have been described.[9-12] In particular, the interaction of $M'(acac)_2$ (M = Co, Ni, Zn or Mg) with $M(OMe)_5$ (M = Ta or Nb) in a hydrocarbon solvent was found to provide $M'_2M_2(acac)_2(OMe)_{12}$ and $M(acac)(OMe)_4$ according to reaction 3.1 (cf. Figure 3.2):

$$M'(acac)_2 + [M(OR)_5]_2 \xrightarrow{\Delta,\text{Toluene}} \tfrac{1}{2}\, M'_2M_2(acac)_2(OMe)_{12} + M(OR)_4(acac) \qquad (3.1)$$

In the Figure 3.2, the dimeric structure of the complex $M'_2M_2(acac)_2(OMe)_{12}$ is built up by four distorted edge-sharing octahedra which contain three types of methoxide groups: terminal μ_1, two triply bridging μ_3 and four bridging μ_2. The acetylacetonate ligand is terminal and attached to the cobalt atom in a η^2 manner.[13]

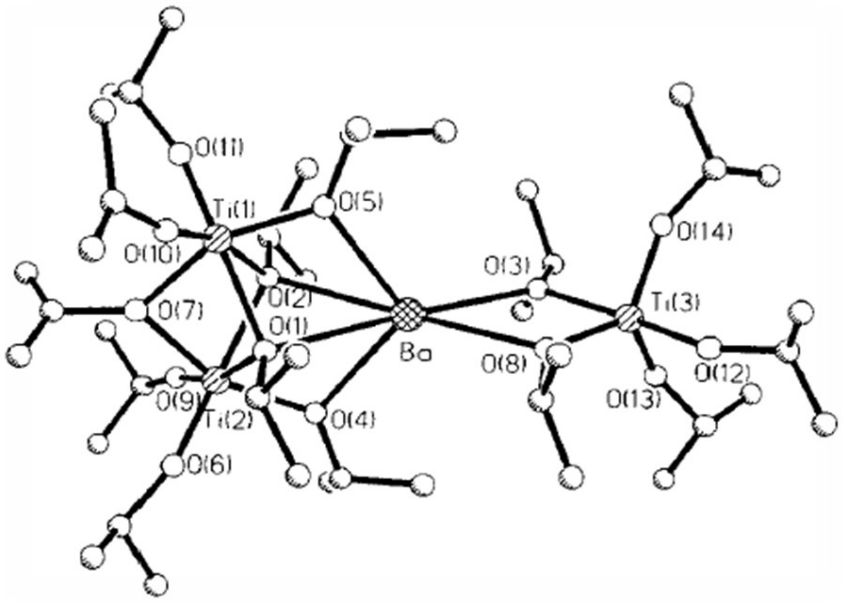

Figure 3.1 Molecular structure of $[Ti_2(OPr^i)_9]Ba[Ti(OPr^i)_5]$

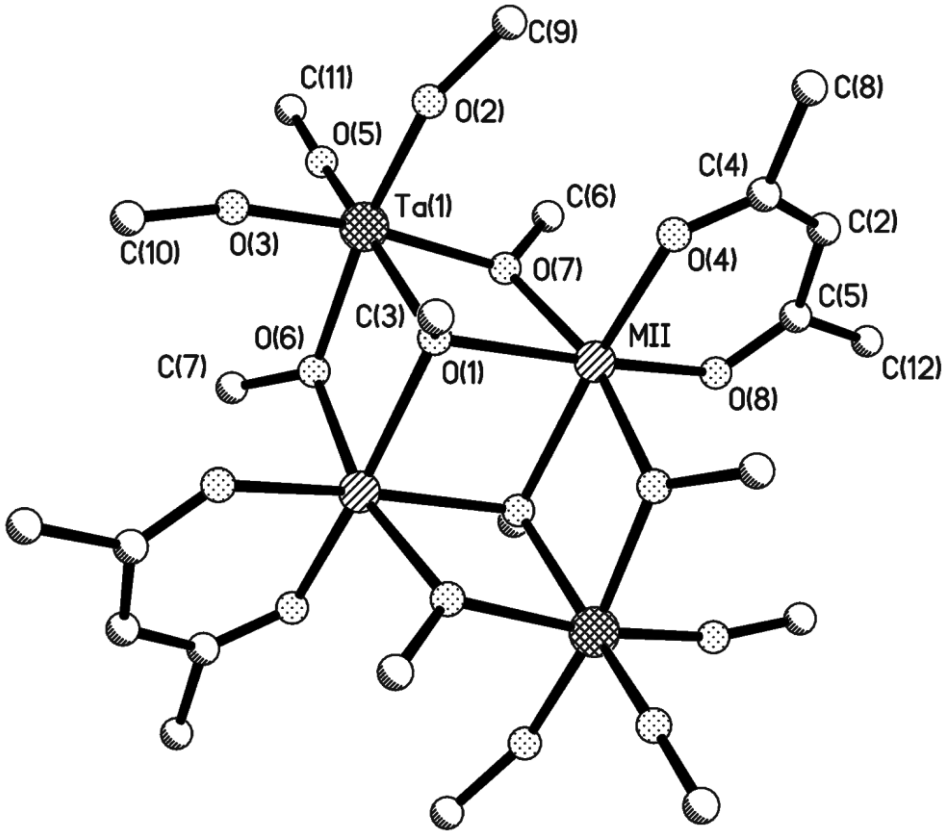

Figure 3.2 Molecular structure of $M_2Ta_2(acac)_2(OMe)_{12}$

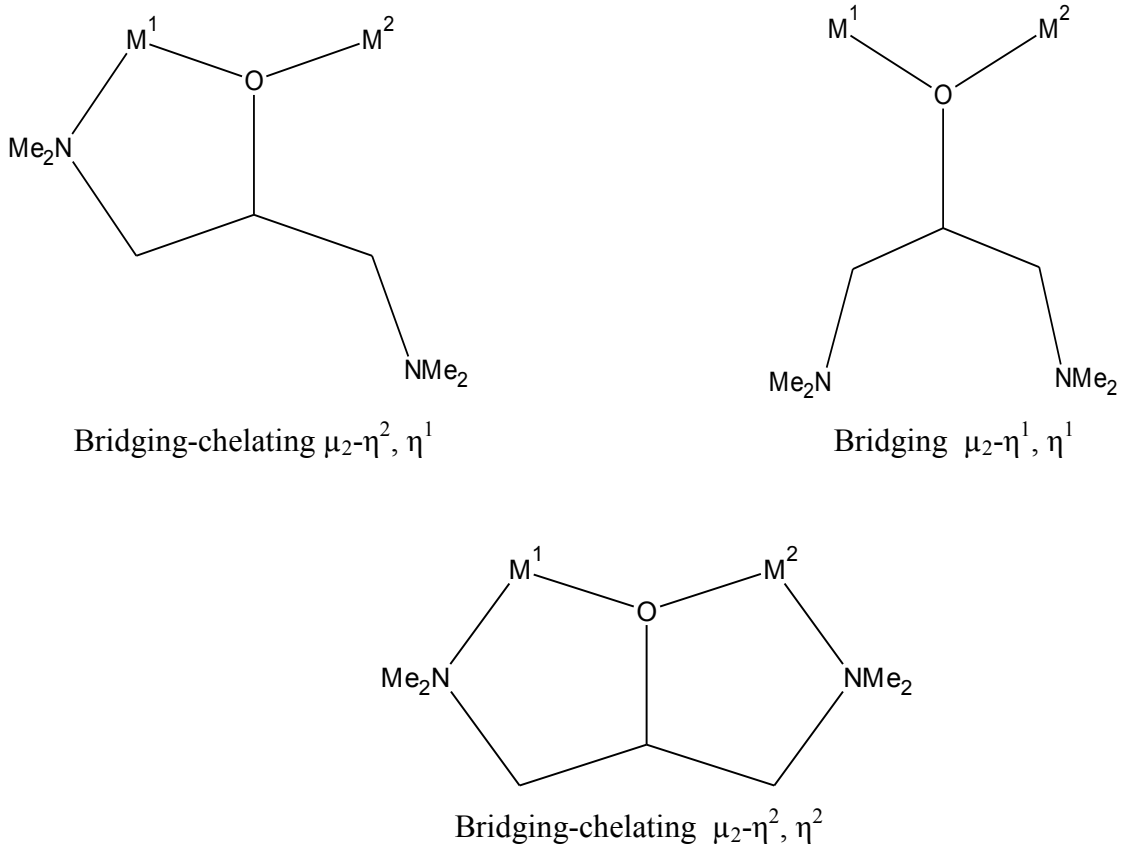

Figure 3.3 The different coordination mode of bdmap ligand

The tridentate and poly-functional amino-alkoxide -OCH[CH_2NMe_2]$_2$, called bdmap has been considered as a strong bridging ligand which shows the possibility to create one or two five membered chelate ring (Figure 3.3).[14-18] Hence, bdmap can adopt different coordination modes, the most common, being μ_2-η^2, η^2 which consists of a dinuclear unit.[19] This allows the synthesis of homo- and hetero-nuclear molecular precursor complexes, in particular for ceramic materials, superconductors, and magnetic materials due to the high solubility and volatility of the resulting compounds. Indeed, amino-alkoxides generally show higher solubility than metal alkoxides.[20] Hence, Hbdmap contains four methyl groups which would enhance the solubility of metal complexes in organic solvents. Besides, requirements for CVD imply the use of assembling ligands forming strong bridges between the metals in order to resist cleavage due to the high temperature during the CVD process. The LI-CVD of $Sr[Ta(OEt)_6]_2$ displays disproportionation of the precursor during its evaporation and transport due to the disparity in volatilities of the parent alkoxides. $Sr[Ta(OEt)_6]_2$ precursor also presents unsaturated sites which creates an unstability of the strontium metal center

towards moisture. The replacement of alkoxide groups by an amino-alcohol, such as dmae and bdmap produces, respectively, $Sr[Ta_2(OEt)_6(\mu_2\text{-}OEt)_4(\mu_2\text{-}dmae)_2]$ and $Sr[Ta_2(OEt)_6(\mu_2\text{-}OEt)_4(\mu_2\text{-}bdmap)_2]$ (Figure 3.4). The donor functionalization increases their stability and prevents them from disproportionation, leading to deposition of $SrTa_2O_6$.[21-23] Consequently, the chelating effect of the amino-alkoxide can be used as a strong bridge to link metals. The structure shows two bdmap ligands which are coordinated μ_2 to tantalum and strontium *via* oxygen and in a chelating manner η^2 to strontium from one nitrogen (Figure 3.4). This leaves in each case the remaining ligand nitrogen non-coordinated, as in related complexes with this ligand (Figure 3.5).

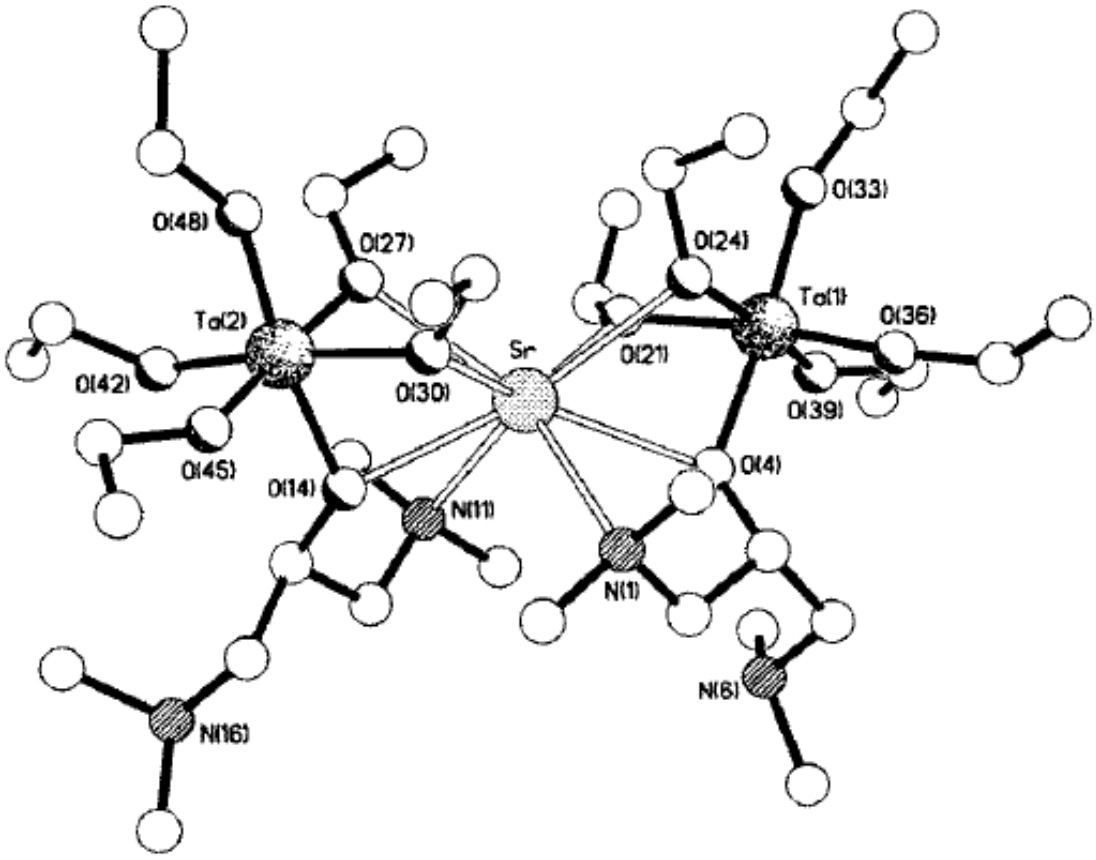

Figure 3.4 Molecular structure of $Sr[Ta_2(OEt)_6(\mu_2\text{-}OEt)_4(\mu_2\text{-}bdmap)_2]$

The reaction of $Cu(OMe)_2$ with bdmapH, as a strong bridging ligand and $Sr(O_2CCF_3)_2$ in ratio 2:3:1 produced $SrCu_2(bdmap)_3(O_2CCF_3)_3$ which shows a triangular arrangement of the metals. The bdmap ligand adopts two types of coordination mode: bridging-chelating $\mu_2\text{-}\eta^2, \eta^2$ and triply-bridging dangling $\mu_3\text{-}\eta^1, \eta^1$ as described as well in the figure 3.5.[24]

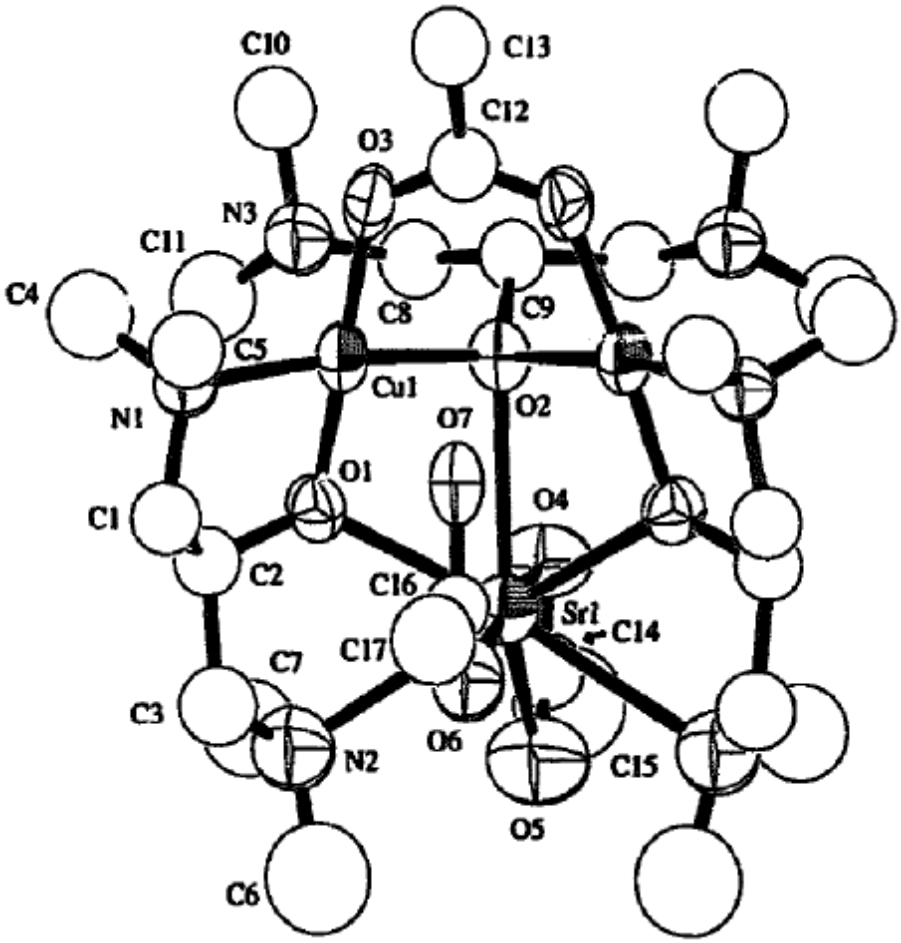

Figure 3.5 Molecular structure of $SrCu_2(bdmap)_3(O_2CCF_3)_3$.
For clarity, fluorine atoms are omitted

We now report the synthesis and characterisation of novel heteroleptic heterometallic species based on tungsten. First of all, this chapter will describe the synthesis and characterisation of heterobimetallic complexes based on the tungsten amino-alkoxide $W(O)(O^iPr)_3(bdmap)$ **(2)** containing a ligand playing the role of robust bridge between two different metals, such as metal alkoxide or diketonate. Secondly, another type of heterobimetallic complex, containing acetylacetonate and bridging methoxide ligands has been synthesised. Prior to the CVD applications, a preliminary study of the thermal behavior was also carried out to determine the stability and the materials obtained after pyrolysis. The thermal decomposition of these synthetic precursors in the air and under RAPET conditions is also presented, as outlined in chapter 2.

3.2 Results and discussion

3.2.1 Synthesis of heterobimetallic tungsten amino-alkoxides complexes

The synthesis of $WO(OPr^i)_3(bdmap)$ **(2)** established in chapter 2 was used as a starting material for the synthesis of the 1:1 adduct complex $WO(OPr^i)_3(bdmap):Ti(OPr^i)_4$. Unfortunately, the expected compound could not be characterised to confirm its formation in solution because the NMR spectra of the adduct complex, which form an oil, is identical to the NMR spectra of its individual components. Instead of obtaining the molecular structure of the adduct complex, colourless crystal of heterobimetallic tungsten amino-alkoxide $Ti_2W_2O_2(OPr^i)_6(\mu_2\text{-}O)_4(\mu_2\text{-}bdmap)_2$ **(7)** appeared in solution in presence of moisture. Based on this observation and the synthesis of polynuclear tungsten amino-alkoxide complexes **(4)**, **(5)** and **(6)** reported in the previous chapter, this reaction was subsequently repeated in order to control the micro-hydrolysis of $WO(OPr^i)_3(bdmap)$ in association with other metal complexes. Hence, the starting material $WO(OPr^i)_3(bdmap)$ **(2)** for the synthesis of **(7)** was used in association with other metal complexes $M(OR)_x$, such as $Ti(OPr^i)_4$, $Al(OPr^i)_3$ and $Zn(acac)_2$ to give respectively $Ti_2W_2O_2(OPr^i)_6(\mu_2\text{-}O)_4(\mu_2\text{-}bdmap)_2$ **(7)**, $Al_2W_2O_2(OPr^i)_2(\mu_2\text{-}O)_4(\mu_2\text{-}bdmap)_4$ **(8)** and $Zn_2W_2O_2(OPr^i)_2(\mu_2\text{-}O)_6(acac)_2(\mu_2\text{-}bdmap)_2$ **(9)**, [Eq.(3.2), (3.3) and (3.4)] in presence of moisture.

Hydrolysis studies have been investigated in order to obtain a reproducible preparation route. The crude product **(2)** was dissolved and hydrolysed in a 4:1 mixture of anhydrous toluene and isopropanol at 0°C in a controlled way by adding a water-isopropanol solution (2 mL) through a syringe over a period of 2-3 h under vigorous stirring. The diminution of temperature and the presence of the parent alcohol of the metal isopropoxide (2-propanol) permit, respectively, slow hydrolysis reaction and homogenisation of the solution in order to prevent precipitation of insoluble oxides. Indeed, the hydrolysis products were isolated from a mixture of solution having the hydrolysis ratio, $h = [H_2O]/\{[WO(OPr^i)_3bdmap] + [M(OR)_x]\} \sim 1$. After allowing the reaction medium to warm up, it was stirred for 20 h at R.T, and then refluxed for 24h. The solution was filtered and then was concentrated to afford a viscous liquid which was re-dissolved in the smallest amount of warm hexane. After cooling down to R.T and then to – 20°C for a few days, the colourless crystals were separated by filtration, washed carefully three times with cold hexane and dried *in vacuo*.

$$2\ WO(OPr^i)_3bdmap + 2\ Ti(OPr^i)_4 \xrightarrow[-\ 8\ ^iPrOH]{4\ H_2O} Ti_2W_2O_2(OPr^i)_6(\mu_2\text{-}O)_4(\mu_2\text{-}bdmap)_2 \quad (3.2)$$
(7)

$$2\ WO(O^iPr)_3bdmap + 2\ Al(OPr^i)_3 \xrightarrow[-\ 4\ ^iPrOH\ -\ acacH]{4\ H_2O} Al_2W_2O_2(O^iPr)_2(\mu_2\text{-}O)_4(\mu_2\text{-}bdmap)_4 \quad (3.3)$$
(8)

$$2\ WO(OPr^i)_3bdmap + 2\ Zn(acac)_2 \xrightarrow[-\ 10\ ^iPrOH]{2\ Hbdmap\ 4\ H_2O} Zn_2W_2O_2(OPr^i)_2(\mu_2\text{-}O)_3(acac)_2(\mu_2\text{-}bdmap)_2 \quad (3.2)$$
(9)

Compound **(10)** has been produced adventitiously by reaction of $Ni(dmap)_2$ with $WO(OMe)_4$ in hot toluene. The resulting oil recrystallised from a mixture hexane/toluene (1:3); the microhydrolysis [Eq.(3.5)] of the mixture gave rise, after several weeks, to crystals of $[Ni(dmap)_2WO_2(OMe)_2]_4$ **(10)**.

$$4\ WO(OMe)_4 + 4\ Ni(dmap)_2 \xrightarrow[-\ 8\ MeOH]{4\ H_2O} [Ni(dmap)_2(\mu_2\text{-}O)WO(OMe)_2]_4 \quad (3.3)$$
(10)

All these compounds has been characterised by X-ray crystallography. Compounds **(7)** and **(9)** have also been characterised by NMR spectrocopy and micro-analysis. The NMR analysis has not been performed on **(8)** and **(10)** due to, respectively, the small amount obtained during the micro-hydrolysis and the paramagnetism of the compound **(10)**.

3.2.1.1 Crystal structures

Compound $Ti_2W_2O_2(O^iPr)_6(\mu_2\text{-}O)_4(\mu_3\text{-}bdmap)_2$ **(7)** crystallizes in the monoclinic space group $P2_1/n$ with unit-cell parameters, a = 12.05500(10), b = 18.28200(10), c = 21.54500(10) Å, β = 97.78°. The selected bond lengths and angles of **(7)** (Figure 3.6) are displayed in the Table 3.1. The structure is a tetranuclear cage with two tungsten and two titanium atoms forming a tetrahedron via four bridging oxygen atoms. Similarly to $W_4O_4(\mu_2\text{-}O)_6(tdmap)_4$ **(4)** (Figure 2.6), the asymmetric unit cell with a central $W_2Ti_2O_6$ core possesses the adamantane-like structure.

The metals (M), tungsten (W) and titanium (Ti), possess distorted octahedral geometries (C.N = 6) with MO_5N coordination. Hence, the *trans* angles of W(1), [O(3)-W(1)-O(8)], [O(7)-W(1)-O(1)] and [O(1)-W(1)-N(2)] are respectively 157.95(10)°, 162.58(9)° and 170.87(9)°. Also, the *trans* angles of Ti(1), [O(12)-Ti(1)-O(1)], [O(11)-Ti(1)-O(5)] and [O(6)-Ti(1)-N(2)] are respectively 155.86(10)°, 166.39(10)° and 172.45(10)°.

Moreover, the longest bond W(1)-N(1) belonging to the chelating bdmap ligand with a distance of 2.384(3) Å is in *trans* position to the short bridging μ_2, η^2-oxo bond W(1)-O(2) [1.773(2) Å]. The bridging μ_2-oxo bond W(1)-O(3) [1.924(2) Å] is *trans* to the terminal alkoxo bond W(1)-O(8) [1.931(2) Å]. The shortest bond W(1)=O(7) [1.720(2) Å] is in *trans* position to the doubly bridging μ_2-O(1) belonging to the bdmap ligand W(1)-O(1) [2.166(2) Å]. Concerning the titanium atom Ti(1), the Ti(1)-N(1) bond is in *trans* position to the bridging μ_2-oxo bond Ti(1)-O(6) [1.809(2) Å]. And the terminal alkoxo bonds Ti(1)-O(11) [1.820(2) Å] and Ti(1)-O(12) [1.829(2) Å] are *trans* respectively to Ti(1)-O(5) [2.088(2) Å] and Ti(1)-O(1) [2.186(2) Å]. As illustrated by the structures **(4)-(6)** (cf. section 2.2.2.1), the phenomenon of bond lengthening *trans* to strong π-donor is also observed in **(7)** for both metals.

Contrary to **(4)**, the oxygen atom O(1) of the bdamp ligand participates in the formation of the $Ti_2W_2O_4$ core by bridging symmetrically Ti(1) to W(1). Also, O(1) has a bent geometry according to the angle W(1)-O(1)-Ti(1) [125.38(9)°]. Moreover, the bond W(1)-O(1) belonging to the bdmap amino-alkoxide [2.166 Å] is longer than those found in **(4)**, **(5)** and **(6)** which are respectively 1.911(2), 1.937(7) and 1.904(7) Å. Thus, the stretching of W(1)-O(1) in **(7)** is partially due to the change of the coordination mode of the amino-alkoxide ligand (μ_1-η^1,η^2) found in the polynuclear homometallic complexes **(4)-(6)** which becomes (μ_2-η^2,η^2) in the structure **(7)**. This corroborates also the difference of bond length between the diverse coordination modes. Subsequently, the W-O and Ti-O bond lengths display distances increasing in the order μ_1-OR > μ_2-OR > μ_3-OR.[25, 26]

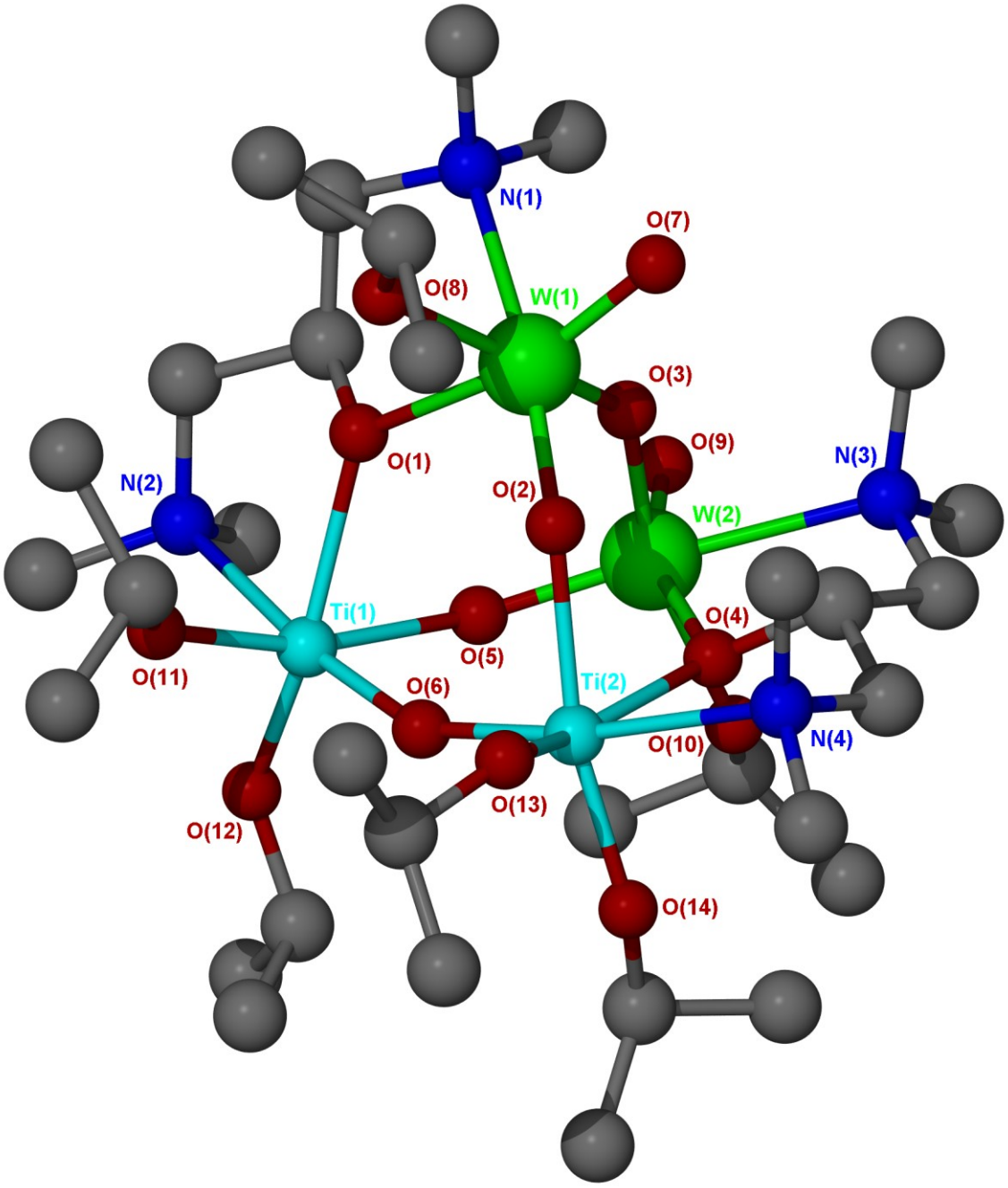

Figure 3.6 Molecular structure of $Ti_2W_2O_2(OPr^i)_6(\mu_2\text{-}O)_4(\mu_2\text{-}bdmap)_2$ **(7)**

Table 3.1 Selected bond lengths (Å) and angles (º) of **(7)**

Bond lengths			
W(1)-O(1)	2.166(2)	W(1)-O(2)	1.773(2)
W(1)-O(3)	1.924(2)	W(1)-O(7)	1.720(2)
W(1)-O(8)	1.931(2)	W(1)-N(1)	2.384(3)
Ti(1)-O(1)	2.186(2)	Ti(1)-O(5)	2.088(2)
Ti(1)-O(6)	1.809(2)	Ti(1)-O(11)	1.829(2)
Ti(1)-O(12)	1.820(2)	Ti(1)-N(2)	2.353(3)
W(2)-O(3)	1.913(2)	W(2)-O(4)	2.178(2)
W(2)-O(5)	1.772(2)	W(2)-O(9)	1.724(2)
W(2)-O(10)	1.927(2)	W(2)-N(3)	2.413(3)
Ti(2)-O(2)	2.053(2)	Ti(2)-O(4)	2.198(2)
Ti(2)-O(6)	1.822(2)	Ti(2)-O(13)	1.816(2)
Ti(2)-O(14)	1.812(2)	Ti(2)-N(4)	2.328(3)
Bond angles			
O(7)-W(1)-O(2)	102.44(10)	O(7)-W(1)-O(3)	97.01(10)
O(2)-W(1)-O(3)	95.76(9)	O(7)-W(1)-O(8)	95.89(10)
O(2)-W(1)-O(8)	98.84(10)	O(3)-W(1)-O(8)	157.95(10)
O(7)-W(1)-O(1)	162.58(9)	O(2)-W(1)-O(1)	94.98(8)
O(3)-W(1)-O(1)	80.72(8)	O(8)-W(1)-O(1)	81.62(8)
O(7)-W(1)-N(1)	86.60(10)	O(2)-W(1)-N(1)	170.87(9)
O(3)-W(1)-N(1)	81.67(9)	O(8)-W(1)-N(1)	81.33(9)
O(1)-W(1)-N(1)	75.99(8)	O(6)-Ti(1)-O(12)	101.97(11)
O(6)-Ti(1)-O(11)	98.65(10)	O(12)-Ti(1)- O(11)	99.50(11)
O(6)-Ti(1)-O(5)	86.69(10)	O(12)-Ti(1)-O(5)	91.54(10)
O(11)-Ti(1)-O(5)	166.39(10)	O(6)-Ti(1)-O(1)	98.77(9)
O(12)-Ti(1)-O(1)	155.86(10)	O(11)-Ti(1)- O(1)	89.38(9)
O(5)-Ti(1)-O(1)	77.40(8)	O(6)-Ti(1)-N(2)	172.45(10)
O(12)-Ti(1)-N(2)	81.63(11)	O(11)-Ti(1)-N(2)	87.19(10)
O(5)-Ti(1)-N(2)	86.58(9)	O(1)-Ti(1)-N(2)	76.40(9)
W(1)-O(1)-Ti(1)	125.38(9)	W(1)-O(2)-Ti(2)	147.79(12)
W(2)-O(3)-W(1)	140.39(11)	W(2)-O(4)-Ti(2)	125.90(9)
W(2)-O(5)-Ti(1)	143.84(12)	Ti(1)-O(6)-Ti(2)	153.31(13)
C(15)-O(8)-W(1)	124.6(2)	C(21)-O(11)-Ti(1)	132.5(2)

$[AlWO(OPr^i)(\mu_2\text{-}O)_2(\mu_2\text{-}bdmap)_2]_2$ **(8)**, which is centrosymmetric, crystallizes in the triclinic space group $P\bar{1}$ with the unit cell parameters: a = 12.6590 (3), b = 13.5940 (3), c = 15.3670 (4) Å, α = 73.1920 (10)°, β = 83.0070 (10)°, γ = 80.3920 (10)°, Z = 2. Compound **(8)** contains two equivalent molecules in the asymmetric unit, only one of which is discussed in detail (Figure 3.7). The selected bond lengths and angles of **(8)** are displayed in Table 3.2. Figure 3.7 displays a cube-like structure with two tungsten and two aluminium atoms, situated in the same plane which formed a square-like arrangement. Each μ_2-oxo bridging and bridging-chelating μ_2-η^2,η^1 bdamp ligand participate in the formation of $W_2Al_2O_6$ core.

The remaining oxo-bridges generate the shape of a pseudo-cube with two edges missing, forming thus the $W_2Al_2O_6$ core depicted. The tetrahedral structure illustrated for **(7)** in Figure 3.6 shows the same type of $M_2W_2O_6$ core in terms of the number of atomic elements but presents a different arrangement. So, the tetrahedral core from the previous structure $Ti_2W_2O_6$ and cube-like core $Al_2W_2O_6$ can be considered as isomers.

This structure is composed of two octahedral tungsten atoms (C.N = 6) with WO_5N coordination and two five-coordinate aluminium atoms of AlO_4N coordination sphere. The latter may exist as both square pyramidal (sp) and trigonal bipyramidal (tbp). The conversion from one stereochemistry to another can occur by a Berry pseudorotation.[27, 28] The distinction between both conformers is however difficult. Indeed, it appears that the structure of the aluminium atom is distorted, resulting in an intermediate isomer between the two ideal geometries (sp) and (tbp). Nevertheless, the aluminium atoms can be considered as a distorted trigonal bipyramidal with N(3) and O(4) occupying the axial positions with a *trans* axial angle of 156.9(4)°; the axial–equatorial *cis* angles are in the range 79.4(3)–102.0(3)° and the equatorial–equatorial *cis* angles O(6)-Al(1)-O(3), O(5)-Al(1)-O(6) O(5)-Al(1)-O(3) are respectively 109.2(3),115.3(4) and 134.7(4).

The coordination geometry of tungsten is also distorted. Indeed, the *trans* angles surrounding W(1), O(4)-W(1)-O(1), O(2)-W(1)-O(3), O(6')-W(1)-N(1) are respectively 146.9(3)°, 166.8(3)° and 167.9(3)°. The shortest bond length which is W(1)=O(2) with a distance of 1.717(7) Å is in the *trans* position to the oxygen O(3) belonging to the bridging-chelating bdmap ligand. As previously said for **(7)**, the terminal oxo ligand O(2) gives rise to the lengthening of W(1)-O(3) [2.260(7) Å] by strong *trans* influence. The longest bond W(1)-N(1) [2.397(9) Å] is also in the *trans* position to the bond W(1)-O(6') [1.818(7) Å] involving a reduced double bond character. These values are consistent with those found in **(7)**. The metals are bridged vertically by two oxo-bridges [O(6), O(6')] and horizontally bonded by two oxo-bridges [O(3), O(4)] on each pseudo-square base. The bond lengths Al(1)-O(5) [1.739(8) Å] and Al(1)-O(3) [1.829(7) Å] are consistent respectively with those seen in the terminal isopropoxide ligand of $[Al(OPr^i)_2(acac)]_3$,[29] and the doubly bridging-chelating μ_2, η^2-O bonded to the aluminium atom in the compound $[EtAl(OC_5H_{12}N)Cl]_2$.[30] The bond angle Al(1)-O(3)-W(1) [96.8(3)°] indicates that O(3) has a bent geometry. The bond lengths W(1)-O(3) [2.260(7) Å] and Al(1)-O(3) [1.829(7) Å] reveals that Al(1) and W(1) are bridged asymmetrically via O(3); but more symmetrically via O(4), as depicted by the bond lengths W(1)-O(4), 1.811(7) Å and Al(1)-O(4), 1.886(8) Å.

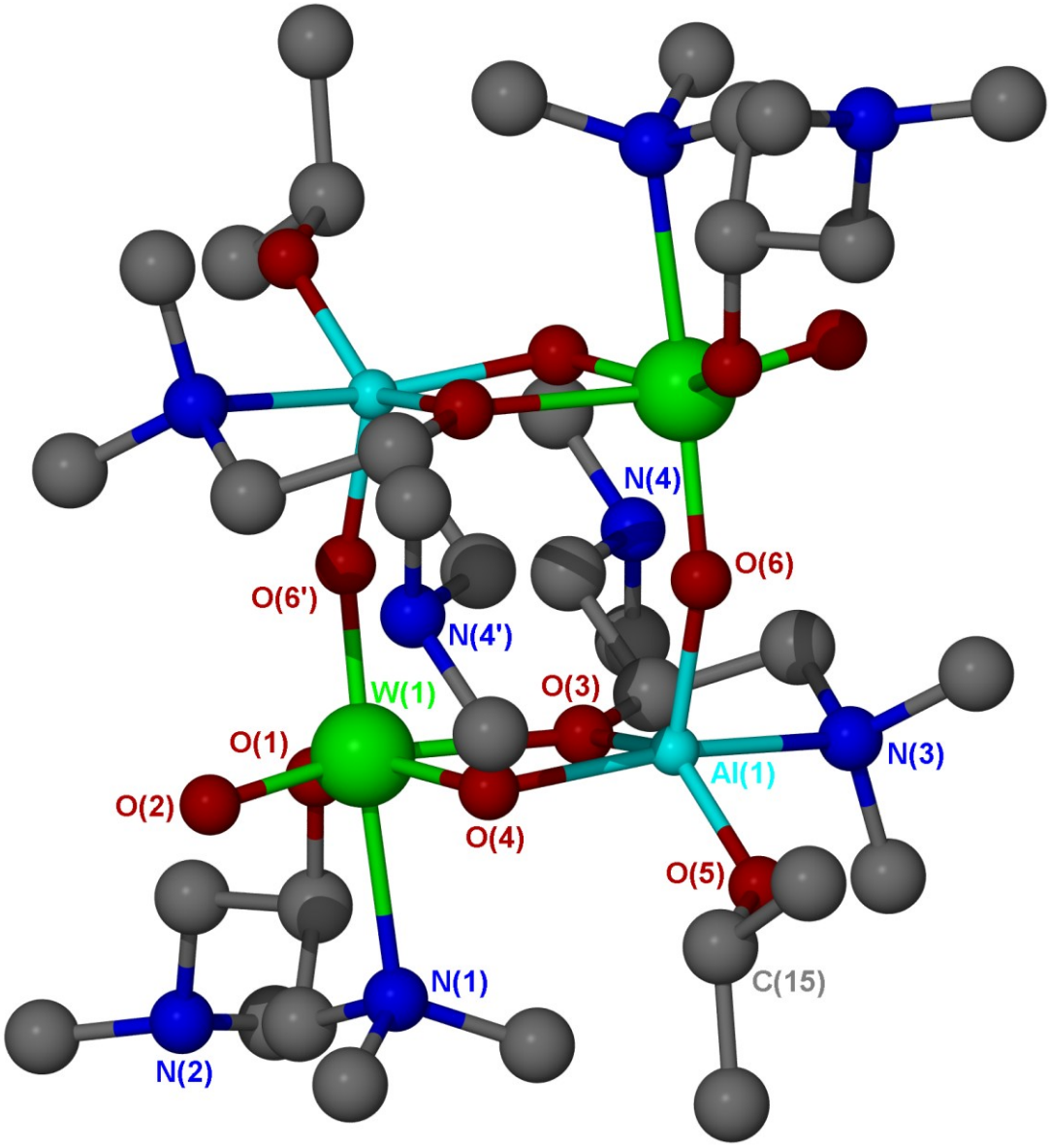

Figure 3.7 Molecular structure of $Al_2W_2O_2(OPr^i)_2(\mu_2\text{-}O)_4(\mu_3\text{-}bdmap)_4$ **(8)**

In addition, the dative bond Al(1)-N(3) of distance 2.143(9) Å is comparable to the dative bond found in other five-coordinated aluminium metal centres.[30, 31]

The type of coordination mode of bdmap changes from a bridging-chelating μ_2-η^2, η^2 for **(7)** to a bridging-chelating μ_2-η^2, η^1 for **(8)**. We note as well the bond length variation within the $AlWO_2$ ring (cf. Figure 3.8). Indeed, the bond length W(1)-O(4) [1.811(7) Å] in **(8)** which is quite short for a μ_2-oxo-bridging metals,[32] is consistent with a double bond character.

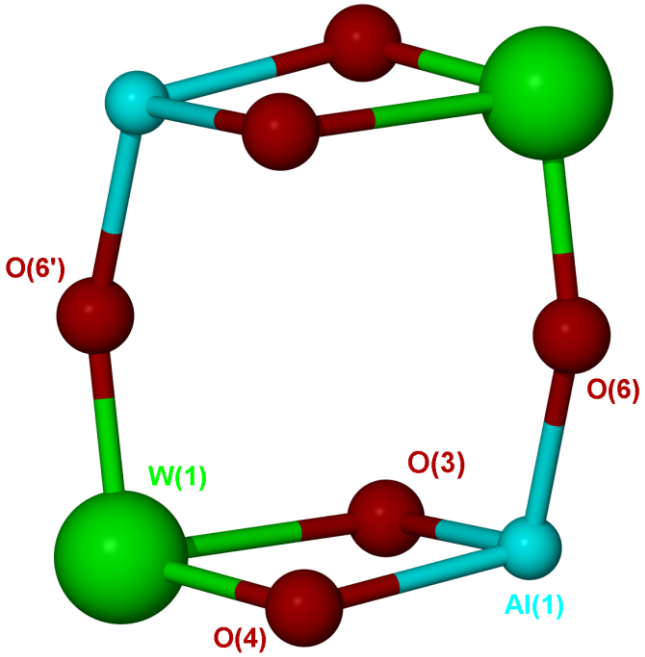

Figure 3.8 Molecular structure of $W_2Al_2O_6$ core in **(8)**

Table 3.2 Selected bond lengths (Å) and angles (°) of $Al_2W_2O_2(OPr^i)_2(\mu_2\text{-}O)_4(\mu_3\text{-}bdmap)_4$ **(8)**

Bond lengths			
W(1)-O(2)	1.717(7)	W(1)-O(4)	1.811(7)
W(1)-O(1)	1.923(7)	W(1)-O(3)	2.260(7)
W(1)-N(1)	2.397(9)	W(1)O(6')	1.818(7)
Al(1)-O(5)	1.739(8)	Al(1)-O(6)	1.778(8)
Al(1)-O(3)	1.829(7)	Al(1)-O(4)	1.886(8)
Al(1)-N(3)	2.143(9)		
Bond angles			
O(2)-W(1)-O(4)	100.2(3)	O(2)-W(1)-O(1)	102.3(3)
O(4)-W(1)-O(1)	146.9(3)	O(2)-W(1)-O(3)	166.8(3)
O(4)-W(1)-O(3)	70.3(3)	O(1)-W(1)-O(3)	83.0(3)
O(2)-W(1)-N(1)	86.4(3)	O(4)-W(1)-N(1)	83.4(3)
O(1)-W(1)-N(1)	74.2(3)	O(3)-W(1)-N(1)	83.5(3)
O(6')-W(1)-N(1)	167.9(3)	O(5)-Al(1)-O(3)	134.7(4)
O(6)-Al(1)-O(3)	109.2(3)	O(5)-Al(1)-O(4)	98.5(4)
O(6)-Al(1)-O(4)	102.0(3)	O(3)-Al(1)-O(4)	79.4(3)
O(5)-Al(1)-N(3)	88.8(4)	O(6)-Al(1)-N(3)	94.4(4)
O(3)-Al(1)-N(3)	79.9(3)	O(4)-Al(1)-N(3)	156.9(4)
O(5)-Al(1)-O(6)	115.3(4)	W(1)-O(4)-Al(1)	112.4(4)
Al(1)-O(3)-W(1)	96.8(3)	C(15)-O(5)-Al(1)	127.3(7)

Symmetry transformations used to generate equivalent atoms (‘): 3-x, -y, 1-z

Compound $Zn_2W_2O_2(OPr^i)_2(\mu_2\text{-}O)_3(acac)_2(\mu_2\text{-}bdmap)_2$ **(9)**, crystallizes in the trigonal, space group *R*3*c* with the unit-cell parameters, a = b = 41.4763(4), c = 13.47590(10) Å, α = β = 90°, γ = 120°. The selected bond lengths and angles in relation to structure **(9)** (Figure 3.9) are displayed in the Table 3.3.

(9) is related to the adamatane-like structure found in **(4)** and **(7)** by loss of one bridging oxygen. Hence, the structure is an open tetranuclear heterobimetallic cage with two tungsten and two zinc atoms forming a pseudo tetrahedron with only three μ_2-oxo and two μ_2-bdamp ligand bridging each of the four metals (Figure 3.9). Indeed, the two zinc atoms are not bonded between each other by an oxo-bridge, like in the case of **(7),** which shows all four metals are bridged by four μ_2-oxo ligands and two bridging amino-alkoxide μ_2, η^2-bdmap.

(9) is composed of two octahedral tungsten geometries (WO_5N) which are distorted and two zinc atoms (C.N = 5) with ZnO_5 coordination spheres which have distorted trigonal pyramidal coordination geometries. The description of the structure will be emphasized mainly around W(1) and Zn(1) due to the similarities of the bond lengths and angles of each identical metal centre. The *trans* bond angles of W(1) [O(5)-W(1)-O(2)], [O(1)-W(1)-O(3)] and [O(4)-W(1)-N(1)] are respectively 161.79(17)°, 159.68(18)° and 167.42(18)°.

The shortest bond length W(1)=O(1) of distance 1.717(7) Å corresponds to the terminal oxo-ligand is in a *trans* position to the μ_2-O(3) bridging Zn(1) and W(1); the bond length W(1)-O(3) is 2.147(4) Å. The longest bond W(1)-N(1) [2.390(5) Å], is in *trans* position to the short bond W(1)-O(4) [1.760(4) Å], which have a reduced bond character. This reveals the phenomenon of *trans* influence. The [C(8)-O(2)-W(1)] bond angle [132.4(4)°] and the W(1)-O(2) bond length [1.915(4) Å] of the methoxide ligand are in agreement with those found in related tungsten oxo-tetra-alkoxides.[33] The shortest bond length which is W(1)=O(2) with a distance of 1.717(7) Å is in *trans* position to the oxygen O(3) belonging to the chelating-bridging bdmap ligand.

All these bond angles and lengths values are consistent with the values found for the structure **(7)**. As already observed in **(7)**, the bdamp ligand which participates in the formation of $W_2Zn_2O_5$ core possesses a μ_2-η^2, η^2 coordination mode.

The zinc metals Zn(1) and Zn(2) adopt distorted trigonal bipyramidal geometries. The *trans* axial angle of Zn(1) [O(6)-Zn(1)-O(3)] is 172.4(2)°; the axial – equatorial *cis* angles are in the range 83.21(18)° – 95.32(19)° and the equatorial–equatorial *cis* angles [O(8)-Zn(1)-N(2)], [O(7)-Zn(1)-N(2)] and [O(7)-Zn(1)-O(8)] are respectively 129.1(2)°, 121.6(2)° and 109.30(19)°. The bond Zn(1)-N(2) of distance 2.144(5) Å is in agreement with the Zn-N bond length found in the tetra-zinc cluster $[Zn_4Li(\mu_4\text{-}O)(\mu_2\text{-}NEt)_5(\mu_2\text{-}NEt(CHCH_2)_2]$.[34]

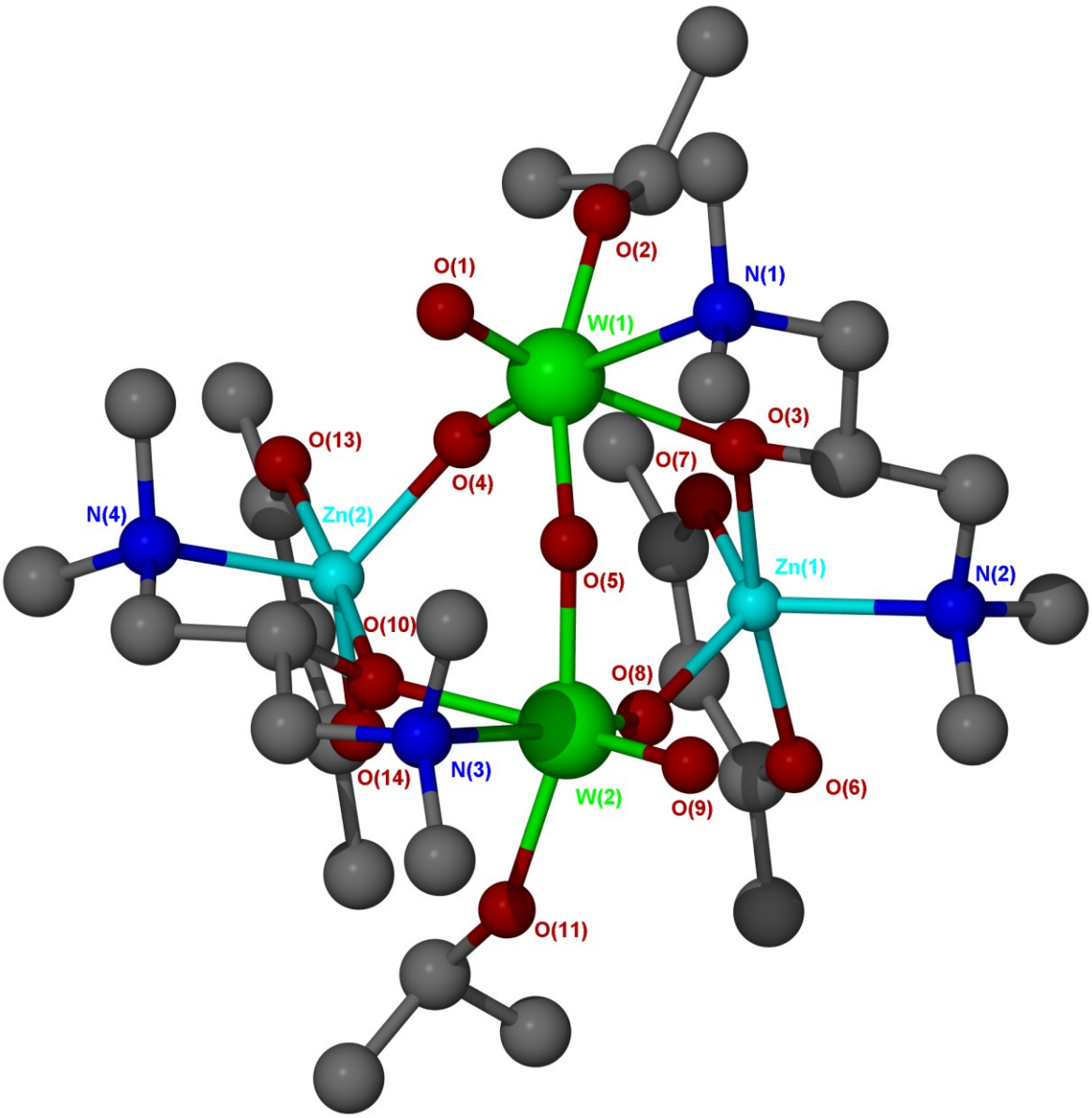

Figure 3.9 Molecular structure of $Zn_2W_2O_2(O^iPr)_2(acac)_2(\mu_2\text{-}O)_3(\mu_2\text{-}bdmap)_2$ **(9)**

On each zinc centre, the bidentate acetylacetonate [O(6), O(7)]-donor and [O(13), O(14)]-donor ligands forms two six-membered chelate ring. In the acetylacetonate ring ZnO_2, the bond Zn-O of distances 2.066(5) and 1.951(5) Å which correspond respectively to the bonds Zn(1)-O(6) and Zn(1)-O(7) match with the bonds seen in bis(acetylacetonate) zinc.[35] The tridentate amino-alkoxide (bdmap) comprising [O(3), N(1), N(2)]-donors and [O(10), N(3), N(4)]-donors ligands produce two five-membered chelate rings on each of tungsten and zinc. The metals Zn(1) and W(1), as also displayed in **(7)**, are bridged symmetrically by μ_2-O(3) which has a bent geometry. Hence, this is illustrated in the bond lengths Zn(1)-O(3) [2.093(4)°], W(1)-O(3) [2.147(4) Å] and the bond angle Zn(1)-O(3)-W(1) which is 106.6(3)°.

Table 3.3 Selected bond lengths (Å) and angles (º) of **(9)**

Bond lengths			
W(1)-O(1)	1.724(4)	W(1)-O(2)	1.915(4)
W(1)-O(3)	2.147(4)	W(1)-O(4)	1.760(4)
W(1)-O(5)	1.915(4)	W(1)-N(1)	2.390(5)
W(2)-O(5)	1.916(4)	W(2)-O(8)	1.765(4)
W(2)-O(9)	1.733(4)	W(2)-O(10)	2.110(4)
W(2)-O(11)	1.923(4)	W(2)-N(3)	2.430(5)
Zn(1)-O(3)	2.093(4)	Zn(1)-O(6)	2.066(5)
Zn(1)-O(7)	1.951(5)	Zn(1)-O(8)	1.983(4)
Zn(1)-N(2)	2.144(5)	Zn(2)-O(4)	1.972(4)
Zn(2)-O(10)	2.113(4)	Zn(2)-O(13)	2.044(5)
Zn(2)-O(14)	1.958(5)	Zn(2)-N(4)	2.117(6)
Bond angles			
O(1)-W(1)-O(4)	106.9(2)	O(1)-W(1)-O(5)	93.66(18)
O(4)-W(1)-O(5)	95.04(17)	O(1)-W(1)-O(2)	96.11(19)
O(4)-W(1)-O(2)	96.77(19)	O(5)-W(1)-O(2)	161.79(17)
O(1)-W(1)-O(3)	159.68(18)	O(4)-W(1)-O(3)	93.08(17)
O(5)-W(1)-O(3)	80.67(15)	O(2)-W(1)-O(3)	84.88(16)
O(1)-W(1)-N(1)	85.64(19)	O(4)-W(1)-N(1)	167.42(18)
O(5)-W(1)-N(1)	83.07(17)	O(2)-W(1)-N(1)	82.39(18)
O(3)-W(1)-N(1)	74.35(16)	O(9)-W(2)-O(8)	106.5(2)
O(5)-W(2)-O(11)	161.71(16)	O(9)-W(2)-O(10)	157.65(18)
O(7)-Zn(1)-O(8)	129.1(2)	O(8)-Zn(1)-O(6)	89.8(2)
O(7)-Zn(1)-O(3)	95.32(19)	O(8)-Zn(1)-O(3)	91.03(16)
O(8)-Zn(1)-N(2)	109.30(19)	O(6)-Zn(1)-N(2)	89.4(2)
O(3)-Zn(1)-N(2)	83.21(18)	O(13)-Zn(2)-O(10)	173.0(2)
O(4)-Zn(2)-N(4)	110.0(2)	C(3)-N(1)-C(1)	110.0(5)
C(3)-N(1)-C(2)	109.2(5)	C(1)-N(1)-C(2)	107.1(5)
C(3)-N(1)-W(1)	107.7(4)	C(1)-N(1)-W(1)	111.6(3)
C(2)-N(1)-W(1)	111.3(4)	C(7)-N(2)-C(5)	111.0(5)
C(7)-N(2)-C(6)	109.0(5)	C(5)-N(2)-Zn(1)	110.6(5)
C(7)-N(2)-Zn(1)	107.6(4)	C(4)-O(3)-Zn(1)	106.0(3)
C(6)-N(2)-Zn(1)	112.7(5)	Zn(1)-O(3)-W(1)	106.6(3)
C(4)-O(3)-W(1)	115.3(3)	W(1)-O(5)-W(2)	124.41(18)
W(1)-O(4)-Zn(2)	145.8(2)	C(14)-O(7)-Zn(1)	140.3(2)
C(12)-O(6)-Zn(1)	124.6(6)	W(2)-O(10)-Zn(2)	126.1(5)
W(2)-O(8)-Zn(1)	144.3(2)	O(6)-Zn(1)-O(3)	172.4(2)

The compound $[Ni(\mu_2,\eta^2\text{-}OR)_2(\mu_2\text{-}O)WO(\mu_2\text{-}OMe)(OMe)]_4$ **(10)** [-OR = dmap, R = $-CH(CH_3)CH_2NMe_2$] crystallizes in the tetragonal space group $P4_2/n$ with unit-cell parameters: a = b = 16.037 Å, c = 15.223 Å, Z = 2 (Figure 3.10). Selected bond lengths and angles in relation to structure **(10)** are displayed in the Table 3.4. The asymmetric unit consists of one $[Ni(\mu_2\text{-}\eta^2\text{-}OR)_2(\mu_2\text{-}O)WO(\mu_2\text{-}OMe)(OMe)]$ with the remainder of the tetramer generated by symmetry.

Compound $[Ni(dmap)_2(\mu_2\text{-}O)WO(OMe)_2]_4$ **(10)** is a tetramer which adopts a square-like structure. This complex is composed of one tungsten and nickel metal in each of the four monomers. The description of monomer will be emphasized around W and Ni due to the equivalence of the bond length and angles of each identical asymmetric unit.

The systems of WO_6 and NiO_4N_2 octahedra (C.N = 6) have distorted geometries. The *trans* angles surrounding W [O(4)-W-O(3)],[O(5)-W-O(1)] and [O(6)-W-O(2)] are 155.30(13)°, 168.89(14)°, and 161.29(15)°. Concerning the nickel atom, the *trans* angles surrounding Ni [O(1)-Ni-O(5')], [O(2)-Ni-N(1)] and [N(2)-Ni-O(3)] are 169.79(14)°, 162.40(18)°, and 153.88(14)°.

Ni and W are bridged by two amino-alkoxides $[\mu_2,\eta^2\text{-}O(1)]$, $[\mu_2,\eta^2\text{-}O(2)]$ and one methoxide ligand $[\mu_2\text{-}O(3)]$. The N(1), N(2) and O(1),O(2)-donors of both dmap amino-alkoxides ligand form two five-membered chelate rings on the nickel atoms. The bond lengths Ni-N(1) and Ni-N(2) which are respectively 2.122(5) and 2.180(4) Å are in agreement with those found in a heterobimetallic Ni-Cu amino-alkoxide.[20]

About the doubly bridging methoxide, the bond length W-O(3) of distance 2.001(3) Å is in *trans* position to terminal methoxide W-O(4) [1.919(3) Å]. The bond length W-O(2) [2.153(3) Å] is in *trans* position to the shortest bond length W-O(6) [1.727(3) Å] which matches with a terminal oxo ligand.[33] The long bond Ni-O(5) [2.033(3) Å] is in *trans* position to W-O(5) [1.763(3) Å]. Hence, the bridging O(5) has a π-bonding character indicating the phenomenon of *trans* influence, already described in the previous structures.

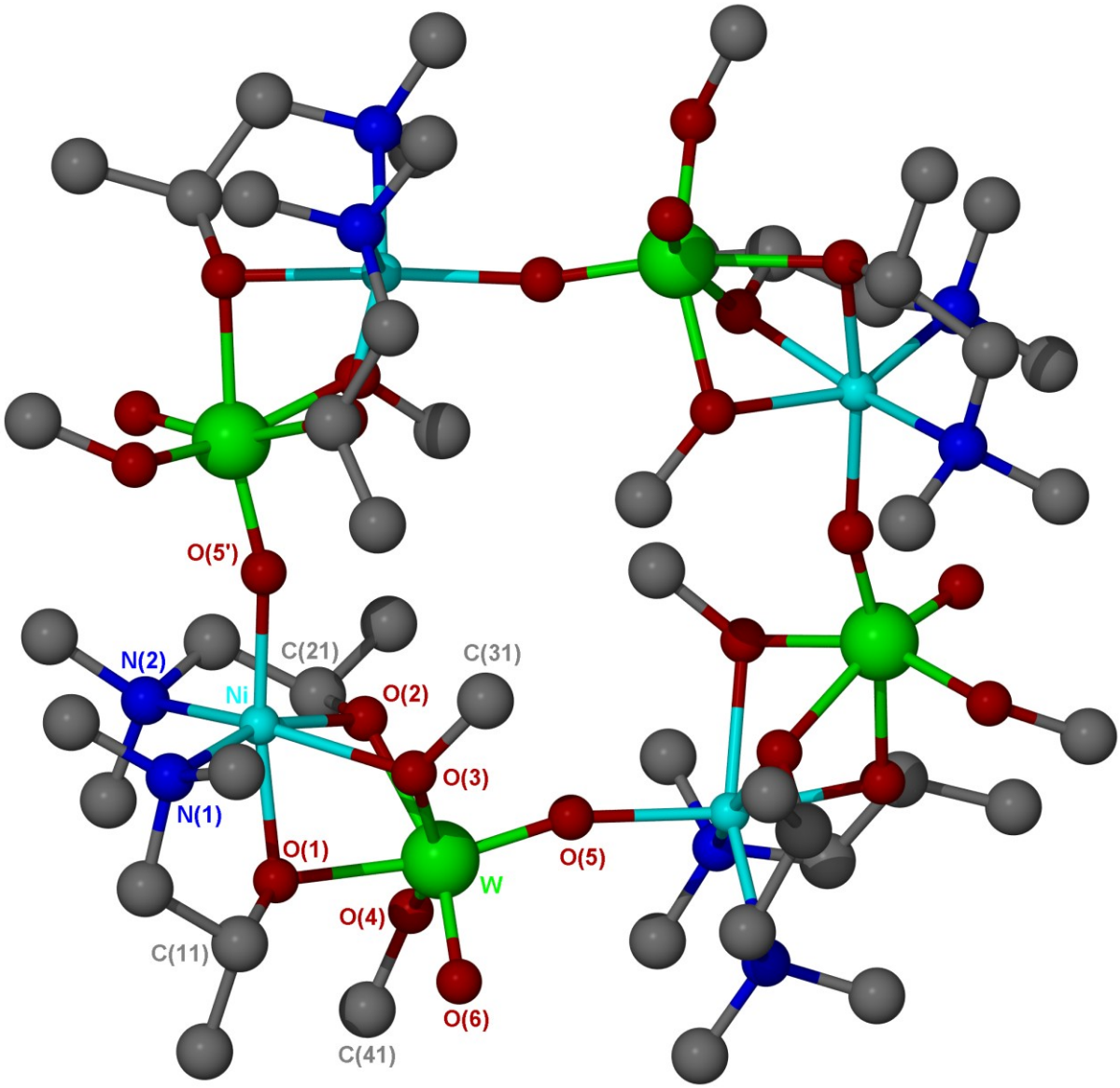

Figure 3.10 Molecular structure of $[Ni(dmap)_2(\mu_2\text{-}O)WO(OMe)_3]_4$ **(10)**

Table 3.4 Selected bond lengths (Å) and angles (º) of **(10)**

Bond lengths			
Ni-O(1)	2.029(3)	Ni-O(5)	2.033(3)
Ni-O(2)	2.039(3)	Ni-N(1)	2.122(5)
Ni-N(2)	2.180(4)	Ni-O(3)	2.206(3)
W-O(6)	1.727(3)	W-O(5)	1.763(3)
W-O(4)	1.919(3)	W-O(3)	2.001(3)
W-O(1)	2.141(3)	W-O(2)	2.153(3)
Bond angles			
O(1)-Ni-O(5')	169.79(14)	O(1)-Ni-O(2)	79.67(13)
O(5')-Ni-O(2)	100.72(13)	O(1)-Ni-N(1)	84.28(17)
O(5')-Ni-N(1)	93.79(16)	O(2)-Ni-N(1)	162.40(18)
O(1)-Ni-N(2)	93.44(16)	O(5')-Ni-N(2)	96.73(15)
O(2)-Ni-N(2)	82.78(15)	N(1)-Ni-N(2)	105.5(2)
O(1)-Ni-O(3)	73.06(12)	O(5')-Ni-O(3)	97.21(12)
O(2)-Ni-O(3)	72.99(12)	N(1)-Ni-O(3)	95.49(19)
N(2)-Ni-O(3)	153.88(14)	O(6)-W-O(5)	101.80(16)
O(5)-W-O(4)	98.66(15)	O(6)-W-O(4)	96.54(16)
O(5)-W-O(3)	96.20(13)	O(6)-W-O(3)	99.60(15)
O(6)-W-O(1)	86.60(15)	O(4)-W-O(3)	155.30(13)
O(4)-W-O(1)	87.46(14)	O(5)-W-O(1)	168.89(14)
O(6)-W-O(2)	161.29(15)	O(3)-W-O(1)	75.03(12)
O(4)-W-O(2)	83.87(13)	O(5)-W-O(2)	96.61(13)
O(1)-W-O(2)	74.72(13)	O(3)-W-O(2)	74.90(12)
C(11)-O(1)-Ni	111.6(3)	Ni-O(1)-W	91.15(12)
C(21)-O(2)-Ni	113.6(3)	C(11)-O(1)-W	122.3(4)
Ni-O(2)-W	90.53(12)	C(21)-O(2)-W	130.9(3)
C(31)-O(3)-Ni	122.8(3)	C(31)-O(3)-W	126.8(3)
C(41)-O(4)-W	126.1(4)	W-O(3)-Ni	90.04(11)

Symmetry transformations used to generate equivalent atoms ('): -y+1/2, x-1, -z+1/2

3.2.1.2 NMR spectroscopy

1D NMR : ^{1}H, ^{13}C (DEPT), and 2D NMR (COSY, HMQC) analysis were performed on **(7)** and **(9)**. Compound **(7)** was also characterised by ^{183}W NMR due to its high solubility whereas **(9)** was insufficiently soluble. The ^{1}H NMR and ^{13}C NMR analysis reported below are correlated to the crystal structures of **(7)** and **(9)** (Figure 3.6 and 3.9).

The ^{1}H NMR spectrum of $[TiWO(OPr^{i})_3(\mu_2\text{-}O)_2(\mu_2\text{-}bdmap)]_2$ **(7)** (Figure 3.11) in C_6D_6 solution displays a multitude of NMR signals, including six doublets between 1.38 and 1.58 ppm matching with the 6 inequivalent methyl groups ($-CH_3$) associated to the isopropoxide ligands ($-O^{i}Pr$). The distinction between the terminal isopropoxide ligands bonding to titanium or tungsten is however difficult due to the overlapping and the complex multiplicity. The –OCH group of the titanium and tungsten isopropoxide are illustrated by multiplets,

respectively at 5.33 and 5.49 ppm. The Figure 3.11 displays each signal of the amino-alkoxide bdmap ligand. The -CH_2- groups of bdmap consist of two apparent triplets for the H_b and H_c at 2.40 and 2.43 ppm and two doublets of doublets for the H_d and H_e at 1.74 and 1.85 ppm. The hydrogen atoms Ha, Hb and Hc are in position axial (ax.) meanwhile Hd and He are in position equatorial (eq.). The vicinal ^{3}J-coupling constants of axial protons ($^3J_{Ha,Hb}$ or $^3J_{Ha,Hc}$; $\Phi_2 \sim 180°$) are greater than ^{3}J-coupling constants of axial protons with equatorial protons ($^3J_{Ha,Hd}$ or $^3J_{Ha,He}$; $\Phi_1 \sim 60°$) due to the difference in the torsion angles as illustrated in Figure 3.12. This was established according to the Karplus equation which demonstrates that the coupling constant is small when the torsion angle is close to 90° and large at angles of 0 and 180°.[36] Hence, each -CH_2- groups show different ^{n}J-coupling constant: $^2J_{Hc,He} = {}^2J_{Hb,Hd} = {}^3J_{Ha,Hb} = {}^3J_{Ha,Hc}$ =11.5 Hz and $^3J_{Ha,He} = {}^3J_{Ha,Hd}$ =1.7 Hz explaining thus the multiplicity of each inequivalent –CH_2- signals.

In addition, the methyl groups $^{\alpha,\beta,\gamma,\delta}CH_3$ bonded to the nitrogen atoms of the bdmap ligand are all inequivalent as depicted by the four singlets in the NMR spectrum. Also, the H_a of the bdmap ligand is displayed by a complex mutiplet at 4.49 ppm.

The ^{13}C NMR spectrum of **(7)** displays the usual chemical shift from 25.77 to 26.95 ppm for the methyl groups belonging to titanium and tungsten isopropoxide. It is interesting to note that the carbon nuclei of the isopropoxides are inequivalent, giving rise to six singlets. There are four singlets from 46.34 to 51.70 ppm corresponding to the four inequivalent methyl groups $^{\alpha,\beta,\gamma,\delta}CH_3$ bonded to the nitrogen associated to the amino-alkoxide ligand. The CH_2 groups are give signals at 64.31 and 64.75 ppm. The CH of bdmap presents a more deshielded signal at 69.35 ppm. The -OCH group of the titanium isopropoxide displays signals at 76.66 and 76.15 ppm. The -OCH group of the tungsten isopropoxide display one signal at 77.5 ppm, assuming that tungsten deshields more the nucleus ^{13}C due to its electronegativity.

The ^{183}W NMR spectrum of **(7)** recorded at 373 K gives a single peak at -111.1 ppm. However, it is interesting to note that the value δ_w recorded for **(4)** is more deshielded than **(7)** due to the difference of the nature of bridging ligands. Indeed, **(4)** displays only oxo-bridges meanwhile **(7)** exhibits oxo-bridges and μ_2-O bridging belonging to the chelating bdamp ligand.

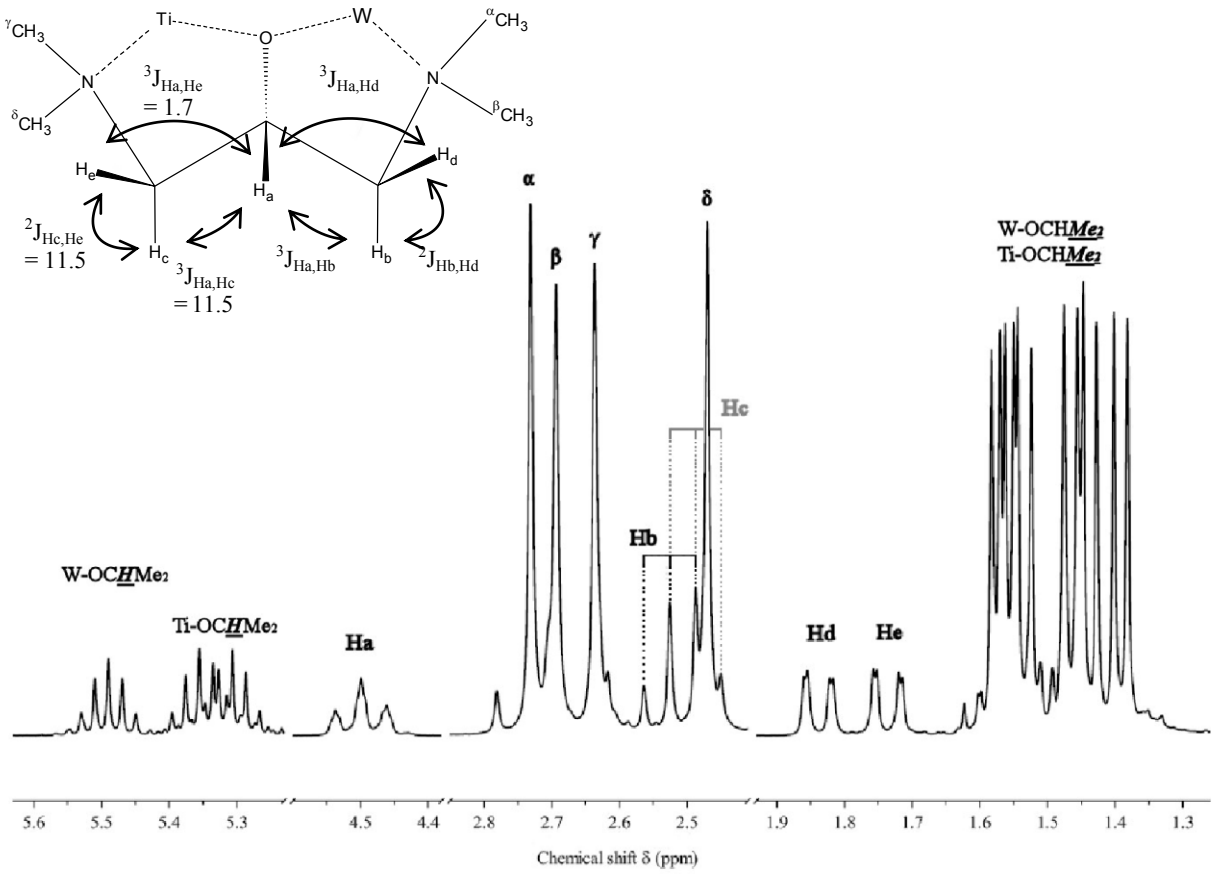

Figure 3.11 ^{1}H NMR spectrum of **(7)** with the schematic representation for the chelating and bridging bdmap ligand

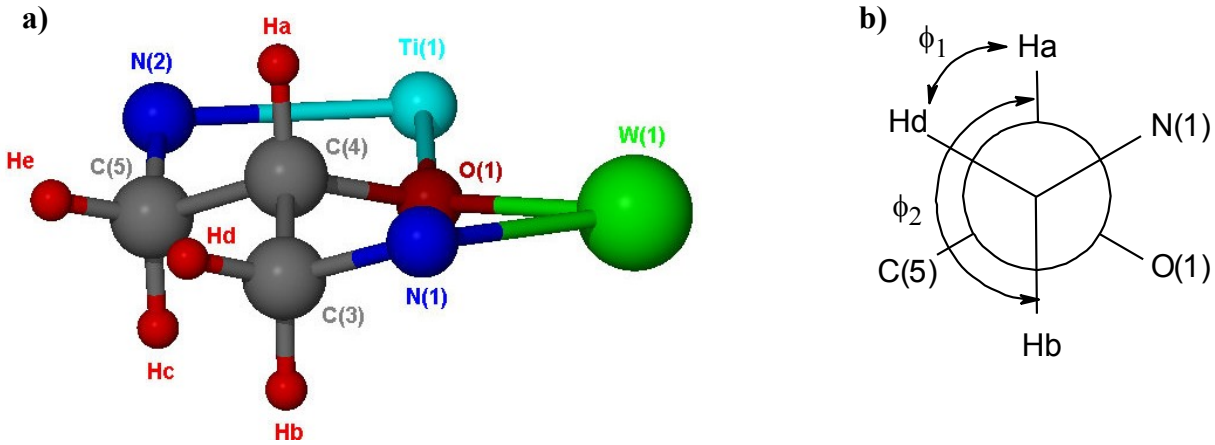

Figure 3.12 **a)** Molecular structure of the amino-alkoxide bonding Ti(1) and W(1) in **(7)**
b) Illustration of the torsion angles Φ_1 and Φ_2 between the hydrogen nuclei in relation with its crystal structure

The ^{1}H NMR spectrum collected for $Zn_2W_2O_2(OPr^i)_2(acac)_2(\mu_2\text{-}O)_3(\mu_2\text{-}bdmap)_2$ **(9)** (Figure 3.13) in C_6D_6 solution show a complex spectrum which displays a pair of doublets at 1.37 and 1.63 ppm with respectively $^{3}J_{H,H} = 6.21$ Hz and $^{3}J_{H,H} = 5.97$ Hz corresponding to the two inequivalent methyl groups of the tungsten isopropoxide -OCH(C***H*****$_3$**$)_2$. This proves that the methyls for the same ligands are inequivalent, as already observed in **(7)**. Also, all the methyl groups of the acetylacetonate ligand (acac) are equivalent, indicated by a singlet at 1.92 ppm. Figure 3.13 displays each signals of the amino-alkoxide bdmap ligand. Hence, all the methyl groups belonging to the bdmap ligand are all inequivalent. However, the signals are surprisingly widespread compared to **(7)** with chemical shift at 1.98, 2.30, 2.72, 2.75, 2.91 ppm. This comes probably from the direct environment of the methyls groups which deshield more or less depending on its spatial position compared to the acetylacetonate ligand. We can see clearly the triplet at 2.33 ppm with $^{2,3}J_{H,H} = 11.2$ Hz assigned to one of the -CH_2-groups belonging to the bdmap ligand.

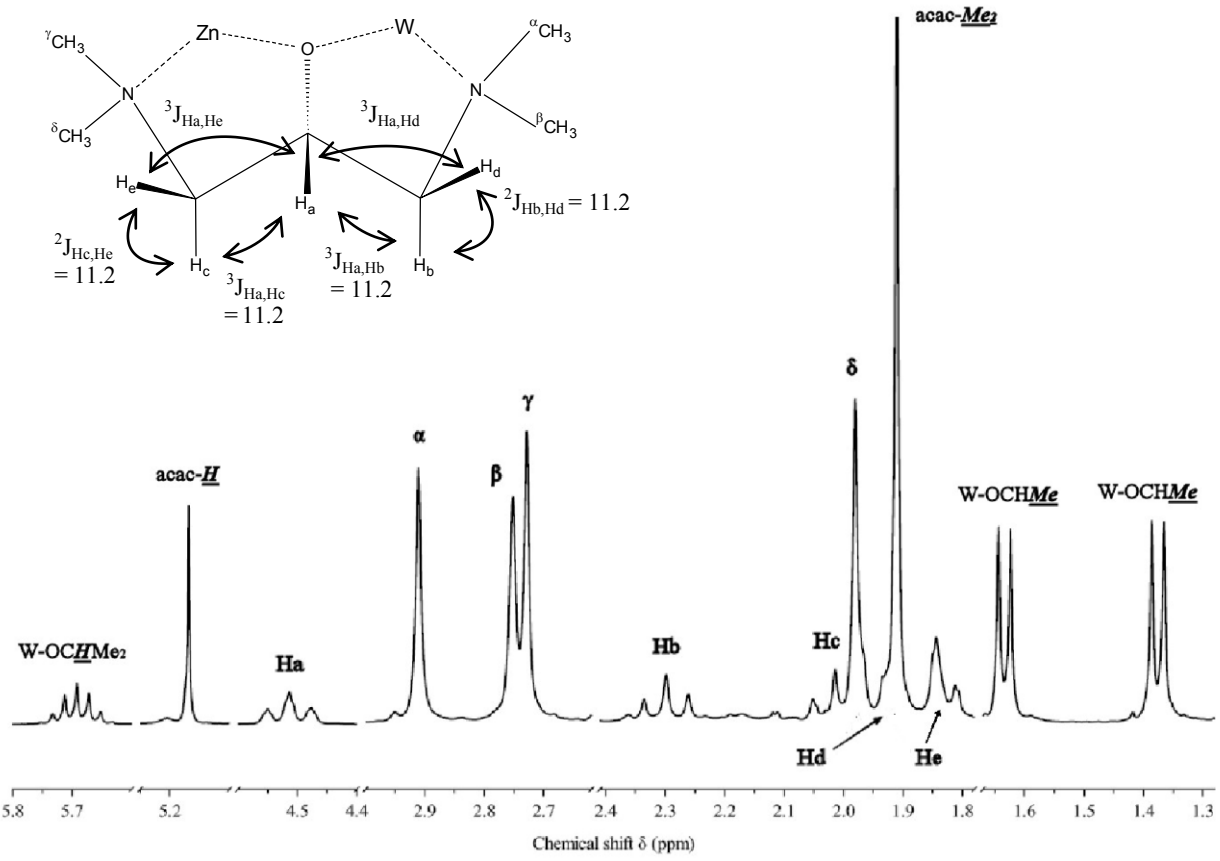

Figure 3.13 ^{1}H NMR spectrum of **(9)** with the schematic representation for the chelating and bridging bdmap ligand

There are three other signals which are overlapped and thus difficult to distinguish the peaks and to determine the other weaker coupling constant $^{3}J_{H,H}$. We note the presence of another triplet and two pairs of doublet signals in the area of 2 ppm, indicated in the Figure 3.13. The multiplet at 4.51 ppm is assigned to H_a of the amino-alkoxide bdmap ligand. As the torsion angles of the Ha proton with the other hydrogen nuclei are similar to the structure **(7)** (Figure 3.12), the vicinal ^{3}J-coupling constant $^{3}J_{Ha,He\ and}$ $^{3}J_{Ha,Hd}$ should be around 2 Hz. The ^{1}H NMR shifts at 5.17 ppm and 5.69 ppm are respectively assigned to the H group of the acetylacetonate and the H group of the tungsten isopropoxide -O(C***H***$(CH_3)_2$).

The ^{13}C NMR consists of the two signals at 25.56 and 26.69 ppm matching to the inequivalent methyls belonging to the tungsten isopropoxide. Also, a unique signal of the equivalent methyl groups of the acac ligand is present at 28.0 ppm. And then, the ^{13}C NMR analysis displays four signals corresponding to the four inequivalent methyl of the aminoalkoxide. As already observed in **(7)**, the two CH_2 signals are displayed at 65.80 and 65.33 ppm. The H group of the tungsten isopropoxide -OC***H***$(CH_3)_2$ shows a signal at 72.05 ppm. The -CH group and the two quaternary carbon of the acac appear respectively at 99.68 and 192.64 ppm.

3.2.2 Synthesis of heterobimetallic tungsten acetylacetonate alkoxide

The synthetic strategy adopted in this section to obtain heterobimetallic tungsten acetylacetonate alkoxide follows the early reports made by V. G. Kessler et al.[10] Here, two equivalents of $Mo^{VI}O(OMe)_4$, were found to react with one equivalent of $M^{II}(acac)_2$ in the minimum of reluxing toluene solvent, leading to the insoluble heterobimetallic molybdenum acetylacetonate alkoxides $M_2Mo_2O_2(acac)_2(OMe)_{10}$ (M = Co, Ni, Zn, Mg), which are then separated by filtration from the excess of the starting material and the by-product $MoO(OMe)_3(acac)$ formed during the reaction. This required the metal ratio reaction M/Mo at lower than 1:2. An excess of the heavier metal alkoxide seems to be a driving force to the completion of the reaction.[13]

In the same way, the insoluble heterobimetallic tungsten acetylacetonate alkoxides $M_2W_2O_2(acac)_2(OMe)_{10}$ [M = Co **(11)**, Ni **(12)**, Mg **(13)**, Zn **(14)**] have been synthesised by mixing, in refluxing toluene solvent, 2 equivalents of $WO(OMe)_4$ and one equivalent of $M^{II}(acac)_2$ [Eq.(3.8)]. In our case, the resulted complexes separated by filtration were also washed with cold toluene to ensure a higher purity by removing the quite soluble by-product $WO(OMe)_3(acac)$ **(15)**. This overall reaction [Eq.(3.8)] incorporates the ligand-exchange

reaction between the two reagents $M(acac)_2$ and $WO(OMe)_4$ [Eq.(3.6)]. Hence, different heterobimetallic tungsten acetylacetonate alkoxides complexes have been synthesised by the Lewis acid-base reaction of the tungsten oxo-tetra-methoxide $WO(OMe)_4$ with divalent metal M(acac)(OMe) (M = Co, Ni, Zn, Mg) according the equations (3.7):

$$M(acac)_2 + WO(OMe)_4 \xrightarrow{\Delta,\text{Toluene}} M(acac)(OMe) + WO(OMe)_3(acac) \quad (3.4)$$

$$M(acac)(OMe) + WO(OMe)_4 \xrightarrow{\Delta,\text{Toluene}} \tfrac{1}{2}\ M_2W_2O_2(acac)_2(OMe)_{10} \quad (3.5)$$

$$M(acac)_2 + 2\ WO(OMe)_4 \xrightarrow{\Delta,\text{Toluene}} \tfrac{1}{2}\ M_2W_2O_2(acac)_2(OMe)_{10} + WO(OMe)_3(acac) \quad (3.6)$$

$WO(OMe)_3(acac)$ has been isolated from the mother liquor obtained during the reaction which gave the heterobimetallic product $Zn_2W_2O_2(acac)_2(OMe)_{10}$ **(14)**. The drawbacks of this reaction are mainly the use of an excess of an expensive metal alkoxide which is not commercially available and the necessity to obtain insoluble complexes in order to ease the purification by difference of solubility. Thus, a second synthetic strategy has involved the use of $WO(OMe)_4$ with $M^{II}(acac)(OMe)$ (M = Co, Ni, Mg) in 1:1 ratio to give directly the corresponding heterobimetallic compounds, as outlined in Eq. (3.7). $M^{II}(acac)(OMe)$ has been first obtained from refluxing $M^{II}(acac)_2$ with KOH (or NaOH) in methanol which gives rise to the tetramer $M^{II}(acac)(OMe)(MeOH)$.[37] However, the reaction [Eq.(3.9)] with zinc acetylacetonate did not succeed as expected and form instead of a linear polymeric chain $NaZn(acac)_3$ **(17)**. The reaction involving the synthesis of the tetramer [Eq.(3.9)] was followed by the drying process of the compound at about 100°C which permits its desolvation required to avoid the decomposition of the resulted heterobimetallic complexes [Eq.(3.8)].[38] This desolvation is accompanied usually with a change of color from dark to pale.

$$M^{II}(acac)_2 + KOH \xrightarrow[\Delta]{MeOH} 4\ [M^{II}(acac)(OMe)(MeOH)]_4 \quad (3.7)$$

This caution to dry $M^{II}(acac)(OMe)(MeOH)$ prior to mixing with the metal oxo-alkoxide, comes after the observation of Kessler et al. which noted the instability of the resulting molybdenum heterobimetallic complexes,[13] to solvolysis by methanol.

Consequently, $M^{II}(acac)(OMe)$ (M = Co, Ni and Mg) has been prepared as starting material in combination with $WO(OMe)_4$ in refluxing toluene for the synthesis of heterobimetallic complexes $M_2W_2O_2(acac)_2(OMe)_{10}$ (M = Co, Ni and Mg) in a single step without further purification from any $WO(OMe)_3(acac)$ by-product. This second synthetic

strategy, which is an improvement compared to the method originally employed by V. G. Kessler, has been utilisized successfully. The two above methods which match in term of results permit to synthesize and characterize compounds of type $M_2W_2O_2(acac)_2(OMe)_{10}$ (M = Co, Ni, Mg and Zn) by elemental analysis, X-ray crystallography and NMR for the diamagnetic nuclei including $Mg_2W_2O_2(acac)_2(OMe)_{10}$ and $Zn_2W_2O_2(acac)_2(OMe)_{10}$.

3.2.2.1 Crystal structures

In the case presented in Figure 3.14 taken as an example, the structure is built up by the centrosymmetic $Co_2W_2O_2(acac)_2(OMe)_{10}$ molecules. The molecular structure of the divalent metal M^{II}-tungsten complexes with M^{II} = Co, Ni, Mg and Zn follows the well-known $[Ti(OMe)_4]_4$ structural type:[39] four edge-sharing octahedra are situated in the same plane, two methoxide groups triply bridging and four doubly bridging. The metal divalent M and tungsten have both octahedral coordination environments with six oxygen atoms. The octahedra surrounding the cobalt and tungsten atom are distorted because of different types of oxygen atoms (terminal-OMe, bridging μ_2-OMe and μ_3-OMe). The *trans* O-W-O angles vary between 162.87(16) Å and 165.68(16) Å and are small compared to the ideal angles of 180°. Moreover, the longest bond W-O(4) [2.170(3) Å] is in the *trans* position to the shortest bond which is the double bond W=O(6) [1.710(3) Å]. Also, the terminal methoxy ligands O(7) and O(8) are respectively *trans* to the bridging μ_2-O(5) and μ_2-O(3). The shortest Co-O distances in **(11)** involve the two oxygen atoms of the acac ring.

The observed Co–O and W-O distances (cf. Table 3.6 to 3.9) are in agreement respectively with those found in $[Co(acac)(OMe)(MeOH)]_4$ [37] and in $WO(OMe)_4$.[33] Moreover, the heterobimetallic compounds obtained with tungsten are consistent with the ones synthesised with molybdenum *e.g* $Co_2Mo_2O_2(acac)_2(OMe)_{10}$.[10] All of these structures **(11)-(14)** determined by single-crystal X-ray studies are isostructural in terms of symmetry and space group. Hence, the only differences are the nature of the metal atoms involved. Despite the difference in the size of the divalent metal M^{II}, all the triclinic structures are quasi identical in regard with the bond lengths and angles. The selected bond lengths and angles of **(11)-(14)** are reported in the Tables 3.5. The octahedron surrounding the Ni, Mg, Zn atoms are distorted, as already depicted in details for Co. The resulting distances of the divalent metal oxygen M-O bond in **(11)-(14)** are comparable to the ranges of distances observed in the structure $M_2M'_2O_2(acac)_2(OMe)_{10}$ (M = Co, Ni, Mg, Zn) and M' = Ta and Nb.[13]

The by-product $WO(OMe)_3(acac)$ **(15)**, isostructural to $MoO(OMe)_3(acac)$ in term of bond length and angles,[10] has been also characterised by X-ray crystallography. Unfortunately, it shows a disordered structure and will not be discussed further.

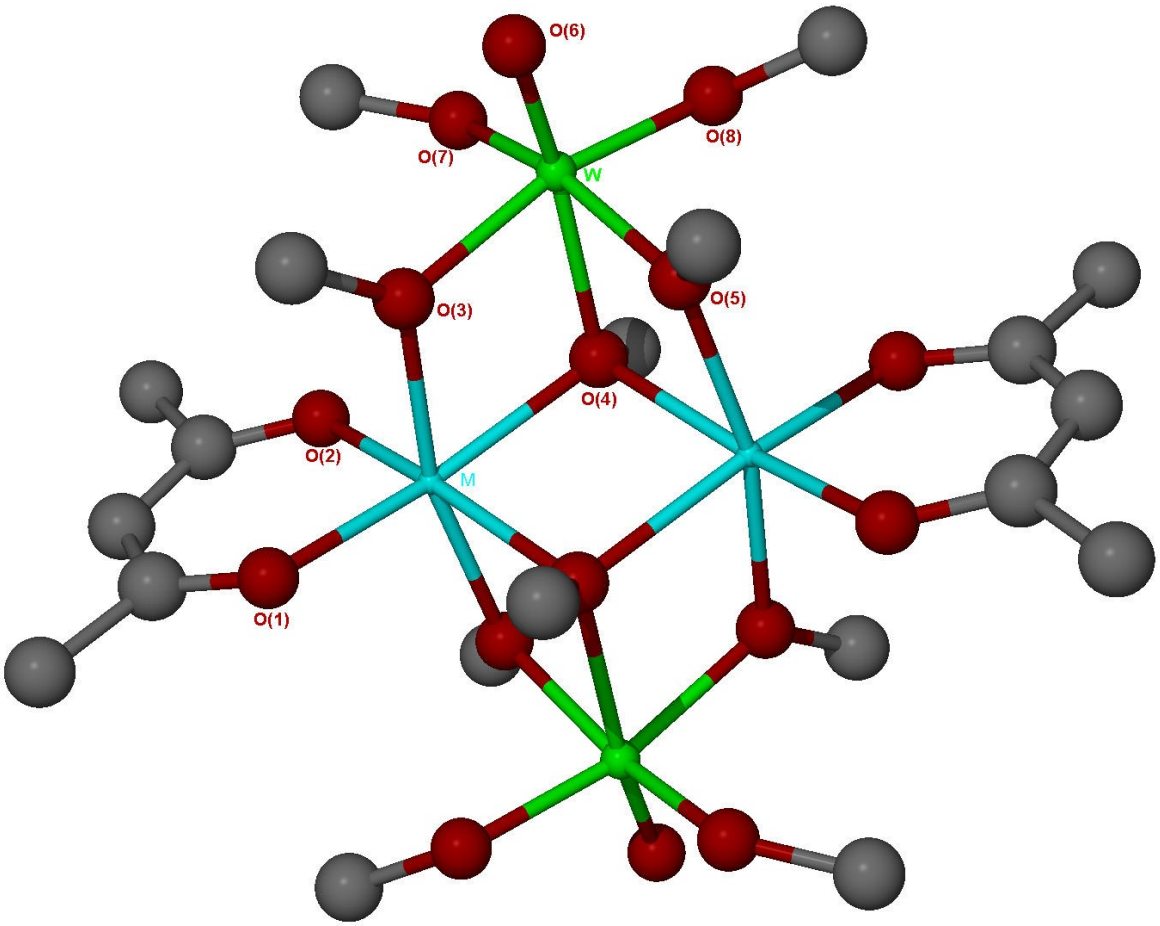

Figure 3.14 Molecular structure of $M_2W_2O_2(acac)_2(OMe)_{10}$ [M = Co **(11)** ,Ni **(12)**, Mg **(13)**, Zn **(14)**]

Table 3.5 Selected bond lengths (Å) and angles (º) of **(11)-(14)**

Complexes W/M	W/Co **(11)**	W/Ni **(12)**	W/Mg **(13)**	W/Zn **(14)**
Bond lengths				
W-O(3)	2.004(3)	2.003(5)	2.0044(18)	1.994(7)
W-O(4)	2.170(3)	2.167(5)	2.1607(19)	2.156(7)
W-O(5)	2.005(3)	2.008(5)	2.009(2)	1.997(7)
W-O(6)	1.710(3)	1.712(5)	1.708(2)	1.713(8)
W-O(7)	1.868(3)	1.853(6)	1.860(2)	1.842(7)
W-O(8)	1.883(3)	1.878(5)	1.878(2)	1.859(7)
M-O(1)	2.017(3)	1.992(5)	2.014(2)	2.008(7)
M-O(2)	2.015(3)	1.987(5)	2.0128(19)	2.002(7)
M-O(3)	2.118(4)	2.077(5)	2.093(2)	2.139(7)
M-O(4)	2.142(3)	2.097(5)	2.1200(19)	2.146(6)
M-O(4')	2.142(3)	2.102(4)	2.134(2)	2.143(6)
M-O(5')	2.109(3)	2.073(5)	2.085(2)	2.118(7)
Bond angles				
O(3)-W-O(4)	75.50(12)	75.19(19)	75.03(8)	74.7(3)
O(3)-W-O(5)	86.19(14)	86.4(2)	85.81(8)	86.3(3)
O(6)-W-O(3)	92.62(17)	92.1(3)	92.64(10)	92.8(3)
O(7)-W-O(3)	90.56(16)	91.1(3)	90.42(9)	90.1(3)
O(8)-W-O(3)	165.68(16)	165.9(2)	165.36(10)	165.1(3)
O(5)-W-O(4)	74.95(11)	74.69(19)	74.52(7)	74.7(2)
O(6)-W-O(4)	162.87(16)	161.9(3)	162.18(10)	161.8(3)
O(7)-W-O(4)	89.09(14)	89.4(2)	89.61(9)	89.8(3)
O(8)-W-O(4)	90.37(14)	90.8(2)	90.55(8)	90.6(3)
O(6)-W-O(5)	92.23(17)	92.1(3)	92.06(10)	91.5(3)
O(7)-W-O(5)	164.02(17)	163.9(3)	164.12(11)	164.5(3)
O(8)-W-O(5)	87.89(14)	87.8(2)	87.93(8)	87.4(3)
O(6)-W-O(7)	103.56(18)	103.9(3)	103.53(12)	103.8(4)
O(6)-W-O(8)	100.63(16)	101.0(2)	100.81(11)	100.8(4)
O(7)-W-O(8)	91.57(16)	90.9(3)	92.01(10)	92.4(3)
O(2)-M-O(1)	91.36(13)	92.6(2)	89.44(8)	91.7(3)
O(1)-M-O(3)	93.45(13)	94.0(2)	93.08(9)	93.3(3)
O(1)-M-O(4)	165.31(12)	166.53(18)	165.60(9)	163.8(3)
O(1)-M-O(4')	93.15(12)	93.6(2)	94.26(8)	93.9(3)
O(1)-M-O(5')	97.75(13)	95.58(19)	98.26(9)	98.5(3)
O(2)-M-O(3)	94.23(14)	93.7(2)	95.47(9)	95.7(3)
O(2)-M-O(4)	96.76(12)	95.68(19)	97.55(8)	97.5(3)
O(2)-M-O(4')	167.04(13)	167.9(2)	166.25(9)	165.1(3)
O(2)-M-O(5')	93.87(13)	92.70(19)	92.74(9)	93.0(3)
O(3)-M-O(4)	73.81(12)	75.2(2)	74.10(8)	72.6(3)
O(3)-M-O(4')	97.62(13)	96.9(2)	98.16(8)	98.1(3)
O(5')-M-O(3)	166.01(13)	167.7(2)	166.05(9)	164.8(3)
O(4)-M-O(4')	81.61(11)	81.29(19)	81.23(8)	80.6(3)
O(5')-M-O(4')	73.49(11)	74.57(17)	73.63(8)	72.2(2)
O(5')-M-O(4)	93.91(12)	94.4(2)	93.60(8)	94.2(3)
Symmetry transformations used to generate equivalent atoms ('): -x+1, -y+1, -z+2				

3.2.2.2 NMR spectroscopy

1D NMR: ^{1}H, ^{13}C (DEPT), and 2D NMR (COSY, HMQC) analysis were performed on the heterobimetallic containing only the diamagnetic atoms **(13)** and **(14)**. However, attempts to obtain ^{183}W NMR spectroscopy has not been successful due the poor solubility of these heterobimetallic alkoxides.

The ^{1}H NMR spectrum of $Mg_2W_2O_2(acac)_2(OMe)_{10}$ **(13)** prepared in $CDCl_3$ displays three different signals at 3.90, 4.39 and 4.61 ppm corresponding respectively to three different alkoxide functions (μ^3-OMe, μ^2-OMe, and terminal OMe). In that order, these singlets give an integration ratio of 1:2:2. As the coordination mode of the oxygen and thus its geometry changes from a terminal to a μ_2-bridging and then μ_3-bridging methoxide, the chemical shift decreases from 4.39 to 3.90 ppm. The other peaks of the spectrum at 1.88 and 5.28 ppm correspond with the two methyls (C***H*****$_3$**) and the hydrogen (C***H***) of the acetylacetonate (acac) ligand bonded to the magnesium atom. It appears according to the NMR analysis that the heterometallic complexes preserve their dimeric molecular structure in solution.

The ^{13}C spectrum of **(13)** displays the different types of carbon expected for the acac ligand at 28.33 ppm for the methyl, at 99.05 ppm for the tertiary carbon and at 191.04 ppm for the quaternary carbon. The other chemical shifts at 55.06, 63.77 and 64.95 ppm correspond to the carbon bonded to the different type of methoxy- ligands which have different type of geometry, depending on their coordination mode.

The ^{1}H NMR spectrum of $Zn_2W_2O_2(acac)_2(OMe)_{10}$ **(14)** (Figure 3.15) displays at 303 K the same type of signals about the acac ligand, *i.e.* C**H$_3$** and C**H** at respectively 1.91 and 5.26 ppm. The spectrum shows a sharp signal at 3.98 ppm (3 hydrogens on integration) corresponding to the triply bridging methoxide μ_3-OMe and at 4.52 ppm (12 hydrogens on integration) a broad signal matching with the two terminal and two μ_2-bridging methoxy ligands. A VT NMR study displays the evolution of the NMR signals as a function of temperature from 233K to 323K.

At low temperature (233 K), the broad peak at 4.52 ppm splits into two sharp peaks at 4.46 and 4.58 ppm which match respectively with terminal and μ_2- bridging methoxy ligands. This shows the molecular rigidity compared to high temperatures. As the temperature increased, the peaks matching with the terminal and μ_2-OMe coalesce to form first a broad peak at 273 K and then a sharper peak as the intramolecular exchange of the terminal and μ_2-bridging methoxy sites become faster. Hence, the coalescence forms a sharp peak at 303 K. It

seems that the terminal, doubly bridging and triply bridging methoxide then coalesce to generate a broad signal at 323 K.

According to the NMR of $Zn_2W_2(acac)_2(OMe)_{10}$ **(14)**, the most facile exchange occurs between the terminal and μ_2- bridging oxygen of the alkoxide ligands. The related compound $Mg_2Ta_2(acac)_2(OMe)_{12}$ displays similar behavior of intermolecular exchange but seems to happen between different type of methoxy groups *i.e* bridging μ_2- and μ_3-OMe. Nevertheless, VT NMR study of $Mg_2Ta_2(acac)_2(OMe)_{12}$ did not succeed to be resolved appropriately at low temperature.[13] Moreover, $Mg_2W_2(acac)_2(OMe)_{10}$ shows molecular rigidity at R.T like $Zn_2Ta_2(acac)_2(OMe)_{12}$.[13] The lability of the alkoxide ligands in this type of heterobimetallic complex seems to be unpredictable.

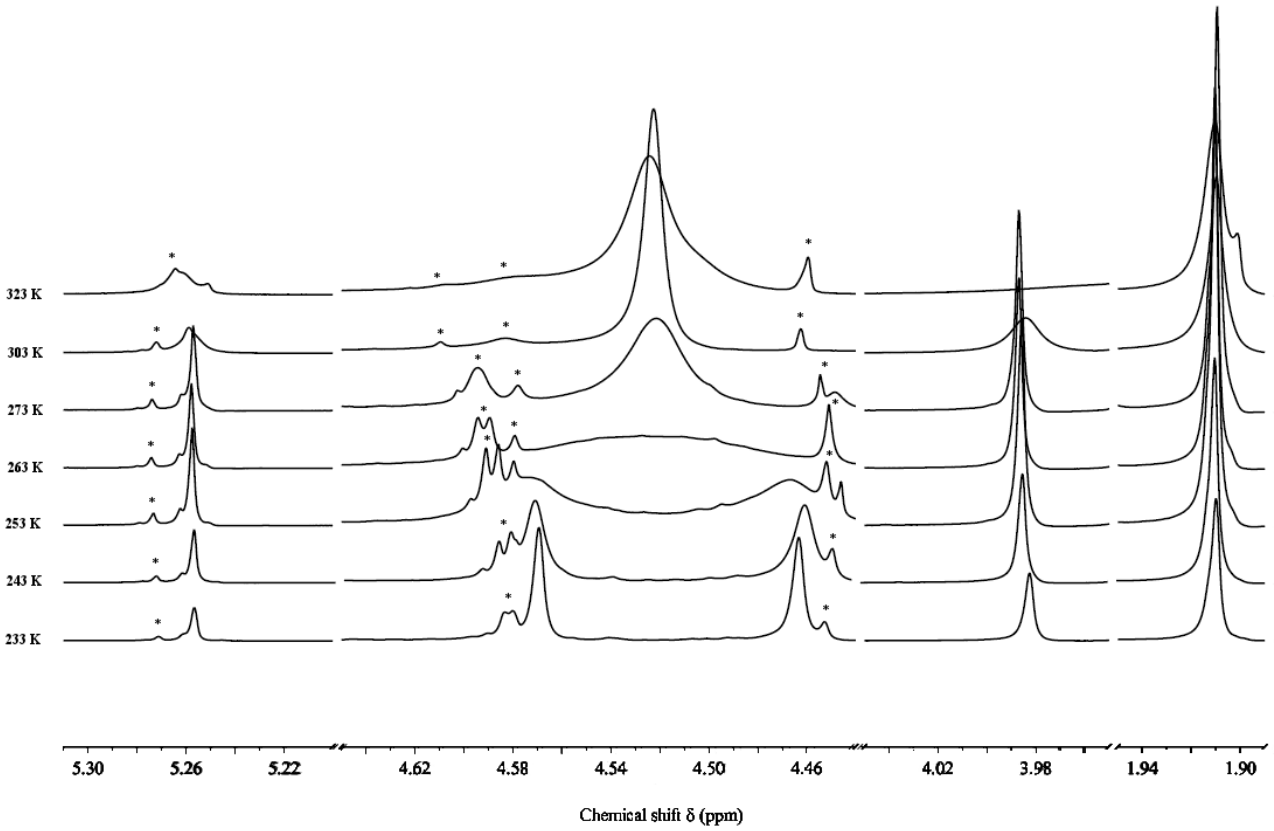

Figure 3.15 VT NMR of $Zn_2W_2O_2(acac)_2(OMe)_{10}$ from 233 to 323 K
(Some impurities, resulting of the by-product appear in the analyzed sample, are indicated by *)

During the reaction to synthesise **(14)** via the first method originally used by Kessler et al., the by-product $WO(OMe)_3(acac)$ **(15)** was obtained. The NMR spectrum of **(15)**, which is similar to $MoO(OMe)_3(acac)$, reveals a *mer* configuration like the complexes $WO(OMe)_3(L)$ **(1)-(3)**.

$WO(OMe)_3(acac)$ **(15)** shows inequivalent methyl groups of the acac ligand at 1.70 and 1.75 ppm. This inequivalence is also reflected in the quaternary carbons of the acac ligand which appear in the spectrum at 186.41 and 194.17 ppm. Moreover, the NMR spectra suggests that two of three terminal methoxide ligands are equivalent due to the presence of methoxy groups signals at 4.41, 4.65 ppm for ^{1}H NMR and 63.3, 65.32 ppm for ^{13}C NMR.

3.2.3 Thermal decomposition studies and applications

Prior to any CVD study and thermal decomposition of the precursors, TGA under inert atmosphere (N_2) at atmospheric pressure were performed for compounds **(7)**, **(9)**, **(11)**, **(12)**, **(13)** and **(14)** in order to study the thermal behaviour and then to predict the product resulting after pyrolysis.

3.2.3.1 TGA measurements

The results of the TGA analysis of **(7)**, **(9)**, **(11)**, **(12)**, **(13)** and **(14)** are summarized in Figures 3.16 to 3.18. All the compounds mentioned above show no significant volatility at atmospheric pressure in the range of temperature investigated.

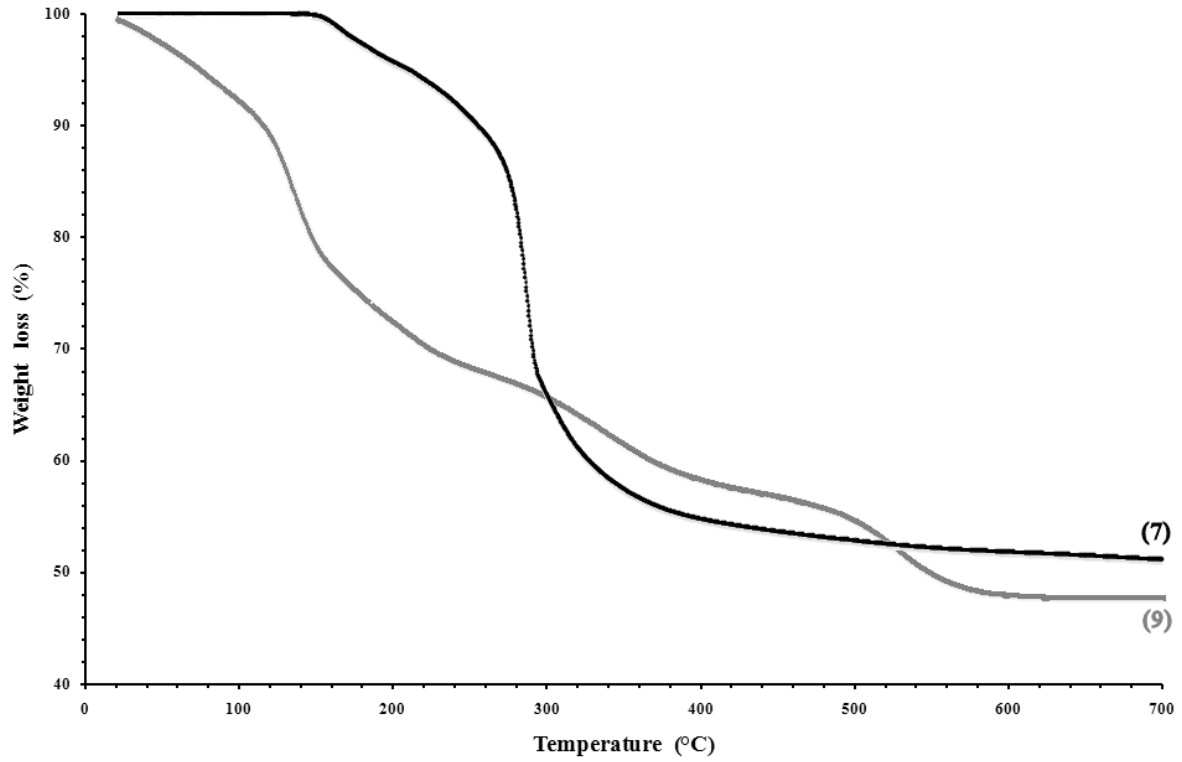

Figure 3.16 TG curves for thermal decomposition in dry nitrogen atmosphere of **(7)** and **(8)** at atmospheric pressure with a heating rate of 20°C/min

Compound $Ti_2W_2O_2(OPr^i)_6(\mu_2\text{-}O)_4(\mu_2\text{-}bdmap)_2$ **(7)** and $Zn_2W_2O_2(OPr^i)_2(acac)_2(\mu_2\text{-}O)_3(\mu_2\text{-}bdmap)_2$ **(9)** (Figure 3.16) exhibit multiple step mass losses with residual percent weight values at respectively for 49.5 % and 47.8 %.

The first decomposition of **(7)** occurring at 180 °C with a weight loss of 5.4 % is quite smooth while the second one with a weight loss of 45.1 % is abrupt from 200°C to 350°C with no further compositional changes on further heating. The total weight loss is 50.5%, hence, the remaining weight of the thermal decomposition of **(7)** under nitrogen atmosphere is at 49.5%, which is consistent with the formation of $TiWO_4$ (theoretical value = 49.1%). The resulting material after TGA analysis was amorphous.

The TG curve of **(9)** shows a smooth and continuous decomposition from 20°C to 600°C. The total weight loss is 52.2%, hence, the remaining weight of the thermal decomposition of **(4)** under nitrogen atmosphere is 47.8%. According to the single molecular precursor **(9)**, we expected to obtain the mixed-metal oxide $ZnWO_4$ in the resulted materials with the remaining weight of theoretical value of 53.6% which is not in prediction with the weight obtained after the TGA experiment. The straightforward correlation of the weight loss is however difficult in this case due to the decomposition of **(9)** starting already at R.T. The probable sensitivity of the compound towards air and moisture and also, the probable solvation or contamination of the compound could be responsible of this early decomposition.

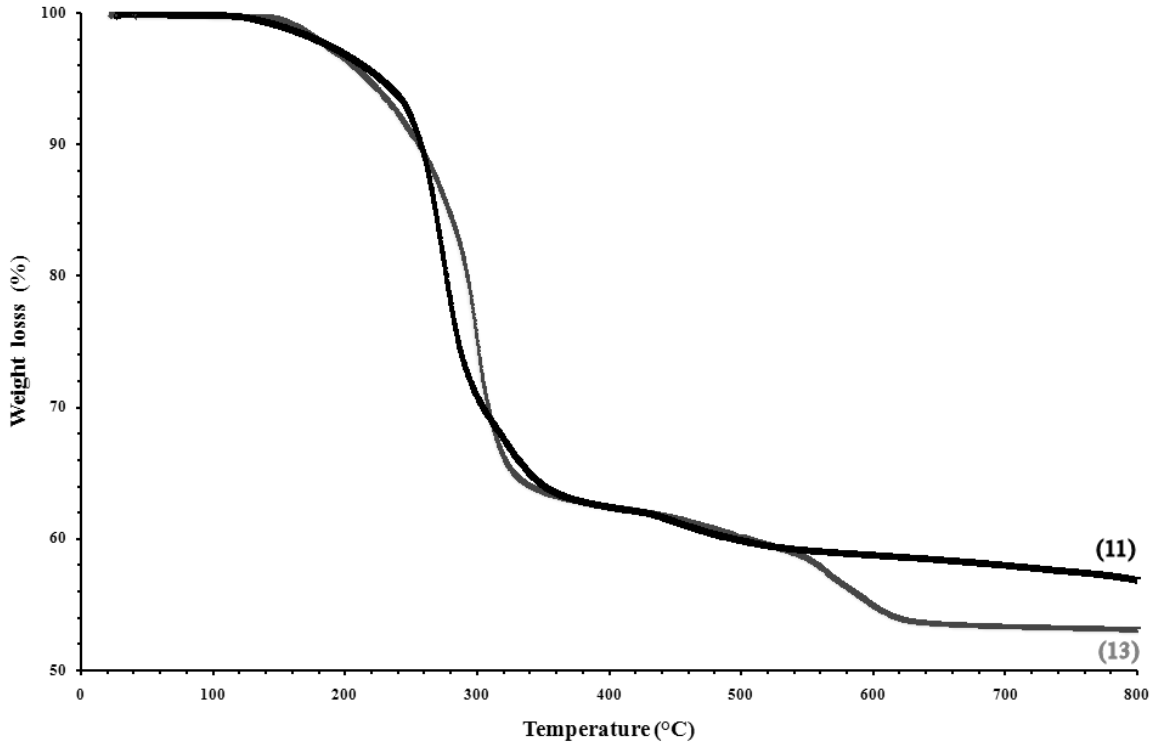

Figure 3.17 TG curves for thermal decomposition in dry nitrogen atmosphere of **(11)** and **(13)** at atmospheric pressure with an heating rate 20 °C/min

The TG curves of $Co_2W_2O_2(acac)_2(OMe)_{10}$ **(11)** and $Mg_2W_2O_2(acac)_2(OMe)_{10}$ **(13)** (Figure 3.17) display multi-step mass losses with similar decomposition pattern up to 550°C. **(11)** shows a first step mass loss starting at 140°C and finishing at 240°C corresponding to the weight loss of 7.4 % and then a sudden step with 29.6 % of weight loss. Finally, the last step shows a very smooth weight loss of 4.9 % at 400°C with no composition change on further heating, reaching a total weight loss of 41.9 % and thus a remaining weight of 58.1 % consistent with the relative weight of $CoWO_4$ (theoretical value = 59.8 %).

The TG curve of **(13)** displays two steps of decomposition occurring from 140°C to 360°C and from 440°C to 660°C after which there is no further compositional changes on further heating. The remaining final weight is 53.7% which is consistent with the expected weight percentage of magnesium tungstate $MgWO_4$ relatively to the single-source precursor $Mg_2W_2O_2(acac)_2(OMe)_{10}$ (theoretical value = 56.9%).

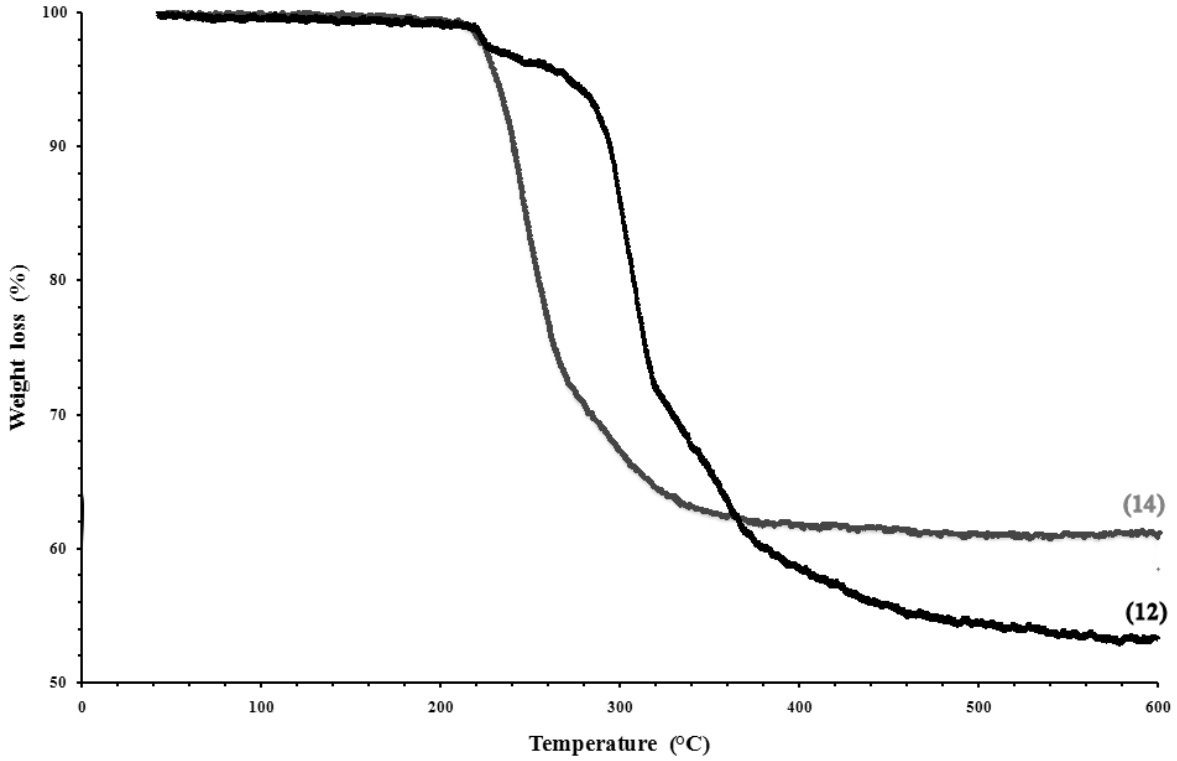

Figure 3.18 TG curves for thermal decomposition in dry nitrogen atmosphere of **(12)** and **(14)** at atmospheric pressure with an heating rate 20 °C/min

The TG curve for $Ni_2W_2O_2(acac)_2(OMe)_{10}$ **(12)** in the figure 3.18 displays also multi-step mass losses. The black curve relevant to the decomposition of **(12)** shows a first step decomposition occurring at about 230°C with a weight loss of 5.1% which is quite smooth

while the second one with a weight loss of 40.2% is abrupt from 280°C to 500°C with no composition change on further heating. The remaining weight percentage (54.7%) is consistent with the relative weight of $NiWO_4$ (theoretical value = 59.6%).

$Zn_2W_2O_2(acac)_2(OMe)_{10}$ **(14) (**Figure 3.18) exhibits a similar decomposition pattern but with only a single mass loss of 39.7%, starting at 230°C and finishing at 350°C corresponds to the loss of the organic ligands leading to the remain component: zinc tungstate ($ZnWO_4$). The final weight (60.7%) is in agreement with the relative weight of $ZnWO_4$ (Theoretical value = 60.3%)

3.2.3.2 Thermal decomposition applications

After having studied the thermal behaviour of different heterobimetallic compounds in inert atmosphere by TGA, the single source precursors $Co_2W_2O_2(acac)_2(OMe)_{10}$ **(11)** and $Mg_2W_2O_2(acac)_2(OMe)_{10}$ **(13)** have been decomposed under specific conditions. On one hand, compounds **(11)** and **(13)** have been decomposed in a closed Swagelok reactor under inert atmosphere at 700°C, as experiment of type A (Table 3.6). These reactions were carried out using the reaction under autogenic pressure at elevated temperature (RAPET) method by dissociating the precursor. On the other hand, **(11)** has been pyrolysed in a graphite melting pot open to the air at 590°C and 700°C, as experiment of type B (Table 3.6).

Table 3.6 Compounds, conditions and microanalysis of different experiments (N* = Non-measured)

Experiments	Type of compounds	Conditions	Yield (%)	C.H.N analysis (%)
B2	**(11)**	T = 590 °C, Δt = 1h	N*	0.08; 0.01;0.0
B3	**(11)**	T = 700 °C, Δt = 1h	N*	0.06;0,0.0;0.0
A4	**(11)**	T = 700 °C, Δt = 2h	62%	19.05; 0.27; 0,04
A5	**(13)**	T = 700 °C, Δt = 2h	59%	18.5, 0.22, 0.00

The experiments B2, B3, A4 and A5 illustrated in Table 3.6 follow the temperature profile described in chapter 2 (cf. section 2.2.3.2). Because the decomposition of **(11)** and **(13)** was carried out in a closed Swagelok cell, it is expected to retain carbon and possibly hydrogen in addition to the metal (Co or Mg), W and O.

3.2.3.3 Characterisations

All the above samples have been characterised by the following analysis: PXRD, SEM-EDX and TEM in order to determine the structure and the morphology.

The Powder XRD patterns of B3, A4 and A5 samples are presented below. The intensity of all the spectra below is in arbitrary units. The thermal decomposition of **(11)** and **(13)** under type A and B conditions show peaks due to the crystallinity of its components.

The Scanning Electron Microscopy (SEM) and Transmission Electron Microscopy (TEM) were performed on B2, B3, A4 and A5 samples to provide visual indications concerning the morphologies of the different samples prepared by thermal decomposition under autogenic pressure and in the air. Also, the Energy Dispersive X-ray spectroscopy (EDX) gave information which identifies the chemical elements present in the samples.

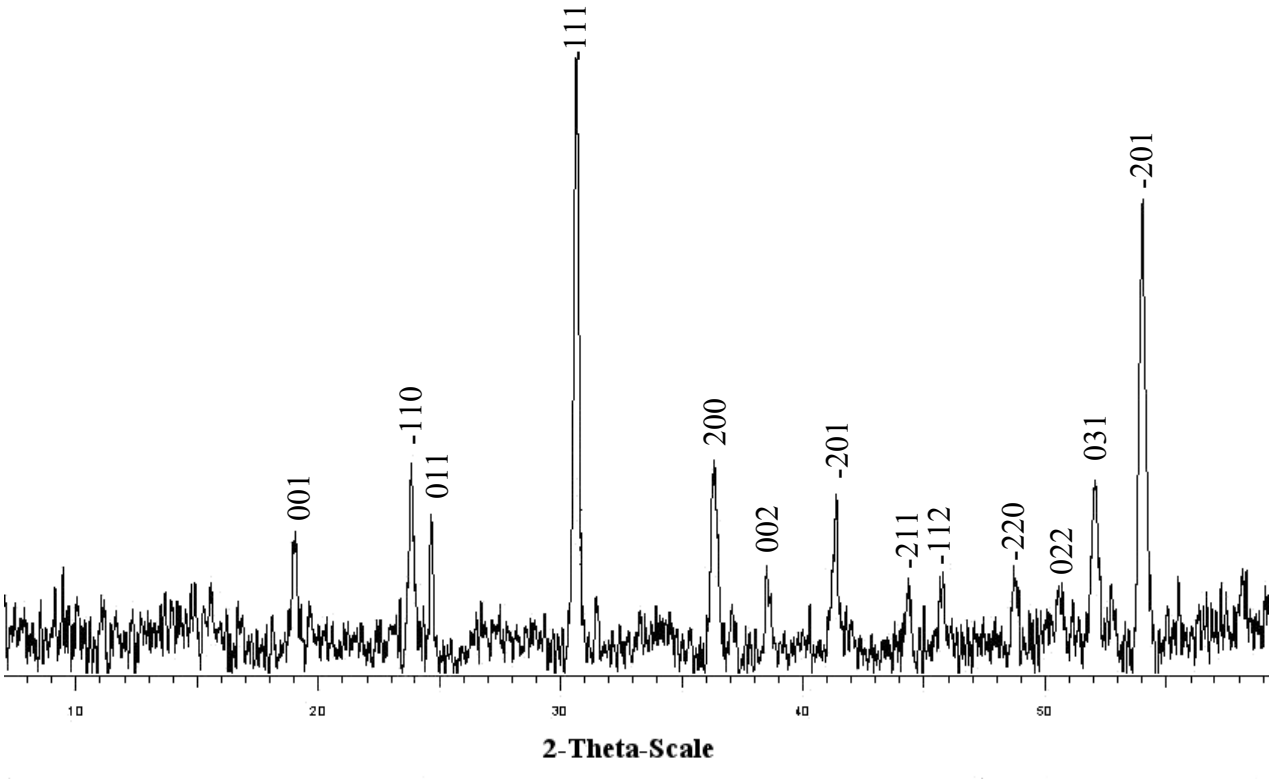

Figure 3.19 PXRD of the thermal decomposition product of $Co_2W_2O_2(acac)_2(OMe)_{10}$ in the air (B3)

The PXRD of B2 sample at 590°C and B3 sample at 700°C give a grey-blue material which demonstrates according to the elemental analysis low carbon content, as the temperature increases (Table 3.6). The as-prepared B2 sample did not show any peaks, revealing its amorphous form but the B3 sample, due to a higher temperature of decomposition at 700°C, displays some small peaks of weak intensity which appear after a long overnight XRD

acquisition. The XRD pattern of the as-prepared B3 sample which shows some crystallinity is presented in Figure 3.18. Peak match software suggested the presence of monoclinic $CoWO_4$. The major diffraction peaks observed at 2θ = 23.801, 24.603, 30.6, 36.325, 54.064° are assigned as (-110), (011), (-111), (200), (-122) reflection lines of the primitive monoclinic phase of $CoWO_4$ which seems to be the main phase in this material. These values are in good agreement with the diffraction peaks intensities of crystalline $CoWO_4$ (PDF 15-0867). And so, this suggests that the phase present in the as-prepared B2 sample is more likely to be amorphous $CoWO_4$.

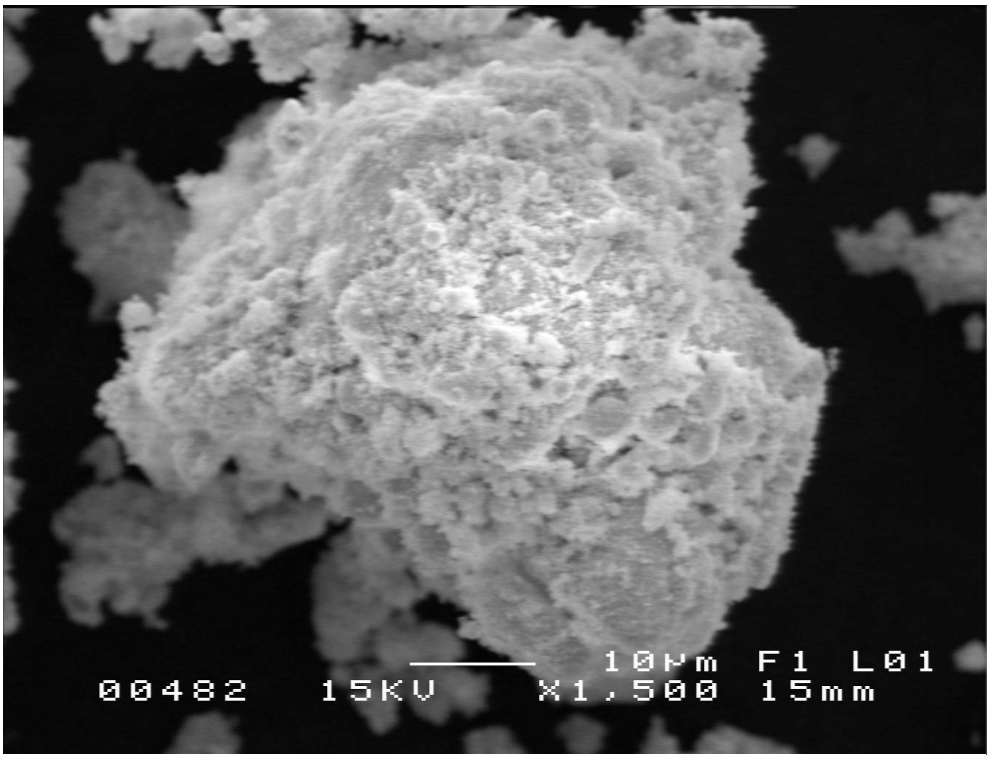

Figure 3.20 Scanning electron micrograph of B2 sample

The thermal decomposition of **(11)** in the air at 590°C (B2 sample) produces different size of lumps which show at the surface smaller particles (Figure 3.20 and 3.21). Currently, no other morphology studies have been done due to the lack of crystallinity of the material. However, TEM could provide information at a lower scale to determine the morphology in more detail. The thermal decomposition of **(11)** in the air at 700°C (B3 sample) produces particles of irregular morphology. It seems that the temperature (700°C) of the decomposition (B3 sample) was too high to yield discrete particles, resulting in the formation of large and gross agglomerates (Figure 3.22).

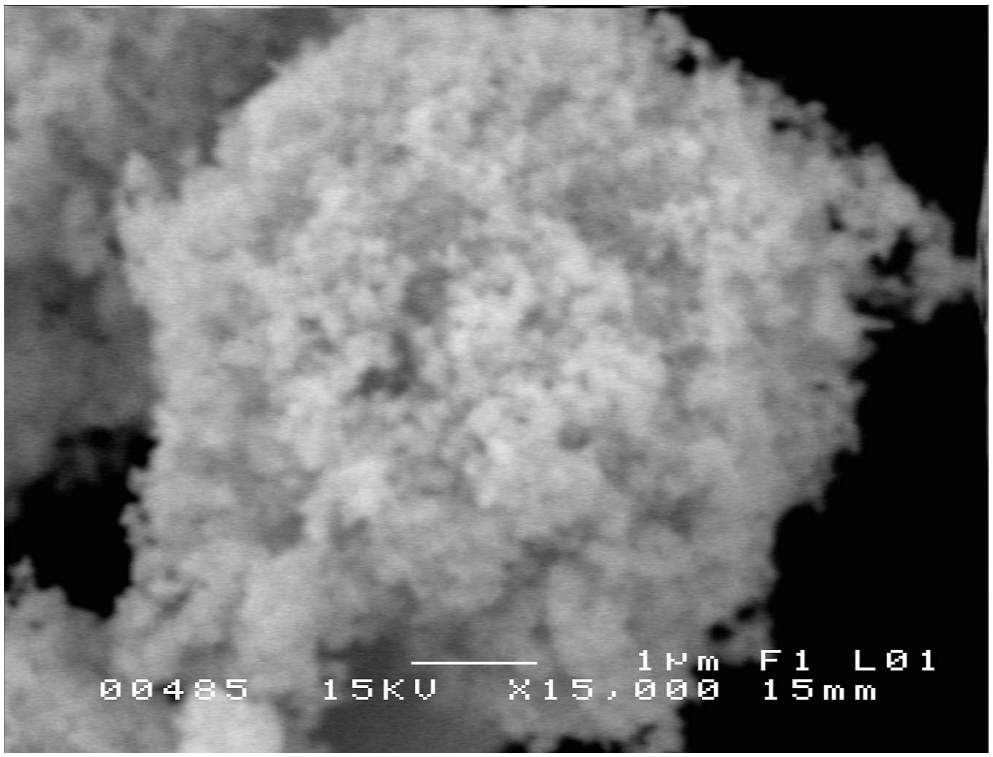

Figure 3.22 Scanning electron micrograph of B2 sample

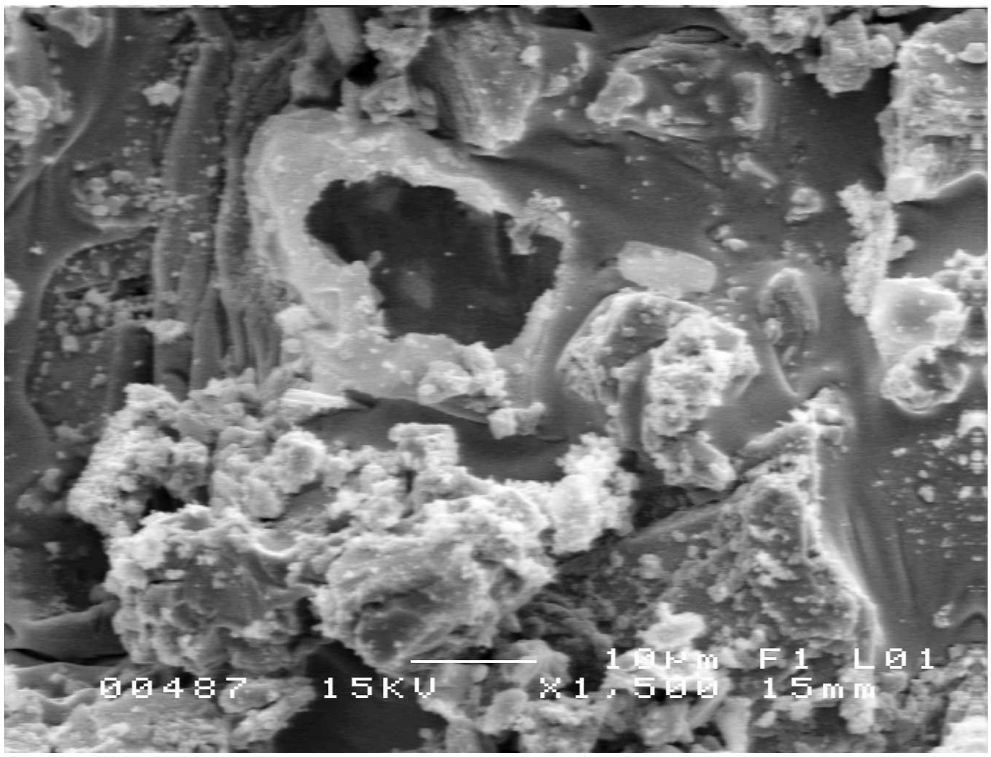

Figure 3.21 Scanning electron micrograph of B3 sample

The XRD pattern of the as-prepared A4 sample is presented in Figure 3.23. Peak match software suggested as well the presence of the primitive monoclinic phase of $CoWO_4$, already reported for the previous products. A4 sample diffracts more intensely than B3, giving a PXRD pattern just after 15 min. of acquisition. The diffraction peaks observed are in good agreement with the diffraction peaks and relative peak intensities of crystalline $CoWO_4$ (PDF 15-0867). The resulted black powder and also the microanalysis confirm the presence of high carbon content (Table 3.6). Indeed, the RAPET reaction of A4 sample contains 19.05% of carbon that is not revealed by the XRD pattern. This suggests the existence in the material of amorphous carbon.

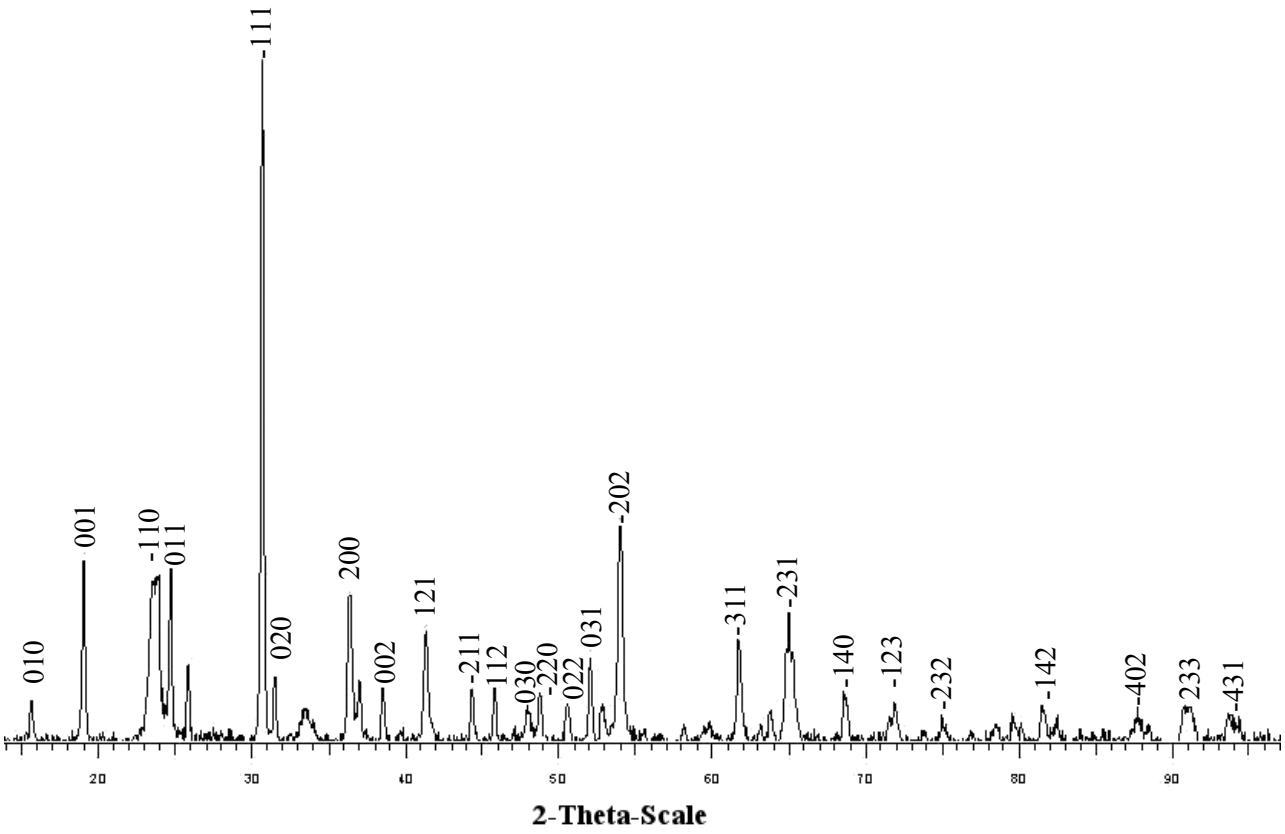

Figure 3.23 Powder XRD of the thermodecomposition product of $Co_2W_2O_2(acac)_2(OMe)_{10}$ under RAPET conditions (A4)

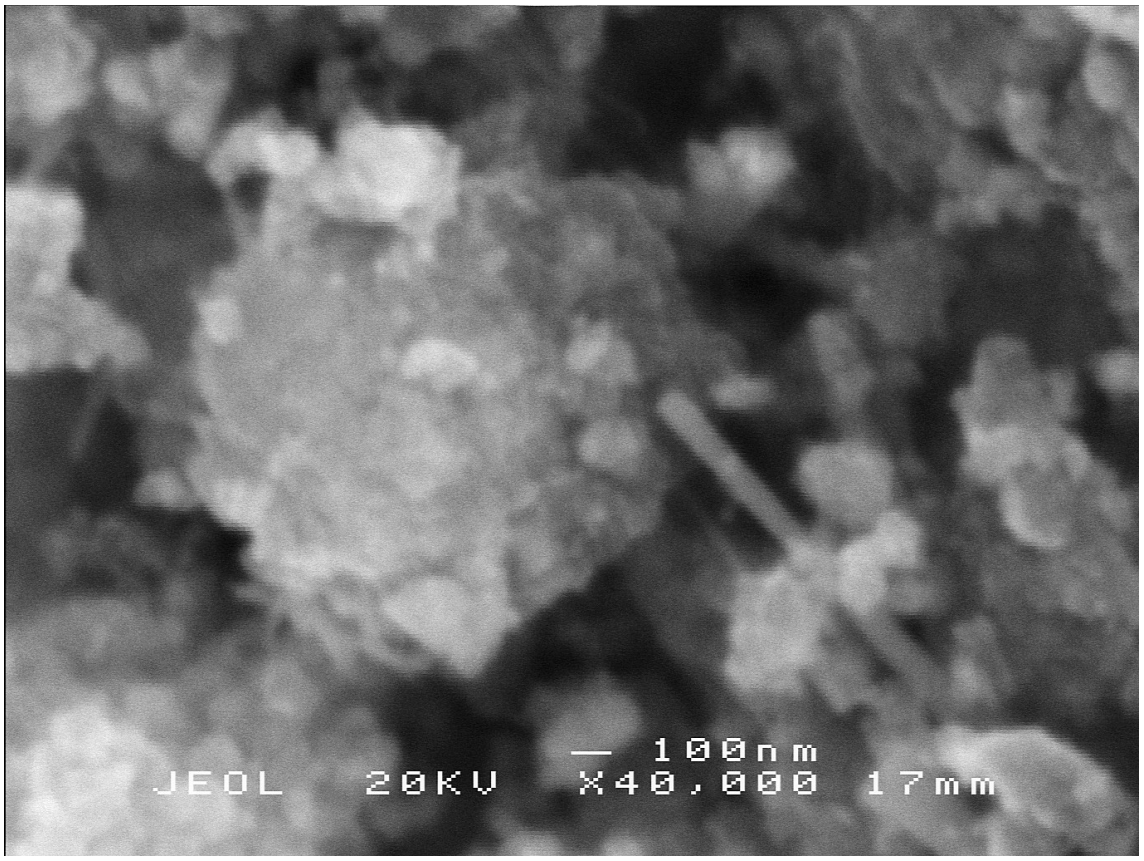

Figure 3.24 Scanning electron micrograph of A4 sample

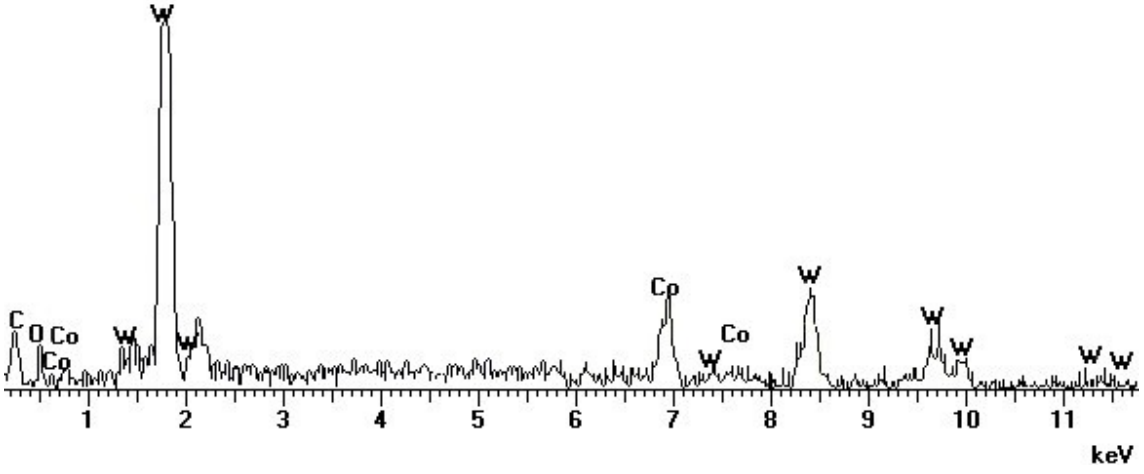

Figure 3.25 EDX of the A4 sample related to the SEM (Figure 3.23)

A preliminary study, including SEM/EDX of A4 sample (Figures 3.24 and 3.25) shows a gross morphology of the bulk, composed of small agglomerates and some thin elongated particles and the presence of the chemical elements Co, W, C and O. The A4 sample

possesses very fine microstructure that was difficult to resolve due to the probable magnetism of the sample containing $CoWO_4$.

TEM was performed on A4 sample, confirming the tube shape and more precisely core-shell nano-structures. The Figures 3.26a-d display independent images of A4 sample, at different magnifications, which show a few lengthened particles of different diameter sizes and of a few micrometers long and also agglomerates of nano-particles.

Hence, these rod shaped structures seem to be surrounded by aggregates of nano-particles containing two types of materials (Figures 3.26a-c):

- Dark nano-particles of irregular shape and size (from a few nanometers to 100nm)
- Bright agglomerates of nano-particles

The Figure 3.26a, composed of two types of components: nanotubes and agglomerates confirms the presence of Co, W, O and C in the A4 sample, as already observed in the SEM/EDX analysis (Figure 3.24 and 3.25). However, the TEM of the nanotubes (Figure 3.26b) reveals by EDX analysis only the presence of W, O and C (Figure 3.28). The presence of Cu is from the copper grid that is used for the TEM sample preparation. It appears most likely that the elongated particles are composed of tungsten oxide WO_x which are probably embedded in a carbon shell. The dark and light contrasts seen in the nanotubes (Figure 3.26d) are composed of two different materials. The core (indicated by a white arrow) and the shell (indicated by a black arrow) are composed respectively of carbon and WO_x. The elemental analysis (Table 3.6) and the EDX (Figures 3.25, 3.27 and 3.28) revealing a high carbon content and the PXRD of A4 sample (Figure 3.23) which does not show any crystalline peak of carbon suggest that the carbon present is presumably amorphous. However, the tube (Figure 3.26d) shows lines oriented along the length of the nanotubes, revealing its crystallinity. Those lines are characteristic to the multi-walled carbon nanotube (Figure 3.26c).[40] The formation of crystalline WO_x in the carbon nanotube is also confirmed by electron diffraction and EDX (Figure 3.28). From these observations, it is clear according to the previous observations that the nanotubes are composed of carbon shell and the core is an *in situ* grown WO_x. The carbon nanotube is surrounded by agglomerates (Figure 3.26c) which contain nano-particles composed of tungsten oxide WO_x, presumably cobalt tungstate $CoWO_4$ in dark color according to the PXRD of A4 (Figure 3.23) and carbon in bright color. The observation of a small amount of WO_x filled nanotubes at the nanoscale by TEM could explain the absence of the significative peaks of carbon and WO_x in the XRD spectrum.

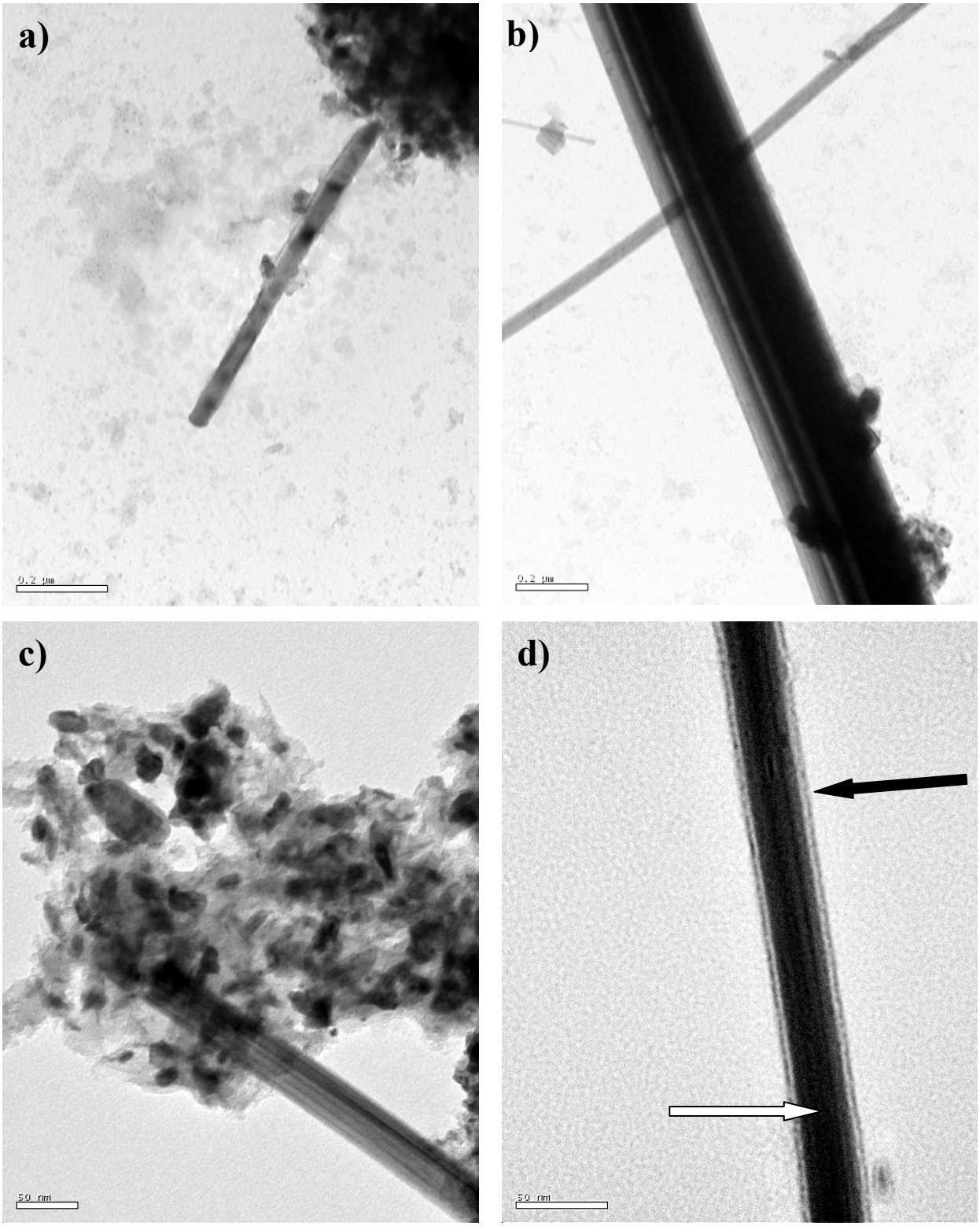

Figure 3.26 Transmission electron micrographs of A4 sample

a) Elongated particle with agglomerates of nanoparticles at its tip
b) Different size of elongated particles
c) Striated tube surrounded by different type of nanoparticles
d) Structure of core/shell nanostructures

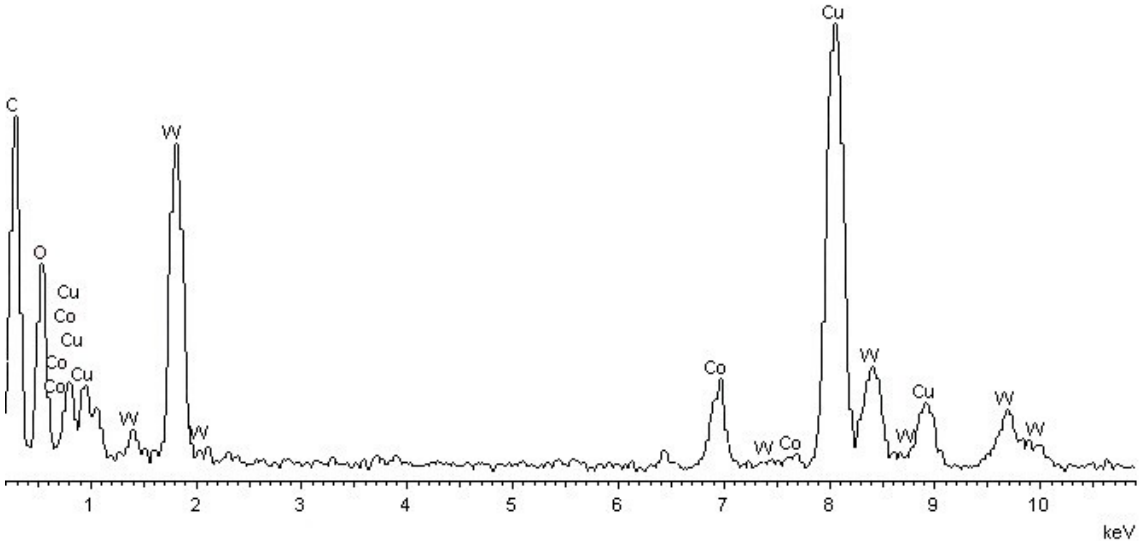

Figure 3.27 EDX of the A4 sample in relation with the TEM (Figure 3.26a)

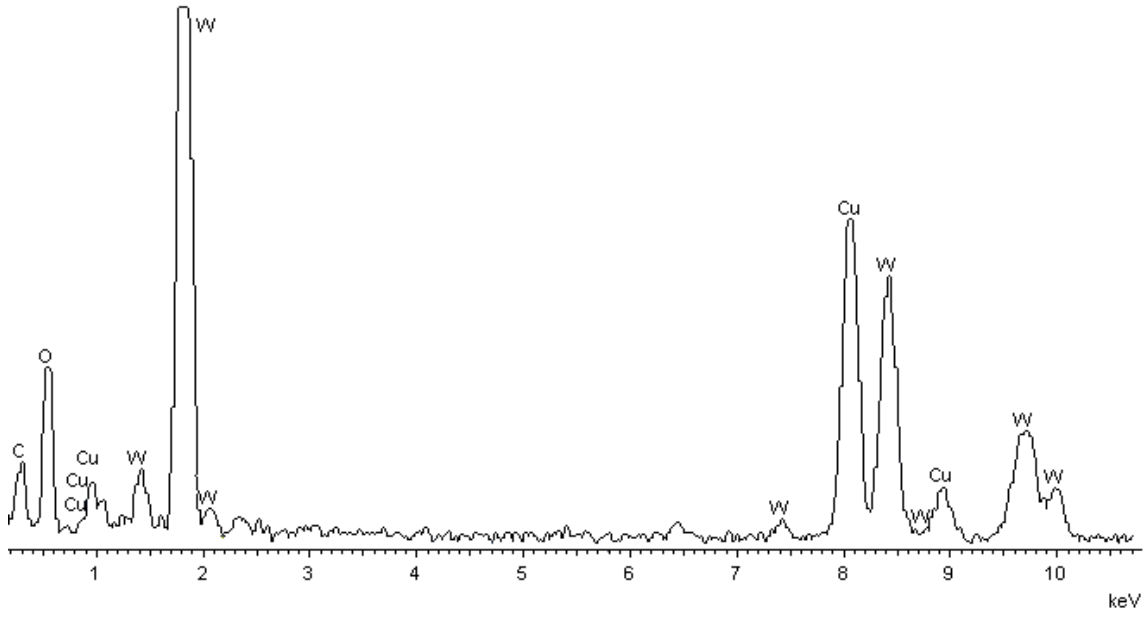

Figure 3.28 EDX of the A4 sample in relation with the TEM (Figure 3.26b)

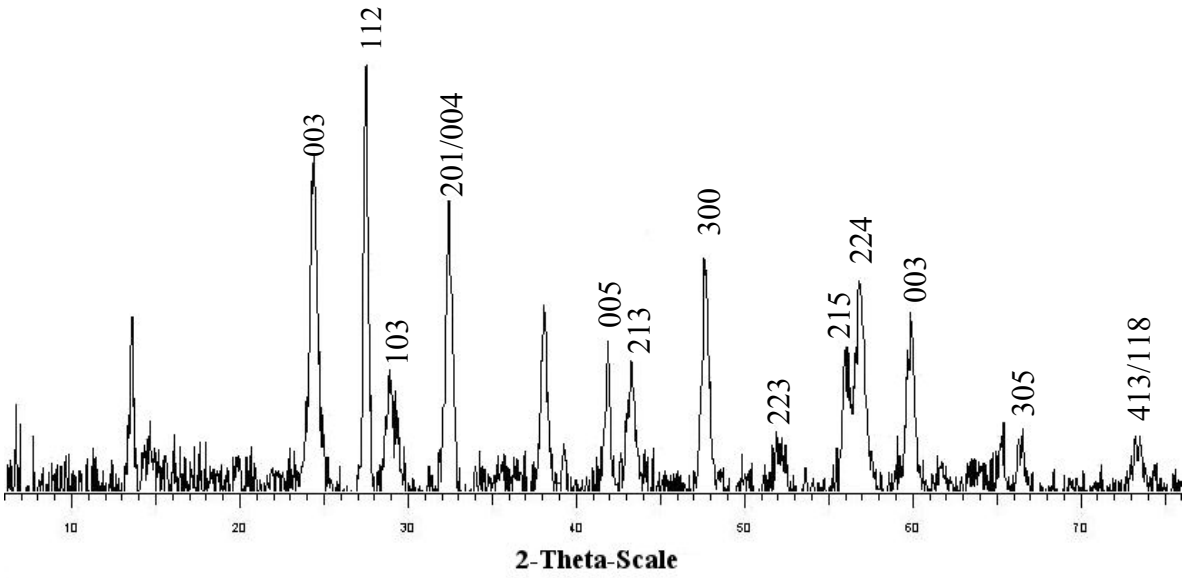

Figure 3.29 Powder XRD of the thermodecomposition product of $Mg_2W_2O_2(acac)_2(OMe)_{10}$ under RAPET conditions (A5)

The XRD pattern of the as-prepared A5 sample is presented in Figure 3.29. Peak match software suggested the presence of the tetragonal phase of $MgWO_4$ in the A5 sample. The diffraction peaks observed at 2θ = 24.191, 27.413, 32.397, 47.410, 56.588° are assigned as (003), (112), (201), (300), (215) reflection lines of the tetragonal phase of $MgWO_4$. These values are in good agreement with the diffraction peaks of $MgWO_4$ (PDF 52-0390). Once again, the XRD spectrum does not display any carbon, in opposition to the elemental analysis which indicates a high carbon content of 18.5%. This reveals the presence of amorphous carbon.

The thermal decomposition in the air of $Mg_2W_2O_2(acac)_2(OMe)_2$ **(13)** at 700°C in a Swagelok cell under inert atmosphere gives rise to a nano-stuctured product. Indeed, the SEM of A5 sample shows large aggregates with smaller individual particles on surface (Figure 3.30). It is composed of some irregular spherical particles of 10 to 30 nm of diameter, some irregular rectangular particles (50 nm of length over 30 nm of large), and also some large rods (Figure 3.31 and 3.32).

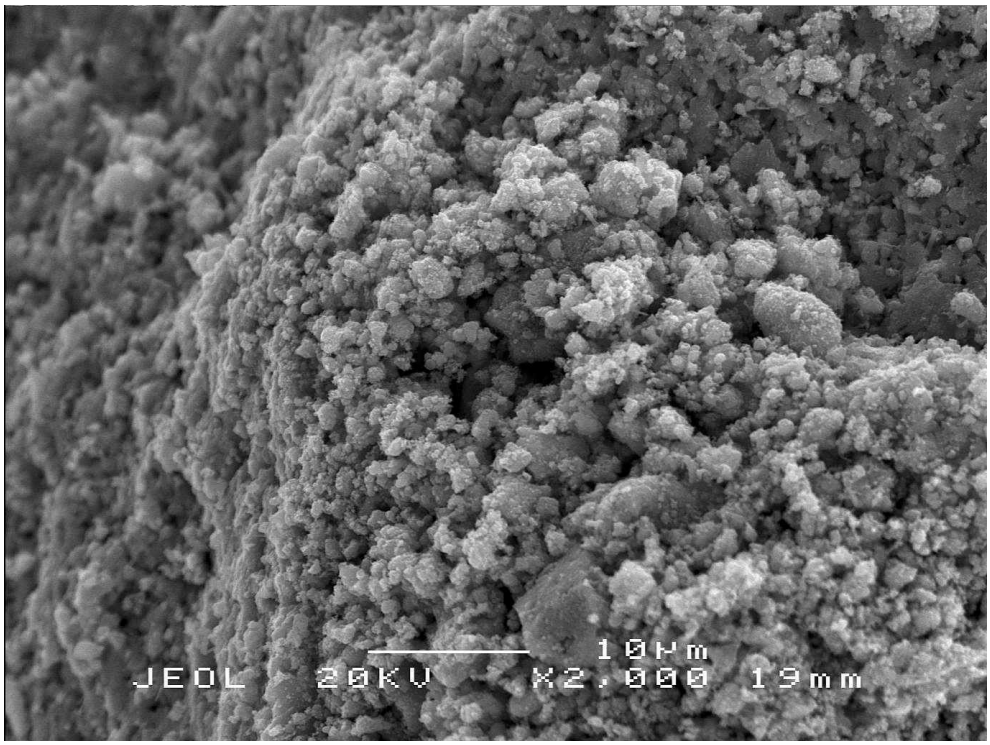

Figure 3.30 Scanning electron micrograph of the A5 sample

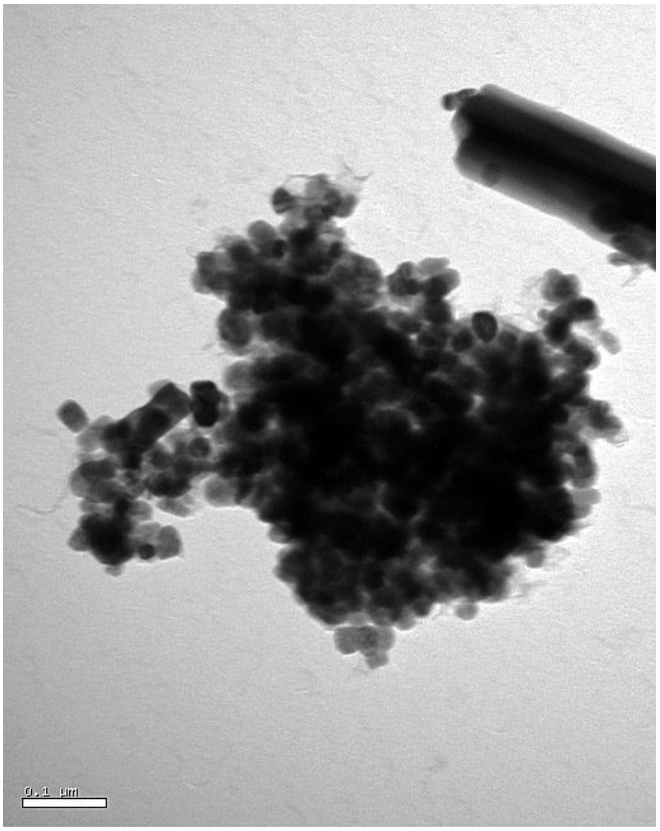

Figure 3.31 Transmission electron micrograph of A5 sample

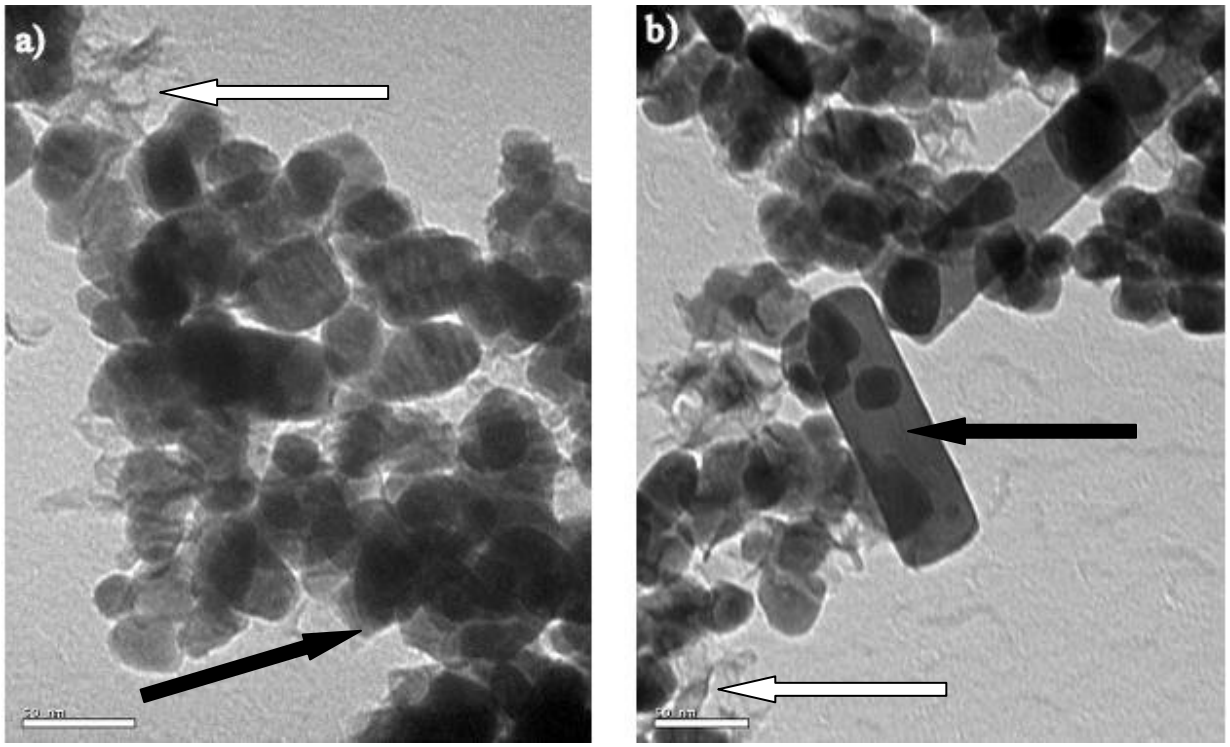

Figure 3.32 Transmission electron micrograph of A5 sample

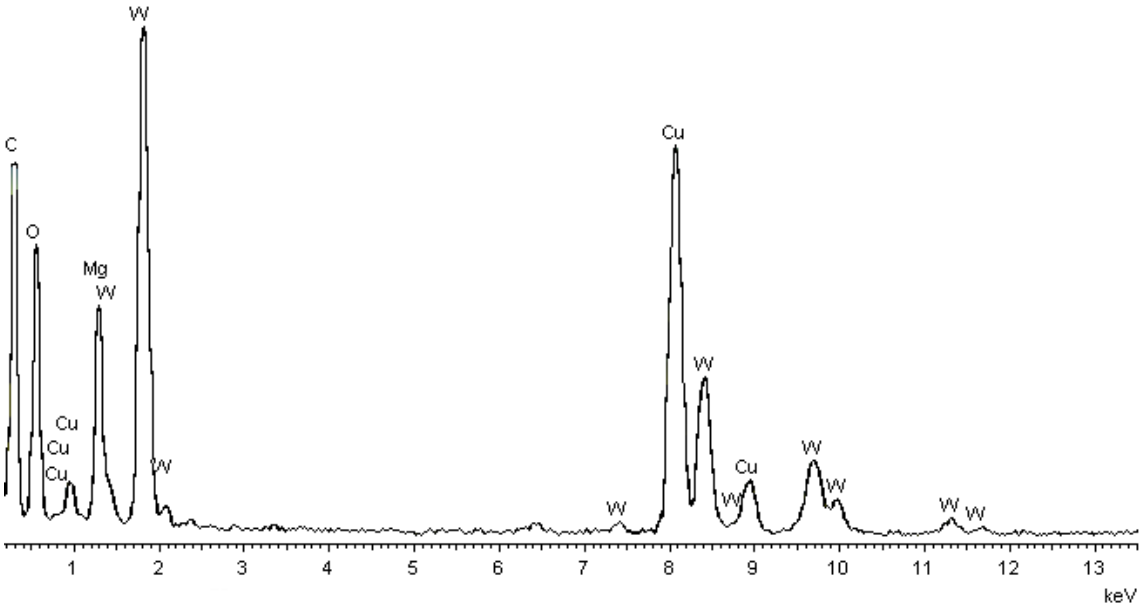

Figure 3.33 EDX of A5 sample in relation to the SEM (Figure 3.32a)

Also, EDX (Figure 3.33) revealed the elements C, W, Mg and O present in the sample. The presence of Cu is from the copper grid that is used for the TEM sample preparation. The microanalysis (18.5%) and the EDX suggest high carbon content. The product obtained during the RAPET decomposition of **(13)** is presumably $MgWO_4$ according to the powder XRD (Figure 3.29).

The A4 sample showed clearly core(WO_x)-shell(C) type nano-structure which is not apparently observed in the case of A5 sample. The dark and light contrast (Figure 3.32a) shows tetragonal $MgWO_4$ in dark color indicated by a black arrow and perhaps carbon nano-particles in bright color indicated by a white arrow. Some rectangular blocks, presumably $MgWO_4$, indicated by a black can further evolve into rods due to the fusion of irregular spheres (Figure 3.32b).

3.3 Conclusion

The application of the single-source precursor approach has permitted the synthesis of diverse heteroleptic heterobimetallic alkoxides. Hence, the interaction of $WO(OPr^i)_3$(bdmap) with $Ti(OPr^i)_4$, $Al(OPr^i)_3$, $Zn(acac)_2$ and $Ni(dmap)_2$ in presence of moisture lead to a range of soluble hetero-metallic tungsten amino-alkoxides compounds: $Ti_2W_2O_2(OPr^i)_6(\mu_2\text{-}O)_4(\mu_2\text{-}bdmap)_2$ **(7)**, $Al_2W_2O_2(OPr^i)_2(\mu_2\text{-}O)_4(\mu_2\text{-}bdmap)_4$ **(8)**, $Zn_2W_2O_2(OPr^i)_2(\mu_2\text{-}O)_3(\mu_3\text{-}bdmap)_2$ **(9)** and $[NiWO(OMe)_2(\mu_2\text{-}O)(\mu_2\text{-}dmap)_2]_4$ **(10)** which have been synthesised and structurally characterised. The use of donor functionalised ligands, such as amino-alkoxides (bdmap, dmap) has allowed formation of strong bridges W-O-M (M = Ti, Al, Zn, Ni) in association with oxo-bridges. These resulting heterobimetallic complexes **(7)-(10)** having all the elements to be incorporated in the deposited film seems to be promising precursor for the AA- and LI-CVD of mixed-metal tungsten oxides due to their solubility and thermal stability.

Prior to the CVD application of the synthesised precursors, a preliminary thermal study under specific conditions (air and RAPET) has been investigated. Hence, the thermo-decomposition of **(10)** under air and RAPET conditions allows respectively formation of nano-particles of $CoWO_4$ and core (C)-shell (WO_x) nanostructures. The thermo-decomposition under RAPET conditions of **(13)** produces nano-particles of $MgWO_4$.

3.4 Experimental section

All manipulations were carried out under a dry nitrogen or argon atmosphere using standard Schlenk techniques and standard glove-box. All dry solvents were purified by an Innovative Technology inc. solvent purification system (SPS).

Anhydrous 2-propanol, Hdmae, was purchased from Aldrich and dried over 3Å molecular sieves. $[W(O)(OR)_4]_2$ (R = -Pr^i, Me)[33] and $Ni(dmap)_2$[20] were synthesised according litterature procedures. $W(O)(OPr^i)_3(bdmap)$ was prepared as described in the experimental section (cf. section 2.3). $Ti(OPr^i)_4$ and $Al(OPr^i)_3$ were purchased from Aldrich and then distilled in vacuum prior to use.

Commercial $Zn(acac)_2.xH_2O$ (x = 1.84; measured by TGA) was purchased from Aldrich and dried with dry toluene and subsequent evaporation, repeated twice and then sublimed twice under vacuum to get an anhydrous Zn(acac). Partially hydrated $Zn(acac).xH_2O$ with (x = 1.0; measured by TGA) was obtained by recrystallisation from dry toluene and then evaporated to dryness. $Co(acac)_2$, $Ni(acac)_2$ were purchased from Aldrich and were dried by vacuum sublimation.[13] $Mg(acac)_2$ was prepared by refluxing magnesium metal with an excess of acetylacetone.[13, 38] The resulting slurry was filtered and the powder obtained were washed with boiling toluene and evaporated to dryness. Co(acac)(OMe), Ni(acac)(OMe), Mg(acac)(OMe) have been synthesised according to the literature procedures.[41-43]

Synthesis of $Ti_2W_2O_2(OPr^i)_6(\mu_2\text{-}O)_4(\mu_2\text{-}Obdmap)_2$ (7)

$W(O)(OPr^i)_3(bdmap)$ was prepared by dissolving $[W(O)(OPr^i)_4]_2$ (2.820 g, 6.42 mmol) in dry toluene (*ca.* 40 mL) and one equivalent of Hbdmap (1.05 mL, 7.05 mmol) was added with stirring. The solution was refluxed for 2 hours and then allowed to cool. Removal of all volatiles *in vacuo* gave a cloudy orange-yellow oily crude product.

This oily crude product was then hydrolysed in a (5:1 mL) mixture of anhydrous toluene and isopropanol at 0°C by adding dropwise a water-isopropanol solution (0.1:2 mL) through a syringe over a period of 2 h under vigorous stirring. The reaction medium was stirred for 20 hours at room temperature, and then refluxed for 24h. The solution was filtered over Celite® and then was concentrated to leave about 3mL of solution. The resulting oil was dissolved in the minimum amount of warm hexane. The flask was then allowed to stand in the fridge (5°C) to give after, a few weeks, colourless crystals. The crystalline white product separated by filtration was washed carefully with cold hexane. Yield = 25%, mp = 136°C

Found (Calc. for) % : C 31.2 (30.86), H 5.36 (6.28), N 4.3 (4.8)

^{1}H NMR (C_6D_6, 300 MHz, 298 K, δ ppm): 1.38-1.58 (6dd, overlapped, 18H, -OCHC***H*****$_3$**, 1.74 (dd, 1H, -C***H*****$_2$**NMe_2, $^{3}J_{HH}$ = 1.7, $^{2}J_{HH}$ = 11.5 Hz), 1.85 (dd, 1H, -C***H*****$_2$**NMe_2, $^{3}J_{HH}$ =1.7, $^{2}J_{HH}$ = 11.47 Hz), 2.40 (t, 1H, -C***H*****$_2$**NMe_2, $^{2}J_{HH}$ = $^{3}J_{HH}$ = 11.47), 2.43 (t, 1H, -C***H*****$_2$**NMe_2, $^{2}J_{HH}$ = $^{3}J_{HH}$ = 11.47), 2.47 (s, 3H, -NC***H*****$_3$**), 2.63 (s, 3H, -NC***H*****$_3$**), 2.69 (s, 3H, -NC***H*****$_3$**), 2.73 (s, 3H, -NC***H*****$_3$**), 4.49 (m, 1H, -OC***H***CH_2NMe_2), 5.33 (m, 2H, Ti-OC***H***Me_2), 5.49 (m, 1H, W-C***H***Me_2)

^{13}C NMR (C_6D_6, 300 MHz, 298 K, δ ppm): 25.77 (-OCH***C***H_3), 25.87 (-OCH***C***H_3), 26.68 (-OCH(***C***H_3), 26.84 (-OCH(***C***H_3), 26.86 (-OCH(***C***H_3), 26.95 (-OCH(***C***H_3),46.34 (-N***C***H_3), 47.72 (-N***C***H_3), 51.65 (-N***C***H_3), 51.7 (-N***C***H_3), 64.31 (-***C***H_2NMe_2), 64.75 (-***C***H_2NMe_2), 69.35 (-***C***HCH_2NMe_2), 76.66 (-O***C***HMe_2), 76.15 (-O***C***HMe_2), 77.5 (-O***C***HMe_2)

E.S.I (tof) M. S. [M-C_3H_8O] + H^+ = 1145.2873 m/z (3.45 ppm error)
Expected $C_{13}H_{31}NO_5W + H^+$

Synthesis of $Al_2W_2O_2(OPr^i)_2(\mu_2\text{-}O)_4(\mu_2\text{-bdmap})_4$ (8)

W(O)(OPr^i)$_3$(bdmap) (0.51 g, 0.98 mmol), Al(OPr^i)$_3$ (0.20 g, 0.98 mmol) and Hbdmap (0.17 mL, 0.98 mmol) were dissolved in dry toluene (10 mL). The solution was refluxed for 15 min. and then allowed to cool. Removal of all volatiles *in vacuo* gave a cloudy orange-yellow oily crude product. This product was then hydrolysed in a (4:1 mL) mixture of anhydrous toluene and isopropanol at 0°C by adding dropwise a water-isopropanol solution (0.1:2 mL) through a syringe over a period of 2 h under vigorous stirring. The reaction medium was stirred for 20 h at room temperature, and then refluxed for 24 h. The solution was filtered over Celite® and then was concentrated to leave about 1 mL. The resulting oil was dissolved in the minimum amount of warm hexane. The flask was then allowed to stand in the fridge (5°C) to give, after a few weeks, colourless crystals. The crystalline white product separated by filtration was washed carefully with cold hexane and then dried *in vacuo* to dryness. Only a small amount has been isolated for X-ray crystallography. No further characterisation has been performed.

Synthesis of $Zn_2W_2O_2(OPr^i)_2(\mu_2\text{-}O)_3(\mu_2\text{-bdmap})_2$ (9)

W(O)(OPr^i)$_3$(bdmap) (0.50 g, 0.957 mmol) was dissolved in 20 mL of toluene, Zn(acac).(H_2O) (0.26 g, 0.92 mmol) was added with stirring. The reaction medium was refluxed for 24h and then allowed to cool. Removal of the volatiles solvent gives an orange-red oil. The recrystallisation of the crude oil in warm hexane afforded after a few weeks at R.T, colorless crystals. The crystalline product separated by filtration was washed with cold hexane and then dried *in vacuo* to dryness. Yield = 10%

Found (Calc. for) %: C 25.8 (30.4) H, 4.76 (5.272), N 4.61 (4.726)

^{1}H NMR (C_6D_6, 300 MHz, 298 K, δ ppm): 1.37 (d, 3H, OCHC***H*****$_3$**, $^{2}J_{HH}$ = 6.21 Hz), 1.63 (d, 3H, $OCHCH_3$, $^{2}J_{HH}$ = 5.97 Hz), 1.82 (dd, overlapped, 1H, OCHC***H*****$_2$**$NMe_2)_2$, 1.92 (s, 6H, acac, C**H$_3$**), 1.93 (dd, overlapped 1H, OCHC***H*****$_2$**$NMe_2)_2$, 1.98 (s, 3H, N(C***H*****$_3$**$)_2$), 2.01(t, 1H, OCHC***H*****$_2$**NMe_2, 2.3 (t, 1H, OCHC***H*****$_2$**NMe_2), 2.72 (s, 3H, N(C***H*****$_3$**$)_2$) 2.75 (s, 3H, N(C***H*****$_3$**$)_2$), 2.91 (s, 3H, N(C***H*****$_3$**$)_2$), 4.51 (m, OC***H***CH_2NMe_2)], 5.17 (s, 1H, acac, C***H***), 5.69 (m, 1H, OC***H***Me_2)

^{13}C NMR (C_6D_6, 300 MHz, 298 K, δ ppm): 25.56 (s, 3H, -OCH***C***H_3), 26.69 (s, -OCH***C***H_3), 28.09 (s, acac, **C**H_3), 44.42 (-N(***C***$H_3)_2$), 48.51 (-N(***C***$H_3)_2$), 48.51 (-N(***C***$H_3)_2$), 51.66 (-N(***C***$H_3)_2$), 65.33 (-$OCHCH_2$***C***H_2NMe_2), 65.88 (-OCH***C***$H_2CH_2NMe_2$), 66.42 (-O***C***$HCH_2CH_2NMe_2$, 72.05 (-O***C***HMe), 99.33 (acac, -***C***H-), 192.28 (acac, -***C***-)

Synthesis of [NiWO(OMe)$_2$(μ$_2$-O)(μ$_2$-dmap)$_2$]$_4$ (10)

$WO(OMe)_4$ (0.50 g, 1.54 mmol) and Ni(dmap) (0.40 g, 0.77 mmol) were dissolved in dry toluene (20 mL). The reaction medium was refluxed for 24h. The green solution was cooled to R.T and then evaporated under reduced pressure to give a green oil. The recrystallisation in toluene/ hexane (1:4) afforded after a few weeks at R.T to green crystals which were separate by filtration**.** Yield = 18 %

Found (Calc. for) % : C 25.5 (25.82), H 4.92 (5.65), N 4.46 (5.23**)**

E.S.I (tof) M. S. $[M\text{-}Na]^+$ = 2185.3885 m/z (6.8 ppm error),
Expected $C_{13}H_{31}NO_5W + H^+$

Synthesis of [CoWO(acac)(OMe)$_5$]$_2$ (11)

1st method

$WO(OMe)_4$ (0.5 g, 1.54 mmol) and $Co(acac)_2$ (0.14 g, 0.73 mmol) (molar ratio Co:W= 1:2.1) were dissolved in dry toluene (7 mL). The reaction medium was refluxed for 15 min. and allow to cool to R.T to afford purple crystals of $[CoWO(acac)(OMe)_5]_2$. After standing at 3°C for 12 hours, the crystals are separated by filtration and then dried *in vacuo*. Yield = 32 %,

2nd method

$WO(OMe)_4$ (2.001 g, 6.17 mmol) and Co(acac)(OMe) (1.185 g, 6.14 mmol) were dissolved in dry toluene (80 mL). The reaction medium was refluxed for 30 min. The yellow solution was

cooled to R.T and then concentrated to afford purple crystals. After standing at 3°C for 12 hours, the crystals were separate by filtration are then evaporated to dryness. Yield = 80%.
mp >230°C
Found (Calc. for) % : C 23.7 (22.7), H 3.85 (4.19)

Synthesis of $[NiWO(acac)(OMe)_5]_2$ (12)

1st method

$WO(OMe)_4$ (0.5 g, 1.54 mmol) and $Ni(acac)_2$ (0.17 g, 0.74 mmol) (molar ratio Co:W= 1:2.1) were dissolved in dry toluene (5mL). The reaction medium was refluxed for 15 min. and allow to cool to R.T to afford colorless crystals of $[NiWO(acac)(OMe)_5]_2$. Yield = 31%

2nd method

Ni(acac)(OMe) (1.184, 6.14 mmol) and $WO(OMe)_4$ (2.001 g, 6.17 mmol) were dissolved in dry toluene (80 mL). The reaction medium was refluxed for 30 min. The clear green solution was cooled to R.T and then concentrated to afford colorless crystals. After standing at 3°C for 12 hours, the crystals were separate by filtration are then evaporated to dryness. Yield = 85%.
mp >230°C
Found (Calc. for) % : C 22.0 (22.71) H 3.95 (4.19)

Synthesis of $[MgWO(acac)(OMe)_5]_2$ (13)

1st method

$WO(OMe)_4$ (0.5 g, 1.54 mmol) and $Mg(acac)_2$ (0.16 g, 0.74 mmol) (molar ratio Mg:W= 1:2.1) were dissolved in dry toluene (5mL). The reaction medium was refluxed for 15 min. and allow to cool to R.T to afford purple crystals of $[CoWO(acac)(OMe)_5]_2$. After standing at 3°C for 12 hours, the crystals are separated by filtration and then dried *in vacuo*. Yield = 31%

2nd method

Mg(acac)(OMe) (1.2 g, 7.62 mmol) and $WO(OMe)_4$ (2.46 g, 7.62 mmol) were dissolved in dry toluene (50 mL). The reaction medium was refluxed for 30 min. The yellow solution was cooled to R.T to afford colorless crystals. After standing at 3°C for 12 hours, the crystals were separate by filtration are then evaporated to dryness. Yield = 85 %. mp >230°C

Found (Calc. for) % : C 25.8 (25.11) H 4.68 (4.64) N 0 (0)
^{1}H NMR ($CDCl_3$, 300 MHz, 298 K, δ ppm) : 1.88 (s, 6H, acac, -C***H₃***), 3.9 (s, 3H, μ_3-OC***H₃***), 4.39 (s, 6H, terminal-OC***H₃***), 4.61 (s, 6H, μ_2-OC***H₃***), 5.28 (s, 1H, acac -CH-)

^{13}C NMR ($CDCl_3$, 300 MHz, 298 K, δ ppm) : 28.33 (s, -O***C***H_3), 55.06 (μ_2-O***C***H_3), 63.77 (μ_3-O***C***H_3), 64.95 (μ_3-O***C***H_3), 99.55 (acac, -***C***H-), 191.04 (acac, -***C***-)

Synthesis of $[ZnWO(acac)(OMe)_5]_2$ (14)

$WO(OMe)_4$ (1.3 g, 4.01 mmol) and $Zn(acac)_2$ (0.503 g, 1.91 mmol), molar ratio Co:W= 1:2.1, were dissolved in dry toluene (20 mL). The reaction medium was refluxed for 15 min. and allow to cool to R.T and then concentrated to afford purple crystals of $[ZnWO(acac)(OMe)_5]_2$. After standing at 3°C for 12 hours, the crystals are separated by filtration and then dried *in vacuo.* The mother liquor is concentrated to give after standing at -20°C for 12 hours the by-product $WO(OMe)_3(acac)$ **(15)**. Yield = 34 %, mp > 230°C

Found (Calc. for) % : C 22.5 (23.12) H 4.00 (4.26)

^{1}H NMR ($CDCl_3$, 300 MHz, 298 K, δ ppm) : 1.91 (s, 6H, acac, -C***H₃***), 3.98 (s, 3H, μ_3-OC***H₃***), 4.52 (s, 12H, terminal and μ_2-OC***H₃***), 5.26 (s, 2H, acac, -C***H***-)

^{13}C NMR ($CDCl_3$, 300 MHz, 298 K, δ ppm): 28.23 (terminal -O***C***H_3), 56.87 (μ_2-O***C***H_3), 64.56 (μ_3-O***C***H_3), 98.93 (s, 1H, acac, -***C***H-), 191.76 (s, acac, -***C***-)

Isolation of $WO(OMe)_3(acac)$ (15) from the Synthesis of $[ZnWO(acac)(OMe)_5]_2$ (14)

Mp = 56°C

Found (Calc. for) % : C 24.2 (21.07) H 4.02 (3.53)

^{1}H NMR (C_7D_8, 300 MHz, 298 K, δ ppm): 1.7 (s, 3H, acac, -C***H₃***), 1.75 (s, 3H, acac, -C***H₃***), 4.41 (s, 6H, -OC***H₃***), 4.65 (s, 3H, -OC***H***-), 5.16 (s, 1H, acac, -C***H***-)

^{13}C NMR (C_7D_8, 300 MHz, 298 K, δ ppm) : 27.23 (s, acac, -***C***H_3), 63.3 (s, -O***C***H_3), 65.32 (s, -O***C***H_3), 104.21 (s, acac, -***C***H-), 186.41 ((s, acac, -***C***-), 194.17 (s, acac, -***C***-)

E.S.I (tof) M. S. $[M\text{-}CH_3O] + H^+$ = 361.0285 m/z (4.91 ppm error)

Expected $C_{13}H_{31}NO_5W + H^+$

Thermodecomposition under "Reaction under autogenic pressure at elevated temperatures"(RAPET)

The thermal decomposition under RAPET conditions of $Co_2W_2O_2(acac)_2(OMe)_{10}$ **(11)** and $Mg_2W_2O_2(acac)_2(OMe)_{10}$ **(11)** were carried out in a 5 mL closed vessel cell. The cell was assembled from stainless steel Swagelok parts.[44] A ½ inch union part was capped on both sides by standard plugs. For these syntheses, 0.5 g of **(11)** and **(13)** are introduced into the vessel at R.T in the nitrogen atmosphere of the glove-box. The filled cell was closed tightly with the other plug and then placed inside an iron pipe in the middle of the furnace. The temperature was raised at a rate of 10°C per minute. The closed vessel reactor (Swagelok) was heated at 700°C for 2 h, then, gradually cooled (1°C/min.) to room temperature, opened with the release of a little pressure, and a dark black powder is collected. The total yields of the above RAPET reaction are respectively 62% and 59%. All yields are relative to the weight of the starting materials.

Thermodecomposition in the air

The decomposition in the air was carried out by introducing in a graphite pot using 0.5 g of $Co_2W_2O_2(acac)_2(OMe)_{10}$ **(11)**. The graphite reactor was placed in the middle of the furnace. The temperature is raised at a rate of 10°C per minute. The graphite vessel is heated at 590°C for 1 h and then gradually cooled (1°C/min.) to R.T. In a second experiment, the decomposition in the air is repeated at 700°C. In both cases, the grey-blue powder product obtained after pyrolysis was not measured.

3.5 References

[1] F. Labrize, L. G. Hubert-Pfalzgraf, J.-C. Daran, S. Halut, P. Tobaly, *Polyhedron* **1996**, *15*, 2707.
[2] A. P. Purdy, C. F. George, *Inorg. Chem.* **1991**, *30*, 1969.
[3] C. P. Love, C. C. Torardi and C. J. Page, *Inorg. Chem.* **1992**, *31*, 1784.
[4] J. V. Singh, R. C. Mehrotra, N. C. Jain, *Synthesis and Reactivity in Inorganic and Metal-Organic chemistry* **1979**, *9*, 79.
[5] M. Veith, S. Mathur and V. Huch, *Inorg. Chem.* **1997**, *36*, 2391.
[6] D. C. Bradley, R. Mehrotra, Ian Rothwell, A. Singh, *Alkoxo and Aryloxo Derivatives of Metals* Elsevier, **2001**.
[7] G.A. Seisenbaeva, E.V. Suslova, M. Kritikos, L. Rapenne, M. Andrieux, S. Parola and V.G. Kessler, *J. Mater. Chem.* **2004**, *14*, 3150.
[8] R. C. Mehrotra, *Coord. Chem.* **1981**, *21*, 113.
[9] G. A. Seisenbaeva, S. Gohil and V.G. Kessler, *J. Mater. Chem.* **2004**, *14*, 3177.
[10] P. Werndrup, G. A. Seisenbaeva, G. Westin, I. Persson, V. G. Kessler, *Eur. J. Inorg. Chem.* **2006**, 1413.
[11] V. G. Kessler, S. Parola, *Dalton. Trans.* **2003**, 544.
[12] E. Suslova, V. G. Kessler, *Inorg. Chem. Comm.* **2002**, *5*.
[13] P. Werndrup, V. G. Kessler, *J. Chem. Soc., Dalton Trans.* **2001**, *5*, 574.
[14] S. Wang, Z. Pang, K. D. L. Smith, Y-S. Hua, C. Deslippe, M. J. Wagner, *Inorg. Chem.* **1995**, *34*, 918.
[15] S. Wang, J. T. Steven, M. J. Wagner, *Inorg. Chem.* **1993**, *32*, 833.
[16] S. Wang, Z. Pang, J. C. Zheng, M. J. Wagner, *Inorg. Chem.* **1993**, *32*, 5975.
[17] S. Wang, Z. Pang, *Inorg. Chem.* **1993**, *32*, 4992.
[18] S. Wang, K. D. L. Smith, Z. Pang, M. J. Wagner, *J. Chem. Soc., Chem.Comm.* **1992**, *21*, 1594.
[19] M. S. El Fallah, F. Badyine, R. Vicente, A. Escuer, X. Solans and M. Font-Bardia, *Dalton Trans.* **2006**, 2934.
[20] P. Werndrup, S. Gohil, V. G. Kessler, M. Kritikos, L. G. Hubert-Pfalzgraf, *Polyhedron* **2001**, *20*, 2163.
[21] M. J. Crosbie, P. J. Wright, H. O. Davies, A. C. Jones, T. J. Leedham, P. O'Brien, G. W. Critchlow, *Chem. Vap. Deposition* **1999**, *5*, 9.
[22] H. O. Davies, A. C. Jones, T. J. Leedham, P. O'Brien, A. J. P. White and D. J. Williams, *J. Mater. Chem.* **1998**, *8*, 2315.
[23] A. C. Jones, N. L. Tobin, P. A. Marshall, R. J. Potter, P. R. Chalker, J. F. Bickley, H. O. Davis, L. M. Smith, G. W. Critchlow, *J. Mater. Chem.* **2004** *14*, 887.
[24] S. R. Breeze, S. R. Breeze, S. Wanga and L. K. Thompson, *lnorganica Chimica Acta* **1996**, *250* 163.
[25] B. F. Johnson, M. C. Klunduk, T. J. OConnell, C. McIntosh and J. Ridland, *J. Chem. Soc., Dalton Trans.* **2001**, 1553.
[26] R. C. Mehrotra, A. Singh, *Chem. Soc. Rev.* **1996**, *25*, 1.
[27] G. Blyholder, J.Springs, *Inorg. Chem.* **1985**, *24*, 224.
[28] D. Braga, F. Grepioni and A. G. Orpen, *Organometallics* **1993**, *12*, 1481.
[29] J. H. Wengrovius, M. F. Carbauskas, E. A. Williams, R. C. Goint, P. E. Donahue, J. F. Smith, *J. Am. Chem. Soc.* **1986**, *108*, 982.
[30] E. Hecht, T. Gelbrich, K.-H. Thiele, J. Sieler, *Z. Anorg. Allg. Chem.* **2000**, *626*, 180.
[31] G. Leggett, M. Motevalli, A. C. Sullivan, *J. Organomet. Chem.* **2000**, *598*, 36.
[32] T. Ozeki, K. Kusaka, Y. N. N. Honma, S. Nakamura, S. Oike, N. Yasuda, H. Imura, H. Uekusa, M. Isshiki, C. Katayama, and Y. Ohashi,, *Chem. Lett.* **2001**, 804

[33] W. Clegg, R. J. Errington, P. Kraxner and C. Redshaw, *J. Chem. Soc. Dalton Trans.* **1992**, 1431
[34] C. K. Williams, A. J. P. White, *J. Organomet. Chem.* **2007**, *692*, 912.
[35] E. L. Lippert, M. R. Truter, *J. Chem. Soc.* **1960**, 4996
[36] M. J. Minch, *Concepts in Magnetic Resonance* **1994**, *6*, 41.
[37] J. A. Bertrand, A. P. Ginsberg, R. I . Kaplan, C.E. Kirkwood, R. L. Martin and R. C. Sherwood, *Inorg. Chem.* **1971**, *10*, 240.
[38] J. A. Bertrand, D. Caine, *J. Am. Chem. Soc.* **1964** *86*, 2298.
[39] D.A. Wright, D. A. Williams, *Acta Crystallogr.* **1968**, *B24*, 1107.
[40] R. andrews, D. Jacques, D. Qian and T. Rantell, *Acc. Chem. Res.* **2002**, *35*, 1008.
[41] J. A. Bertrand, A. P. Ginsberg, R. I . Kaplan, C. E. Kirkwood, R. L. Martin and R. C. Sherwood, *Inorg. Chem.* **1971**, *10*, 240.
[42] J. A. Bertrand, D. Caine, *J. Amer. Chem. Soc.* **1964**, *86*, 2298.
[43] M. A. Halcrow, J-S. Sun, J. C. Huffman and G. Christou, *Inorg. Chem.* **1995**, *34*, 4167.
[44] S. V. Pol, V. G. Pol, A. Gedanken, *Chem. Eur. J.* **2004**, *10*, 4467

Chapter 4
Homo- and Hetero-Metallic Tungsten Amides complexes

4.1 Introduction

Tungsten oxide WO_x and tungsten WN_x films have a number of chemical and physical properties, used for a multitude of applications. On the one hand, the applications of tungsten oxide include gas sensors, electrochromic and photocatalyst devices. On the other hand, tungsten nitride is considered as mechanically resistant coatings and thin layers for diffusion barriers in integrated circuits.

Volatile precursors that allow the deposition of both metal nitride MN_x and metal oxide MO_x are the metal amide complexes, of type $M(NR_2)_x$, which are currently the focus of increasing research activity. Indeed, the use of an inert gas (Ar/N_2) or reductive (H_2/NH_3) as carrier gas with a metal amide precursor is a general route to deposit a metal nitride MN_x.[1, 2] Moreover, metal amides, in combination with an oxygen source, such as water or oxygen gas are used as volatile, oxygen-free precursors for metal oxides films grown by ALD or CVD. The metal amides are simple to prepare because of their volatility,[3] and react rapidly with water (by elimination of amine) or oxygen (by insertion into the M–N bonds), leading to deposition of high quality oxide films. Hence, tantalum(V) oxide has been deposited from $Ta[(NMe_2)]_5$ or $Ta(NEt)(NEt_2)_3$ with H_2O.[4-6] Monometallic amides $M(NR_2)_4$ (M = Zr, Hf, R = Me) type have been used successfully in combination with oxygen in a LP-CVD process to produce carbon, nitrogen-free zirconium and hafnium oxides.[4]

In order to improve the structural, optical, electronic properties of tungsten oxide[7] for photocatalytic and gas sensor devices, the combination of WO_x with another element, such as nitrogen, would permit the preparation of tungsten oxynitride WO_xN_y due to the partial oxidation of the metal nitride deposited. This type of oxidation could proceed during the CVD process or after by post-annealing.

Metal amides can be synthesised by alkane (R = alkyl) or hydrogen (R = H) elimination using a metal alkyl or hydride and an amine.[8]

$$L_nMR + HNR'_2 \rightarrow L_nM(NR'_2) + RH \quad (4.1)$$

Ammonium halide elimination routes have been more widely used for most metal amides, except those of heavy p-block elements due to the creation *in situ* of a stable amino-chloride intermediate.

$$L_nMCl + 2\ HNR_2 \rightarrow L_nM(NR_2) + [H_2NR_2]Cl \quad (4.2)$$

Recently, transmetallation also plays an important role in synthesis of metal amides generalized for most elements M:

$$L_nMX + M'NRR' \rightarrow L_nMNRR' + M'X \quad (M' = Li \text{ or } Na) \qquad (4.3)$$

Different tungsten precursors, such as $W(NBu^t)_2(NHBu^t)_2$,[9] have been synthesised from the ammonium chloride elimination route and have been used as a CVD precursor for the deposition of WN_x. Other complexes, such as $W(NBu^t)_2(NMe_2)_2$, have also been prepared in order to improve their thermal decomposition pathway, *i.e* to reduce the amount of carbon impurity incorporated into WN_x films deposited.[2, 9, 10] These modified precursors can also be used to deposit tungsten oxy-nitride WO_xN_y.[2] $W_2(NMe_2)_6$ has been also utilized for the deposition of tungsten oxide W_2O_3 films by ALD.[11] Furthermore, it is possible to extend the applications of these above precursors by incorporating another metallic element because of the versatile coordination modes of the imido (–NR) and amido ($–NR_2$) complexes, as illustrated in the Figure 4.1.

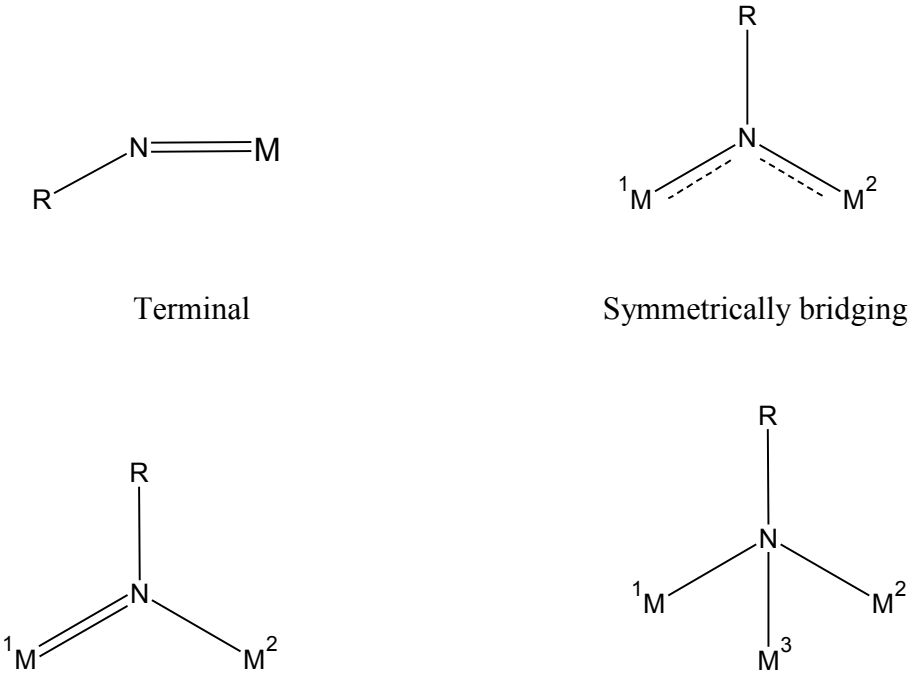

Figure 4.1 Bonding modes of metal imido complexes

In order to obtain heterobimetallic amides, two different routes will be described to functionalize the tungsten amide $W(NBu^t)_2(NHBu^t)_2$. The first involves the deprotonation of $W(NBu^t)_2(NHBu^t)_2$ by a metal organic compound. For instance, the total deprotonation of

$W(NBu^t)_2(NHBu^t)_2$ by LiMe gives rise to $[\{Li_2(\mu\text{-}N^tBu)_3W(N^tBu)\}_2]$, according to the equation (4.4).[12]

$$W(NBu^t)_2(NH^tBu)_2 + 2LiR \rightarrow Li_2W(^tBuN)_4 + 2RH^{\uparrow} \quad (4.4)$$

However, the application with other metal organic reagents which might also be expected to eliminate alkane, such as $ZnMe_2$ and $AlMe_3$ didn't succeed.[12] Hence, the reaction of $W(NBu^t)_2(NHBu^t)_2$ with $ZnMe_2$ leads to a supposed heterobimetallic compound $(^tBuN)(^tBuNH)_2MeW[(N^tBu)ZnMe]$ according to spectroscopic data.[12, 13] This aspect will be discussed below in more details in this chapter. The second way is to use the lithiated species $[\{Li_2(\mu\text{-}N^tBu)_3W(N^tBu)\}_2]$ as suitable starting material for metathesis reactions with metal halides. The reaction with Lewis acids MCl_3 has produced the heterobimetallic amide compounds $W[(\mu\text{-}NBu^t)_2MCl_2]_2$ (M = Ga, Al).[12]

$$Li_2W(N^tBu)_4 + 4\ MCl_3 \rightarrow W[(\mu\text{-}N^tBu)_2MX_2]_2 + 2\ LiMX_4 \quad (4.5)$$

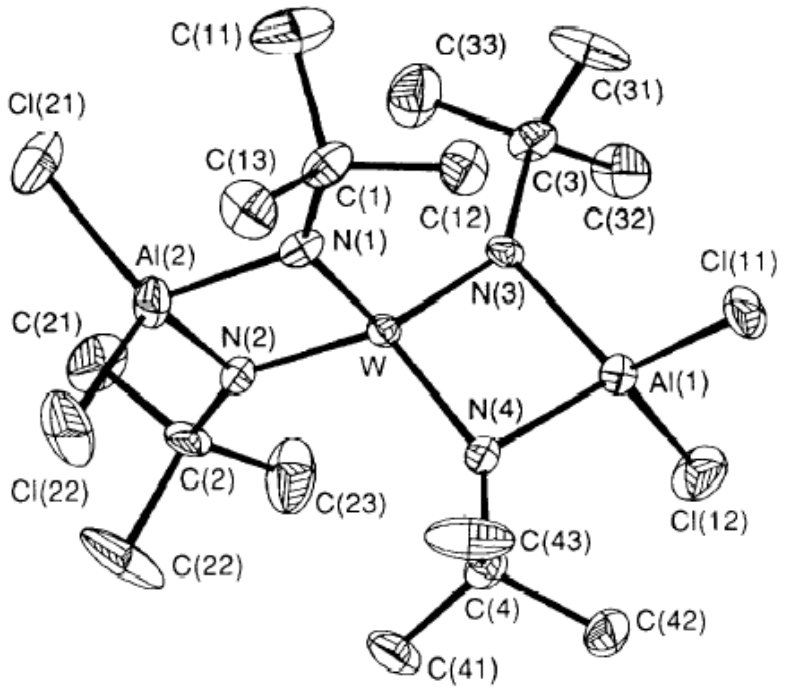

Figure 4.2 Molecular structure of $W[(\mu\text{-}NBu^t)_2AlCl_2]_2$ [12]

However, the same reaction with two equivalents of PX_3 (X = Br, Cl) leads to a more complicated product $W(NBu^t)X_2[P_2(NBu^t)_3]$.[14]

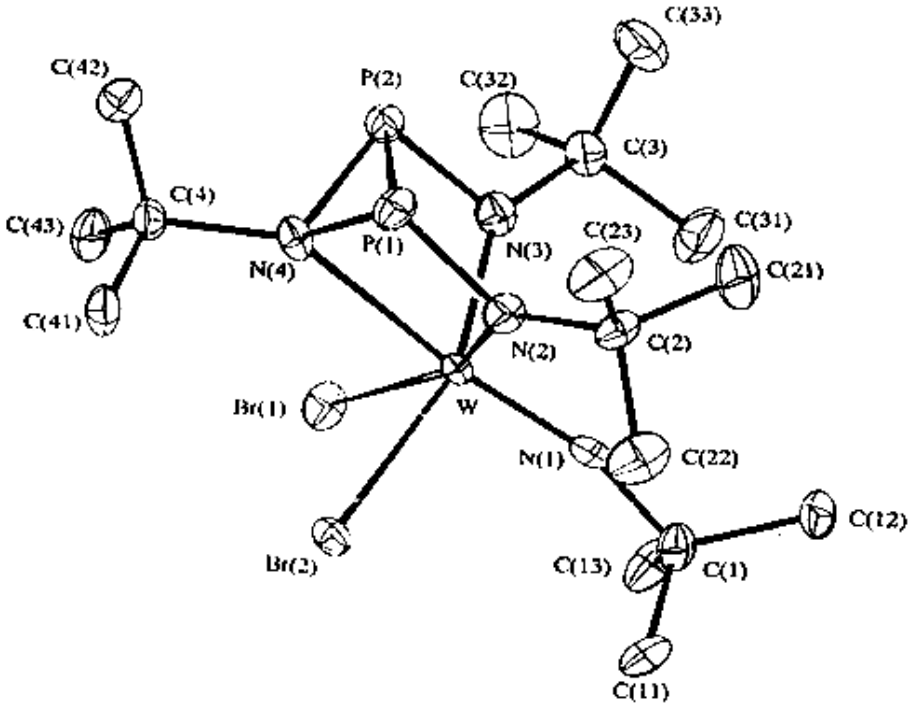

Figure 4.3 Molecular structure of $W(N^tBu)Br_2[P_2(N^tBu)_3]$ [14]

In addition, a new example of a heterometallic amido tin(II) compound $[\{Sn(\mu\text{-}N^tBu)_2W(NBu^t)_2\}_2]$ has been prepared and characterized by reacting $[\{Li_2(\mu\text{-}N^tBu)_3W(NBu^t)\}_2]$ with $SnCl_2$.

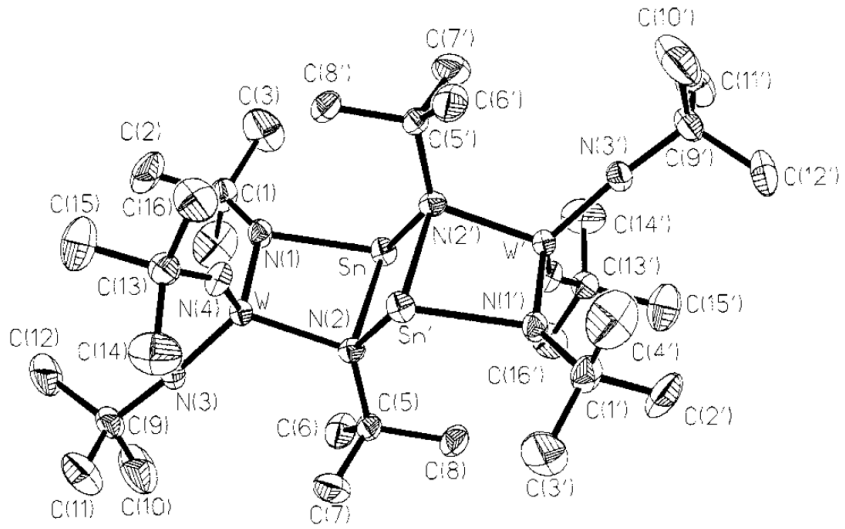

Figure 4.4 Molecular structure of $[\{Sn(\mu\text{-}NBu^t)_2W(NBu^t)_2\}_2]$ [15]

The substituents $-NR^{2-}$ in the molecules described above play an important role of bridging between metals. Very little has been reported concerning the synthesis of hetero-metallic amide complexes as unimolecular precursors for the deposition of multi-component compounds. A novel and promising heterometallic alkoxide-amides $[Ti(O^iPr)_3\{(N(SnMe_3)_2\}]$ in combination with $Zr(O^tBu)_4$ and oxygen as carrier gas, has been shown to be a potential candidate for the MO-CVD of $ZrSn_xTi_yO_z$ films. This has been successfully realized in a first step to obtain this multi-component material. However, it is necessary in a second step to go further in order to eliminate the multi-source approach,[16] that is to say synthesize a SSP possessing all three elements required for the deposition of the desired material.

We report, in this chapter the synthesis, and characterisation of heterobimetallic tungsten amide complexes from $W(NBu^t)_2(^tBuNH)_2$ with potential application in the CVD of $WM_xN_yO_z/WM_xO_y$ and WM_xN_y films in the presence or absence, respectively of oxidative environment.

4.2 Results and discussion

4.2.1 Synthesis and structure of $W(^tBuNH)_2(^tBuN)_2$

Bis(tert-butylimido)bis(tert-butylamido)tungsten $W(NBu^t)_2(NHBu^t)_2$, prepared according to the established procedure, was utilized as a starting material. Hence, tungsten hexachloride WCl_6 reacts in hexane at 0°C with excess of tert-butylamine (1:10) to produce $W(NBu^t)_2(NHBu^t)_2$:[17]

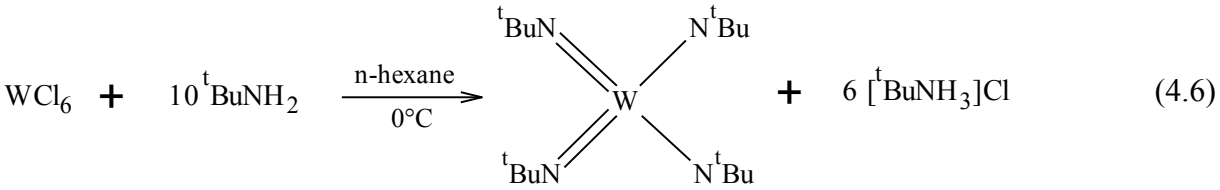

(16) (4.6)

Compound **(16)** is soluble in hexane and was separated easily by filtration from the insoluble tert-butylammonium chloride. The crude pale yellow air and moisture sensitive product was considered pure enough, according to the NMR already reported,[15] to use it as intermediate. No further recrystallisations have been carried out due to the extremely high solubility of **(16)** and the low temperature (-40°C) required to crystallize the compound to remove the impurities. The yield (52%), using this way, is considerably greater than the classic recrystallisation at very low temperature (11 %). In order to obtain a pure compound required

for certain reactions, **(16)** can also be purified easily by sublimation under vacuum (mp: 89-90°C) to increase the yield.[17]

The molecular structure of **(16)** is currently unknown. Indeed, one report has stated it to be monomeric and disordered, though without further comment.[13, 18] The isopropyl analogue, $[W(\mu\text{-}NPr^i)(NPr^i)(NHPr^i)_2]_2$, prepared by the reaction of $W(NBu^t)_2(NHBu^t)_2$ with excess $^iPrNH_2$ in hexane, is known to be dimeric in the solid state.[18, 19] A crystal of **(16)** was obtained by sublimation under vacuum. Nevertheless, the structure (Figure 4.5) is disordered, that is to say the position of the bonds and the atoms represent an average of the real molecule where all the functions are differentiated. Indeed, the imido bond length and angle (W-N(sp)-C) should be *ca.* 1.747 Å and 174° instead of 1.887(11) Å and 151.03(11)° and for the amido bond length and angle (W-N(sp^2)-C) *ca.* 1.975 Å and 132° instead of 1.826(12) Å and 150.74(13)° (Table 4.1) when compared to the structure of $[W(\mu\text{-}NPr^i)(NPr^i)(NHPr^i)_2]_2$.[19]

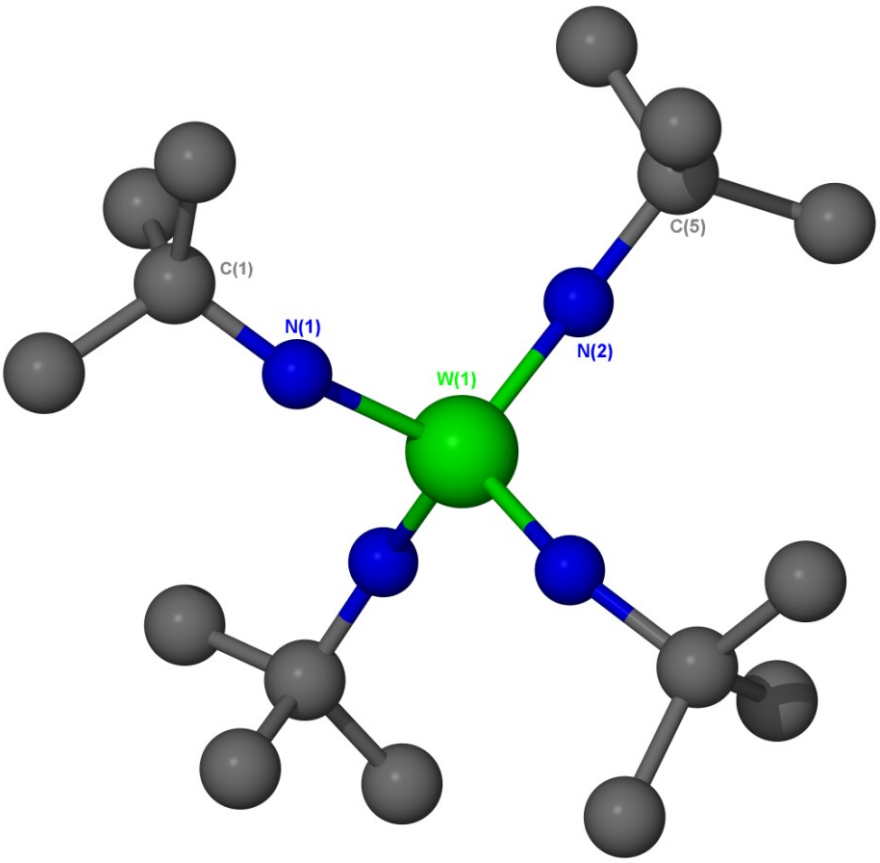

Figure 4.5 Molecular structure of $W(^tBuNH)_2(^tBuN)_2$ **(16)**

Table 4.1 Selected bond lengths (Å) and angles (°) of **(16)**

W-N(1)	1.887(11)	W-N(2)	1.826(12)
N(2)-W- N(2)	111.8(10)	N(2)-W-N(1)	106.0(6)
N(2)-W-N(1)	112.5(5)	N(2)-W-N(1)	112.5(5)
N(2)-W-N(1)	106.0(6)	N(1)-W-N(1)	108.0(10)
C(1)-N(1)-W	151.03(11)	C(5)-N(2)-W	150.74(13)

Symmetry equivalent atoms generated by symmetry transformation: x, ½-y, ½-z

Due to the uncertainty of the structure **(16)** (Figure 4.5) which shows a disordered molecule, gas-phase electron diffraction (GED) was performed in order to determine its molecular structure in the gas-phase according to theoretical *ab initio* calculations. This work has been carried out with the collaboration of Prof. D. Rankin at Edinburgh University.[20] It appeared that **(16)** has two conformers in different proportions in the gas phase. Perhaps, this can explain the disordered structure observed in the solid state. Hence, GED in combination with computional calculations shows this tendency and resolves the molecular structure into two conformers which exist in different proportion (Figure 4.6). Also, C1 conformer is doubly-degenerate (two forms are identical confirmed by GED) meanwhile C2 conformer shows no degeneracy. All these ambiguities suggest perhaps why it is difficult to characterize **(16)** in its solid state. (Figure 4.5).

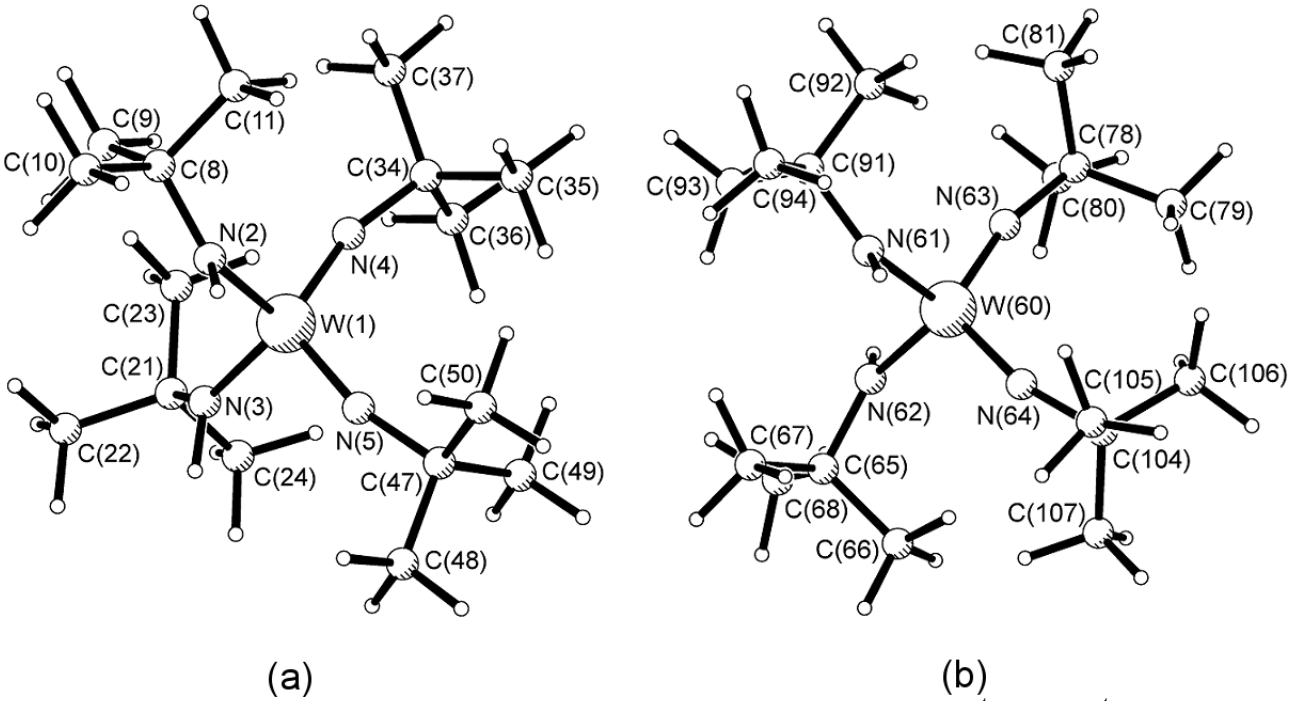

Figure 4.6 Gas-phase molecular structures of the two conformers of $W(NBu^t)_2(NHBu^t)_2$ **(16)**: (a) conformer 1 with C_1 symmetry, and (b) conformer 2 with C_2 symmetry.

4.2.2 Synthesis and structure of $MeZn(NH_2{}^tBu)(\mu_2\text{-}N{}^tBu)_2W(N{}^tBu)Me$

$MeZn(NH_2{}^tBu)(\mu_2\text{-}N{}^tBu)_2W(N{}^tBu)Me$ **(17)** was prepared from the reaction of $W(NHBu^t)_2(NBu^t)_2$ (freshly sublimed) with $ZnMe_2$ in anhydrous hexane solution at -78°C, as displayed in the equation (4.7):

$$W(^tBuNH)_2(N^tBu)_2 \textbf{(16)} + ZnMe_2 \xrightarrow[-CH_4]{\text{Hexane/-78°C}} MeZn(NH_2{}^tBu)(\mu\text{-}N^tBu)_2W(N^tBu)Me \textbf{(17)} \quad (4.7)$$

The solution was warmed to room temperature until complete solubilisation, resulting in a clear yellow solution. Recrystallisation in hexane afforded the air and moisture sensitive compound **(17)**. Prior to use, **(16)** was sublimed in order to give quantitative yield.

Under the same conditions, a hexane solution of $AlMe_3$ was added in excess, slowly at R.T, to a solution of freshly sublimed $W(NBu^t)_2(NHBu^t)_2$ in hexane. The resulted clear brown solution, stirred for 12 hours, was concentrated and then cooled to -20°C to produce red-orange crystals of $[Me_2(N^tBu)W(\mu\text{-}N^tBu)]_2$ **(18)**.

$$W(^tBuNH)_2(N^tBu)_2 \textbf{(16)} + AlMe_3 \text{ (excess)} \xrightarrow{\text{Hexane}} [Me_2(N^tBu)W(\mu\text{-}N^tBu)]_2 \textbf{(18)} \quad (4.8)$$

According to Nugent et al.,[12] $Me_2Al(\mu\text{-}N^tBu)_2(N^tBu)(NH^tBu)$ **(18')** was actually obtained during the deprotonation reaction of **(16)** with $AlMe_3$ [Eq.(4.8)]. This interpretation was made by Nugent without further comment.[12] Perhaps, assuming that **(18')** was actually formed according to Nugent et al., the compound **(18')** could be synthesised in stoichiometric ratio (1:1) as an intermediate of **(18)**.

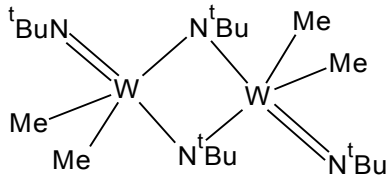

(18)

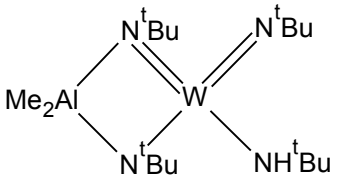

(18')

In the reaction between **(16)** with $AlMe_3$ [Eq.(4.8)], the unknown by-product containing the aluminium metal has not been isolated due to its high solubility in hexane and the presence of impurities. Compound **(18)** can be explained by a ligand exchange between $W(^tBuNH)_2(^tBuN)_2$ and $AlMe_3$. We can presume according to the ligand exchange occurring during the reaction [Eq.(4.8)] that $[AlMe(NBu^t)]_n$ is present in the mother liquor. The known

compound **(18)** has been already synthesised from a different route.[13] Indeed, **(18)** has been previously synthesised from **(16)** in two steps [Eq.(4.9)], instead of one, as reported above [Eq.(4.9)] .

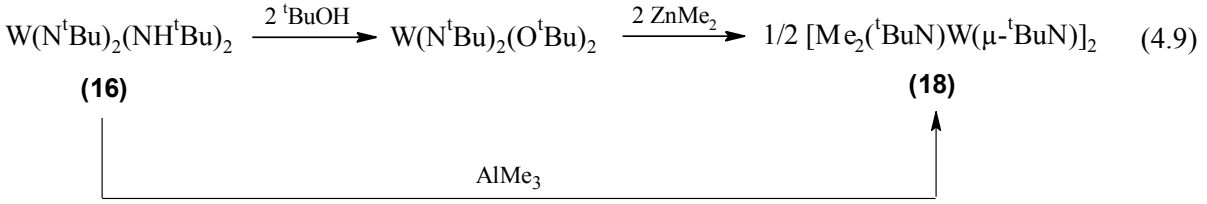

(4.9)

Nugent et al. had attempted a direct synthesis from **(16)** to **(18)** using $ZnMe_2$, but instead, an heterobimetallic compound, believed to be (^{t}BuN)(^{t}BuNH)$_2$MeW[(N^{t}Bu)ZnMe] **(17')** was generated, according to the NMR study.[13] The formulation of the compound synthesised by the reaction of **(16)** with $ZnMe_2$ is erroneous. Instead of **(17')**, MeZn(NH$_2$^{t}Bu)(N^{t}Bu)$_2$W(N^{t}Bu)Me **(17)**, which has the same ^{1}H NMR spectrum as **(17')**, was actually synthesised, according to the crystal structure illustrated in the Figure 4.7, which shows the presence of a neutral amine ^{t}BuNH$_2$. Indeed, there is a ligand exchange of one tert-butylamine (^{t}BuNH) and one methyl (Me) group between W(^{t}BuNH)$_2$(^{t}BuN)$_2$ and $ZnMe_2$ but also a rearrangement with migration of one hydrogen from a tert-butylamine (^{t}BuNH-) bounded to W to the tert-btubylamine (^{t}BuNH-) linked to Zn, resulting in the tert-butylamine ^{t}BuNH$_2$ coordinated via a dative bond to the zinc atom.

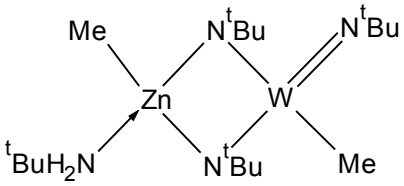

(17)

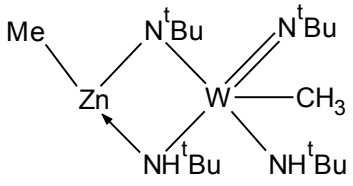

(17')

Compound **(17)** crystallizes in the monoclinic space group $P2_1/n$ with unit-cell parameters, a = 13.7450(2), b = 11.8790(1), c = 15.6730(2) Å, β = 95.366(1), Z = 4. The selected bond lengths and bond angles in relation to the structure (Figure 4.7) are given in Table 4.2. The molecular structure shows a pseudo-planar $ZnWN_2$ square ring in which both tungsten and zinc atoms are tetrahedral. The methyl ligands C(18) and C(17) bound, respectively, to zinc and tungsten atoms are in *trans* position to each other. Also, the tert-butylamine ^{t}BuH$_2$N(4):→Zn associated to the zinc atom by a dative bond is *trans* to the

terminal tert-butylimido ^{t}BuN(1). Indeed, Zn(1) possesses similar Zn-N distances of 2.150(3) Å for Zn(1)-N(3), 2.154(2) Å for Zn(1)-N(4) and 2.147(2) Å for Zn(1)-N(2) which are among the longest bonds of the structure. Zn(1)-C(18) is the shortest bond of zinc coordination sphere with a distance of 1.972(3) Å, consistent with the usual bond [*ca.* 1.94 Å] found in the cubane-like structures [$(MeZnOR)_4$] (M = H, Me, ^{t}Bu).[21] The metals tungsten and zinc are bridged symmetrically by the tert-butyl amido groups ^{t}BuN(2) and ^{t}BuN(3). The terminal ^{t}BuN(1) ligand, near linear with a C(1)-N(1)-W(1) angle of 178.7(2)° and the shortest bond W-N(1) [1.751(2) Å], is consistent with a terminal imido ligand. The bond angles [C(9)-N(3)-W(1)] and [C(5)-N(2)-W(1)] have angles respectively of 142.5(2)° and 141.74(19)°. And, the comparable bond lengths W-N(2) [1.838(2) Å] and W-N(3) [1.841(2) Å] are equivalent with the bridging tert-butylimido found in $[AlMe_2]_2W(\mu\text{-}N^{t}Bu)_4$.[12, 15]

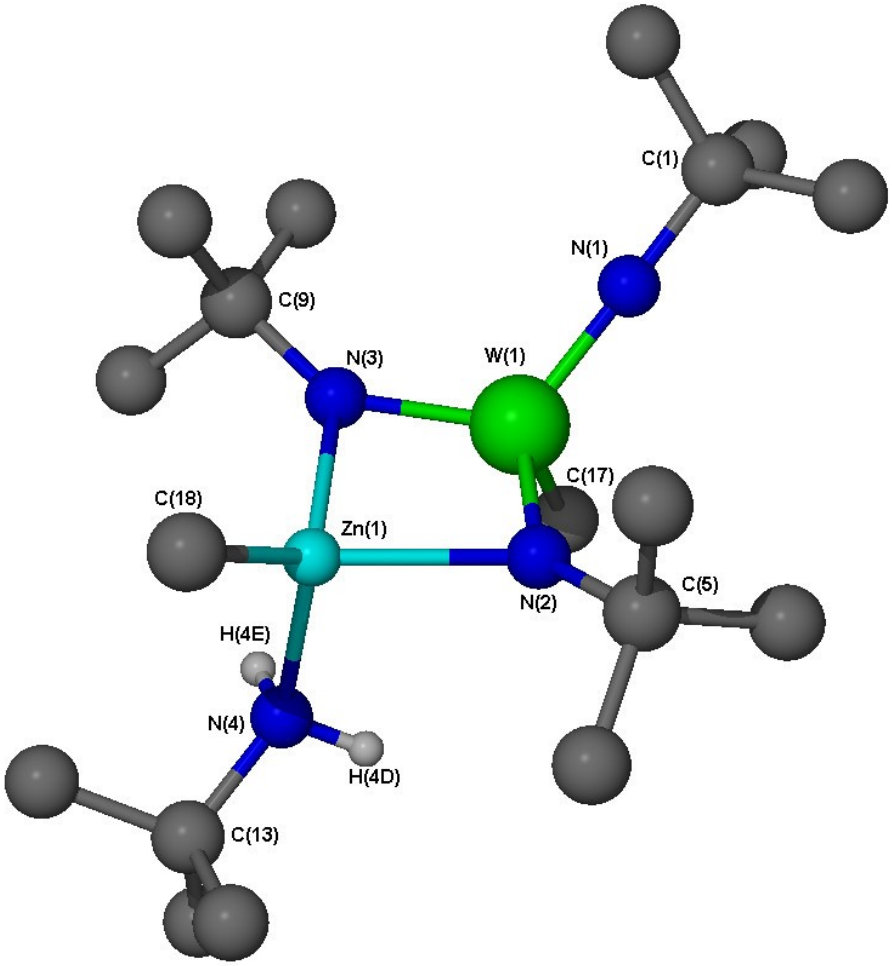

Figure 4.7 Molecular structure of $MeZn(NH_2{}^{t}Bu)(\mu\text{-}N^{t}Bu)_2(N^{t}Bu)WMe$ **(17)**

Table 4.2 Selected bond lengths (Å) and angles (°) of **(17)**

Bond lengths			
W(1)-N(1)	1.751(2)	W(1)-N(2)	1.838(2)
W(1)-N(3)	1.841(2)	W(1)-C(17)	2.149(3)
Zn(1)-C(18)	1.972(3)	Zn(1)-N(3)	2.147(2)
Zn(1)-N(4)	2.150(3)	Zn(1)-N(2)	2.154(2)
N(1)-C(1)	1.450(4)	N(2)-C(5)	1.466(3)
N(3)-C(9)	1.462(4)	N(4)-C(13)	1.497(4)
Bond angles			
N(1)-W(1)-N(2)	118.78(11)	N(1)-W(1)-N(3)	119.74(11)
N(2)-W(1)-N(3)	101.88(10)	N(1)-W(1)-C(17)	103.07(12)
N(2)-W(1)-C(17)	106.49(11)	N(3)-W(1)-C(17)	105.65(12)
C(18)-Zn(1)-N(3)	126.32(13)	C(18)-Zn(1)-N(4)	118.85(13)
N(3)-Zn(1)-N(4)	96.83(10)	C(18)-Zn(1)-N(2)	125.25(14)
N(3)-Zn(1)-N(2)	83.23(8)	N(4)-Zn(1)-N(2)	97.64(9)
C(1)-N(1)-W(1)	178.7(2)	C(13)-N(4)-Zn(1)	124.0(2)
C(5)-N(2)-W(1)	141.74(19)	C(5)-N(2)-Zn(1)	126.53(18)
W(1)-N(2)-Zn(1)	87.32(8)	C(9)-N(3)-W(1)	142.5(2)
C(9)-N(3)-Zn(1)	127.70(19)	W(1)-N(3)-Zn(1)	87.45(9)

4.2.3 Synthesis of tungsten-picnogen amido compounds

4.2.3.1 Synthesis of $Sb_2W(NBu^t)(\mu_2\text{-}NBu^t)(\mu_3\text{-}NBu^t)_2Cl_3(\mu_2\text{-}Cl)$

Firstly, the lithiated compound $Li_2W(NBu^t)_4$ was synthesized according to the literature by total deprotonation of $W(^tBuNH)_2(^tBuN)_2$ **(16)** by LiMe.[12, 15] Prior to the reaction, $SbCl_3$ was purified by azeotropic distillation and multiple sublimations under vaccum.[22] Two equivalents of $SbCl_3$ in toluene were added slowly to the lithiatied solution of $Li_2W(NBu^t)_4$ in toluene at - 78°C :

$$Li_2W(NBu^t)_4 + 2\ SbCl_3 \xrightarrow[-\ 2\ LiCl]{toluene} Sb_2W(NBu^t)(\mu_2\text{-}NBu^t)(\mu_3\text{-}NBu^t)_2Cl_3(\mu_2\text{-}Cl) \quad (4.10)$$

(19)

On slow warming to R.T, the pale yellow solution becomes deep yellow with precipitation of a white powder. Then, the reaction medium turns into an orange-red solution. Solvent removal results in a red oil. The extraction from toluene affords, after concentration and cooling at -20°C, orange-red crystals. The synthesis yields the moderately air and moisture sensitive compound $Sb_2W(NBu^t)(\mu_2\text{-}NBu^t)(\mu_3\text{-}NBu^t)_2Cl_3(\mu_2\text{-}Cl)$ **(19)**, which could be explained by the lithium chloride elimination reaction between $Li_2W(N^tBu)_4$ and two equivalents of $SbCl_3$. This is also accompanied by ligand exchange or migration of chlorine

from antimony to the tungsten atoms. This multi-step reaction implies the formation of unisolable intermediates. The reaction is thus complicated because intermolecular and intramolecular processes may also be involved. However, $Sb_2W(NBu^t)(\mu_2\text{-}NBu^t)(\mu_3\text{-}NBu^t)_2Cl_3(\mu_2\text{-}Cl)$ **(19)** can be thought for simplification as the association of $WCl_2(NBu^t)_2$ and $[Sb(NBu^t)Cl]_2$.

4.2.3.2 Crystal structure of $Sb_2W(NBu^t)(\mu_2\text{-}NBu^t)(\mu_3\text{-}NBu^t)_2Cl_3(\mu_2\text{-}Cl)$

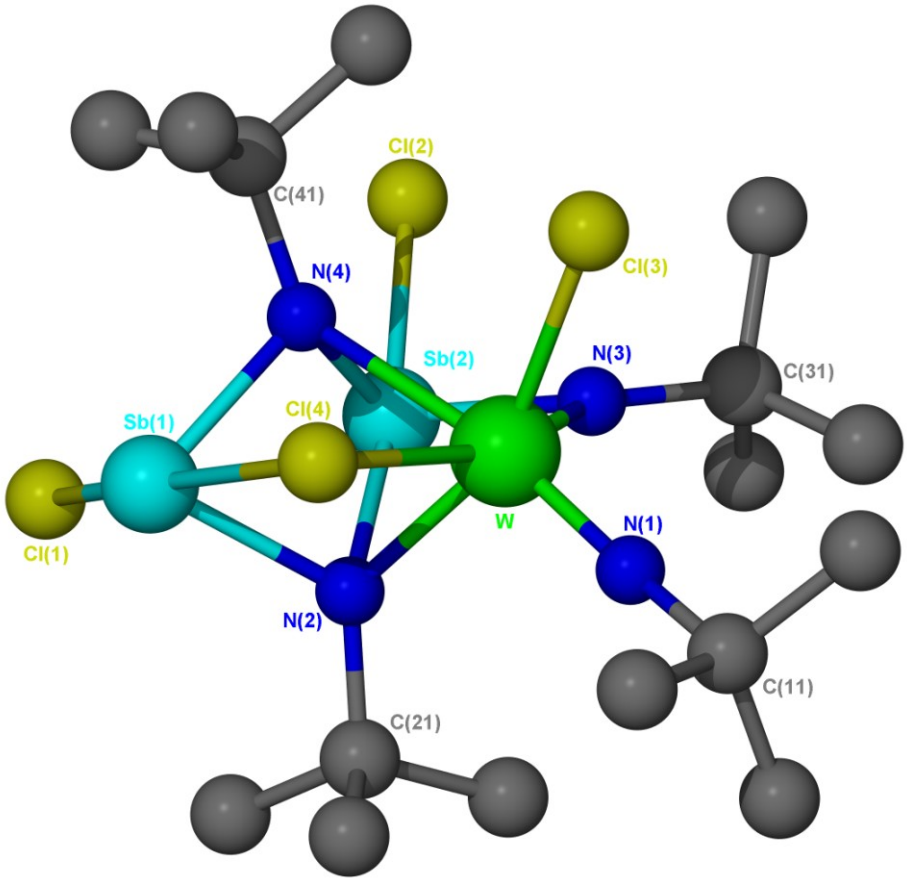

Figure 4.8 Molecular structure of $Sb_2W(NBu^t)(\mu_2\text{-}NBu^t)(\mu_3\text{-}Bu^tN)_2Cl_3(\mu_2\text{-}Cl)$ **(19)**

The compound $Sb_2W(NBu^t)(\mu_2\text{-}NBu^t)(\mu_3\text{-}Bu^tN)_2Cl_3(\mu_2\text{-}Cl)$ **(19)** crystallizes in the monoclinic space group $P2_1/n$ with the unit-cell parameters: a = 14.2340(2), b = 11.8730(2), c = 16.3270(2) Å, β = 105.2920(10), Z = 4. The structure of **(19)** is shown in Figure 4.8 and selected bond lengths, angles are given in Table 4.3. The tungsten atom has an octahedral

geometry forming a WN_4Cl_2 coordination sphere with Cl(3) which is *cis* to Cl(4). The two antimony atoms are trigonal bipyramidal with different chemical environment (SbN_2Cl_2(L) and SbN_3Cl(L)) where L = stereochemically active lone pair.

The shortest bond length W-N(1) [1.735(3) Å] which presents a near linear angle N(1)-W-N(4) [170.69°] is consistent with a terminal imido bond character. The structure has also two types of bridging nitrogen atoms: one is μ_2-bridging SbW[N(3)] and the others two are μ_3-bridging Sb_2W[N(2), N(4)]. The other W-N(3) bond length [1.904(3) Å] is consistent with the amido character of the planar nitrogens.

Table 4.3 Selected bond lengths (Å) and angles (°) of **(19)**

Bond lengths			
W-N(1)	1.735(3)	W-N(3)	1.904(3)
W-N(2)	2.083(3)	W-Cl(3)	2.3770(10)
W-N(4)	2.406(3)	W-Cl(4)	2.5547(10)
Sb(1)-N(2)	2.079(3)	Sb(1)-N(4)	2.092(3)
Sb(1)-Cl(1)	2.4949(12)	Sb(1)-Cl(4)	2.8282(11)
Sb(2)-N(3)	2.117(3)	Sb(2)-Cl(2)	2.4854(10)
Sb(2)-N(4)	2.139(3)	Sb(2)-N(2)	2.473(3)
Bond angles			
N(1)-W-N(3)	106.81(15)	N(1)-W-N(2)	105.55(14)
N(3)-W-N(2)	90.98(13)	N(1)-W-Cl(3)	94.62(11)
N(3)-W-Cl(3)	95.68(10)	N(2)-W-Cl(3)	155.94(10)
N(1)-W-N(4)	170.69(13)	N(3)-W-N(4)	79.25(12)
N(2)-W-N(4)	66.78(12)	Cl(3)-W-N(4)	91.75(8)
N(1)-W-Cl(4)	92.57(11)	N(3)-W-Cl(4)	160.61(10)
N(2)-W-Cl(4)	83.13(10)	Cl(3)-W-Cl(4)	82.98(4)
N(4)-W-Cl(4)	81.45(8)	N(2)-Sb(1)-N(4)	73.13(12)
N(2)-Sb(1)-Cl(1)	95.01(10)	N(2)-Sb(1)-Cl(4)	76.58(9)
N(4)-Sb(1)-Cl(1)	91.62(10)	Cl(1)-Sb(1)-Cl(4)	169.99(4)
N(4)-Sb(1)-Cl(4)	80.83(9)	N(3)-Sb(2)-N(4)	81.41(12)
N(3)-Sb(2)-N(2)	76.18(11)	N(4)-Sb(2)-N(2)	64.74(12)
N(3)-Sb(2)-Cl(2)	103.55(9)	N(4)-Sb(2)-Cl(2)	102.50(9)
N(2)-Sb(2)-Cl(2)	167.22(9)	Sb(2)-N(4)-W	82.40(11)
W-Cl(4)-Sb(1)	73.13(3)	C(11)-N(1)-W	168.2(3)
C(21)-N(2)-Sb(1)	122.2(2)	C(21)-N(2)-W	127.3(2)
Sb(1)-N(2)-W	101.12(14)	C(21)-N(2)-Sb(2)	122.3(3)
Sb(1)-N(2)-Sb(2)	90.61(11)	W-N(2)-Sb(2)	81.91(10)
C(31)-N(3)-W	139.8(3)	C(31)-N(3)-Sb(2)	122.7(3)
W-N(3)-Sb(2)	96.38(13)	C(41)-N(4)-Sb(1)	115.8(2)
C(41)-N(4)-Sb(2)	125.9(2)	Sb(1)-N(4)-Sb(2)	100.27(14)
C(41)-N(4)-W	132.2(3)	Sb(1)-N(4)-W	90.93(11)

The W-μ_3[N(2)] of distance 2.083(3) Å is shorter than the bond W-μ_3[N(4)] [2.406(3) Å] because the steric congestion between the tert-butylamine [^{t}BuN(4)] and Cl(3) seems more important than between [^{t}BuN(2)] and [^{t}BuN(1)]. The Sb-N(4)-Sb bridging nitrogen [N(4)] is *trans* to the remaining tungsten-bonded imido ligand [^{t}BuN(1)].

There are four chlorine atoms: one is bridging [Cl(4)] and the other three are terminal. The Sb(1)-Cl(4) bond length [2.8282(11) Å] is longer than terminal chlorine [Sb(1)-Cl(1), 2.4949(12) Å], [Sb(2)-Cl(2), 2.4854(10) Å], and is consistent with a doubly bridging Chlorine [μ_2-Cl(4)]. The range of W-N, W-N-C, W-Cl bond lengths and angles are as expected for tungsten(VI) species.[12] This structure shows similarities in term of bond length and angles to the structure W(NBu^t)Br$_2$[P$_2$(NBu^t)$_3$] but they are different due to presence of the P-P bond (Figure 4.3).[14]

4.2.3.3 NMR spectrum of $Sb_2W(NBu^t)(\mu_2\text{-}NBu^t)(\mu_3\text{-}NBu^t)_2Cl_3(\mu_2\text{-}Cl)$

The NMR spectrum of Sb$_2$W(N^{t}Bu)(μ_2-N^{t}Bu)(μ_3-^{t}BuN)$_2$Cl$_3$(μ_2-Cl) **(19)** (Figure 4.9) collected in d$_6$-benzene shows three narrow peaks at 1.00, 1.37, 1.46 ppm with approximately a 2:1:1 integrals ratio. A broad peak at 1.8 ppm indicating a molecular exchange is presumably an impurity in relation with free ^{t}BuNH$_2$. There is also an overlapping between the narrow peaks and broad peaks in the area from 1.1 to 1.5 ppm which have made difficult the evaluation of the integrals ratio. Other impurity peaks are indicated by asterics (*). The number of peaks matches with the three different type of ^{t}BuN- ligands in the molecule Sb$_2$W(N^{t}Bu)(μ_2-N^{t}Bu)(μ_3-^{t}BuN)$_2$Cl$_3$(μ_2-Cl) **(19)** (Figure 4.8). Indeed, the signal at 1.0, 1.37 and 1.46 ppm are consistent respectively with the triply bridging μ_3-NBu^t, doubly bridging μ_2-NBu^t and terminal imido ligand of Sb$_2$W(N^{t}Bu)(μ_2-N^{t}Bu)(μ_3-^{t}BuN)$_2$Cl$_3$(μ_2-Cl) **(19)**, illustrated in the Figure 4.8. The NMR spectrum demonstrates that the presence of three types of NBu^t groups, indicating two magnetically equivalent groups. We can note the presence of impurities with similar solubility which may result from hydrolysis products (see next section 4.2.3.4). This could explain the low yield of almost pure product which never exceeds *c.a* 25% based on tungsten.

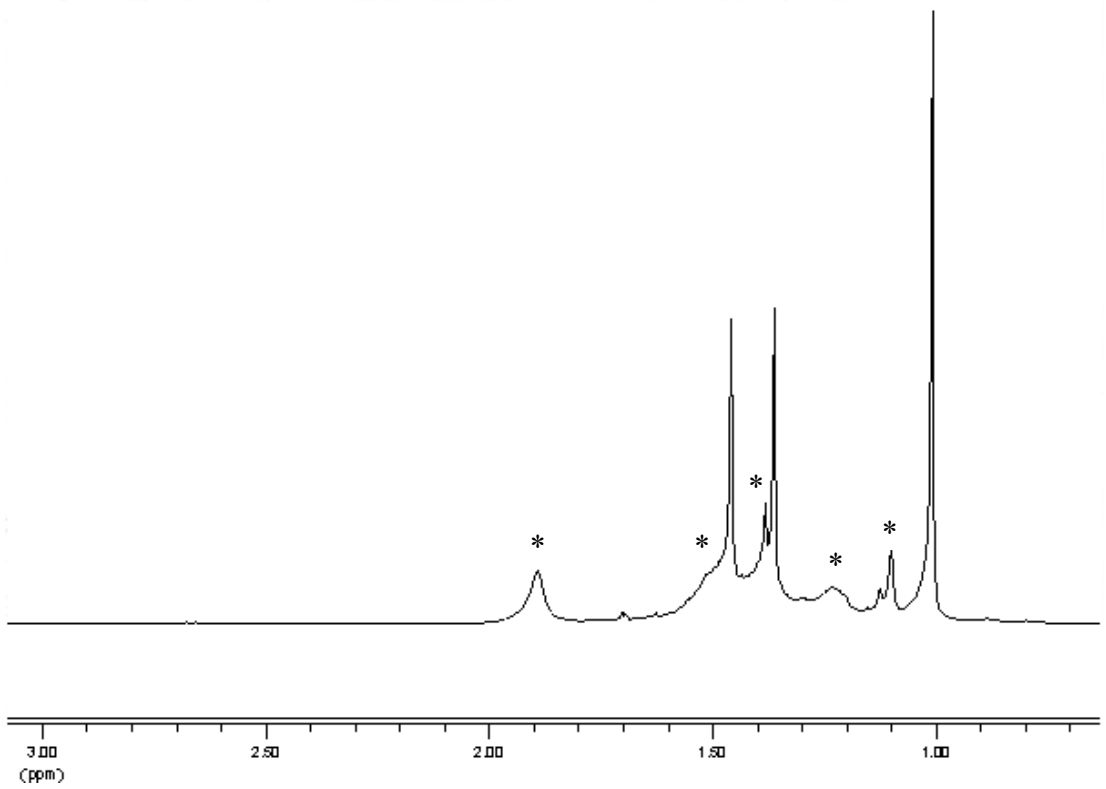

Figure 4.9 NMR of $Sb_2W(NBu^t)(\mu_2\text{-}NBu^t)(\mu_3\text{-}Bu^tN)_2Cl_3(\mu_2\text{-}Cl)$ **(19)** at 298 K

4.2.3.4 Hydrolysis products

The complicated reaction of $Li_2W(N^tBu)_4$ with $SbCl_3$ provides additional products, in particular when a large excess of metal chloride is added (4:1) in regard to the lithiated species. This Sb/W ratio follow the stoichiometry used by G. Wilkinson et al. for the reaction $Li_2W(NBu^t)_4$ with Lewis acid, such as $AlCl_3$ [cf. Eq.(4.5)]. Indeed, the reaction was repeated several times as it proved very sensitive to moisture, and a variety of products was formed resulting from the adventitious incursion of moisture. Hence, different dimeric products $[W(NBu^t)_2(NH_2Bu^t)Cl(\mu_2\text{-}Cl)]_2$ **(20)** and $[Sb(\mu_2\text{-}NBu^t)Cl]$ **(21)**, probably under the presence of moisture (x H_2O), have been synthesised according to the reaction [Eq.(4.11)]. The products isolated from the reaction of $Li_2W(NBu^t)_4$ with $SbCl_3$ [Eq.(4.11)] involve some hydrolysis.

$$2\ Li_2W(NBu^t)_4 + 2\ SbCl_3 \xrightarrow[x\ H_2O]{\text{Toluene}} \underset{\textbf{(20)}}{[W(NBu^t)_2(NH_2Bu^t)Cl(\mu_2\text{-}Cl)]_2} + \underset{\textbf{(21)}}{[Sb(\mu_2\text{-}NBu^t)Cl]_2} \qquad (4.11)$$

Besides the products **(20)** and **(21)** obtained in [Eq.(4.11)], other hydrolysis products have been identified by crystallography, including **(20)** + $SbCl_3$, $Sb_2W_3Cl_7(\mu_2\text{-}O)(\mu_3\text{-}$

$O)_2(NBu^t)_3(NHBu^t)(\mu_2\text{-}NBu^t)_2$ **(22),** $Sb_2W(NBu^t)(\mu_2\text{-}NBu^t)(\mu_3\text{-}NBu^t)_2Cl_3(\mu_2\text{-}Cl)$ **(19) + (22)**. It reveals that the unisolable intermediates of **(19)** are quite unstable in presence of moisture. **(20)** and the starting material $SbCl_3$ have been also isolated from the same type of reaction involving $Li_2W(NBu^t)_4$ and an excess of $SbCl_3$, as already described above. The latest co-crystal seems to be an intermediate of **(20)** and **(21)**. $SbCl_3$ in presence of moisture seems to generate HCl in solution. Hence, the hydrolysis of $SbCl_3$ gives rise first to the antimony oxy-chloride $[SbOCl]_2$ and HCl due to its extreme reactivity, according to the equation [Eq. (4.12)]:

$$2\ SbCl_3 + 2\ H_2O \rightarrow [Sb(\mu\text{-}O)Cl]_2 + 4\ HCl \qquad (4.12)$$

Indeed, the reaction [Eq.(4.10)] requires anhydrous conditions, including dry solvent, purified $SbCl_3$ and also rigorous manipulation under inert atmosphere.

This reaction can be explained by the hydrolysis of $SbCl_3$ which produces HCl in solution which afterwards reacts with $Li_2W(NBu^t)_4$ to yield the monomer $W(NBu^t)_2(NH_2Bu^t)Cl_2$ with an elimination of $^tBuNH_2$. The resulting monomeric compound $W(NBu^t)_2(NH_2Bu^t)Cl_2$, as described by Wilkinson et al.[12] dimerises to give **(20)**. In turn, this by-product $^tBuNH_2$ interacts with $SbCl_3$ to provide $[Sb(\mu_2\text{-}NBu^t)Cl]_2$ **(21)** and HCl, according to the reaction shown in equation (4.13) and suggested by others:[23]

$$SbCl_3 + {}^tBuNH_2 \leftrightarrow \tfrac{1}{2}\,[Sb(\mu_2\text{-}NBu^t)Cl]_2 + 2\ HCl \qquad (4.13)$$

(21)

Concomitantly, HCl reacts again either with $^tBuNH_2$ giving $[^tBuNH_3^+]Cl^-$ or with $Li_2W(^tBuN)_4$ giving the dimer **(20)**. This favors the formation of **(21)** by displacing the equilibrium of the equation [Eq.(4.13)]. Also, **(20)** and **(21)** could also be produced by the hydrolysis of **(19)**.

From the reaction [Eq.(4.10)] involving $Li_2W(NBu^t)_4$ and $SbCl_3$, another compound $Sb_2W_3Cl_7(\mu_2\text{-}O)(\mu_3\text{-}O)_2(NBu^t)_3(NHBu^t)(\mu_2\text{-}NBu^t)_2$ **(22)** has been synthesised in presence of moisture. Here, we presume that a higher amount of moisture has been introduced in regard to the products obtained during the reaction [Eq.(4.11)] due to the presence of oxo-bridges in **(22)**. It seems that the product (**22)** has been formed by partial hydrolysis of **(19)** because another structure (Figure 4.12) showing that **(22)** and **(19)** can co-crystallize in the same unit cell. However, the origin of **(22)** is clearly complex as the W:Sb ratio (3:2) in **(22)** differs from that in **(19)** (1:2), due probably to the greater oxophilic character of tungsten. It could

also involve a reaction with **(20)** according to the coordination sphere surrounding W(2) (Figure 4.12).

An attempt to produce the heterobimetallic bismuth analogue of $Sb_2W(NBu^t)(\mu_2\text{-}NBu^t)(\mu_3\text{-}Bu^tN)_2Cl_3(\mu_2\text{-}Cl)$ **(19)** using the same reaction conditions [Eq.(4.10)], that is to say $Li_2W(NBu^t)_4$ reacting with sublimed $BiCl_3$ in a ratio (1:2), resulted in the synthesis of an air and moisture sensitive compound $[Li(THF)_4]_2[Bi_2Cl_6(NH_2{}^tBu)_2(\mu_2\text{-}Cl)_2]$ **(23)**. In certain cases, another compound $[Li(THF)_4]_2[Bi_2Cl_6(THF)_2(\mu_2\text{-}Cl)_2]$ similar to **(23)**, already reported, has been also isolated when a large excess (4:1) of $BiCl_3$ is used in regard to $Li_2W(NBut)_4$.[24] The appearance of tert-butylamine suggests the introduction of moisture via the solvent and/or the starting material $BiCl_3$. The isolation of **(23)** and $[Li(THF)_4]_2[Bi_2Cl_6(THF)_2(\mu_2\text{-}Cl)_2]$ reveals that the other compound containing the tungsten atom remains presumably in the solution which was not identified.

As observed for $Sb_2W(NBu^t)(\mu_2\text{-}NBu^t)(\mu_3\text{-}NBu^t)_2Cl_3(\mu_2\text{-}Cl)$ **(19)** (see section 4.2.3.1), it is difficult to speculate on the detailed mechanism of the different reaction products due to complex multi-step reactions, but we do recognize the same structural motif $[Sb(\mu\text{-}N^tBu)Cl]$ and $[W(N^tBu)_2Cl_2]$ which re-appears in all the molecules. The intermediate reactions are probably complicated and quite sensitive to moisture.

4.2.3.5 Crystal structures of the hydrolysis products

The reaction of $Li_2W(N^tBu)_4$ with $SbCl_3$ gives rise to a range of hydrolysis products which have been isolated and structurally characterised.

$[Sb(\mu\text{-}NBu^t)Cl]_2$ **(21)** and $[W(NBu^t)_2(NH_2Bu^t)Cl(\mu\text{-}Cl)]_2$ **(20)** co-crystallise in the monoclinic space group $P2_1/n$ with the unit cell parameters: a = 12.5690(3), b = 9.7380(2), c = 21.0410(5) Å, β= 92.1830(10)°, Z = 2. The solid-state structure of **(21)** possesses a dimeric Sb_2N_2 framework with two NBu^t fragments bridging the antimony centers together. The dimeric units **(20)** and **(21)**, each lies on a centre of symmetry. Compound **(21)** has a *trans* geometry, Sb-Cl(3) is *trans* to Sb-Cl(3'). The Sb-Cl bond lengths in the dimeric core are equal [2.408(2) Å] as are the Sb-N bond lengths [2.004(7) Å; 2.021(7) Å]. The angles in the core of Sb-N(4)-Sb" is 102.4(3) Å and the N(4)-Sb-N(4") is 77.6(3)°. $[Sb(NBu^t)Cl]_2$ **(21)** has been synthesized previously but not structurally characterized. The definitive structural investigation of **(21)** was lacking. According to a previous report about $[PCl(NBu^t)]_2$ and $[AsCl(NBu^t)]_2$ which both have a *cis*-geometry, it was assumed that **(21)** also had a *cis*-geometry.[23] Recently, this assumption was challenged by a X-ray diffraction study which

revealed that the conformation of analogous molecules $[Sb(\mu\text{-}NBu^t)(OBu^t)]_2$ and $[SbCl(NHMe_2)(\mu\text{-}NBu^t)]_2$ are *trans*-isomers.[23, 25] The structure **(21)** obtained as part of the co-crystal (Figure 4.10) confirmed definitely the *trans* geometry. The dimeric structure of **(22)** (Figure 4.9) has been reported previously, but as a single species with disordered ^{t}Bu groups linked to NH_2.[12] The two imido ligands W-N(1) [1.741(7) Å] and W-N(2) [1.722(7) Å] have near linear geometries and normal distance. Short hydrogens bonds N-H**….**Cl-W (2.4 Å) are present in both sides of the plane W_2Cl_2 (Figure 4.10). The orientation of **(21)** in regard to **(20)** could probably be explained by the Van der Waals intermolecular interaction between antimony and chlorine atoms Sb'**….**Cl(1) [3.64 Å] which is shorter than the sum of the Van der Waals radii of these element Sb-Cl [4.0 Å]. The tungsten (VI) centers have a distorted octahedral geometry due to the steric interactions between the tert-butyl-imido and amine ligands. The W-Cl-W bridge system is slightly asymmetric with W-Cl distances of 2.613(2) and 2.786(2) Å and a Cl(1)-W-Cl(1') angle of 73.40(6)°.

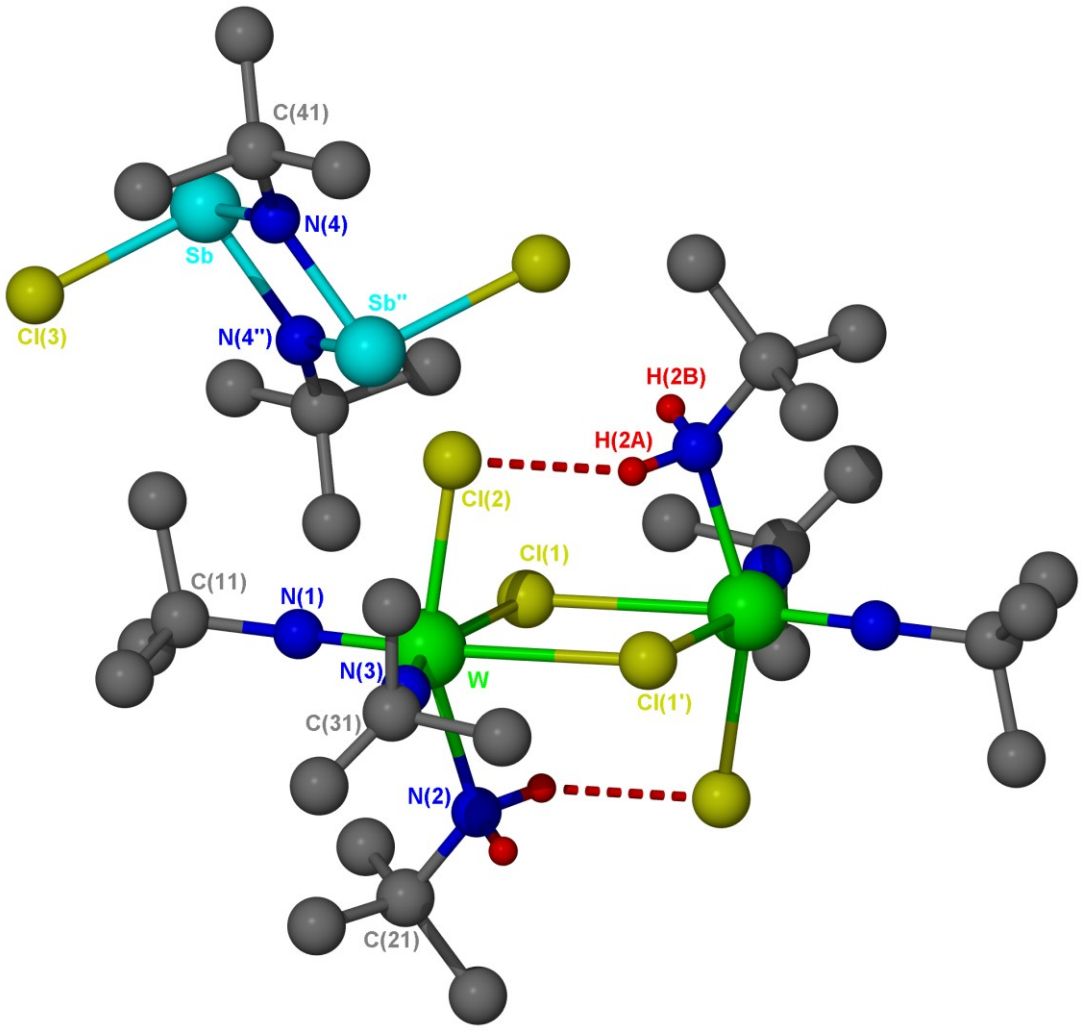

Figure 4.10 Molecular structure of $[W(NBu^t)_2(NH_2Bu^t)Cl(\mu_2\text{-}Cl)]_2$ **(20)** and $[Sb(\mu_2\text{-}NBu^t)Cl]_2$ **(21)** which co-crystallize

Table 4.4 Selected bond lengths (Å) and angles (°) of **(20)** and **(21)**

Bond lengths			
W-N(1)	1.741(7)	W-N(2)	2.209(8)
W-N(3)	1.722(7)	W-Cl(1)	2.613(2)
W-Cl(1')	2.786(2)	W-Cl(2)	2.408(2)
N(1)-Cl(1)	1.469(14)	N(2)-C(21)	1.517(14)
N(3)-C(31)	1.460(12)	N(4)-C(41)	1.474(14)
Sb-N(4)	2.004(7)	Sb-N(4'')	2.021(7)
Sb-Cl(3)	2.423(3)		
Bond angles			
N(3)-W-N(2)	94.1(3)	N(3)-W-N(1)	107.5(4)
N(3)-W-Cl(2)	94.4(3)	N(2)-W-Cl(2)	155.3(3)
N(1)-W-N(2)	102.6(3)	N(1)-W-Cl(2)	96.8(3)
N(3)-W-Cl(1)	160.0(3)	N(1)-W-Cl(1)	92.5(3)
N(2)-W-Cl(1)	79.3(3)	Cl(2)-W-Cl(1)	84.81(7)
N(3)-W-Cl(1)	86.6(3)	N(1)-W-Cl(1)	165.9(3)
N(2)-W-Cl(1')	74.8(2)	Cl(2)-W-Cl(1')	82.59(8)
Cl(1)-W-Cl(1')	73.40(6)	W-Cl(1)-W'	106.60(6)
C(11)-N(1)-W	156.1(7)	C(21)-N(2)-W	126.9(7)
C(31)-N(3)-W	173.5(8)	N(4)-Sb-Cl(3)	98.5(3)
N(4")-Sb-Cl(3)	99.4(3)	C(41)-N(4)-Sb	128.3(6)
C(41)-N(4)-Sb"	129.2(6)	Sb-N(4)-Sb"	102.4(3)
N(4)-Sb-N(4")	77.6(3)		

Symmetry transformations used to generate equivalent atoms: (') -x+2,-y+1,-z ; (") -x+1,-y+1,-z.

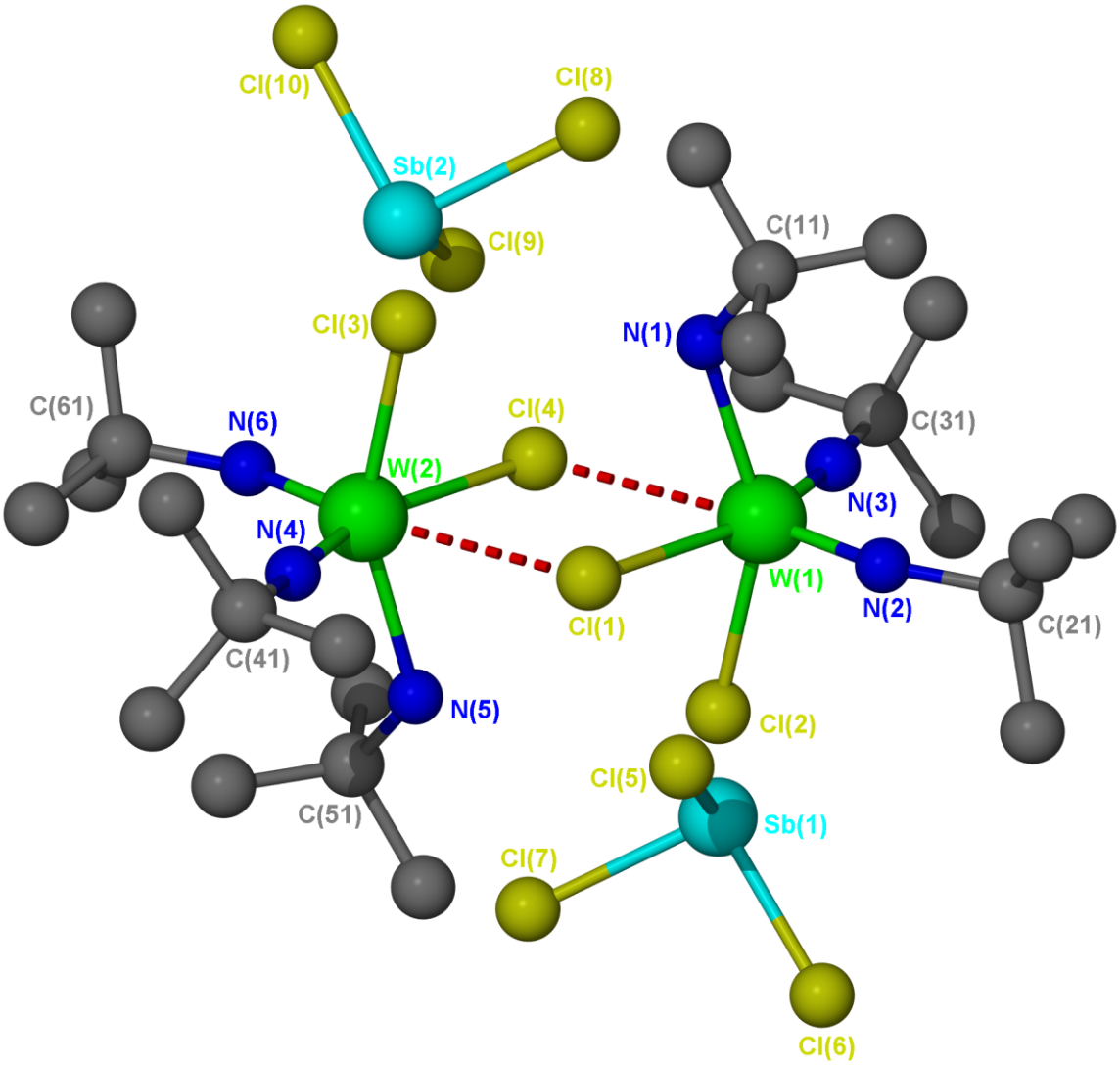

Figure 4.11 Molecular structure of $W(NBu^t)_2(NH_2Bu^t)Cl_2$ **(20)** which co-crystallises with $SbCl_3$

Table 4.5 Selected bond length (Å) and angles (°) of **(20)** and $SbCl_3$

Bond lengths			
W(1)-N(1)	2.231(14)	W(1)-N(2)	1.773(14)
W(1)-N(3)	1.76(2)	W(1)-Cl(1)	2.608(4)
W(1)-Cl(2)	2.394(5)	W(2)-N(4)	1.768(16)
W(2)-N(5)	2.216(16)	W(2)-N(6)	1.802(15)
W(2)-Cl(3)	2.405(4)	W(2)-Cl(4)	2.591(4)
Sb(1)-Cl(5)	2.353(7)	Sb(1)-Cl(6)	2.374(6)
Sb(1)-Cl(7)	2.363(6)	Sb(2)-Cl(8)	2.344(5)
Sb(2)-Cl(9)	2.365(6)	Sb(2)-Cl(10)	2.376(5)
Bond angles			
N(3)-W(1)-N(2)	103.9(8)	N(3)-W(1)-N(1)	97.8(6)
N(2)-W(1)-N(1)	104.8(6)	N(3)-W(1)-Cl(2)	94.2(5)
N(2)-W(1)-Cl(2)	97.1(6)	N(1)-W(1)-Cl(2)	151.7(4)
N(3)-W(1)-Cl(1)	159.3(5)	N(2)-W(1)-Cl(1)	96.8(6)
N(1)-W(1)-Cl(1)	77.0(4)	Cl(2)-W(1)-Cl(1)	82.83(14)
N(4)-W(2)-N(6)	108.4(7)	N(4)-W(2)-N(5)	94.5(6)
N(6)-W(2)-N(5)	103.7(7)	N(4)-W(2)-Cl(3)	94.6(6)
N(6)-W(2)-Cl(3)	96.2(6)	N(5)-W(2)-Cl(3)	154.1(4)
N(4)-W(2)-Cl(4)	158.7(4)	N(6)-W(2)-Cl(4)	92.9(6)
N(5)-W(2)-Cl(4)	79.5(4)	Cl(3)-W(2)-Cl(4)	83.20(14)
Cl(5)-Sb(1)-Cl(7)	94.5(3)	Cl(5)-Sb(1)-Cl(6)	91.5(3)
Cl(7)-Sb(1)-Cl(6)	96.2(2)	Cl(8)-Sb(2)-Cl(9)	94.8(2)
Cl(8)-Sb(2)-Cl(10)	94.5(2)	Cl(9)-Sb(2)-Cl(10)	92.8(2)
C(11)-N(1)-W(1)	126.8(10)	C(21)-N(2)-W(1)	152.5(15)
C(31)-N(3)-W(1)	172.5(14)	C(41)-N(4)-W(2)	173.7(13)

The compound $[W(NBu^t)_2(NH_2Bu^t)Cl_2]_2$ **(20)** also crystallises with the starting material $SbCl_3$ in the orthorhombic space group $Pc2_1n$ with the unit cell parameters: a = 9.72800(10), b = 21.3290(3), c = 22.1190(2) Å, Z = 4 (Figure 4.11). Selected bond lengths and angles are displayed in the Table 4.5. Hence, **(20)** and $SbCl_3$ have been obtained as a co-crystal. There are two such co-crystallized structures per asymmetric unit (Figure 4.11). The antimony atom adopts a distorted trigonal pyramidal geometry with its active lone pair. The bond lengths and angles are in the same range than the structure $SbCl_3$ obtained as a single species [Sb-Cl = 2.37(2) Å, Cl-Sb-Cl = 95.2°].[26]

All the bond lengths and angles in the tungsten coordination sphere of **(20)** are equivalent to those found in the previous co-crystal of $[W(NBu^t)_2(NH_2Bu^t)Cl_2]_2$ **(20)** and $[Sb(\mu_2\text{-}NBu^t)Cl]_2$ **(21)**, excepted for the weak bonds W(1)....Cl(4) and W(2)....Cl(1). Indeed, in the co-crystal with **(21)**, the W(1)-Cl(1') bond distance of 2.786(2) Å involved in a

bridging chlorine ligand becomes here longer (*ca.* 2.9 Å). Hence, the monomeric structures $W(NBu^t)_2(NH_2Bu^t)Cl_2$ based on **(20)** are weakly interconnected comparatively to the previous co-crystal. There are some Van der Waals intermolecular bondings Sb(1)...Cl(1) and Sb(2)...Cl(4) (*ca.* 3.0 Å) which is significantly shorter than the sum of Van der Waals radii of these elements (4.0 Å). This type of interaction is here stronger compared to the previous co-crystal where the intermolecular bond Sb'...Cl(1) has an intermolecular distance of 3.6 Å. This is due possibly to the steric hindrance of the ^{t}BuN groups bound to the Sb.

Moreover, the W-N(1) is in close contact with the chlorine Cl(3). Since the hydrogens have not been located in this structure due to the low quality of the crystal, the hydrogens bonds cannot be discussed further. The strong Lewis character and the low steric hindrance of $SbCl_3$ comparatively to $[Sb(\mu\text{-}NBu^t)Cl]_2$ might explain the difference of configuration of $[W(NBu^t)_2(NH_2Bu^t)Cl_2]_2$ **(20)**.

Another hydrolysis product, $Sb_2W_3Cl_7(\mu_2\text{-}O)(\mu_3\text{-}O)_2(NBu^t)_3(NHBu^t)(\mu_2\text{-}NBu^t)_2$ **(22)** crystallizes in the triclinic space group $P\ \bar{1}$ with the unit cell parameters: a = 12.19400(10), b = 12.8310(2), c = 18.2980(3) Å, α = 76.3140(10), β= 85.3960(10), γ = 71.8370(10), Z = 2. The structure **(22)** and selected bond lengths, angles are depicted in Figure 4.12 and Table 4.6. The solid-state structure shows three different types of coordination at the tungsten atom: $W(1)Cl_2N_2(\mu\text{-}O)O$, $W(2)ClN_2(\mu\text{-}O)O$, $W(3)Cl_2N(\mu\text{-}O)_2$. W(1) and W(3) form an octahedral geometry while W(2) has a trigonal pyramidal geometry. Each tungsten atom is surrounded by two types of nitrogen atoms: one of them presents the amido character, such as N(3), N(4), N(6) and the others the imido character like N(1), N(2), N(5). These are confirmed by the bond lengths and angles of W-amido (*c.a* W-N ~ 1.89 Å, W-N-C ~ 140°) and of W-imido (*ca* W-N ~ 1.74 Å, W-N-C ~ 168°). A strong intramolecular hydrogen bond (*ca.* 2.5 Å) between N(4)-H(4)**….**Cl(1)-W(1) is present in the structure **(22)**, as displayed in the Figure 4.12. Also, the Sb-O, Sb-Cl and W-Cl bond lengths are as expected for normal bonds compared to the literature examples examined.[12, 17, 23] The structure has doubly bridging oxygen atom for O(1) and triply for O(2) and O(3). As expected, the bond lengths involving a doubly bridging oxygen W(1)-μ_2-O(1) of 2.036(5) Å are shorter than the bond [W(1)-μ_3-O(3); 2.193(5) Å]. The corresponding angles W-O-W are respectively 154.2(3)° at O(1) and 129.9(2)° at O(2) and 139.0(2)° at O(3). At W(1), Cl(1) is *trans* to Cl(2) while W(4) is *cis* to Cl(5) at W(3). As well, Cl(7) is *cis* to Cl(1) but *trans* to Cl(2) and Cl(3) is *cis* to Cl(6). The W-O(2)-W and W-O(3)-W bridging oxygen [O(2), O(3)] is *trans* to the metal-bonded imido ligand respectively N(2) and N(5).

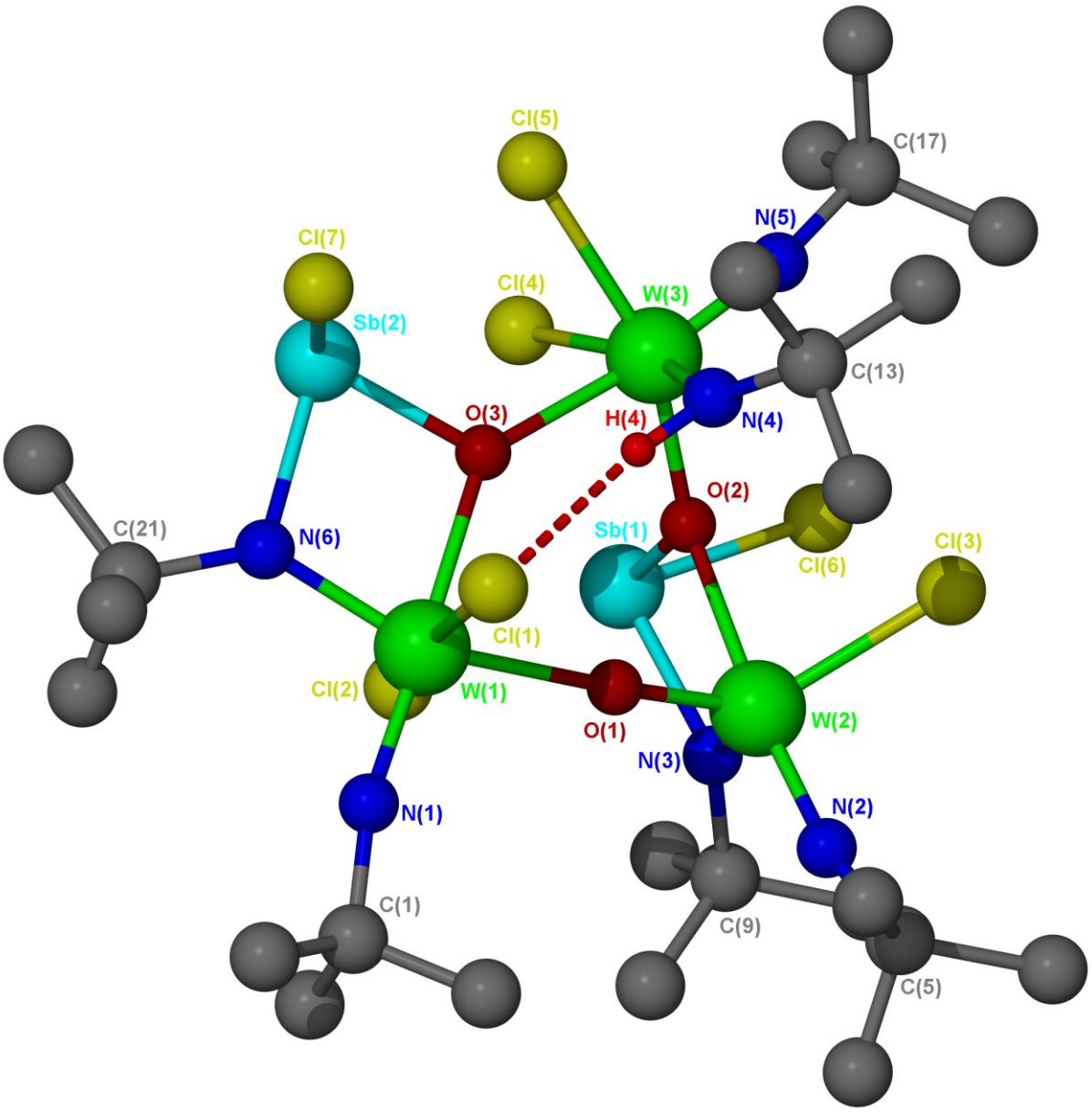

Figure 4.12 Molecular structure of $Sb_2W_3Cl_7(\mu_2\text{-}O)(\mu_3\text{-}O)_2(NBu^t)_3(NHBu^t)(\mu_2\text{-}NBu^t)_2$ **(22)**

Also, $Sb_2W_3Cl_7(\mu_2\text{-}O)(\mu_3\text{-}O)_2(NBu^t)_3(NHBu^t)(\mu_2\text{-}NBu^t)_2$ **(22)** co-crystallizes with $Sb_2W(NBu^t)(\mu_2\text{-}NBu^t)(\mu_3\text{-}NBu^t)_2Cl_3(\mu_2\text{-}Cl)$ **(19)** in the monoclinic space group $P2_1/n$ with the unit cell parameters: a = 12.02300(10), b = 31.2910(3), c = 20.7330(3) Å, β= 102.2230(10), Z = 4. Hence, **(19)**, was obtained under anhydrous conditions, co-crystallises with the hydrolysis product **(22)** (Figure 4.13) with apparently no intermolecular interactions. The bond lengths and angles are in the same range as the molecules obtained as single species.

Table 4.6 Selected bond lengths (Å) and bond angles (°) of **(22)**

Bond lengths			
W(1)-N(1)	1.726(7)	W(1)-N(6)	1.912(7)
W(2)-N(2)	1.741(6)	W(2)-N(3)	1.873(6)
W(3)-N(4)	1.918(6)	W(3)-N(5)	1.729(7)
W(1)-O(1)	2.036(5)	W(1)-O(3)	2.193(5)
W(2)-O(1)	1.830(5)	W(2)-O(2)	2.195(5)
W(3)-O(2)	1.988(4)	W(3)-O(3)	2.138(5)
W(1)-Cl(1)	2.3817(18)	W(1)-Cl(2)	2.4487(18)
W(2)-Cl(3)	2.337(2)	W(3)-Cl(5)	2.4094(17)
W(3)-Cl(4)	2.5338(17)	Sb(1)-O(2)	1.988(4)
Sb(1)-N(3)	2.151(6)	Sb(1)-Cl(6)	2.415(2)
Sb(2)-O(3)	1.961(5)	Sb(2)-N(6)	2.119(7)
Sb(2)-Cl(7)	2.380(2)	N(4)-H(4)	0.97(2)
Bond angles			
C(1)-N(1)-W(1)	166.7(8)	C(5)-N(2)-W(2)	164.3(6)
C(9)-N(3)-W(2)	134.9(5)	C(13)-N(4)-W(3)	142.8(5)
C(17)-N(5)-W(3)	168.6(6)	C(21)-N(6)-W(1)	136.9(6)
N(1)-W(1)-O(1)	99.3(3)	N(1)-W(1)-O(3)	177.8(3)
N(6)-W(1)-O(1)	159.3(3)	N(2)-W(2)-O(2)	174.6(3)
Sb(1)-O(2)-W(3)	128.6(2)	N(5)-W(3)-O(3)	173.4(2)
Cl(1)-W(1)-Cl(2)	166.64(7)	Cl(5)-W(3)-Cl(4)	81.81(6)
Sb(1)-O(2)-W(2)	99.66(18)	Sb(2)-O(3)-W(1)	100.5(2)
W(2)-N(3)-Sb(1)	105.1(3)	N(3)-Sb(1)-Cl(6)	92.59(19)
O(3)-Sb(2)-N(6)	77.7(2)	O(3)-Sb(2)-Cl(7)	100.43(15)
N(1)-W(1)-N(6)	101.2(4)	N(6)-W(1)-O(3)	77.0(2)
W(2)-O(1)-W(1)	154.2(3)	W(3)-O(2)-W(2)	129.9(2)
Sb(2)-O(3)-W(3)	120.2(2)	W(3)-O(3)-W(1)	139.0(2)
O(1)-W(1)-O(3)	82.48(18)	O(2)-Sb(1)-N(3)	76.6(2)
O(2)-Sb(1)-Cl(6)	91.31(15)	N(6)-Sb(2)-Cl(7)	92.04(19)

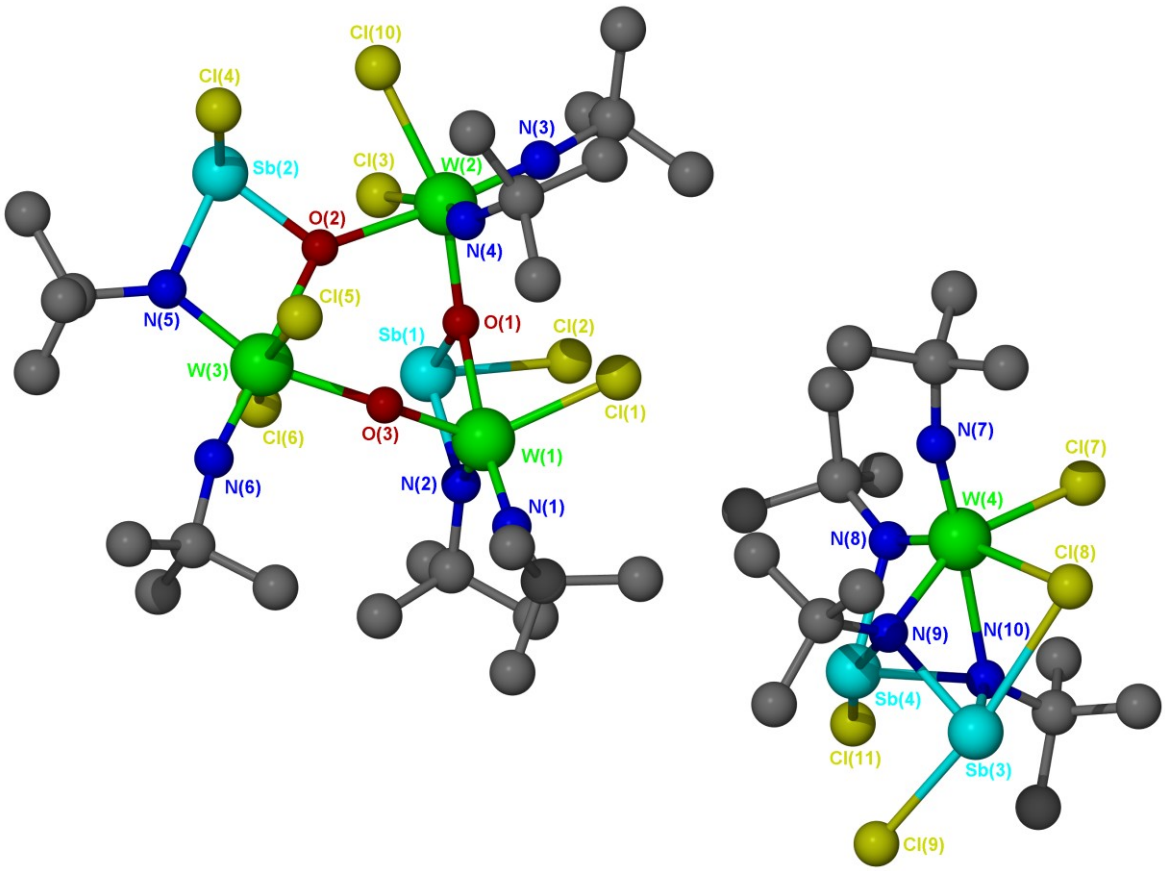

Figure 4.13 Molecular structure of $Sb_2W(NBu^t)(\mu_2\text{-}NBu^t)(\mu_3\text{-}Bu^tN)_2Cl_3(\mu_2\text{-}Cl)$ **(19)** and $Sb_2W_3Cl_7(\mu_2\text{-}O)(\mu_3\text{-}O)_2(NBu^t)_3(NHBu^t)(\mu_2\text{-}NBu^t)_2$ **(22)** which co-crystallise

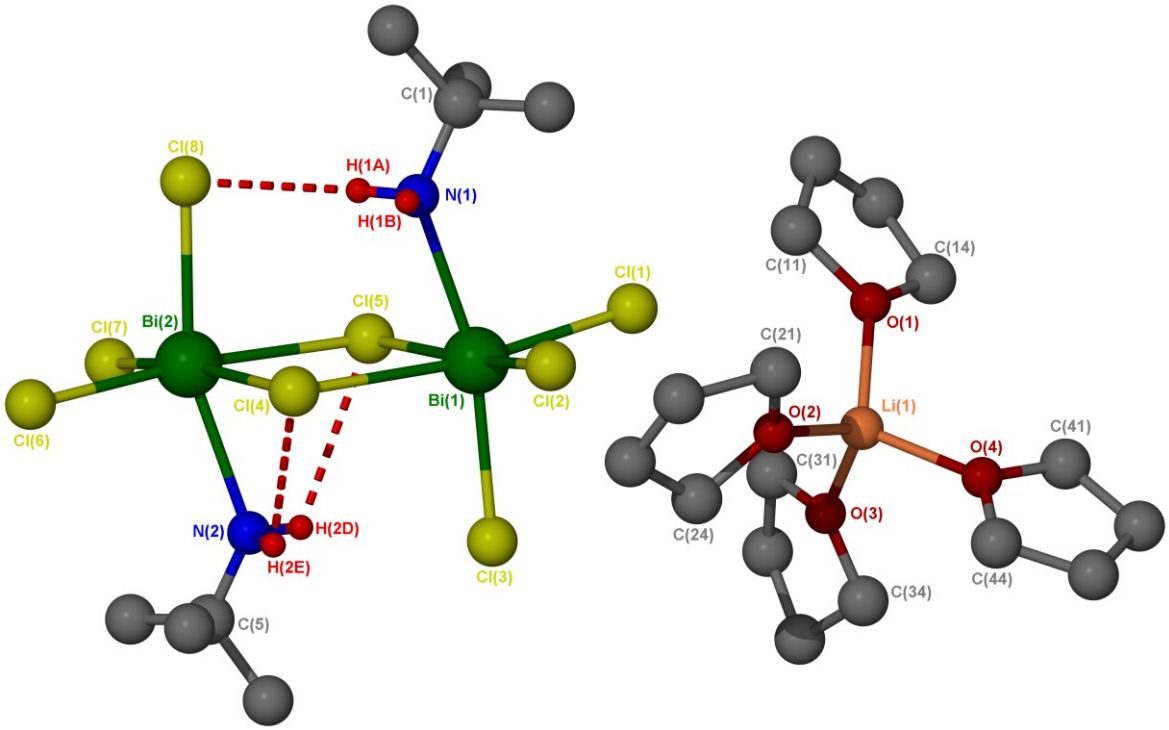

Figure 4.14 Molecular structure of $[Li(THF)_4]^-$ monoanion and $[Bi_2C1_6(^tBuNH_2)_2(\mu\text{-}C1)_2]^{2-}$ dianion in $[Li(thf)_4]_2.[Bi_2C1_6(^tBuNH_2)_2(\mu\text{-}C1)_2]$

The compound $[Li(thf)_4]_2[Bi_2C1_6(^tBuNH_2)_2(\mu\text{-}C1)_2]$ **(23)** crystallizes in the orthorhombic space group $P2_1nb$ with the unit-cell parameters: a = 15.49700(10), b = 18.5810(2), c = 20.6130(2) Å. **(23)** comprises separated ions with long inter-ionic contacts. Only one of counter-cations is represented in the figure 4.14. The dianion (Figure 4.14) forms an edge-shared bi-octahedral structure in which the tert-butylamine $^tBuN(1)$ and $^tBuN(2)$ and chlorine [Cl(3), Cl(8)] occupy terminal sites perpendicular to the $Bi_2Cl_4(\mu\text{-}C1)_2$ plane. Indeed, $^tBuN(1)$ is in a *trans* position to $^tBuN(2)$. Both bismuth atoms adopt irregular octahedral geometries with *trans* bond angles varying from 160.5(5) to 173.88(13)°. This type of arrangements $[BiCl_3(L)]_n$ have been already described elsewhere.[27] The terminal chloride atom Cl(3) and Cl(8) bound respectively to Bi(1) and Bi(2) are in *trans* to the tert-butylamine $^tBuN(1)$ and $^tBuN(2)$ ligands. The bond Bi(1)-Cl(3) and Bi(2)-Cl(8) of respective distances 2.607(4) and 2.630(4) Å, are longer than the short Bi-Cl terminal bonds [Bi(2)-Cl(7), 2.572(3) Å and Bi(1)-Cl(1), 2.590(4) Å], belonging to the plane $Bi_2(\mu\text{-}Cl)_2Cl_2$. The chloride bridging ligands are quite symmetrical with Bi-Cl bond having distance of 2.866(3) Å for Bi(1)-Cl(4), 2.886(3) Å for Bi(1)-Cl(5), 2.849(3) Å for Bi(2)-Cl(5), 2.875(3) Å for Bi(2)-Cl(4). As expected, the bridging Bi-Cl distances are longer than the terminal Bi-Cl bond. The tert-butylamine $^tBuNH(2E)$ and $^tBuNH(2D)$ has respectively hydrogen bonds with the bridging chlorine Cl(4) and Cl(5) [*ca* 2.8 Å]. The tert-butylamine $^tBuNH(1A)$ bounds to bismuth Bi(2) has an hydrogen bond with the terminal chlorine ligand Cl(8) (*ca.* 2.7 Å). We can note that the *trans* angle bent [N(1)-Bi(1)-Cl(3), 164.2(4)°] is less bent than the *trans* [N(2)-Bi(2)-Cl(8), 160.5(5)°] due to the difference of intramolcular attraction resulting of hydrogen bonds. The anionic dimer $[Bi_2C1_6(^tBuNH_2)_2(\mu\text{-}C1)_2]^{2-}$ is surrounded by 2 $[Li(THF)_4]^+$ cations. The lithium atom adopts a tetrahedral structure. The Li^+ counterions are coordinated by four THF molecules in a tetrahedral structure with a mean Li–O distance of 1.937 Å with angles at about 110°. The structure **(23)** is very similar to $[Li(THF)_4]_2[Bi_2C1_6(THF)_2(\mu\text{-}C1)_2]$ in term of distances and angles.[24]

Table 4.7 Selected bond lengths (Å) and angles (°) of **(23)**

Bond lengths			
Bi(1)-N(1)	2.579(12)	Bi(1)-Cl(1)	2.590(4)
Bi(1)-Cl(2)	2.562(3)	Bi(1)-Cl(3)	2.607(4)
Bi(1)-Cl(4)	2.866(3)	Bi(1)-Cl(5)	2.886(3)
Bi(2)-N(2)	2.550(16)	Bi(2)-Cl(4)	2.875(3)
Bi(2)-Cl(5)	2.849(3)	Bi(2)-Cl(6)	2.594(3)
Bi(2)-Cl(7)	2.572(3)	Bi(2)-Cl(8)	2.630(4)
N(1)-C(1)	1.45(2)	N(2)-C(5)	1.405(17)
Li(1)-O(1)	1.91(3)	Li(1)-O(2)	1.95(2)
Li(1)-O(3)	1.94(3)	Li(1)-O(4)	1.95(3)
Li(2)-O(5)	1.87(3)	Li(2)-O(6)	1.92(3)
Li(2)-O(7)	2.01(3)	Li(2)-O(8)	1.94(3)
Bond angles			
Cl(2)-Bi(1)-N(1)	84.2(3)	Cl(2)-Bi(1)-Cl(1)	92.60(12)
N(1)-Bi(1)-Cl(1)	98.0(4)	Cl(2)-Bi(1)-Cl(3)	94.45(13)
N(1)-Bi(1)-Cl(3)	164.2(4)	Cl(1)-Bi(1)-Cl(3)	97.75(14)
Cl(2)-Bi(1)-Cl(4)	89.38(11)	N(1)-Bi(1)-Cl(4)	74.5(4)
Cl(1)-Bi(1)-Cl(4)	172.04(11)	Cl(3)-Bi(1)-Cl(4)	89.78(13)
Cl(2)-Bi(1)-Cl(5)	171.28(11)	N(1)-Bi(1)-Cl(5)	88.6(3)
Cl(1)-Bi(1)-Cl(5)	93.24(10)	Cl(3)-Bi(1)-Cl(5)	91.18(13)
Cl(4)-Bi(1)-Cl(5)	83.98(9)	Bi(1)-Cl(4)-Bi(2)	95.67(9)
N(2)-Bi(2)-Cl(7)	94.9(7)	N(2)-Bi(2)-Cl(6)	96.6(8)
Cl(7)-Bi(2)-Cl(6)	92.04(12)	N(2)-Bi(2)-Cl(8)	160.5(5)
Cl(7)-Bi(2)-Cl(8)	98.09(12)	Cl(6)-Bi(2)-Cl(8)	97.30(14)
N(2)-Bi(2)-Cl(5)	77.7(8)	Cl(7)-Bi(2)-Cl(5)	90.74(11)
Cl(6)-Bi(2)-Cl(5)	173.88(13)	Cl(8)-Bi(2)-Cl(5)	87.70(12)
N(2)-Bi(2)-Cl(4)	76.1(7)	Cl(7)-Bi(2)-Cl(4)	170.53(11)
Cl(6)-Bi(2)-Cl(4)	91.97(11)	Cl(8)-Bi(2)-Cl(4)	89.90(11)
Cl(5)-Bi(2)-Cl(4)	84.48(9)	Bi(2)-Cl(5)-Bi(1)	95.83(9)
C(1)-N(1)-Bi(1)	131.2(12)	C(5)-N(2)-Bi(2)	134.9(17)
O(1)-Li(1)-O(3)	108.9(11)	O(1)-Li(1)-O(2)	110.8(13)
O(3)-Li(1)-O(2)	112.4(14)	O(1)-Li(1)-O(4)	113.5(14)
O(3)-Li(1)-O(4)	105.0(12)	O(2)-Li(1)-O(4)	106.2(11)
C(14)-O(1)-C(11)	108.8(12)	C(14)-O(1)-Li(1)	122.8(13)
C(11)-O(1)-Li(1)	124.9(12)	C(21)-O(2)-C(24)	111.4(12)
C(21)-O(2)-Li(1)	125.8(14)	C(24)-O(2)-Li(1)	122.7(11)
C(34)-O(3)-C(31)	110.8(13)	C(34)-O(3)-Li(1)	130.1(11)
C(31)-O(3)-Li(1)	116.7(13)	C(44)-O(4)-C(41)	109.8(15)
C(44)-O(4)-Li(1)	127.8(13)	C(41)-O(4)-Li(1)	121.1(11)
O(5)-Li(2)-O(6)	115.9(12)		

4.3 Conclusion

$W(^tBuNH)_2(^tBuN)_2$ **(16)** has been synthesized and characterized structurally by X-ray crystallography and gas-phase electron diffraction using computational chemistry. The solid-state structure reveals a disordered structure. The gas phase structure determination of **(16)** shows the presence of two conformers in different proportion.

The deprotonation reaction of $W(NHBu^t)_2(NBu^t)_2$ **(16)** with $ZnMe_2$ gives rise to an unexpected compound $MeZn(NH_2Bu^t)(NBu^t)_2W(NBu^t)Me$ **(17)** which has been successfully characterized by X-ray crystallography and so formulated. This reaction shows a ligand exchange followed by a hydrogen migration, resulting in **(17)**. The structure also shows that the initial formulation of **(17)**, as described by G. Wilkinson et al. was incorrect.

$[Me_2(N^tBu)_2W(\mu\text{-}N^tBu)]_2$ **(18)** has been synthesized in a single step from the reaction of **(16)** with $AlMe_3$ which display ligands exchange between the aluminium and tungsten atoms.

The reaction of $Li_2W(NBu^t)_4$ with $SbCl_3$ proves to be complex and gives rise to a remarkable compound $Sb_2W(NBu^t)(\mu_2\text{-}NBu^t)(\mu_3\text{-}Bu^tN)_2Cl_3(\mu_2\text{-}Cl)$ **(19)** which has been fully characterized. Also, additional complex products have also been produced during the metathesis of $Li_2W(NBu^t)_4$ with $SbCl_3$ with the incursion of adventitious moisture. Hence, mixtures of $[W(NBu^t)_2(NH_2Bu^t)Cl(\mu_2\text{-}Cl)]_2$ **(20)** with $[Sb(\mu_2\text{-}NBu^t)Cl]_2$ **(21)** or $SbCl_3$, and $Sb_2W_3Cl_7(\mu_2\text{-}O)(\mu_3\text{-}O)_2(NBu^t)_3(NHBu^t)(\mu_2\text{-}NBu^t)_2$ **(22)**, without and as a co-crystal with **(19)**, have been characterized structurally. The attempt to synthesize the bismuth analogue to **(19)** afford to the ionic compound $[Li(thf)_4]_2[Bi_2C1_6(^tBuNH_2)_2(\mu\text{-}C1)_2]$ **(23)**.

4.4 Experimental section

All manipulations were carried out under argon atmosphere using standard Schlenk techniques and standard glove-box. All solvents were purified by an Innovative Technology inc. solvent purification system (SPS) and stored under argon over activated 4Å molecular sieves. $W(NHBu^t)_2(NBu^t)_2$ [17] and $Li_2W(N^tBu)_4$ [12, 15] was prepared as described in the literature. Solution of $AlMe_3$ (2.0 M) in hexane, $ZnMe_2$ (2.0 M) in toluene were purchased from Aldrich and use as received. $SbCl_3$ and $BiCl_3$ was purchased from Aldrich. Prior to the reaction, $SbCl_3$ was purified by azeotropic distillation and then by multiple sublimations under vaccum. Meanwhile, $BiCl_3$ was purified by two consecutives sublimations.[22]

Synthesis of $MeZn(NH_2Bu^t)(NBu^t)_2W(NBu^t)Me$ **(17)**

To a solution of (freshly sublimed) $W(N^tBu)_2(NH^tBu)_2$ (2.00 g, 4.25 mmol) in hexane (75 mL) at -78°C was slowly added a solution of $ZnMe_2$ (5.5 mL, 2 $mol.L^{-1}$) in toluene. After warming to room temperature, the solution was stirred for 24h. The clear solution was then concentrated until crystallisation began. Cooling at -20°C (12 h) gave colourless needles which were collected by filtration at 0°C and dried in vacuum (73%). Mp = 76°C

Found (Calc. for) % : C 37.9 (38.2) H 7.83 (7.84) N 9.06 (9.9)

^1H NMR (C_6D_6, 300 MHz, 298 K, δ ppm): -0.063 (s, 3 H, ZnC***H₃***), 0.756 **(s,** 3 H, WC***H₃***, J(^{183}W-^1H) = 9Hz), 0.9 (s, 9 H, ZnNC(C***H₃)₃***), 1.479 (**s,** 18H, μ_2-NC(C***H₃)₃***), 1.506 (**s,** 9H, $NH_2C(C\boldsymbol{H_3})_3$) 1.83 (br **s,** 2 H, $(CH_3)_3CN\boldsymbol{H_2}$)

^{13}C NMR (C_6D_6, 300 MHz, 298 K, δ ppm): -12.91 (s, Zn***C***H_3), 6.76 (s, W***C***H_3), 30.96 [s, $NH_2C(\boldsymbol{C}H_3)_3$], 34.03 [s, μ_2-$NC(\boldsymbol{C}H_3)_3$], 36.00 [s, $WNC(\boldsymbol{C}H_3)_3$], 50.1 [s, $NH_2\boldsymbol{C}(CH_3)_3$], 62.74 [s, μ_2-$N\boldsymbol{C}(CH_3)_3$], 66.94 [s, $WN\boldsymbol{C}(CH_3)_3$]

Synthesis of $[Me_2(N^tBu)_2W(\mu\text{-}N^tBu)]_2$ **(18)**

To a solution of (freshly sublimed) $W(N^tBu)_2(NH^tBu)_2$ (1.00 g, 2.13 mmol) in hexane (40 mL) was slowly added a solution of $AlMe_3$ (5 mL, 2 $mol.L^{-1}$) in hexane. On warming to room temperature a white crystalline precipitate is formed and can be dissolved by warming the solution to obtain a clear solution. After 3 hours, the solvent was removed *in vacuo* and the solution is concentrated until crystallisation began. Cooling at -20°C (12 h) gave colourless needles which were collected by filtration at 0°C and then dried and stored in the glovebox (60%). Mp = 133°C

Found (Calc. for) % : C 33.7 (33.72) H 6.80 (6.79) N 7.93 (7.86)

^1H NMR (C_7D_8, 300 MHz, 298 K, δ ppm): 1.0 (br s, 12 H, C***H₃***), 1.40 (br s, 36H, μ_2-$NC(C\boldsymbol{H_3})_3$)

Synthesis of $Sb_2W(NBu^t)(\mu_2\text{-}NBu^t)(\mu_3\text{-}Bu^tN)_2Cl_3(\mu_2\text{-}Cl)$ **(19)**

A solution of (freshly sublimed) $SbCl_3$ (0.29 g, 0.13 mmol) in toluene (20 mL) was added dropwise to a solution of $Li_2W(N^tBu)_4$ (0.30 g, 0.622 mmol) in toluene (50 mL). On warming, a white crystalline precipitate was formed in the deep yellow solution between -20 and 10°C. After warming to room temperature, the white solid disappears to give an orange-red solution. The solution was stirred for 24 hours and filtered through Celite®. Afterwards, the solution

was concentrated to *ca.* 3 mL giving rise to an oily solution. Recrystallisation from toluene/hexane (1:3) at -20°C for 3 days afforded to orange blocks. Those crystals from washed with (3 x 3 mL) hexane were collected and then dried under vacuum to yield an orange-yellow solid. Yield = 25%, mp = 110°C

Found (Calc. for) %: C 22.5 (22.51) H 4.35 (4.25) N 6.65 (6.56)

^{1}H NMR (C_6D_6, 300 MHz, 298 K, δ ppm): 1.0 (s, 18 H, μ_3-NC(C***H*****$_3$**)$_3$), 1.37 (**s,** 9H, μ_2-NC(C***H*****$_3$**)$_3$), 1.46 (**s,** 9H, NC(C***H*****$_3$**)$_3$)

^{13}C NMR (C_6D_6, 300 MHz, 298 K, δ(ppm): 30.0[s, μ_3-NC(***C***H_3)$_3$], 31.0 [s, μ_2-NC(***C***H_3)$_3$], 34.0 [s, NC(***C***H_3)$_3$], 55.9 [s, μ_3-N***C***$(CH_3)_3$], 65.0[s, μ_2-N***C***$(CH_3)_3$], 75.8 [s, N***C***$(CH_3)_3$]

Synthesis of $[Li(thf)_4]_2.[Bi_2C1_6(^tBuNH_2)_2(\mu\text{-}C1)_2]$ **(23)**

A solution of $BiCl_3$ (freshly sublimed) (0.4 g, 1.24 mmol) in THF (20 mL) was added dropwise to a solution of $Li_2W(N^tBu)_4$ (0.30 g, 0.62 mmol) in THF (50 mL). After warming to room temperature, the yellow solution was stirred for 24 hours. Afterwards, the clear solution was concentrated to *ca.* 20 mL and cooled at -20°C (12 h), giving colourless prisms. Only the X-ray crystal structure was performed on **(23)**.

4.5 References

[1] Lisa McElwee-White, *Dalton Trans.* **2006**, 5327.
[2] J. S. Becker, S. Suh and R. G. Gordon, *Chem. Mater.* **2003**, *15*, 2969.
[3] D. C. Bradley and M. H. Gitlitz, *Chem. Commun.* **1965**, 289.
[4] J. S. M. Lehn, Saba Javed and D. M. Hoffman, *Chem. Vap. Deposition* **2006**, *12*, 280.
[5] L. Xinjian, J. A. T. Norman*, Vol. 6552209*, Air Products and Chemicals, Inc. (Allentown, PA) U.S, **2003**.
[6] D.M. Hausmann, P. de Rouffignac, A. Smith, R. Gordon and D. Monsma, *Thin Solid Films* **2003**, *443*, 1.
[7] S. H. Mohamed, A. Anders, *Surface & Coatings Technology* **2006**, *201* 2977.
[8] M. F. Lappert, P. P. Power, A. R. Sanger and R. C. Srivastava, in *Metal and Metalloid amides, Vol. 12*, Ellis Horwood, **1980**, p. 640.
[9] H-T. Chiu and S.-H. Chuang, *Mat. Res. Soc. symp. Proc.* **1992**, *250*, 317.
[10] O. M. El-Kadri, M. J. Heeg and C. H. Winter, *Dalton Transactions* **2006**, 1943.
[11] C. L. Dezelah, O. El-kadri, I. Sziligyi, J. M. Campbell, K. Arstila, L. Niinistö and C. H. Winter, *J. Am. Chem. Soc.* **2006**, *128*, 9638.
[12] A. A. Danopoulos, G. Wilkinson, B. Hussain and M. B. Hursthouse, *J. Chem. Soc., Dalton Trans.* **1990**, 2753.
[13] W. A. Nugent, *Inorg. Chem.* **1983**, *22*, 965.
[14] A. A. DanopouIos, G. Wilkinson, *Polyhedron* **1994**, *13*, 2899.
[15] G. M. de Lima and D. J. Duncalf, *Organometallics* **1999**, *18*, 4884.
[16] Q. Shao, A. Li, W. Zhang, D. Wu, Z. Liu, N. Ming, *Chem. Vap. Deposition* **2006**, *12*, 423.
[17] W. A. Nugent and R. L. Harlow, *Inorg. Chem.* **1980**, *19*, 777.
[18] A. S. Batsanov, A. E. Goeta, J. A. K. Howard, A. K. Hughes, A. L. Johnson and K. Wade, *J. Chem. Soc., Dalton Trans.* **2001**, 1210.
[19] H-T. Chiu, S-H. Chuang, G-H. Lee and S-M. Peng, *Polyhedron* **1994**, *13*, 2443.
[20] H. Choujaa, K. C. Molloy, in *publication in progress*.
[21] R. Steudel, Y. Steudel, *J. Phys. Chem. A* **2006**, *110*, 8912.
[22] W. L. F. Armanego and C. L. L. Chai, *Purification of laboratory chemicals*, Elsevier, **2002**.
[23] D. C. Haagenson and L. Stahl, *Inorg. Chem.* **2001**, *40*, 4491.
[24] S. C. James, N. C. Norman, *Acta Cryst.* **1997**, *C53*, 1024.
[25] A. J. Edwards, Paul R. Raithby, N. E. Leadbeater, M. A. Paver, P. R. Raithby, C. A. Russell and D. S. Wright, *J. Chem. Soc. Dalton Trans.* **1994**, *1*, 1479.
[26] I. Lindqvist, A. Niggli, *J. of Inorganic and Nuclear Chemistry* **1956**, *2*, 345.
[27] C. J. Carmalt, W. Clegg, M. R. J. Elsegood, R. J. Errington, J. Havelock, P. Lightfoot, N. C. Norman and A. J. Scott, *Inorg. Chem.* **1996**, *35*, 3709.

Chapter 5
Conclusion and Future work

5. Conclusion and future work

This thesis has investigated the molecular design of CVD precursors from the single-source approach for targeted mixed-metal oxide materials based on tungsten. This promising approach of producing single-source molecules offers a new perspective for CVD of multi-elements, such as ceramics, alloys. This strategy is the chemist's answer to overcome the problems posed by the multi-sources approach which requires highly volatile precursor. This work involves the synthesis of soluble homo- and hetero-metallic alkoxides and amides for the CVD of mixed-metal tungsten oxide. Indeed, they exhibit high solubility in the appropriate organic solvents. This is the case for the compounds synthesised in this work, especially those containing amino-alkoxide ligands. Hence, CVD using precursor delivery, such as aerosol, injection or spray can be applied to these highly soluble compounds. The quest for clean decomposition over volatilities is thus more important, in particular for electronic industry. This thus raises the question of thermal stability and mechanism of decomposition for all the compounds. These highly soluble compounds can also benefit the sol-gel process for mixed-metal tungsten oxide films and nanoparticles.

The functionalized tungsten oxo-alkoxide/amino-alkoxide complexes $[WO(O^iPr)_3(L)]$ (L = dmae, bdmap, tdmap) containing different proportions of nitrogen depending on the ligand (L) have been synthesised. The CVD of these compounds could allow the preparation of nitrogen doped tungsten oxide via the impurity incorporation of these precursors in the deposited film. An evaluation of the synthesised single-source precursors for the deposition of WO_3 and nitrogen doped tungsten oxide WO_xN_y by AA- or LP-CVD is currently in progress. The incorporation of nitrogen impurities may narrow the band gap by nitrogen doping and increase the photocatalytic activity of the film under solar radiation.

The hydrolysis study of monomeric tungsten oxo-alkoxide/amino-alkoxide has produced polymeric structures which have been structurally characterized. The substitution of one isopropoxide $-O^iPr$ with one amino-alcohol (L) has only been investigated. Another promising route is the hydrolysis-condensation of tungsten oxo-tetra-amino-alkoxide $[WO(L)_4]$. Hence, the increase of amino-alkoxide ligand (L) number in the coordination sphere of tungsten can permit to control more efficiently the synthesis of different hydrolysis products with various types of ligand and with various hydrolysis ratio. Moreover, the micro-hydrolysis of functionalized tungsten oxo-alkoxide $[WO(L)_4]$ in association with other type of complexes could also allow the preparation of heterobimetallic compounds.

Contrary to the sol-gel process, the thermal stability of these compact polymeric compounds could then be studied with precision in relation to their structure. Further studies could also give a mechanistic understanding of their condensation pathway occurring in the sol-gel process.

Heterobimetallic acetylacetonate alkoxides of type $M_2W_2O_2(acac)_2(OMe)_{10}$ (M = Co, Ni, Mg, Zn) could probably be used as LP-CVD precursors in specific conditions (pressure and temperature) of sublimation. Also, their chemical modification by amino-alkoxide could also prevent their disproportionation. Their application as AA- or LI-CVD precursor is doubtful due to their low solubility at R.T in organic solvent. However, the use of amino-alkoxide ligand instead of acetylacetonate ligand in the synthesis of $M_2W_2O_2(L)_2(OMe)_{10}$ (M = Co, Ni, Mg, Zn) can improve dramatically the solubility of (L = amino-alkoxide); Contrary to the original synthetic pathway used by Kessler et al., the novel route giving a unique product could be utilised to synthesise a soluble complex $M_2W_2O_2(acac)_2(OPr^i)_{10}$ by mixing $M(O^iPr)(acac)$ with $WO(O^iPr)_4$ in 1:1 ratio without further purification. Indeed, this type of alkyl chain (^iPr) confers to the resulting heterobimetallic alkoxide a high solubility.

The interaction of $W(NHBu^t)_2(NBu^t)_2$ with, respectively $ZnMe_2$ and $AlMe_3$ gives rise to the highly soluble heterobimetallic amides $MeZn(NH_2Bu^t)(\mu\text{-}NBu^t)_2(NBu^t)WMe$ and $[Me_2W(NBu^t)(\mu\text{-}NBu^t)]_2$. They could be used as single-source precursors for WZn_xN_y and WN_xC_y in presence of an inert gas carrier. CVD of $WZn_xN_yO_z$ and $WN_xC_yO_z$ could also be carried out in combination with an oxidative carrier gas (H_2O vapor/O_2/ethylacetate).

The reaction of $W(NHBu^t)_2(NBu^t)_2$ with other metal alkyl, such as CdR_2, GaR_3 and InR_3 could also be investigated to provide a wide range of heterobimetallic compounds available from this original method. Indeed, it offers a new and easy way to prepare heterobimetallic compounds for the deposition of multi-metallic materials, via AA-CVD and LP-CVD from respectively soluble and volatile precursors. Preliminary to the CVD experiment, the thermal stability needs to be assessed by TGA. The decomposition pathway can also be studied by GC-MS and EI-MS.

The reaction of $Li_2W(NBu^t)_4$ with $SbCl_3$ and $BiCl_3$, giving respectively $Sb_2W(NBu^t)(\mu_2\text{-}NBu^t)(\mu_3\text{-}Bu^tN)_2Cl_3(\mu_2\text{-}Cl)$ **(19)** and $[Li(THF)_4]_2.Bi_2Cl_8(NH_2Bu^t)_2$ **(23)**, a by-product, could be improved by using pyridine as a solvent or co-solvent which would act as a

strong base forming C_5H_5N:HCl. Indeed, this would limit the acid hydrolysis by HCl of the lithiated species and increase the yield of **(19)** and its bismuth homologue.

Finally, the photocatalytic and gas sensor activity of all the type of deposited films could also be tested and measured. A correlation of these properties with the nitrogen doping concentration or the type of metal can also be established.

Appendices

APPENDIX 1 *Precursor system delivery*

The system deliveries can be divided into two approaches:

- The *conventional precursor deliveries*, which gather the gases contained in a cylinder (GDS) (Figure A1.1), the liquids (LIS) and solids (SDS) (Figure A1.2) contained in a bubbler can be heated to improve the volatility.

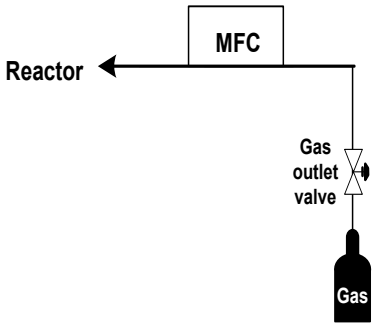

Figure A1.1 Schematic gas supply for a precursor or the carrier gas

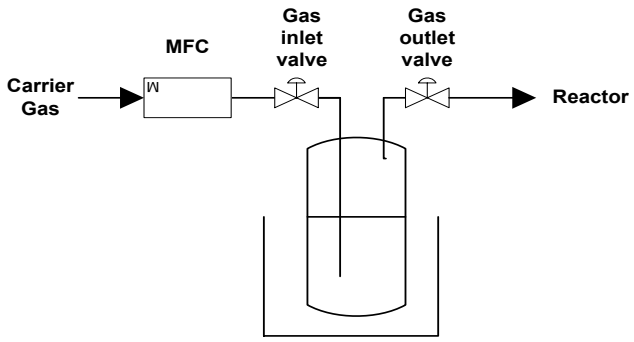

Figure A1.2 Schematic Bubbler equiped with a Mass flow controller (MFC) to measure the flow

- The *modified precursor deliveries*, such as Aerosol-Assisted Delivery Systems (AADS) (Figure A1.3) where an aerosol containing the precursor is formed. AADS is a good alternative for precursors showing a low volatility, whereas it requires a high solubility for the chosen solvent. There are others types of precursor delivery but only AADS is described below.

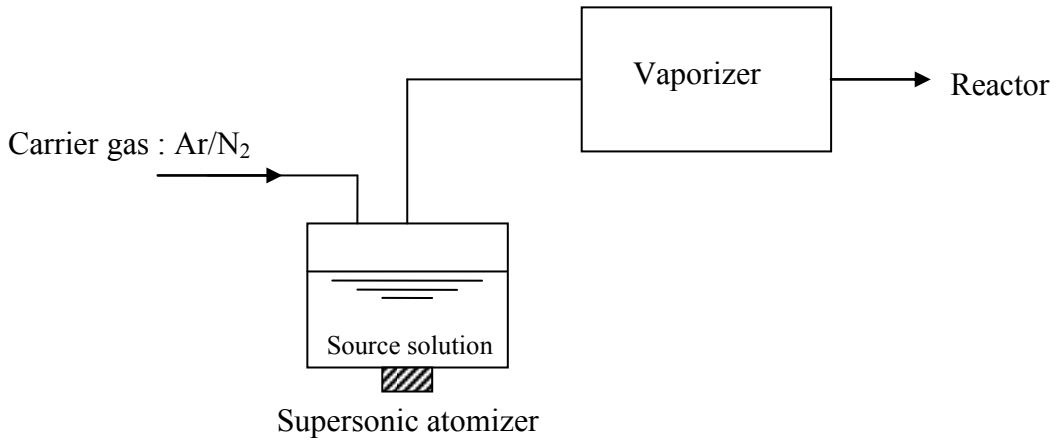

Figure A1.3 Aerosol precursor delivery

APPENDIX 2 *Instrumentation*

^{1}H, ^{13}C and ^{183}W Nuclear Magnetic Resonance Spectroscopy

^{1}H and ^{13}C, NMR spectra were recorded on a Bruker 300 or 400 and referenced to the solvent as internal standard. ^{183}W NMR was recorded on a Bruker 500 Mhz spectrometer. d_6-benzene and d_8-toluene (from Aldrich) were dried over metal potassium or sodium and d-chloroform over calcium hydride, and then distilled and finally stored over activated molecular sieves (4Å).

Single crystal X-ray crystallography

Single-crystal X-ray diffraction data were collected on a Nonius Kappa CCD diffractometer at 150°K using an Oxford Cryosystems Cryostream Cooler. Crystals coated with a hydrocarbon oil were mounted on a glass fibre with silicone grease under an argon atmosphere.

Microanalysis

Carbon, hydrogen and nitrogen were analysed for using an Exeter Analytical CE-440 microanalyser operating at 1000°C. Results were calibrated against an acetanilide [$PhNHC(O)CH_3$] standard.

Thermo Gravimetric Analysis (TGA)

The TGA was performed by using a Perkin Elmer TGA7 which measures weight changes in sample materials as a function of temperature or time.

Powder X-Ray Diffraction

The X-ray diffraction (XRD) pattern of the products was measured with a Bruker D8 powder diffractometer powder X-ray diffractometer (using Cu $K\alpha = 1.5418$ Å).

Scanning electron microscopy (SEM)

The elemental composition and the SEM were analysed by energy dispersive X-ray (EDX) analysis on a JEOL JSM6310 equiped of Energy-dispersive x-ray detector.

Transmission electron microscopy (TEM)

The particle morphology and structure were studied with TEM on a JEOL JEM1200 equiped of An Oxford Instruments INCA x-sight x-ray detector for chemical analysis.

Samples for TEM were prepared by ultrasonically dispersing the products into dry 2-propanol, placing a drop of this suspension onto a carbon copper grid.

Mass spectrometry

Mass spectrometry was performed by the EPSRC Service at the University of Bath using a Bruker Daltonik GmbH MicrOTOF-Q mass spectrometer equipped with an electrospray

ionization source. Samples were prepared under inert-atmosphere conditions in an MBraun glovebox by dissolving 1 mg of compound in 1 mL of anhydrous dichloromethane, and then diluting 1 μL of the mixture to 1 mL.

APPENDIX 3 *Crystal data and structure refinement for:*

(4) $W_4O_4(\mu_2\text{-}O)_6(tdmap)_4$	**h06kcm15**
(4') $W_4O_4(\mu_2\text{-}O)_6(tdmap)_4 \cdot 4H_2O$	**k06kcm9**
(5) $W_4O_4(OiPr)_4(\mu_2\text{-}O)_4(bdmap)_4$	**k05kcm32**
(6) $W_6O_6(\mu_2\text{-}O)_9(tdmap)_6$	**h05kcm32**
(7) $Ti_2W_2O_2(OiPr)_6(\mu_2\text{-}O)_4(\mu_3\text{-}Obdmap)_2$	**h05kcm17**
(8) $Al_2W_2O_2(OiPr)_2(\mu_2\text{-}O)_4(\mu_3\text{-}Obdmap)_4$	**k06kcm19**
(9) $[ZnW(\mu_2\text{-}Obdmap)(\mu_2\text{-}O)_3(acac)(OiPr)]_2$	**k07kcm18**
(10) $[Ni(dmap)_2(\mu_2\text{-}O)WO(OMe)_3]_4$	**k06kcm14**
(11) $[Co(acac)WO(OMe)_5]_2$	**h06kcm8**
(12) $[Ni(acac)WO(OMe)_5]_2$	**h06kcm9**
(13) $[Mg(acac)WO(OMe)_5]_2$	**k07kcm24**
(14) $[Zn(acac)WO(OMe)_5]_2$	**h06kcm25**
(15) $WO(OMe)_3(acac)$	**k07kcm25**
(16) $W(NHBu^t)_2(NBu^t)_2$	**k04kcm6**
(17) $MeZn(NH_2tBu)(NtBu)_2W(NtBu)Me$	**k06kcm15**
(19) $Sb_2W(NBu^t)(\mu_2\text{-}NBu^t)(\mu_3\text{-}Bu^tN)_2Cl_3(\mu_2\text{-}Cl)$	**k04kcm22**
(19') $Sb_2W(NBu^t)(\mu_2\text{-}NBu^t)(\mu_3\text{-}Bu^tN)_2Cl_3(\mu_2\text{-}Cl)$ + toluene	**h05kcm3**
(20) + **(21)** $[W(NBu^t)_4(NH_2Bu^t)Cl(\mu_2\text{-}Cl)]_2 + Sb_2(\mu_2\text{-}NBu^t)_2Cl_2$	**k07kcm4**
(20) + $SbCl_3$	**h05kcm5**
(22) $Sb_2W_3Cl_7(\mu_2\text{-}O)(\mu_3\text{-}O)_2(NBu^t)_3(NHBu^t)(\mu_2\text{-}NBu^t)_2$	**k05kcm1**
(19) + **(22)**	**h05kcm3**
(23) $[Li(THF)]_2.[Bi_2Cl_6(NH_2tBu)_2(\mu_2\text{-}Cl)_2]$	**h05kcm10**

Identification code	h06kcm15
Empirical formula	$C_{40}\ H_{96}\ N_{12}\ O_{14}\ W_4$
Formula weight	1704.69
Temperature	150(2) K
Wavelength	0.71073 Å
Crystal system	tetragonal
Space group	$I\ 4_1/a$
Unit cell dimensions	a = 24.9270(2)Å α = 90° b = 24.9270(2)Å β = 90° c = 9.68400(10)Å γ = 90°
Volume	6017.21(9) $Å^3$
Z	4
Density (calculated)	1.882 Mg/m^3
Absorption coefficient	7.685 mm^{-1}
F(000)	3312
Crystal size	0.25 x 0.10 x 0.05 mm
Theta range for data collection	5.40 to 30.03°
Index ranges	-35<=h<=34; -35<=k<=35; -13<=l<=13
Reflections collected	71613
Independent reflections	4370 [R(int) = 0.0569]
Reflections observed (>2σ)	3988
Data Completeness	0.993
Max. and min. transmission	0.6999 and 0.2496
Refinement method	Full-matrix least-squares on F^2
Data / restraints / parameters	4370 / 0 / 166
Goodness-of-fit on F^2	1.132
Final R indices [I>2σ(I)]	R~1 = 0.0248 wR~2 = 0.0596
R indices (all data)	R~1 = 0.0284 wR~2 = 0.0613
Largest diff. peak and hole	1.717 and -1.326 $e.Å^{-3}$

Identification code	k06kcm9
Empirical formula	$C_{40}H_{104}N_{12}O_{18}W_4$
Formula weight	1776.75
Temperature	150(2) K
Wavelength	0.71073 Å
Crystal system	Tetragonal
Space group	$I4_1/a$
Unit cell dimensions	a = 24.9240(5)Å α = 90° b = 24.9240(5)Å β = 90° c = 9.7720(2)Å γ = 90°
Volume	6070.4(2) $Å^3$
Z	4
Density (calculated)	1.944 Mg/m^3
Absorption coefficient	7.627 mm^{-1}
F(000)	3472
Crystal size	0.12 x 0.10 x 0.05 mm
Theta range for data collection	3.96 to 27.44 °
Index ranges	-32<=h<=31; -32<=k<=32; -12<=l<=12
Reflections collected	45789
Independent reflections	3466 [R(int) = 0.1427]
Reflections observed (>2σ)	2652
Data Completeness	0.994
Absorption correction	Semi-empirical from equivalents
Max. and min. transmission	0.48 and 0.33
Refinement method	Full-matrix least-squares on F^2
Data / restraints / parameters	3466 / 2 / 182
Goodness-of-fit on F^2	1.107
Final R indices [I>2σ(I)]	R^1 = 0.0405 wR_2 = 0.0766
R indices (all data)	R^1 = 0.0646 wR_2 = 0.0877
Largest diff. peak and hole	1.056 and -1.499 $eÅ^{-3}$

Notes: Asymmetric unit consists of one quarter of a molecule (with O3 located on a 2-fold rotation axis implicit in the space group symmetry) and one molecule of water. The water hydrogen atoms were located and refined at 0.89 Å from the parent oxygen, O5.

Identification code	k05kcm32
Empirical formula	$C_{80}\ H_{192}\ N_{16}\ O_{32}\ W_8$
Formula weight	3361.30
Temperature	150(2) K
Wavelength	0.71073 Å
Crystal system	monoclinic
Space group	P 21/n
Unit cell dimensions	a = 27.4610(3)Å α = 90° b = 14.6920(2)Å β = 106.243(4)° c = 30.7850(3)Å γ = 90°
Volume	11924.6(2) $Å^3$
Z	4
Density (calculated)	1.872 Mg/m^3
Absorption coefficient	7.755 mm^{-1}
F(000)	6528
Crystal size	0.35 x 0.20 x 0.15 mm
Theta range for data collection	2.91 to 21.71°
Index ranges	-28<=h<=28; -15<=k<=15; -31<=l<=32
Reflections collected	81557
Independent reflections	14039 [R(int) = 0.0753]
Reflections observed (>2σ)	12145
Data Completeness	0.995
Max. and min. transmission	0.3892 and 0.1722
Refinement method	Full-matrix least-squares on F^2
Data / restraints / parameters	14039 / 0 / 1272
Goodness-of-fit on F^2	1.179
Final R indices [I>2σ(I)]	R~1 = 0.0460 wR~2 = 0.1025
R indices (all data)	R~1 = 0.0559 wR~2 = 0.1071
Largest diff. peak and hole	1.888 and -1.383 $e.Å^{-3}$

Identification code	h05kcm32
Empirical formula	$C_{45}\,H_{99.50}\,N_{12}\,O_{21.50}\,W_6$
Formula weight	2255.97
Temperature	150(2) K
Wavelength	0.71073 Å
Crystal system	triclinic
Space group	P $\bar{1}$
Unit cell dimensions	a = 17.8400(3)Å α = 81.0700(10)° b = 18.8680(4)Å β = 72.2060(10)° c = 22.7710(5)Å γ = 87.8660(10)°
Volume	7209.3(3) $Å^3$
Z	4
Density (calculated)	2.079 Mg/m^3
Absorption coefficient	9.605 mm^{-1}
F(000)	4278
Crystal size	0.20 x 0.20 x 0.20 mm
Theta range for data collection	3.61 to 27.56°
Index ranges	-23<=h<=23; -24<=k<=24; -29<=l<=29
Reflections collected	98239
Independent reflections	29502 [R(int) = 0.0628]
Reflections observed (>2σ)	19922
Data Completeness	0.884
Max. and min. transmission	0.2496 and 0.2496
Refinement method	Full-matrix least-squares on F^2
Data / restraints / parameters	29502 / 0 / 1578
Goodness-of-fit on F^2	1.054
Final R indices [I>2σ(I)]	R~1 = 0.0500 wR~2 = 0.1114
R indices (all data)	R~1 = 0.0902 wR~2 = 0.1316
Largest diff. peak and hole	3.223 and -2.358 $e.Å^{-3}$

Identification code	h05kcm17
Empirical formula	$C_{32}H_{76}N_4O_{14}Ti_2W_2$
Formula weight	1204.47
Temperature	150(2) K
Wavelength	0.71073 Å
Crystal system	monoclinic
Space group	$P\ 2_1/n$
Unit cell dimensions	a = 12.05500(10) Å α = 90° b = 18.28200(10) Å β = 97.78° c = 21.54500(10) Å γ = 90°
Volume	4704.57(5) $Å^3$
Z	4
Density (calculated)	1.701 Mg/m^3
Absorption coefficient	5.260 mm^{-1}
F(000)	2400
Crystal size	0.40 x 0.25 x 0.20 mm
Theta range for data collection	3.59 to 30.00°
Index ranges	-16<=h<=16; -25<=k<=25; -30<=l<=30
Reflections collected	93828
Independent reflections	13659 [R(int) = 0.0651]
Reflections observed (>2sigma)	12367
Data Completeness	0.995
Max. and min. transmission	0.4193 and 0.2274
Refinement method	Full-matrix least-squares on F^2
Data / restraints / parameters	13659 / 0 / 507
Goodness-of-fit on F@2	1.091
Final R indices [I>2sigma(I)]	R~1 = 0.0298 wR~2 = 0.0737
R indices (all data)	R~1 = 0.0347 wR~2 = 0.0779
Largest diff. peak and hole	1.288 and -2.577 $e.Å^{-3}$

Identification code	k06kcm19
Chemical formula	$C_{34}H_{82}Al_2N_8O_{12}W_2$
M_r	1216.74
Cell setting, space group	Triclinic, P $\bar{1}$
Temperature (K)	150 (2)
a, b, c (Å)	12.6590 (3), 13.5940 (3), 15.3670 (4)
α, β, γ (°)	73.1920 (10), 83.0070 (10), 80.3920 (10)
V (Å^3)	2488.39 (10)
Z	2
D_x (Mg m^{-3})	1.624
Radiation type	Mo $K\alpha$
μ (mm^{-1})	4.71
Crystal form, colour	Irregular shape, pale yellow
Crystal size (mm)	0.25 × 0.10 × 0.08
T_{min}	0.385
T_{max}	0.704
No. of measured, independent and observed reflections	37813, 11321, 7198
Criterion for observed reflections	$I > 2\sigma(I)$
R_{int}	0.130
θ_{max} (°)	27.5
Refinement on	F^2
$R[F^2 > 2s(F^2)]$, $wR(F^2)$, S	0.063, 0.142, 1.04
No. of relections	11321 reflections
No. of parameters	536
H-atom treatment	Mixture of independent and constrained refinement
Weighting scheme	Calculated $w = 1/[s^2(F_o^2) + (0.0306P)^2 + 45.5683P]$ where $P = (F_o^2 + 2F_c^2)/3$
$(D/s)_{max}$	0.001
Dr_{max}, Dr_{min} (e Å^{-3})	5.30, –5.97

Identification code	k07kcm18
Chemical formula	$C_{30}H_{62}N_4O_{13}W_2Zn_2$
M_r	1185.28
Cell setting, space group	Trigonal, *R*3*c*
Temperature (K)	436 (2)
a, *b*, *c* (Å)	41.4763 (4), 41.4763 (4), 13.47590 (10)
α (°)	90.00
V (Å^3)	20076.5 (3)
Z	18
D_x (Mg m^{-3})	1.765
Radiation type	Mo Kα
μ (mm^{-1})	6.26
Crystal form, colour	Prism, colourless
Crystal size (mm)	0.25 × 0.08 × 0.08
Diffractometer	Nonius Kappa CCD
Data collection method	238 1.5 degree images with scans
Absorption correction	Multi-scan (based on symmetry-related measurements)
T_{min}	0.289
T_{max}	0.603
No. of measured, independent and observed reflections	73759, 10025, 9335
Criterion for observed reflections	$I > 2\sigma(I)$
R_{int}	0.111
θ_{max} (°)	27.5
Refinement	
Refinement on	F^2
$R[F^2 > 2s(F^2)]$, $wR(F^2)$, *S*	0.029, 0.067, 1.03
No. of relections	10025 reflections
No. of parameters	472
H-atom treatment	Not refined
Weighting scheme	Calculated $w = 1/[\sigma^2(F_o^2) + (0.0306P)^2 + 45.5683P]$ where $P = (F_o^2 + 2F_c^2)/3$
$(\Delta/\sigma)_{max}$	0.009
$\Delta\rho_{max}$, $\Delta\rho_{min}$ (e Å^{-3})	0.58, –0.95

Identification code	h06kcm8
Empirical formula	$C_{10}H_{22}CoO_8W$
Formula weight	513.06
Temperature	150(2) K
Wavelength	0.71073 Å
Crystal system	triclinic
Space group	$P\bar{1}$
Unit cell dimensions	a = 8.00600(10)Å α = 111.9000(10)° b = 10.54000(10)Å β = 91.4630(10)° c = 10.8350(2)Å γ = 111.6170(10)°
Volume	774.450(19) Å3
Z	2
Density (calculated)	2.200 Mg/m3
Absorption coefficient	8.522 mm-1
F(000)	494
Crystal size	0.50 x 0.25 x 0.10 mm
Theta range for data collection	5.30 to 30.07 deg.
Index ranges	-11<=h<=11; -14<=k<=14; -15<=l<=15
Reflections collected	18262
Independent reflections	4459 [R(int) = 0.0988]
Reflections observed (>2σ)	4317
Data Completeness	0.982
Max. and min. transmission	0.4828 and 0.1002
Refinement method	Full-matrix least-squares on F2
Data / restraints / parameters	4459 / 0 / 188
Goodness-of-fit on F2	1.060
Final R indices [I>2σ(I)]	R~1 = 0.0434 wR~2 = 0.1114
R indices (all data)	R~1 = 0.0443 wR~2 = 0.1125
Largest diff. peak and hole	3.714 and -4.833 e.-3

Identification code	h06kcm9
Empirical formula	$C_{10} H_{22} Ni O_8 W$
Formula weight	512.84
Temperature	150(2) K
Wavelength	0.71073 Å
Crystal system	triclinic
Space group	$P\ \bar{1}$
Unit cell dimensions	a = 8.00500(10) Å α = 112.0450(10)° b = 10.5280(2) Å β = 91.4130(10)° c = 10.7930(2) Å γ = 111.6310(10)°
Volume	769.57(2) $Å^3$
Z	2
Density (calculated)	2.213 Mg/m^3
Absorption coefficient	8.721 mm^{-1}
F(000)	496
Crystal size	0.38 x 0.15 x 0.10 mm
Theta range for data collection	5.67 to 30.09°
Index ranges	-11<=h<=11; -14<=k<=14; -15<=l<=15
Reflections collected	14711
Independent reflections	4461 [R(int) = 0.1720]
Reflections observed (>2σ)	4194
Data Completeness	0.988
Max. and min. transmission	0.4759 and 0.1363
Refinement method	Full-matrix least-squares on F^2
Data / restraints / parameters	4461 / 0 / 188
Goodness-of-fit on F^2	1.050
Final R indices [I>2σ(I)]	R~1 = 0.0728 wR~2 = 0.1803
R indices (all data)	R~1 = 0.0747 wR~2 = 0.1842
Largest diff. peak and hole	5.669 and -6.825 $e.Å^{-3}$

Identification code	k07kcm24
Chemical formula	$C_{20}H_{44}Mg_2O_{16}W_2$
M_r	956.87
Cell setting, space group	Triclinic, *P*-1
Temperature (K)	150 (2)
a, *b*, *c* (Å)	8.0177 (1), 10.5773 (1), 10.8150 (2)
α, β, γ (°)	111.978 (1), 91.274 (1), 111.763 (1)
V (Å^3)	775.89 (2)
Z	1
D_x (Mg m^{-3})	2.048
Radiation type	Mo *K*α
□ (mm^{-1})	7.52
Crystal form, colour	Block, colourless
Crystal size (mm)	0.35 × 0.30 × 0.15
Diffractometer	Nonius Kappa CCD
Data collection method	215 2.0 degree images with □ scans
Absorption correction	Multi-scan (based on symmetry-related measurements)
T_{min}	0.145
T_{max}	0.323
No. of measured, independent and observed reflections	14803, 4524, 4396
Criterion for observed reflections	$I > 2\sigma(I)$
R_{int}	0.045
θ_{max} (°)	30.1
Refinement on	F^2
$R[F^2 > 2\sigma(F^2)]$, $wR(F^2)$, *S*	0.024, 0.059, 1.12
No. of relections	4524 reflections
No. of parameters	188
H-atom treatment	Not refined
Weighting scheme	Calculated $w = 1/[\sigma^2(F_o^2) + (0.0271P)^2 + 0.6494P]$ where $P = (F_o^2 + 2F_c^2)/3$
$(\Delta/\sigma)_{max}$	0.002
$\Delta\rho_{max}$, $\Delta\rho_{min}$ (e Å^{-3})	1.26, –2.39

Identification code	h06kcm25
Empirical formula	$C_{20}\ H_{44}\ O_{16}\ W_2\ Zn_2$
Formula weight	1038.99
Temperature	150(2) K
Wavelength	0.71073 Å
Crystal system	triclinic
Space group	P $\bar{1}$
Unit cell dimensions	a = 8.016 Å α = 111.98° b = 10.561Å β = 91.30° c = 10.837Å γ = 111.68°
Volume	776.6 $Å^3$
Z	1
Density (calculated)	2.221 Mg/m^3
Absorption coefficient	8.974 mm^{-1}
F(000)	500
Crystal size	0.15 x 0.10 x 0.05 mm
Theta range for data collection	3.14 to 27.51°
Index ranges	-10<=h<=10; -13<=k<=13; -13<=l<=14
Reflections collected	5821
Independent reflections	2841 [R(int) = 0.0592]
Reflections observed (>2σ)	2371
Data Completeness	0.793
Max. and min. transmission	0.6625 and 0.3463
Refinement method	Full-matrix least-squares on F^2
Data / restraints / parameters	2841 / 0 / 188
Goodness-of-fit on F^2	1.027
Final R indices [I>2sigma(I)]	R~1 = 0.0538 wR~2 = 0.1289
R indices (all data)	R~1 = 0.0666 wR~2 = 0.1355
Largest diff. peak and hole	1.726 and -4.066 $e.Å^{-3}$

Identification code	k07kcm25
Empirical formula	$C_8 H_{16} O_6 W$
Formula weight	392.06
Temperature	150(2) K
Wavelength	0.71073 Å
Crystal system	monoclinic
Space group	P 2_1/m
Unit cell dimensions	a = 7.1950(3) Å α = 90° b = 12.0270(6) Å β = 113.044(2)° c = 7.3670(3) Å γ = 90°
Volume	586.63(5) Å3
Z, Calculated density	2, 2.220 Mg/m^3
Absorption coefficient	9.852 mm^{-1}
F(000)	372
Crystal size	0.35 x 0.25 x 0.25 mm
Theta range for data collection	3.00 to 27.46°
Limiting indices	-9<=h<=9, -15<=k<=15, -7<=l<=9
Reflections collected / unique	4243 / 1416 [R(int) = 0.0408]
Completeness to theta = 27.46	99.9 %
Max. and min. transmission	0.1920 and 0.1299
Refinement method	Full-matrix least-squares on F^2
Data / restraints / parameters	1416 / 1 / 86
Goodness-of-fit on F^2	1.214
Final R indices [I>2σ(I)]	R1 = 0.0255, wR2 = 0.0586
R indices (all data)	R1 = 0.0260, wR2 = 0.0588
Largest diff. peak and hole	1.028 and -2.178 e.$Å^{-3}$

Identification code	k04kcm6
Empirical formula	C_{16} H_{38} N_4 W
Formula weight	470.35
Temperature	150(2)
Wavelength	0.71073 Å
Crystal system	monoclinic
Space group	P 2_1/m
Unit cell dimensions	a = 9.3070(2) Å α = 90° b = 18.2440(2) Å β = 90° c = 12.7590(3) Å γ = 90°
Volume	2166.44(7) $Å^3$
Z, Calculated density	4, 1.442 Mg/m^3
Absorption coefficient	5.333 mm^{-1}
F(000)	944
Crystal size	0.30 x 0.10 x 0.08 mm
Theta range for data collection	3.71 to 30.04°
Limiting indices	-12<=h<=13, -25<=k<=25, -17<=l<=17
Reflections collected / unique	3158 / 1966 [R(int) = 0.0408]
Completeness to theta = 27.46	99.9 %
Max. and min. transmission	0.6905 and 0.2976
Refinement method	Full-matrix least-squares on F^2
Data / restraints / parameters	1416 / 1 / 86
Goodness-of-fit on F^2	1.164
Final R indices [I>2σ(I)]	R1 = 0.0784, wR2 = 0.1155
R indices (all data)	R1 = 0.0487, wR2 = 0.1311
Largest diff. peak and hole	1.028 and -2.178 $e.A^{-3}$

Identification code	k06kcm15
Empirical formula	C_{18} H_{44} N_4 W Zn
Formula weight	565.79
Temperature	150(2) K
Wavelength	0.71073 Å
Crystal system	Monoclinic
Space group	P21/n
Unit cell dimensions	a = 13.7450(2) Å α = 90° b = 11.8790(1) Å β = 95.366(1)° c = 15.6730(2) Å γ = 90°
Volume	2547.82(5) $Å^3$
Z	4
Density (calculated)	1.475 Mg/m^3
Absorption coefficient	5.459 mm^{-1}
F(000)	1136
Crystal size	0.40 x 0.40 x 0.40 mm
Theta range for data collection	4.01 to 30.07°
Index ranges	-19<=h<=19; -16<=k<=16; -22<=l<=22
Reflections collected	54143
Independent reflections	7456 [R(int) = 0.0792]
Reflections observed (>2σ)	6738
Data Completeness	0.995
Absorption correction	Multiscan
Max/min transmission factors	0.578 and 0.112
Refinement method	Full-matrix least-squares on F^2
Data / restraints / parameters	7456 / 2 / 240
Goodness-of-fit on F^2	1.106
Final R indices [I>2σ(I)]	R1 = 0.0257 wR2 = 0.0624
R indices (all data)	R1 = 0.0304 wR2 = 0.0669
Largest diff. peak and hole	1.489 and -1.367 $eÅ^{-3}$

Notes: Hydrogens on N4 located and refined at 0.9 Å from the parent atom.

Identification code	k04kcm22
Empirical formula	C_{16} H_{36} Cl_4 N_4 Sb_2 W
Formula weight	853.64
Temperature	150(2) K
Wavelength	0.71073 Å
Crystal system	monoclinic
Space group	P 2_1/n
Unit cell dimensions	a = 14.2340(2) Å alpha = 90° b = 11.8730(2) Å beta = 105.2920(10)° c = 16.3270(2) Å gamma = 90°
Volume	2661.57(7) $Å^3$
Z, Calculated density	4, 2.130 Mg/m^3
Absorption coefficient	6.738 mm^{-1}
F(000)	1616
Crystal size	0.40 x 0.30 x 0.15 mm
Theta range for data collection	4.42 to 30.07°
Limiting indices	-20<=h<=18, -16<=k<=16, -22<=l<=22
Reflections collected / unique	56702 / 7699 [R(int) = 0.0954]
Completeness to theta = 30.07	98.7 %
Max. and min. transmission	0.4314 and 0.1736
Refinement method	Full-matrix least-squares on F^2
Data / restraints / parameters	7699 / 0 / 256
Goodness-of-fit on F^2	1.183
Final R indices [I>2σ(I)]	R1 = 0.0336, wR2 = 0.0834
R indices (all data)	R1 = 0.0357, wR2 = 0.0850
Largest diff. peak and hole	2.334 and -2.932 e.Å-3

Identification code	k05kcm3
Empirical formula	$C_{23}\ H_{44}\ Cl_4\ N_4\ Sb_2\ W$
Formula weight	945.77
Temperature	150(2) K
Wavelength	0.71073 Å
Crystal system	monoclinic
Space group	P 21/a
Unit cell dimensions	a = 11.91500(10) Å σ = 90° b = 14.5460(2) Å β = 97.1950(10)° c = 18.7420(3) Å γ = 90°
Volume	3222.70(7) $Å^3$
Z	4
Density (calculated)	1.949 Mg/m^3
Absorption coefficient	5.576 mm^{-1}
F(000)	1816
Crystal size	0.35 x 0.30 x 0.10 mm
Theta range for data collection	3.45 to 30.99°
Index ranges	-17<=h<=17; -21<=k<=21; -27<=l<=27
Reflections collected	49544
Independent reflections	10112 [R(int) = 0.0678]
Reflections observed (>2σ)	9598
Data Completeness	0.987
Max. and min. transmission	0.6055 and 0.2457
Refinement method	Full-matrix least-squares on F^2
Data / restraints / parameters	10112 / 0 / 320
Goodness-of-fit on F^2	1.155
Final R indices [I>2σ(I)]	R~1 = 0.0373 wR~2 = 0.0983
R indices (all data)	R~1 = 0.0396 wR~2 = 0.0995
Largest diff. peak and hole	3.318 and -2.604 $e.Å^{-3}$

Identification code	k07kcm4
Chemical formula	$C_{32}H_{76}Cl_6N_8Sb_2W_2$
M_r	1396.91
Cell setting, space group	Monoclinic, P 21/n
Temperature (K)	150 (2)
a, b, c (Å)	12.5690 (3), 9.7380 (2), 21.0410 (5)
α , β, γ (°)	90.00, 92.1830 (10), 90.00
V (Å^3)	2573.48 (10)
Z	2
D_x (Mg m^{-3})	1.803
Radiation type	Mo $K\alpha$
μ (mm^{-1})	5.84
Crystal form, colour	needle, pale yellow
Crystal size (mm)	0.20 × 0.05 × 0.05
T_{min}	0.388
T_{max}	0.759
No. of measured, independent and observed reflections	26964, 5860, 4084
Criterion for observed reflections	$I > 2\sigma(I)$
R_{int}	0.063
θ_{max} (°)	27.5
Intensity decay (%)	0
Refinement	
Refinement on	F^2
$R[F^2 > 2\sigma(F^2)]$, $wR(F^2)$, S	0.048, 0.134, 1.03
No. of relections	5860 reflections
No. of parameters	306
H-atom treatment	Mixture of independent and constrained refinement
Weighting scheme	Calculated $w = 1/[\sigma^2(F_o^2) + (0.0537P)^2 + 17.022P]$ where $P = (F_o^2 + 2F_c^2)/3$
$(\Delta/\sigma)_{max}$	0.001
$\Delta\rho_{max}$, $\Delta\rho_{min}$ (e Å^{-3})	2.69, –2.41

Identification code	h05kcm5
Empirical formula	$C_{24}\ H_{54}\ Cl_{10}\ N_6\ Sb_2\ W_2$
Formula weight	1392.43
Temperature	150(2) K
Wavelength	0.71073 A
Crystal system	orthorhombic
Space group	P c 2_1 n
Unit cell dimensions	a = 9.72800(10) Å α = 90° b = 21.3290(3) Å β = 90° c = 22.1190(2) Å γ = 90°
Volume	4589.44(9) A^3
Z, Calculated density	4, 2.015 Mg/m^3
Absorption coefficient	6.767 mm^{-1}
F(000)	2640
Crystal size	0.35 x 0.30 x 0.10 mm
Theta range for data collection	2.95 to 30.03 deg.
Limiting indices	-13<=h<=13, -30<=k<=30, -31<=l<=31
Reflections collected / unique	54206 / 13037 [R(int) = 0.1229]
Completeness to theta = 30.03	99.4 %
Max. and min. transmission	0.5510 and 0.2004
Refinement method	Full-matrix least-squares on F^2
Data / restraints / parameters	13037 / 1 / 388
Goodness-of-fit on F^2	2.181
Final R indices [I>2σ(I)]	R1 = 0.1222, wR2 = 0.2892
R indices (all data)	R1 = 0.1289, wR2 = 0.2963
Absolute structure parameter	0.346(15)
Largest diff. peak and hole	30.881 and -5.590 $e.Å^{-3}$

Identification code	k05kcm1
Empirical formula	$C_{30}\ H_{70}\ Cl_7\ N_6\ O_{4.50}\ Sb_2W_3$
Formula weight	1630.12
Temperature	150(2) K
Wavelength	0.71073 Å
Crystal system	Monoclinic
Space group	P21/c
Unit cell dimensions	a = 12.19400(10) Å α= 76.3140(10)° b = 12.8310(2) Å β = 85.3960(10)° c = 18.2980(3) Å γ = 71.8370(10)°
Volume	2642.98(6) $Å^3$
Z	2
Density (calculated)	2.048 Mg/m^3
Absorption coefficient	7.903 mm^{-1}
F(000)	1542
Crystal size	0.50 x 0.40 x 0.20 mm
Theta range for data collection	3.16 to 25.08°
Index ranges	-14<=h<=14; -15<=k<=15; -21<=l<=21
Reflections collected	35200
Independent reflections	9308 [R(int) = 0.0468]
Reflections observed (>2σ)	9007
Data Completeness	0.989
Absorption correction	None
Refinement method	Full-matrix least-squares on F^2
Data / restraints / parameters	9308 / 3 / 522
Goodness-of-fit on F^2	1.190
Final R indices [I>2σ(I)]	R~1 = 0.0367 wR~2 = 0.0907
R indices (all data)	R~1 = 0.0389 wR~2 = 0.0920
Largest diff. peak and hole	2.121 and -2.817 $e.Å^{-3}$

Identification code	h05kcm3
Empirical formula	$C_{46}\ H_{103}\ Cl_{11}\ N_{10}\ O_3\ Sb_4\ W_4$
Formula weight	2456.73
Temperature	150(2) K
Wavelength	0.71073 Å
Crystal system	Monoclinic
Space group	P21/c
Unit cell dimensions	a = 12.02300(10) Å α = 90° b = 31.2910(3) Å β = 102.2230(10)° c = 20.7330(3) Å γ = 90°
Volume	7623.18(15) $Å^3$
Z	4
Density (calculated)	2.141 Mg/m^3
Absorption coefficient	7.830 mm^{-1}
F(000)	4640
Crystal size	0.30 x 0.13 x 0.13 mm
Theta range for data collection	3.41 to 27.47°
Index ranges	-15<=h<=15; -40<=k<=40; -26<=l<=26
Reflections collected	73250
Independent reflections	17012 [R(int) = 0.0963]
Reflections observed (>2σ)	11369
Data Completeness	0.974
Absorption correction	None
Refinement method	Full-matrix least-squares on F^2
Data / restraints / parameters	17012 / 3 / 762
Goodness-of-fit on F^2	0.978
Final R indices [I>2σ(I)]	R~1 = 0.0482 wR~2 = 0.0963
R indices (all data)	R~1 = 0.0904 wR~2 = 0.1081
Largest diff. peak and hole	2.742 and -2.323 $e.Å^{-3}$

Identification code	h05kcm10
Empirical formula	C_{40} H_{86} Bi_2 Cl_8 Li_2 N_2 O_8
Formula weight	1438.55
Temperature	150(2) K
Wavelength	0.71073 Å
Crystal system	orthorhombic
Space group	P 2_1 n b
Unit cell dimensions	a = 15.49700(10) Å α = 90°
	b = 18.5810(2) Å β = 90°
	c = 20.6130(2) Å γ = 90°
Volume	5935.51(9) $Å^3$
Z	4
Density (calculated)	1.610 Mg/m^3
Absorption coefficient	6.324 mm^{-1}
F(000)	2848
Crystal size	0.40 x 0.35 x 0.35 mm
Theta range for data collection	4.93 to 27.54 °.
Index ranges	-20<=h<=20; -24<=k<=24; -26<=l<=23
Reflections collected	90898
Independent reflections	13524 [R(int) = 0.0887]
Reflections observed (>2σ)	10648
Data Completeness	0.988
Absorption correction	None
Refinement method	Full-matrix least-squares on F^2
Data / restraints / parameters	13524 / 2 / 560
Goodness-of-fit on F^2	1.090
Final R indices [I>2σ(I)]	R~1 = 0.0706 wR~2 = 0.1695
R indices (all data)	R~1 = 0.0861 wR~2 = 0.1838
Absolute structure parameter	0.499(10)
Largest diff. peak and hole	3.319 and -1.095 e.Å-3